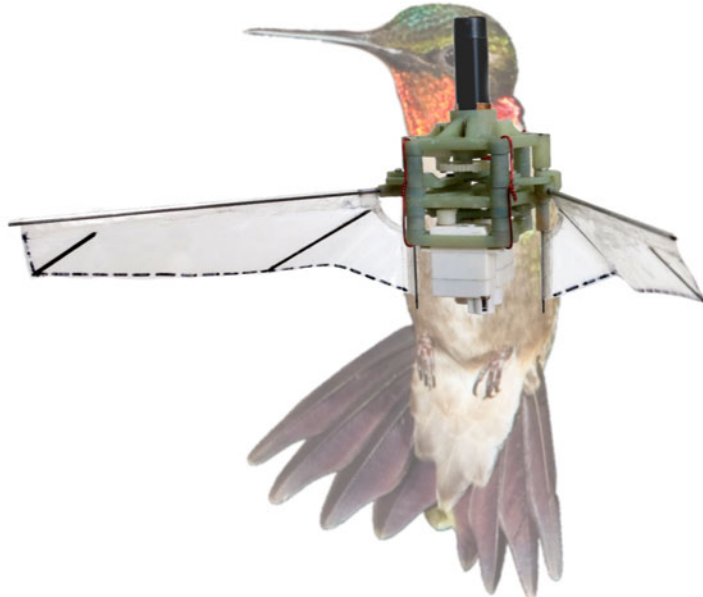


École polytechnique de Bruxelles

Robotic hummingbird:  
Design of a control mechanism for a hovering  
flapping wing micro air vehicle

Matěj KARÁSEK



*Thesis submitted in candidature for the  
degree of Doctor in Engineering Sciences*

November 2014

---

Active Structures Laboratory  
Department of Mechanical Engineering and Robotics

---

---

The composite image at the front cover uses a photograph of Ruby-throated hummingbird by Jason Paluck: <http://www.flickr.com/photos/jasonpaluck/4744474530/>

# **Jury**

Supervisor: Prof. André Preumont (ULB)

President: Prof. Patrick Hendrick (ULB)

Secretary: Prof. Johan Gyselinck (ULB)

Membres:

Dr. Guido de Croon (Delft University of Technology)

Dr. Franck Ruffier (CNRS / Aix-Marseille University)

Prof. Jean-Louis Deneubourg (ULB)

Prof. Emanuele Garone (ULB)



To my grandfather, Stano...



# Acknowledgements

First of all, I would like to thank to my supervisor, professor André Preumont, for inviting me to join the Active Structures Laboratory (ASL) as a visiting researcher and, after one year, for giving me the opportunity to stay and continue with my PhD on the exciting project of robotic hummingbird for another nearly four years. I am extremely grateful for his guidance, for his many ideas as well as challenging questions and, last but not least, for his permanent availability.

I remain also deeply obliged to my former supervisor, professor Michael Valášek from Czech Technical University in Prague, who gave me the chance to go to Belgium while taking the risk of losing me.

Many thanks belong to all my ASL colleagues. In particular, I would like to thank to Laurent Gelbgras for introducing me to the hummingbird project and for all his work at the project beginning. I really enjoyed our collaboration and the numerous discussions we had. Many thanks go to Yanghai Nan and Mohamed Lalami, who joined the project later, but quickly became valuable members of the team with whom it was a pleasure to cooperate. They deserve special thanks for assembling and testing the prototypes, designing and manufacturing the wings and for their work on the control design. I am also grateful to Renaud Bastaits for helping me a lot with my FRIA fellowship proposal, among other things. I want to thank to Iulian Romanescu together with Mihaita Horodinca and Ioan Burda for their expertise in manufacturing, technology and electronics that was behind all the experimental setups used in this work. I would like to thank to Geoffrey Warniez for manufacturing many parts. Hussein Altartouri deserves my thanks for helping me with the final version corrections. And I thank to all other lab members (Martin, José, Bilal, Christophe, David A., Elodie, Isabelle, Pierre, David T., Gonçalo, ...) for their advices and for the friendly atmosphere there was among us.

I must not forget to thank to all the interns and students whose projects and master theses were, closely or remotely, related to this work, namely to Servane Le Néel, Lin Jin, Yassine Loudad, Michael Ngoy Kabange, El Habib Damani, Arnaud Ronse

De Craene, Beatriz Aldea Pueyo, Ilias El Makrini, Raphael Girault, Mathieu Dumas, Neda Nourshamsi, Roger Tilmans, Nicolas Cormond, Alexandre Hua, Romain Hamel, Małgorzata Sudol, Tristan de Crombrugghe, Hava Özdemir and others that I might have already forgotten.

I want to thank to the BEAMS department for lending us their high speed camera many times.

I am very grateful to Marie Curie Research Training Networks, which financed my first year as a visiting researcher at ASL, and to F.R.S.-FNRS for the F.R.I.A. fellowship (FC 89554) financing most of my PhD studies.

I would like to thank to all my Czech friends for paying me numerous visits in Brussels and for finding some time to meet me whenever I went back home. Many thanks goes also to my friends in Brussels for all the outdoor activities, which worked great for taking my mind off this work every now and then.

Finally, I want to thank all my family, my brother and sister, my grandparents and my parents for their love, continuous support and encouragements! And to Barney, the dog, of course...

# Abstract

The use of drones, also called unmanned aerial vehicles (UAVs), is increasing every day. These aircraft are piloted either remotely by a human pilot or completely autonomously by an on-board computer. UAVs are typically equipped with a video camera providing a live video feed to the operator. While they were originally developed mainly for military purposes, many civil applications start to emerge as they become more affordable.

Micro air vehicles are a subgroup of UAVs with a size and weight limitation; many are designed also for indoor use. Designs with rotary wings are generally preferred over fixed wings as they can take off vertically and operate at low speeds or even hover. At small scales, designs with flapping wings are being explored to try to mimic the exceptional flight capabilities of birds and insects.

The objective of this thesis is to develop a control mechanism for a robotic hummingbird, a bio-inspired tail-less hovering flapping wing MAV. The mechanism should generate moments necessary for flight stabilization and steering by an independent control of flapping motion of each wing.

The theoretical part of this work uses a quasi-steady modelling approach to approximate the flapping wing aerodynamics. The model is linearised and further reduced to study the flight stability near hovering, identify the wing motion parameters suitable for control and finally design a flight controller. Validity of this approach is demonstrated by simulations with the original, non-linear mathematical model.

A robotic hummingbird prototype is developed in the second, practical part. Details are given on the flapping linkage mechanism and wing design, together with tests performed on a custom built force balance and with a high speed camera. Finally, two possible control mechanisms are proposed: the first one is based on wing twist modulation via wing root bars flexing; the second modulates the flapping amplitude and offset via flapping mechanism joint displacements. The performance of the control mechanism prototypes is demonstrated experimentally.



# Glossary

## List of abbreviations

ASL	Active Structures Laboratory
BL DC	Brushless Direct Current electric motor
BR DC	Brushed Direct Current electric motor
CFRP	Carbon Fibre Reinforced Polymer
COG	Centre of Gravity
CP	Centre of Pressure
DARPA	Defense Advanced Research Projects Agency, United States
DOF	Degree of Freedom
FDM	Fused Deposition Modelling
IMU	Inertial Measurement Unit
LQR	Linear-Quadratic Regulator
MAV	Micro Air Vehicle
RC	Radio-Controlled
SISO	Single-Input Single-Output (system)
SMA	Shape Memory Alloy
SLS	Selective Laser Sintering
UAV	Unmanned Aerial Vehicle
ULB	Université Libre de Bruxelles

## Nomenclature

$\dot{x}$	First derivative of $x$ with respect to time
$\ddot{x}$	Second derivative of $x$ with respect to time
$\bar{x}$	Cycle averaged value of $x$ ( $x$ represents forces, moments, speed), average value of $x$ ( $x$ represents dimensions)
$\hat{x}$	$x$ divided by mass ( $x$ represents forces), by inertia (moments) or by characteristic length (dimensions)
$x_e$	Equilibrium value of $x$
$\Delta x$	Difference from equilibrium value of $x$

$F'$	Wing section force
$F_{tr}, F_r, F_a$	Quasi-steady components of force $F$ due to translation, rotation and added mass
$F_x = \frac{\partial F}{\partial x}, M_x = \frac{\partial M}{\partial x}$	Stability derivatives (partial derivatives of force $F$ / moment $M$ with respect to system state $x$ )
$F_p = \frac{\partial F}{\partial p}, M_p = \frac{\partial M}{\partial p}$	Control derivatives (partial derivatives of force $F$ / moment $M$ with respect to control parameter $p$ )
$A(s)/B(s)$	Transfer function of Laplace transforms of input $b(t)$ to output $a(t)$

## List of symbols

$\alpha, \alpha_g$	Angle of attack, geometric angle of attack
$\alpha_0, \alpha_m$	Angle of attack offset and magnitude around mid-stroke
$\alpha_{34}$	Angle of intermediary link 34 of the flapping mechanism
$\alpha^*$	Wing inclination angle
$\beta$	Mean stroke plane angle
$\delta$	Wing deviation angle
$\delta_{m1}, \delta_{m2}$	Amplitudes of oval and figure-of-eight deviation patterns
$\Delta x, \Delta y$	x and y distance from the nominal position of the displaced joints
$\epsilon_L, \epsilon_R$	Left and right offset servo angle
$\eta$	Roll servo angle
$\eta_m$	Motor efficiency
$\gamma$	Wing root bar angle
$\Gamma$	Circulation
$\lambda$	System pole
$\nu$	Kinematic viscosity
$\omega$	Body angular velocity vector
$\omega_m$	Motor angular velocity
$\omega_W, \omega_{wx}, \omega_{wy}, \omega_{wz}$	Wing angular velocity vector and its components
$\Omega_W$	Wing angular velocity skew-symmetric matrix
$\phi, \phi_0, \phi_m$	Sweep angle, sweep angle offset and amplitude
$\phi_{max}, \phi_{min}$	Maximal and minimal measured flapping angle
$\phi_{root}, \phi_{tip}$	Flapping angle measured at wing root and at wing tip
$\Phi$	Flapping amplitude
$\varphi, \vartheta, \psi$	Roll, pitch and yaw body angles
$\varphi_\alpha$	Phase shift between wing inclination and wing sweep
$\Psi, \psi_3$	Intermediary link 34 amplitude and angle
$\rho$	Air density

$\theta$	Flapping mechanism input angle
$\mathcal{A}R$	Wing aspect ratio
$A_1, A_2$	Flapping mechanism dimensions
$\mathbf{A}_{\text{long}}, \mathbf{A}_{\text{lat}}$	System matrices of longitudinal and lateral dynamics
$B$	Distance between force balance sensors
$\mathbf{B}_{\text{long}}, \mathbf{B}_{\text{lat}}$	Input matrices of longitudinal and lateral dynamics
$c, \bar{c}, \hat{c}$	Wing chord, mean wing chord and normalized wing chord
$C_L, C_D$	Lift and drag coefficients
$C_N, C_T$	Normal and tangential force coefficients
$e$	Chest width (distance between wing shoulders)
$f$	Flapping frequency
$F_L, F_D$	Lift and drag forces
$F_N, F_T$	Normal and tangential forces
$g$	Gravity acceleration
$H$	Vertical distance of the prototype from the force sensors
$I_{xx}, I_{yy}, I_{zz}, I_{xz}$	Moments of inertia and inertia product in body axes
$J$	Advance ratio
$\mathbf{J}, \mathbf{J}_S, \mathbf{J}_A, \mathbf{J}_{\text{red}}$	Matrix of control derivatives, for symmetric, asymmetric and reduced set of wing motion parameter changes
$k_\alpha, k_\phi$	Wing inclination and sweep angle function shape parameters
$k_{\text{hover}}$	Reduced frequency in hover
$k_p, k_q$	Gains of roll and pitch rate feedback
$L, M, N$	Moments around body axes $x_B$ , $y_B$ and $z_B$
$L_1, \dots, L_6$	Flapping mechanism link dimensions
$L_{ext}, M_{ext}, N_{ext}$	External moments around body axes $x_B$ , $y_B$ and $z_B$
$m$	body mass
$O_B, x_B, y_B, z_B$	Body coordinate system
$O_G, x_G, y_G, z_G$	Global coordinate system
$O_W, x_W, y_W, z_W$	Wing coordinate system
$O_{SP}, x_{SP}, y_{SP}, z_{SP}$	Stroke plane coordinate system
$p, q, r$	Body angular velocity components around $x_B$ , $y_B$ and $z_B$ axes
$\mathbf{p}, p_i$	Wing motion parameters vector, its $i$ th element
$P_{el}$	Motor electrical power
$P_{mech}$	Mechanical power at the motor output
$r, \hat{r}$	Radial distance from the wing root, absolute and normalized
$\mathbf{r}$	Centre of pressure position vector in body frame
$R$	Wing length
$\mathbf{R}$	Rotation matrix
$\hat{r}_2$	Normalized radial centre of pressure position
$\mathbf{r}_c$	Centre of pressure position vector in wing frame

$R_{CP}$	Radial centre of pressure position
$\mathbf{r}_w$	Wing shoulder position vector in body frame
$R_x$	Force balance reaction
$\mathbf{R}_x, \mathbf{R}_y, \mathbf{R}_z$	Rotation matrices for rotations around x, y and z axes
$Re$	Reynolds number
$s$	Laplace transformation parameter
$S$	Wing area
$S_1, S_2$	Sensor 1 and 2 forces
$St$	Strouhal number
$t, t^+$	Time, nondimensional cycle time
$T_m$	Motor torque
$u, v, w$	Body velocity components around $x_B$ , $y_B$ and $z_B$ axes
$U, U_\infty, U_{CP}$	Wing speed, free stream speed, centre of pressure speed
$\mathbf{U}, U_x, U_y, U_z$	Wing speed vector and its components in body axes
$\mathbf{v}$	Body velocity vector
$X, Y, Z$	Forces along body axes $x_B$ , $y_B$ and $z_B$
$\mathbf{x}$	State vector
$\hat{x}_0$	Non-dimensional position of wing rotation axis
$X_{ext}, Y_{ext}, Z_{ext}$	External forces along body axes $x_B$ , $y_B$ and $z_B$
$x_w, z_w$	Wing shoulder position in body frame
$z$	Transfer function zero

# Contents

<b>Jury</b>	<b>iii</b>
<b>Acknowledgements</b>	<b>vii</b>
<b>Abstract</b>	<b>ix</b>
<b>Glossary</b>	<b>xi</b>
<b>1 Introduction</b>	<b>1</b>
1.1 UAV applications . . . . .	1
1.2 UAV types . . . . .	3
1.3 Flapping wing MAVs . . . . .	5
1.3.1 Actuators and flapping mechanisms . . . . .	5
1.3.2 Tail stabilized and passively stable MAVs . . . . .	7
1.3.3 MAVs controlled by wing motion . . . . .	9
1.4 Motivation and outline . . . . .	11
1.5 References . . . . .	13
<b>2 Flapping flight</b>	<b>17</b>
2.1 Fixed wing aerodynamics . . . . .	17
2.2 Flight in nature . . . . .	21
2.2.1 Gliding flight . . . . .	21
2.2.2 Flapping forward flight . . . . .	24
2.2.3 Hovering flight . . . . .	25
2.3 Hovering flapping flight aerodynamics . . . . .	30
2.3.1 Dynamic scaling . . . . .	30
2.3.2 Lift enhancing aerodynamic mechanisms . . . . .	31
2.3.3 Flight stability . . . . .	35
2.3.4 Attitude stabilization . . . . .	37
2.3.5 Flight control . . . . .	40
2.4 References . . . . .	40

<b>3 Mathematical modelling</b>	<b>47</b>
3.1 Flapping flight aerodynamics . . . . .	47
3.1.1 Wing kinematics . . . . .	48
3.1.2 Quasi-steady aerodynamics . . . . .	50
3.1.2.1 Force due to wing translation . . . . .	51
3.1.2.2 Force due to wing rotation . . . . .	52
3.1.2.3 Force due to the inertia of added mass . . . . .	53
3.1.2.4 Total force . . . . .	54
3.1.3 Centre of pressure velocity and angle of attack . . . . .	55
3.1.4 Comparison with CFD . . . . .	58
3.2 Body dynamics . . . . .	60
3.2.1 System linearisation . . . . .	62
3.2.2 Stability and control derivatives . . . . .	64
3.3 Reduced model of a flapping wing MAV . . . . .	65
3.4 Stability predicted by various aerodynamic models . . . . .	66
3.4.1 Stability derivatives . . . . .	67
3.4.2 Longitudinal system poles . . . . .	68
3.4.3 Lateral system poles . . . . .	69
3.4.4 Effect of derivatives $\hat{X}_q$ and $\hat{Y}_p$ . . . . .	72
3.4.5 Effect of inertia product $I_{xz}$ . . . . .	72
3.4.6 Conclusion . . . . .	74
3.5 References . . . . .	74
<b>4 Stability of near-hover flapping flight</b>	<b>77</b>
4.1 Hummingbird robot parameters . . . . .	77
4.2 Pitch dynamics . . . . .	78
4.2.1 Pitch stability derivatives . . . . .	78
4.2.2 System poles . . . . .	83
4.2.3 Active stabilization . . . . .	85
4.3 Roll dynamics . . . . .	89
4.3.1 Roll stability derivatives . . . . .	89
4.3.2 System poles . . . . .	93
4.3.3 Active stabilization . . . . .	95
4.4 Vertical and yaw dynamics stability . . . . .	96
4.5 Wing position choice . . . . .	98
4.6 Rate feedback gains . . . . .	99
4.7 Conclusion . . . . .	101
4.8 References . . . . .	101

<b>5 Flapping flight control</b>	<b>103</b>
5.1 Control design . . . . .	103
5.1.1 Pitch dynamics . . . . .	104
5.1.2 Roll dynamics . . . . .	109
5.1.3 Yaw and vertical dynamics . . . . .	112
5.1.4 Complete controller . . . . .	114
5.2 Control moment generation . . . . .	115
5.2.1 Control derivatives . . . . .	115
5.2.2 Choice of control parameters . . . . .	117
5.3 Simulation results . . . . .	118
5.4 Conclusion . . . . .	122
5.5 References . . . . .	122
<b>6 Flapping mechanism</b>	<b>125</b>
6.1 Flapping mechanism concept . . . . .	125
6.1.1 Kinematics . . . . .	126
6.1.2 Mechanism design . . . . .	128
6.1.3 Wing design . . . . .	130
6.2 Experiments . . . . .	133
6.2.1 Wing kinematics . . . . .	133
6.2.2 Force balance . . . . .	137
6.2.3 Lift production . . . . .	140
6.2.4 Wing design optimization . . . . .	140
6.3 References . . . . .	146
<b>7 Control mechanism</b>	<b>147</b>
7.1 Moment generation via wing twist modulation . . . . .	148
7.1.1 Moment generation principle . . . . .	149
7.1.2 Manually operated control mechanism performance . . . . .	150
7.1.3 SMA actuated control mechanism . . . . .	154
7.1.4 SMA driven control mechanism performance . . . . .	156
7.1.5 Conclusion on wing twist modulation . . . . .	158
7.2 Moment generation via amplitude and offset modulation . . . . .	158
7.2.1 Amplitude and offset modulation . . . . .	159
7.2.2 Control mechanism prototype . . . . .	162
7.2.3 Wing kinematics . . . . .	162
7.2.4 Control mechanism dynamics . . . . .	166
7.2.5 Pitch moment and lift generation . . . . .	168
7.2.6 Combined commands . . . . .	171
7.2.7 Conclusion on amplitude and offset modulation . . . . .	174
7.3 Discussion and conclusions . . . . .	174

7.4 References . . . . .	176
<b>8 Summary and conclusions</b>	<b>177</b>
8.1 Original aspects . . . . .	178
8.2 Future work . . . . .	178
8.3 Publications . . . . .	179
<b>General Bibliography</b>	<b>181</b>

# Chapter 1

## Introduction

Drones, also called unmanned aerial vehicles (UAVs), are aircraft without a human pilot on board that can be either remotely piloted or completely autonomous. UAVs are slowly becoming part of our daily lives. While 20 years ago they were almost exclusively used by the military, the recent technological advancements made them accessible even to the general public. Nowadays, UAVs are being used in many fields ranging from aerial photography to remote inspection and small drones can be found in hobby stores for less than €150, including a live video link.

Micro air vehicles (MAVs) are a class of UAVs restricted in size. DARPA originally defined an MAV as a micro-drone of no more than 15 cm. The term, however, started to be used more broadly and refers to smaller UAVs. Thus, palm sized UAVs are sometimes called nano air vehicles. Most MAVs can perform hovering flight and operate indoors, although this is not a requirement. Their popularity over larger UAVs increases as they are easily portable, more discreet and less dangerous in case of a crash.

### 1.1 UAV applications

UAVs are being used in various fields and their number is growing (Figure 1.1). Traditionally, UAVs are equipped with an on-board camera and provide a live video feed to the operator or to the ground station. They can be, however, also equipped with other sensor types (chemical, biological, radiation, ...).

The obvious application of camera equipped UAVs is video surveillance and reconnaissance. Apart from military use, the UAVs are starting to be employed by police and fire brigades. No men aboard and much lower costs compared to traditional

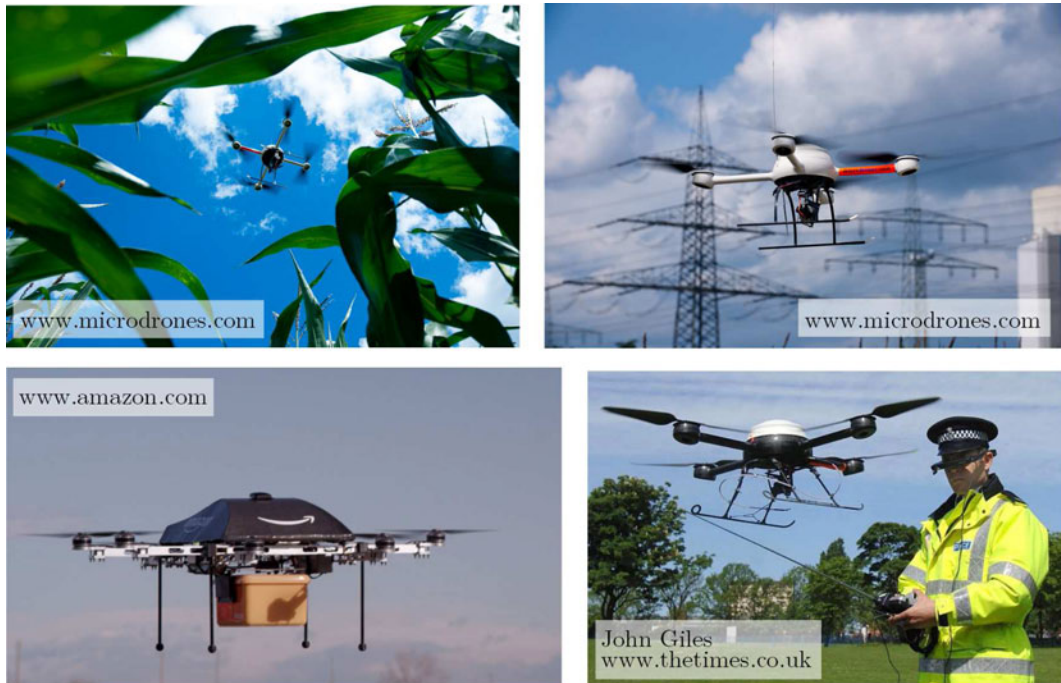


**Figure 1.1:** UAV applications: monitoring of crops, inspection of power lines, transport of packages or police air reconnaissance are just a few examples.

aircraft allows their use even in risky conditions. The UAVs can be deployed during natural catastrophes or after terrorism acts to quickly map the situation, find access routes, identify potential dangers, look for victims, ... Their small size allows them even to enter into buildings through windows and fly through confined spaces.

Another field of application is aerial photography. Images from a bird's-eye view are used for cartography, but also in archaeology, biology or in urbanism. UAVs were also quickly adopted in sports-photography and cinematography to shoot action scenes from unusual perspectives.

UAVs are further used for remote inspection of pipelines or power lines, as well as by farmers for inspecting their fields and choosing the optimal moment for fertilization or harvest. Security applications like patrolling around private properties or along the borderlines are also emerging. Last but not least, the use of UAVs for goods deliveries is being explored.

## 1.2 UAV types

UAVs can be split into three groups according to the way they generate lift force. The *fixed wing UAVs* are similar to aeroplanes. To produce enough lift, the wing needs to keep moving above certain minimal speed. This limits the use of fixed wing UAVs mostly to outdoors. On the other hand, it makes them efficient, as most energy is spent to overcome drag, and thus suitable for applications where maximum flight time is the key factor. The forward thrust is usually produced by one or several propellers. Designs with tail wings are passively stable, however, smaller MAVs are often built as flying wings, which usually require some stability augmentation by an on-board computer. Autonomous flight requires sophisticated trajectory planning, as all the manoeuvres need to stay within the aircraft's flight envelope. Some examples of fixed wing UAVs are shown in Figure 1.2.



**Figure 1.2:** Examples of fixed wing UAVs.

*Rotary wing UAVs* generate the lift by one or several rotating bladed rotors. Nowadays, four and more rotor designs, known as quadrocopters and multicopters, are the most popular UAV platform. These designs are inherently unstable and require an on-board autopilot for attitude control. This, however, makes the designs also very manoeuvrable and agile yet relatively insensitive to disturbances. Nevertheless, the smallest commercially available professional MAV, the Black Hornet by Proxdynamics, uses a traditional helicopter design with one main rotor and a stabilizing tail rotor. Examples of rotary wing UAVs are shown in Figure 1.3.

The advantage of rotary wing UAVs over fixed wing designs is the capability of vertical take-off, hovering and slow flight in any direction, which makes them useful especially in confined urban environments or even indoors. Autonomous opera-



**Figure 1.3:** Examples of rotary wing UAVs: The Black Hornet is the smallest UAV used by the British military, the firefly represents a commercial hex-rotor. For comparison, the Ladybird is a €150 mini-quadrotor for hobbyist equipped with a live video feed.

tion represents much smaller challenge: a trajectory between two waypoints can be planned as a straight line, limited only by the maximal speed. On the other hand, the rotary wing designs are less efficient compared to fixed wing UAVs and thus their flight times are limited. Hybrid designs combining the vertical take-off and low speed flight of rotary wings with flight endurance of fixed wings are also being developed.

The last group, the *flapping wing UAVs*, takes the inspiration in birds and insects. The existing designs are still immature and their performance is, for the moment, worse compared to the previous two groups. However, natural flyers with flapping wings exhibit long flight times (without any energy income) together with acrobatic skills which are far superior to any man made aircraft, especially at small scales. Thus, the vision of potentially achieving these exceptional flight qualities is what drives the active research field of flapping flight. More details on the current state of the art will be given in the next section.

Bio-mimetic approach is used also in other fields of UAV and MAV design in particular. Optical flow sensors and attitude sensors inspired by the insect compound eyes and simple eyes (Ruffier and Franceschini, 2005; Fuller et al., 2014) or MAVs flying and communicating in swarms (Hauert et al., 2009) are just a few examples.

### 1.3 Flapping wing MAVs

People have always been fascinated by flying animals. A sketch of one of the first flying machines with flapping wings, although human powered, can be found in Leonardo da Vinci's Paris Manuscript B dated 1488-1490 (Figure 1.4). However, it took another five centuries to reach a sufficient technology level that allowed us to build first bio-inspired MAVs. The field of flapping wing MAVs is still very young and provides plenty of space for improvement. The biggest challenge of flapping wing MAV design remains the integration of relatively complex flapping and control mechanisms into a small and lightweight package that can be lifted by the thrust produced.

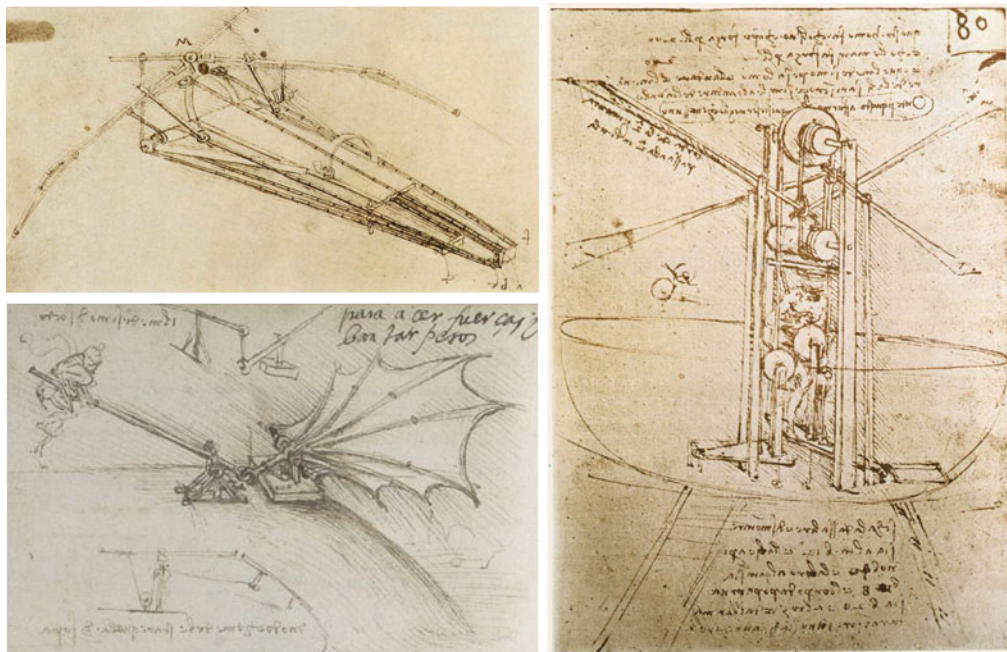


**Figure 1.4:** Sketches of human powered flying machines with flapping wings by Leonardo da Vinci from Paris Manuscript B, 1488-1490.

#### 1.3.1 Actuators and flapping mechanisms

When designing flying machines that mimic nature we need to find a replacement for the animal's powerful flight muscles as well as for their rapid metabolism supplying energy at high rates. Thanks to recent technological advancements in mobile electronic devices, batteries with high energy densities emerged. Their high capacity to mass ratio made them a very attractive power source for MAVs. Thus, the

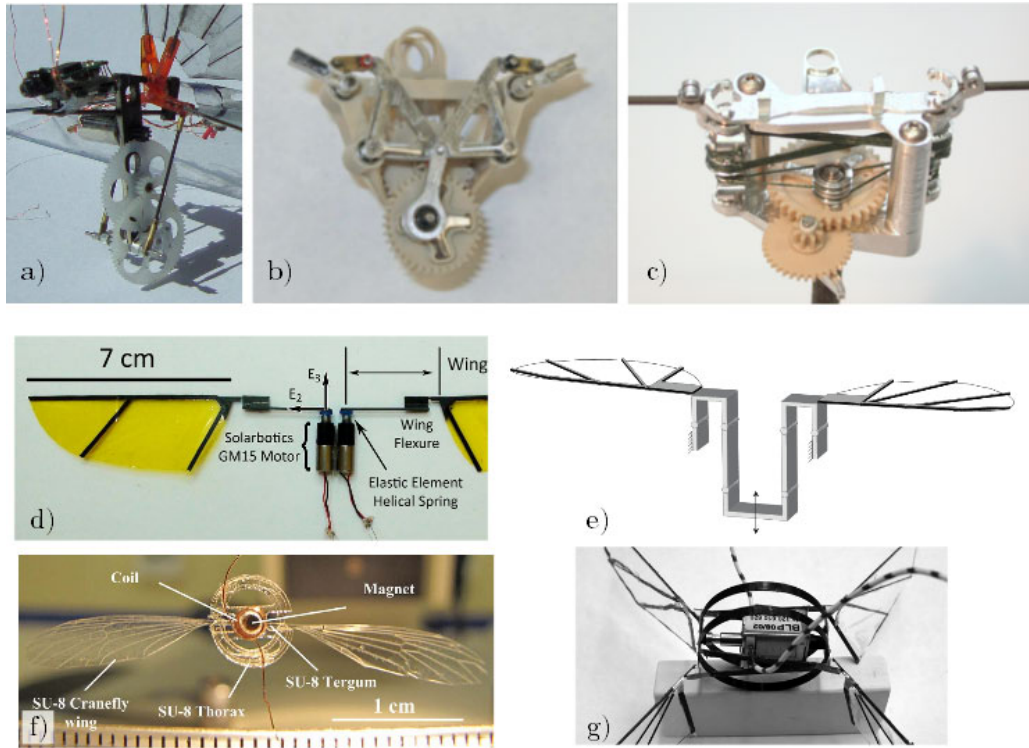


**Figure 1.5:** Examples of flapping mechanisms. a) DelFly Micro mechanism (Bruggeman, 2010), b)+c) Nano Hummingbird linkage and cable mechanism (Keenon et al., 2012), d) direct drive mechanism (Hines et al., 2014), e) compliant mechanism of Harvard robotic fly (Finio and Wood, 2010), f) flexible resonant wing (Vanneste et al., 2011), g) resonant thorax (Goosen et al., 2013).

majority of existing MAVs uses electric actuators driven by Lithium-ion (Li-ion) or Lithium-ion polymer (Li-Pol) batteries.

The most common actuator is a DC motor, either with brushes (e.g. Keenon et al., 2012) or brushless (e.g. de Croon et al., 2009). It is usually combined with a reduction gearbox and a transmission mechanism producing the flapping motion, which can either be a linkage mechanism as in Figures 1.5 a)+b) or a cable mechanism as in Figure 1.5 c). However, a direct drive option exploiting resonance is also being explored (Hines et al., 2014), see Figure 1.5 d).

Piezo-actuators are another option as they can be directly operated at the flapping frequency. They are usually combined with a (compliant) linkage mechanism (Finio and Wood, 2010), Figure 1.5 e). Some flapping mechanisms try to mimic the res-

onant thorax of insects, as this should provide high flapping amplitudes with low energy expenditure (Vanneste et al., 2011; Goosen et al., 2013). These designs are driven by electro-magnetic actuators, see Figures 1.5 f)+g).

Apart from electric drives, an internal combustion engine was successfully used to drive a larger flapping wing MAV in the past (Zdunich et al., 2007). Also a rather exotic chemical micro engine has been considered to drive a resonant thorax mechanism (Meskers, 2010).

### 1.3.2 Tail stabilized and passively stable MAVs

The first designed flapping wing MAVs were either built passively stable, or used tail surfaces for attitude stabilization. Majority of these designs have four wings and take advantage of the clap-and-fling lift enhancement mechanism, which will be explained in Section 2.3.2.

One of the first flapping wing MAVs was the Mentor shown in Figure 1.6 a), developed under a DARPA program and presented in 2002. The first generation of the vehicle had a wingspan of 36 cm and weighted, from today's perspective enormous, 580 g due to an internal combustion engine driving the device. Nevertheless the vehicle was able to take-off and hover at a flapping frequency of 30 Hz. Two pairs of wings were located at the top of the vehicle, flapping with 90° amplitude and using the clap-and-fling at both extremities. The flight was stabilized and actively controlled by fins exposed to the airflow coming from the wings. The flight endurance was up to 6 minutes. The second generation used a brushless motor and was a bit smaller and lighter (30 cm, 440 g). Its flight time was limited to only 20 s by the discharge rate of the batteries available at that time.

DelFly was developed in 2005 by TU Delft (Lentink and Dickinson, 2009) and represents one of many ornithopter projects (e.g. Park and Yoon, 2008; Yang et al., 2009). Unlike most ornithopters that fly only forward, the DelFly can also operate near hovering or even fly slowly backwards, all controlled by tail control surfaces operated by servos. Its two pairs of flapping wings are driven by a brushless motor and a linkage mechanism. It takes advantage of the clap-and-fling mechanism twice: when the lower wings meet the upper wings and also when the upper wings touch each other. The current version, the DelFly Explorer shown in Figure 1.6 b), has a wingspan of 28 cm, weights 20 g and has a flight endurance of 9 minutes (Wagter et al., 2014). It is capable of fully autonomous flight thanks to an on-board stereo-vision system (Tijmons et al., 2013). A smaller DelFly Micro shown in Figure 1.6 c) has a wingspan of 10 cm and weights only 3.07 g, including an on-board camera.

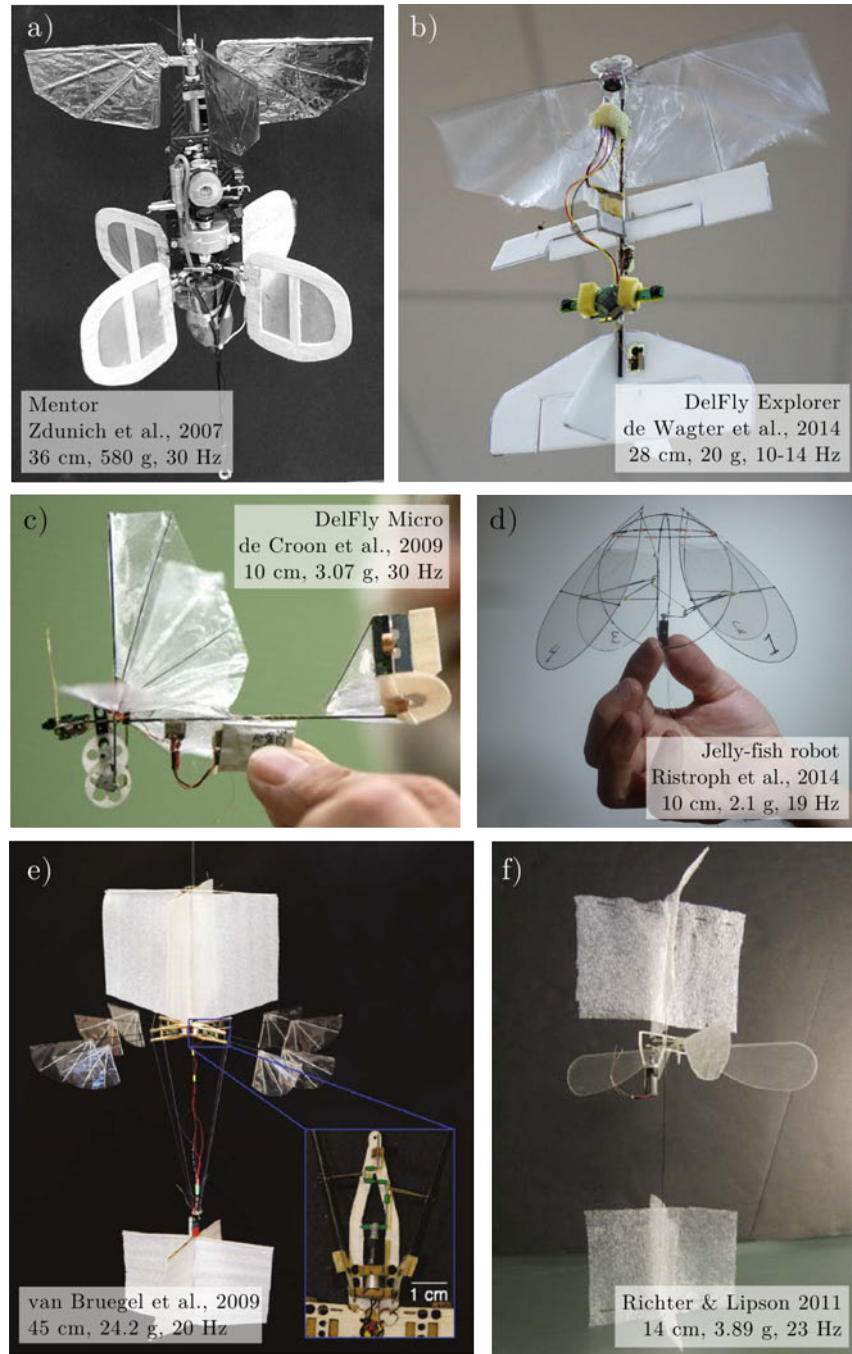


**Figure 1.6:** Examples of flapping wing MAVs that are stabilized by tail or that are passively stable.

The first hovering passively stable MAV was built at Cornell University by van Breugel et al. (2008), see Figure 1.6 e). It uses four pairs of wings, that flap and fold at both extremities. The vehicle has a 45 cm wingspan, although the wings themselves are rather short (around 85 mm). The flapping is driven by 4 DC pager motors, one for each wing pair, and the total weight is 24.2 g. The passive stability is achieved by two lightweight sails, one above the wings and one at a greater distance below the wings. The vehicle can stay in the air, without any control, for 33 s. An updated version of the previous flyer, using only 2 wing pairs and a single motor was presented by Richter and Lipson (2011). The major part of the robot, shown in Figure 1.6 f), is 3D printed, including the wings. With sails for passive stability the robot weight is 3.89 g and it can fly for 85 s.

The last passively stable MAV has been presented recently by Ristroph and Childdress (2014). Unlike the previous robots, the inspiration comes from a swimming jellyfish, see Figure 1.6 d). The vehicle has four wings, one on each side. The wings do not flap horizontally like in insects, but rather vertically. The opposing wings flap together while the neighbouring wings are in anti-phase. The vehicle is very small (10 cm) and very light (2.1 g). It carries only a DC pager motor but no power source; flying was demonstrated at 19 Hz flapping frequency while being tethered to an external power source. The jelly-fish-like wings make the vehicle inherently stable and thus it doesn't need any additional stabilizing surfaces.

### 1.3.3 MAVs controlled by wing motion

Compared to the majority of MAVs from the previous section, designs that are stabilized and controlled by adjusting the wing motion are much closer in function to their biological counterparts, insects and hummingbirds. However, they are also more complex because of the necessary control mechanisms that modify the wing kinematics. First MAV stabilized and controlled through wing motion was presented in 2011 and only three designs have demonstrated stable hovering flight so far.

The Nano Hummingbird shown in Figure 1.7 a) is an MAV funded by DARPA, presented in 2011 by AeroVironment, mimicking a hummingbird (Keenon et al., 2012). It is the only flapping wing MAV capable of true hovering as well as of flight in any direction while carrying an on-board camera with live video feed. All this is integrated into a robot with 16.5 cm wingspan weighting 19 g that has a flight endurance of up to 4 minutes. The necessary control moments are generated by independent modulation of the wing twist.

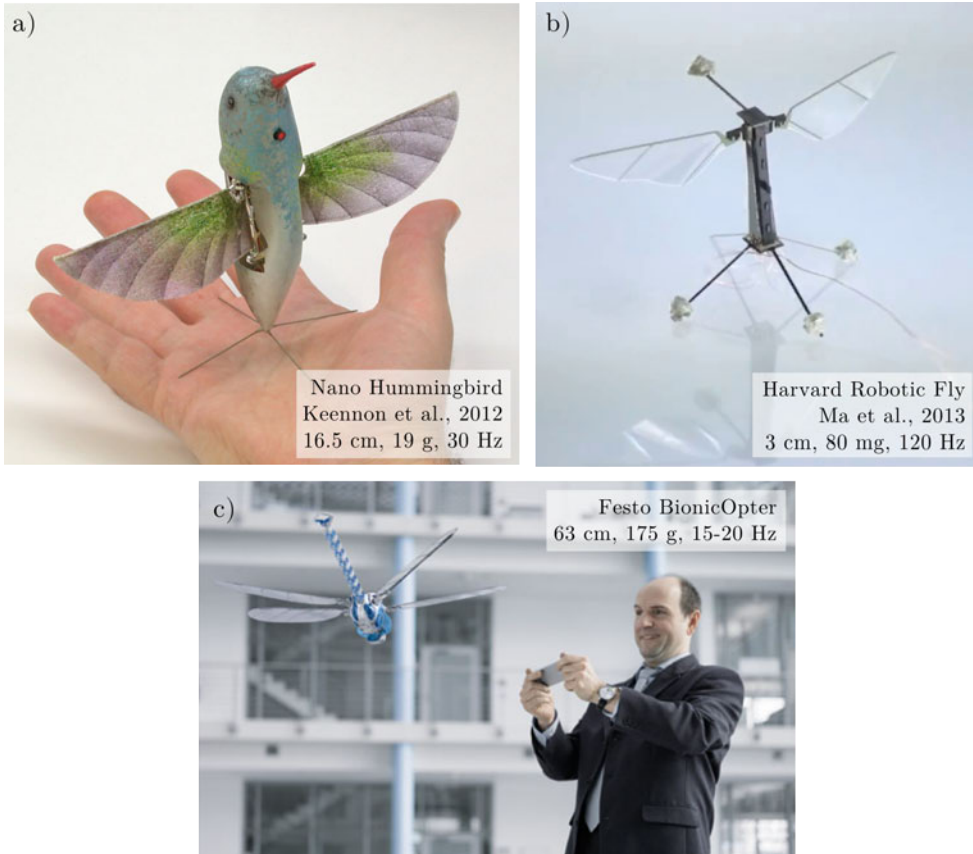


**Figure 1.7:** Examples of flapping wing MAVs that are actively controlled by wing motion.

The Harvard RoboBee with a wingspan of only 3 cm and weight of 80 mg is the smallest and lightest MAV, see Figure 1.7 b). It took off for the first time in 2008 while using guide wires for stabilization (Wood, 2008) and performed first controlled hovering flight five years later (Ma et al., 2013). It mimics insects of the Diptera order, the true flies. It has a single pair of wings that are driven independently by a pair of piezoelectric bimorph actuators. Each wing can be operated with different amplitude, different mean position and different speed in each half-stroke, so that moments along the three body axis can be produced to stabilize the robot in air. The power source as well as flight controller remain off-board for the moment.

The BionicOpter, Figure 1.7 c), was built as a technology demonstrator of Festo company (Festo, 2013). It mimics a dragonfly, although it is much larger (63 cm wingspan) and heavier (175 g). It uses four flapping wings that are driven by a single motor and that beat at a frequency of 15 Hz to 20 Hz. Their amplitude and flapping

plane inclination can be controlled independently by 8 servo motors in total, which allows independent drag and lift modulation of each wing. Thus, the vehicle can hover as well as fly in any direction without the need to pitch or roll.

## 1.4 Motivation and outline

The goal of our project is to develop a tail-less flapping wing MAV capable of hovering flight. The flight should be stabilized and controlled by adapting the wing motion. Looking into the nature, only insects and hummingbirds are capable of sustained hovering. Their wing beat frequency and total mass are linearly correlated with the wing length, see Figure 1.8. Interestingly, existing flapping wing MAVs also follow this trend.

To make our lives easier, we have chosen to mimic larger hummingbirds, which should allow us to use, at least to some extent, some of the off-the-shelf components as well as traditional technologies. Thus, the target specification for the designed robotic hummingbird was set to: 20 g total mass, 25 cm wingspan and flapping frequency between 20 and 30 Hz.

The aim of this thesis is to design a working prototype of the wing motion control mechanism that generates the control moments necessary to stabilize and control the flight. The thesis was split into two parts, theoretical (Chapters 2 - 5) and practical (Chapters 6 - 7).

Chapter 2 recalls the basics of fixed wing aerodynamics. Then, different types of flight observed in nature are explained. More details are given on hovering flapping flight, its aerodynamic mechanisms as well as control mechanisms observed in nature.

Chapter 3 introduces a mathematical model of flapping flight, which combines quasi-steady aerodynamics and rigid body dynamics. Further, the model is linearised and reduced and its validity is demonstrated by comparisons to other models, including a CFD study.

Chapter 4 is devoted to near-hover flapping flight stability. The damping effects coming from the flapping wings are explained, with a special attention given to the effect of wing position, and a simplified solution of the stability problem is proposed.

Chapter 5 describes the control design for the developed MAV, based on the linearised mathematical model. Wing kinematics parameters suitable for flight control are identified and the control performance is demonstrated on numerical simulations.

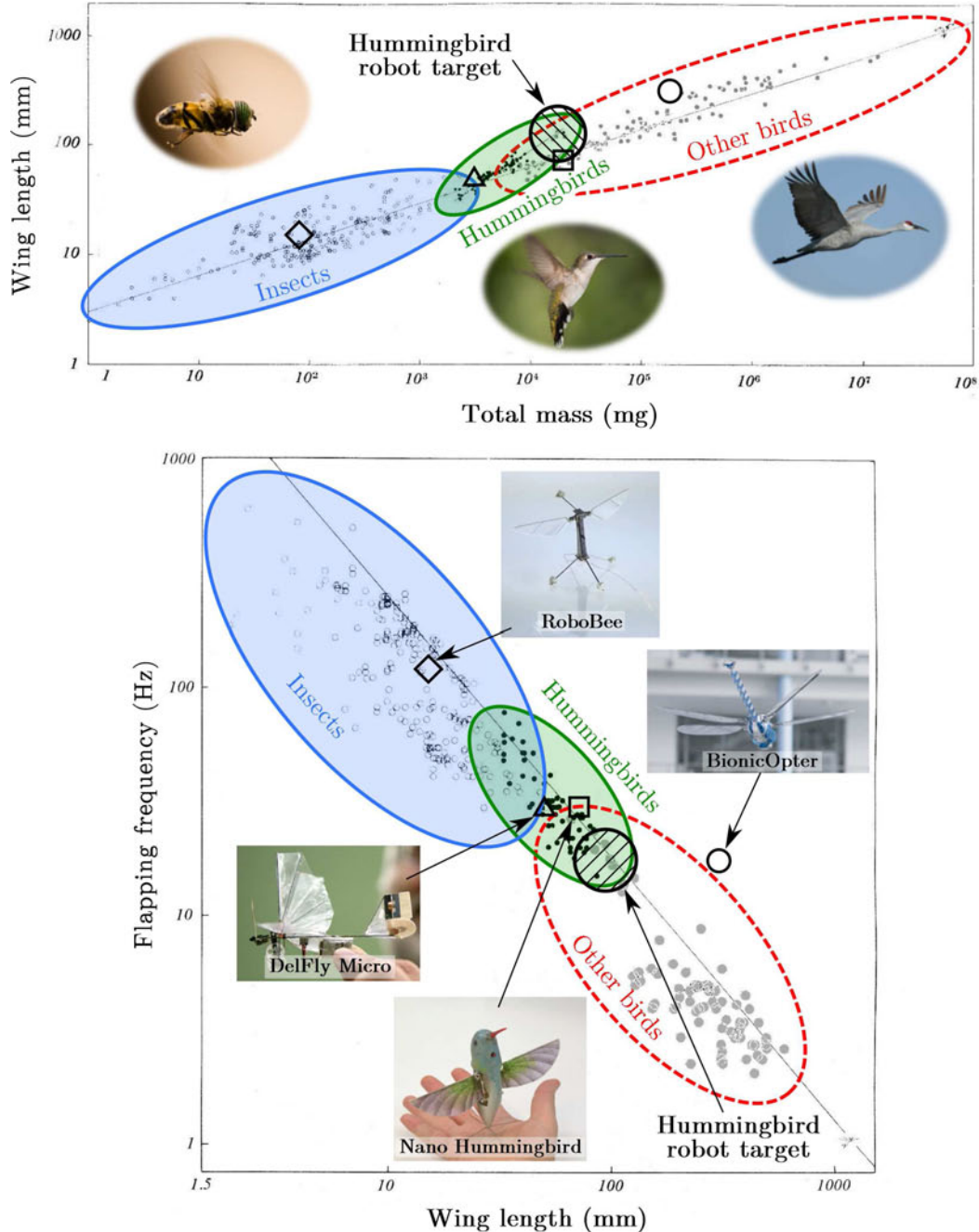


**Figure 1.8:** Relationship between the wing length, the flapping frequency and the total mass in nature, adapted from Greenewalt (1990). Interestingly, existing flapping wing MAVs follow nearly the same trend as nature.

Chapter 6 gives details on the development of the flapping mechanism and of the wing shape and presents experimental results obtained with a high speed camera and a custom built force balance.

Finally, Chapter 7 describes the development of two control mechanisms and their implementation to the robot prototype. Their performance is demonstrated by force and moment measurements and by high speed camera wing kinematics measurements.

## 1.5 References

- B. Bruggeman. Improving flight performance of delfly ii in hover by improving wing design and driving mechanism. Master's thesis, Delft University of Technology, 2010.
- G. de Croon, K. de Clerq, R. Ruijsink, B. Remes, and C. de Wagter. Design, aerodynamics, and vision-based control of the DelFly. *International Journal of Micro Air Vehicles*, 1(2):71–97, Jun. 2009. doi:10.1260/175682909789498288.
- Festo. BionicOpter. [http://www.festo.com/cms/en\\_corp/13165.htm](http://www.festo.com/cms/en_corp/13165.htm), 2013. Accessed: 18/08/2014.
- B. M. Finio and R. J. Wood. Distributed power and control actuation in the thoracic mechanics of a robotic insect. *Bioinspiration & biomimetics*, 5(4):045006, 2010. doi:10.1088/1748-3182/5/4/045006.
- S. B. Fuller, M. Karpelson, A. Censi, K. Y. Ma, and R. J. Wood. Controlling free flight of a robotic fly using an onboard vision sensor inspired by insect ocelli. *Journal of The Royal Society Interface*, 11(97), 2014. doi:10.1098/rsif.2014.0281.
- J. F. Goosen, H. J. Peters, Q. Wang, P. Tiso, and F. van Keulen. Resonance based flapping wing micro air vehicle. In *International Micro Air Vehicle Conference and Flight Competition (IMAV2013), Toulouse, France, September 17-20*, page 8, 2013.
- C. H. Greenewalt. *Hummingbirds*. Dover Publications, 1990.
- S. Hauert, J.-C. Zufferey, and D. Floreano. Evolved swarming without positioning information: an application in aerial communication relay. *Autonomous Robots*, 26(1):21–32, 2009. ISSN 0929-5593. doi:10.1007/s10514-008-9104-9.
- L. Hines, D. Campolo, and M. Sitti. Liftoff of a motor-driven, flapping-wing microaerial vehicle capable of resonance. *IEEE Transactions on Robotics*, 30(1):220–231, 2014. doi:10.1109/TRO.2013.2280057.

- M. T. Keenon, K. R. Klingebiel, H. Won, and A. Andriukov. Development of the nano hummingbird: A tailless flapping wing micro air vehicle. *AIAA paper 2012-0588*, pages 1–24, 2012.
- D. Lentink and M. H. Dickinson. Biofluidynamic scaling of flapping, spinning and translating fins and wings. *Journal of Experimental Biology*, 212(16):2691–2704, 2009. doi:10.1242/jeb.022251.
- K. Y. Ma, P. Chirarattananon, S. B. Fuller, and R. J. Wood. Controlled flight of a biologically inspired, insect-scale robot. *Science*, 340:603–607, 2013. doi:10.1126/science.1231806.
- A. Meskers. High energy density micro-actuation based on gas generation by means of catalysis of liquid chemical energy. Master’s thesis, Delft University of Technology, 2010.
- J. H. Park and K.-J. Yoon. Designing a biomimetic ornithopter capable of sustained and controlled flight. *Journal of Bionic Engineering*, 5(1):39–47, 2008.
- C. Richter and H. Lipson. Untethered hovering flapping flight of a 3d-printed mechanical insect. *Artificial life*, 17(2):73–86, 2011. doi:10.1162/artl.a.00020.
- L. Ristroph and S. Childress. Stable hovering of a jellyfish-like flying machine. *Journal of The Royal Society Interface*, 11(92):1–13, 2014. doi:10.1098/rsif.2013.0992.
- F. Ruffier and N. Franceschini. Optic flow regulation: the key to aircraft automatic guidance. *Robotics and Autonomous Systems*, 50(4):177–194, 2005. doi:10.1016/j.robot.2004.09.016.
- S. Tijmons, G. Croon, B. Remes, C. Wagter, R. Ruijsink, E.-J. Kampen, and Q. Chu. Stereo vision based obstacle avoidance on flapping wing mavs. In Q. Chu, B. Mulder, D. Choukroun, E.-J. Kampen, C. Visser, and G. Looye, editors, *Advances in Aerospace Guidance, Navigation and Control*, pages 463–482. Springer Berlin Heidelberg, 2013. doi:10.1007/978-3-642-38253-6\_28.
- F. van Breugel, W. Regan, and H. Lipson. From insects to machines. *Robotics Automation Magazine, IEEE*, 15(4):68–74, 2008. doi:10.1109/MRA.2008.929923.
- T. Vanneste, A. Bontemps, X. Q. Bao, S. Grondel, J.-B. Paquet, and E. Cattan. Polymer-based flapping-wing robotic insects: Progresses in wing fabrication, conception and simulation. In *ASME 2011 International Mechanical Engineering Congress and Exposition*, pages 771–778. American Society of Mechanical Engineers, 2011.

- C. D. Wagter, S. Tijmons, B. Remes, and G. de Croon. Autonomous flight of a 20-gram flapping wing mav with a 4-gram onboard stereo vision system. Accepted at ICRA 2014, 2014.
- R. J. Wood. The first takeoff of a biologically inspired at-scale robotic insect. *IEEE Transactions on Robotics*, 24(2):341–347, Apr. 2008. doi:10.1109/TRO.2008.916997.
- L.-J. Yang, C.-K. Hsu, F.-Y. Hsiao, C.-K. Feng, and Y.-K. Shen. A micro-aerial-vehicle (mav) with figure-of-eight flapping induced by flexible wing frames. In *Conference proceedings of 47th AIAA Aerospace Science Meeting, Orlando, USA, 5-8, Jan., 2009 (AIAA-2009-0875)*, page 14. 47th AIAA Aerospace Science Meeting, Orlando, USA, 2009.
- P. Zdunich, D. Bilyk, M. MacMaster, D. Loewen, J. DeLaurier, R. Kornbluh, T. Low, S. Stanford, and D. Holeman. Development and testing of the Mentor flapping-wing micro air vehicle. *Journal of Aircraft*, 44(5):1701–1711, 2007.



# Chapter 2

## Flapping flight

This chapter introduces the reader to the problematic of flapping flight. Because the majority of man made aircraft uses fixed wings, basic concepts of fixed wing aerodynamics are reviewed first. Then, three flight types observed in nature (gliding, flapping and hovering flapping flight) are described. An extra attention is given to the hovering flapping flight and its aerodynamic mechanisms enhancing the lift production as well as to flight control in nature.

### 2.1 Fixed wing aerodynamics

Considering an incompressible steady flow around a 2D airfoil according to Figure 2.1, the lift production can be explained by two basic laws of physics: the continuity of mass and the conservation of energy. As the flow approaches the airfoil the streamlines above the airfoil get closer to each other and, because of the mass continuity ( $AU = \text{const.}$ ), the flow velocity increases. On the contrary, below the airfoil the streamlines get further away and as a result the flow velocity drops. To comply with the Bernoulli equation ( $p + \frac{1}{2}\rho U^2 = \text{const.}$ ), which can be derived from

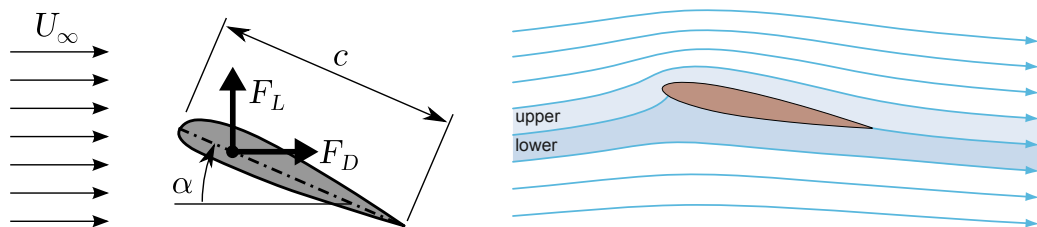


**Figure 2.1:** Steady flow around a 2D airfoil. Nomenclature:  $\alpha$  angle of attack,  $F_L$  lift,  $F_D$  drag,  $c$  chord width and  $U_\infty$  free-stream velocity (left) and typical streamlines (right).

the conservation of energy, the static pressure needs to drop above the wing and rise below the wing. This pressure difference results in a suction force lifting the airfoil: the lift force.

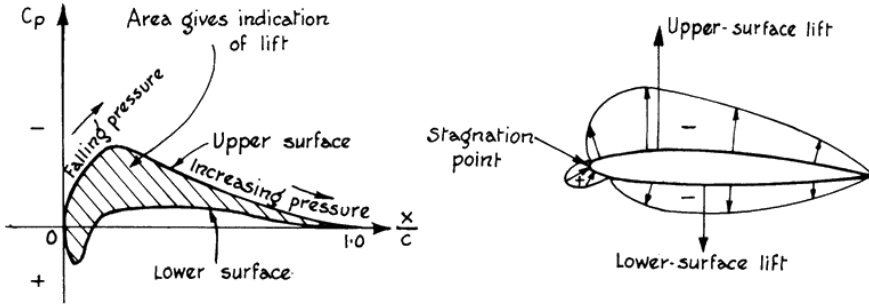


**Figure 2.2:** Pressure distribution around an airfoil (left) and the resulting lift force distribution (right), from Whitford (1987).

The distribution of the lift force is given by the pressure distribution, as in Figure 2.2. Thus, the resultant lift force vector is placed at the *centre of pressure* (CP). For an airfoil of a general shape, the CP location is varying with the angle of attack. However, it can be demonstrated by employing the thin airfoil theory that for a symmetric airfoil the CP lies in 1/4 of the chord from the leading edge.

If we start moving an airfoil from rest the flow pattern at the very beginning will look like in Figure 2.3 (left). A circulation  $\Gamma$  will develop around the airfoil to fulfil the Kutta condition, i.e. move the stagnation point to the trailing edge as in Figure 2.3 (right). This circulation is associated to a vortex that remains bound to the wing and is thus called the *bound vortex*. According to Kelvin's theorem, stating that the total circulation is conserved, the bound vortex needs to be compensated

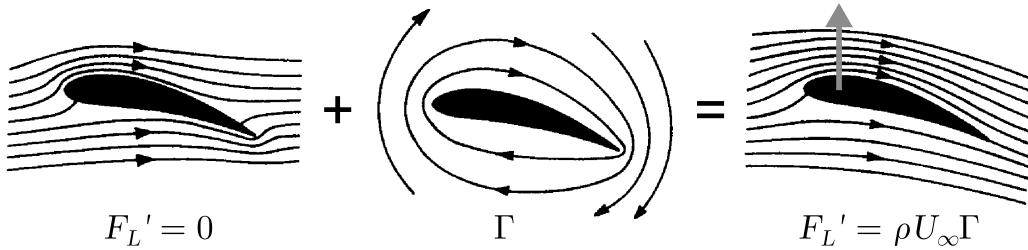


**Figure 2.3:** Circulation theory of lift: inviscid flow around an airfoil producing zero lift (left), circulation according to the Kutta condition (centre) and combined flow fulfilling the Kutta condition and generating lift (right). Figure adapted from Ellington (1984c).

by a vortex with an opposite circulation. This vortex is formed near the trailing edge due to high velocity gradients and is called the *starting vortex*. Once the trailing edge is reached the flow reaches steady conditions: the bound vortex stops growing and the starting vortex is shed into the wake. Similar transverse vortex is shed whenever the bound circulation changes, e.g. due to a change of angle of attack.

In a finite wing another pair of counter-rotating vortices is present in the wake behind the wing tips, one on each side. They are called the *wing-tip vortices* and are caused by an opposite spanwise flow above and below the wing. The whole vortex system of a finite wing is shown in Figure 2.4. Stopping the wing suddenly makes also the bound vortex shed, forming a ring vortex. It will be shown in the next section that similar vortex systems can be observed around flapping wings.

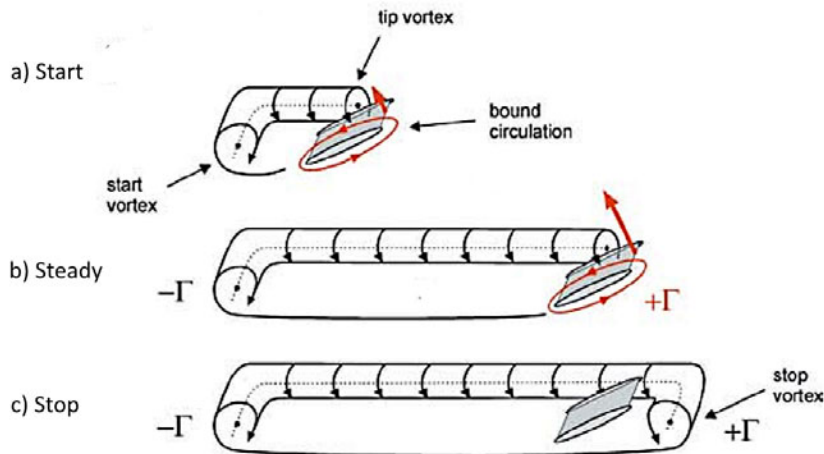


**Figure 2.4:** Vortex system of a finite span wing: a) Development of the starting vortex as the wing starts moving, b) steady state, c) vortex ring shed when the wing is stopped. Figure adapted from Lehmann (2004).

For a steady flow around a flat 2D airfoil the circulation of the bound vortex can be expressed using the thin airfoil theory as

$$\Gamma = \pi \alpha c U_\infty, \quad (2.1)$$

where  $\alpha$  is the angle of attack,  $c$  the chord width and  $U_\infty$  the free stream velocity. Combining the result with the Kutta-Joukowski theorem,  $F'_L = \rho U_\infty \Gamma$ , we obtain the lift force as

$$F'_L = \rho U_\infty \Gamma = \pi \alpha c \rho U_\infty^2, \quad (2.2)$$

where  $\rho$  is the fluid density.

The lift coefficient is a dimensionless characteristic of the airfoil profile defined as

$$C_L = \frac{F_L}{\frac{1}{2}\rho U_\infty^2 S} = \frac{F'_L(1)}{\frac{1}{2}\rho U_\infty^2 c(1)}, \quad (2.3)$$

where  $S = c(1)$  is the surface of a unity span wing with a chord  $c$ . By combining the last two equations we obtain the lift coefficient for a flat airfoil as  $C_L = 2\pi\alpha$ .

According to equation (2.2) the lift of a theoretical flat airfoil increases linearly with angle of attack. In reality the lift drops above certain value of angle of attack, see Figure 2.5. The pressure gradients on the upper airfoil side become too high, which results into flow separation due to viscosity. The pressure in the separated region does not drop any more and as a consequence the lift is reduced. This phenomenon is called *stall*.

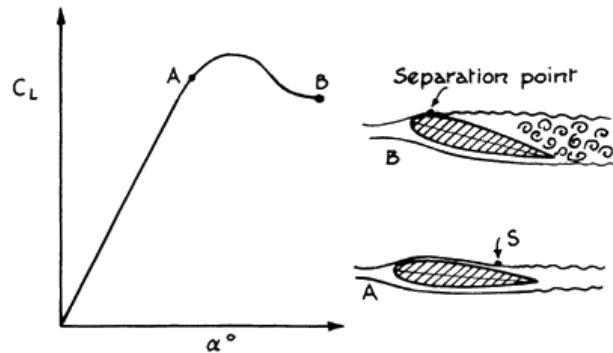


**Figure 2.5:** Stall: Lift coefficient drops at high angles of attack due to flow separation, from Whitford (1987).

While the lift force is given by the pressure distribution around the airfoil, there are several sources of drag force. The total drag of a 2D airfoil is called the profile drag. It is given by terms due to viscosity (skin friction drag) and due to pressure and subsequent separation (form drag). The total drag coefficient is defined similarly to the lift coefficient

$$C_D = \frac{F_D}{\frac{1}{2}\rho U_\infty^2 S} = \frac{F'_D(1)}{\frac{1}{2}\rho U_\infty^2 c(1)}. \quad (2.4)$$

In a finite wing, a small downward flow component, called the *downwash*  $w$ , is superposed to the flow around the wing, coming from the wing tip vortices (Figure 2.6). The downwash varies along the wingspan and as a result the local angle of attack changes. The original, geometric, angle of attack  $\alpha_g$  decreases by an induced

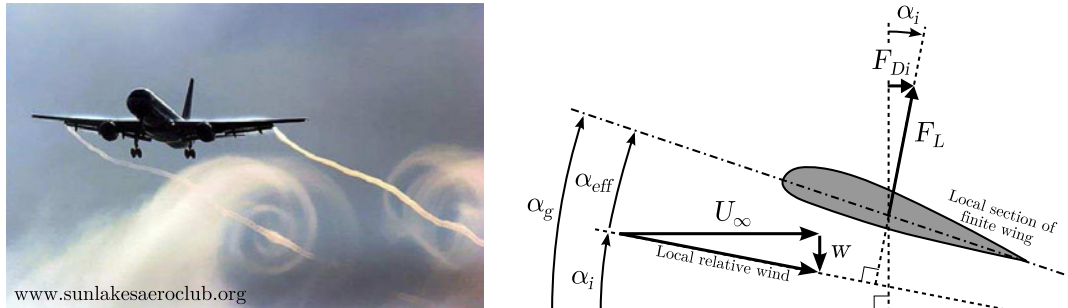


**Figure 2.6:** Wing tip vortices formed in clouds behind Boeing B-757 (left) and the effects of the resulting downwash on a local section of a finite length wing (right).

angle of attack  $\alpha_i$ . The local lift is then produced according to an effective angle of attack  $\alpha_{eff} = \alpha_g - \alpha_i$  measured with respect to the relative flow.

Since the local lift vector  $F_L$  is perpendicular to the relative flow vector, it has a component in the direction of  $U_\infty$  called the *induced drag*  $F_{Di}$ . The induced drag increases with increasing angle of attack. It is proportional to the inverse of the square of velocity and so it is mostly important at low speeds. The induced drag can be reduced by several design means (high aspect ratio wing, tapered wing, twisted wing, winglets, ...).

## 2.2 Flight in nature

No matter how big progress has been made in aviation since the first powered flight of the Wright brothers in 1903, the flight qualities and agility of modern aircraft remain incomparable to flying animals that have evolved over several hundred millions of years. When looking into nature, three types of flight can be observed: gliding flight, flapping flight and hovering.

### 2.2.1 Gliding flight

In gliding flight the animal is moving forward and descending at the same time. The necessary thrust to maintain the forward speed is produced by the gravity force. It is a common flight technique for bats and larger birds, but gliding flight was also observed among certain fish, frogs, reptiles or even squirrels. The aerodynamics of most gliding animals can be described by the theory for fixed wing aircraft.

The ratio between the lift and drag is equal to the glide ratio, which relates the travelled horizontal distance to the vertical descent. The best natural gliders, vultures

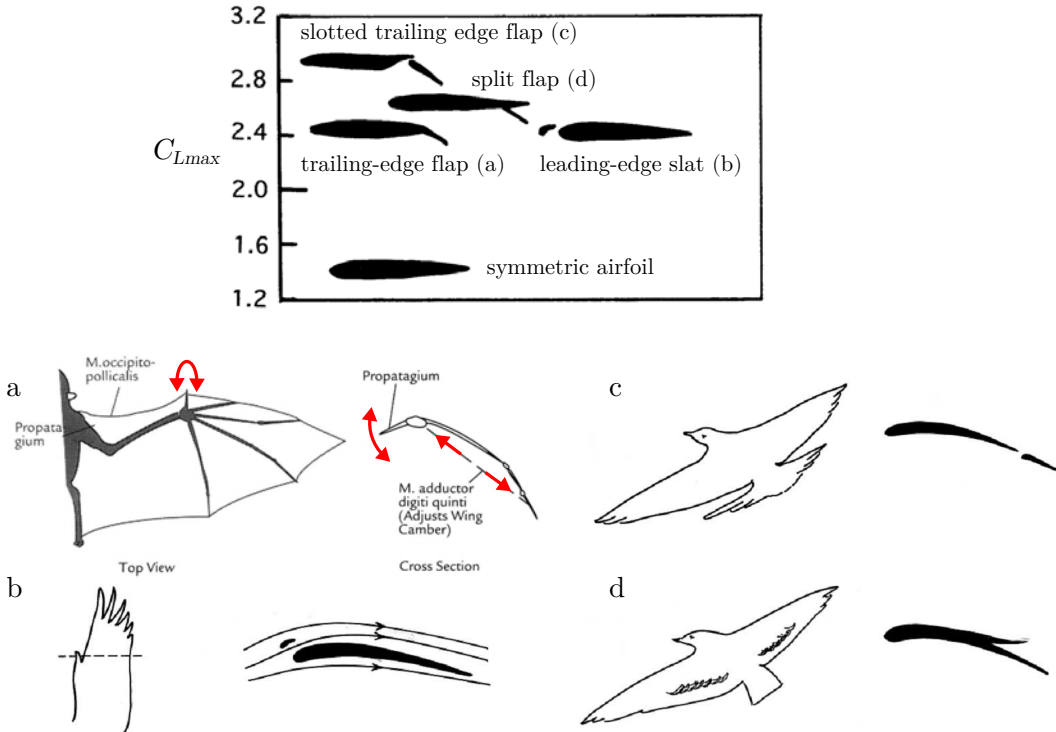


**Figure 2.7:** High lift devices used in aircraft and their equivalents in flying animals, from Norberg (2002).

and albatrosses, can achieve glide ratios higher than 20:1 (Pennycuick, 1971). For comparison, the best man made glider has a glide ratio of 70:1 (Flugtechnik & Leichtbau, 2001). To keep the altitude some animals glide in ascending air that rises due to convenient atmospheric conditions or due to terrain relief. Such flight is called soaring.

Several mechanisms are used to increase the maximal lift coefficient of fixed wing aircraft. These *high lift devices*, consisting of flaps and slats, are used particularly at low flight speeds, i.e. during take-off and landing, see Figure 2.7 (top). Equivalent mechanisms can be observed in natural flyers (Norberg, 2002). Bats can actively control the camber of their wing (Figure 2.7 a), which increases the lift coefficient and delays the stall. It is equivalent to trailing edge flaps and Kreuger flaps or drooped leading edges used in aircraft. Stall can be further delayed by leading-edge slats and slotted trailing edge flaps. The role of these devices, which deviate part of the flow from below the wing above the wing, is to delay the stall by modifying the pressure distribution above the wing and energizing the upper surface boundary

layer. Birds can achieve similar effect by lifting their “thumb” with several feathers on the leading edge (Figure 2.7 b). Equivalent to the slotted trailing edge flaps can be observed in birds with long forked tail, which they can spread wide to help keeping the flow attached even at high angles of attack (Figure 2.7 c). During landings, a raised covert feathers can be observed in many birds (Figure 2.7 d). This self-activated mechanism prevents backward flow of the turbulent air and delays flow separation. It is similar to split flaps, used during aircraft landings to increase the gliding angle.

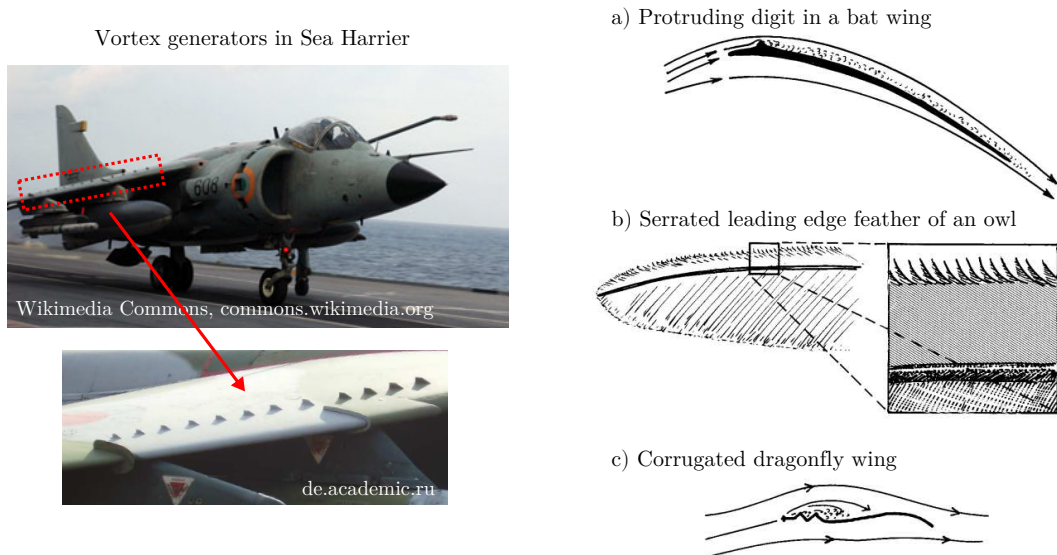


**Figure 2.8:** Vortex generators used in aircraft to introduce turbulence into the boundary layer (left) and their equivalents in flying animals, from Norberg (2002); Neuweiler (2000), (right).

Another way to delay the stall is to introduce turbulence in the boundary layer of the upper wing surface. The turbulence helps to maintain an interchange of momentum between the slow layers close to the wing and the free flow, so the flow separation occurs at higher angles of attack. In aircraft, this is done by vortex generators, which are typically placed close to the thickest part of the wing and distributed along the span, see Figure 2.8 (left). A protruded digit on bat wing, serrated feathers at the wing leading edge in owls and corrugated wings of dragonflies have the same role, see Figure 2.8 (right). Apart from delaying the stall, this solution also reduces the flight noise.

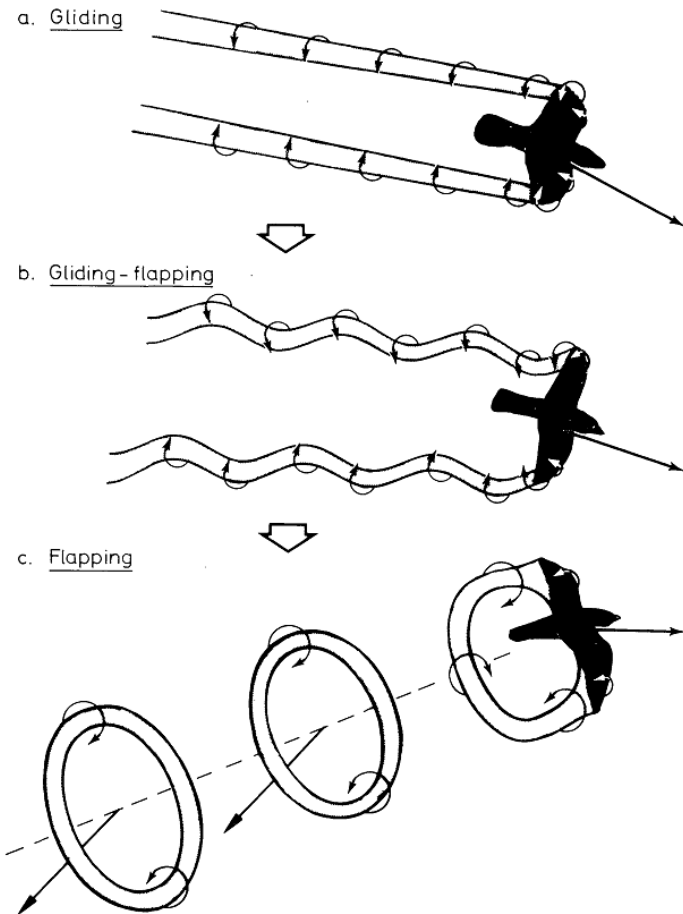


**Figure 2.9:** Flow structures behind the wings in different flight modes, from Norberg (1985).

### 2.2.2 Flapping forward flight

Apart from soaring, the animals need to actively produce thrust to stay airborne without loosing altitude. They do so by flapping their wings. The flow around a flapping wing is unsteady as the bound vortex gets distorted by the wing motion. The unsteady effects get more important as the forward speed decreases compared to the flapping speed.

This can be observed on the flow structures behind the wings (Figure 2.9). In gliding flight a pair of tip vortices is observed as in fixed-wing aircraft (Figure 2.9 a). For fast flapping flight the tip vortices remain continuous but undulate due to flapping

(Figure 2.9 b). For slower speeds the downstroke becomes dominant in thrust generation. Transverse vortices are being periodically created on the trailing edge at the beginning and at the end of each downstroke (Shyy et al., 2013). It is similar to the starting vortex and to the shedding of bound vortex when a fixed wing starts and stops to move, respectively. These transverse vortices connect with the two wing tip vortices and a vortex ring is shed at the end of each downstroke (Figure 2.9 c).

With decreasing flight speed the animals adapt the flapping motion direction. The flapping plane is almost vertical for cruising speeds but it inclines backwards as the speed decreases (Figure 2.10). The body posture is also adapted.

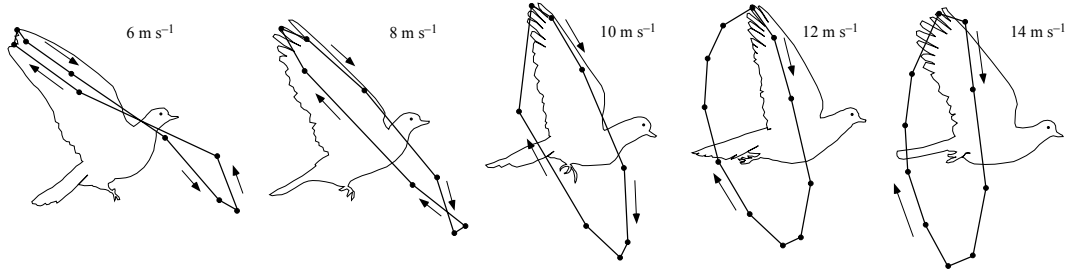


**Figure 2.10:** Wing-tip path of a pigeon flying at speeds of  $6-14 \text{ m.s}^{-1}$ . Adapted from Tobalske and Dial (1996).

### 2.2.3 Hovering flight

Hovering flight can be mostly observed in insects and hummingbirds. While bats (Muijres et al., 2008) and other birds (Tobalske et al., 1999) are also capable of hovering, they only use it in transitions (taking off, landing, perching) as hovering can require more than twice the power necessary for cruising (Dial et al., 1997). Apart from hummingbirds, birds generate most of the lift during downstroke when their wing is fully extended; they flex their wings in upstroke to reduce drag (Figure 2.11). We call this type of hovering asymmetric hovering (Norberg, 2002) or avian stroke (Azuma, 2006).

Hummingbirds and many insects can hover for much longer periods as they use symmetric hovering, also called insect stroke (Figures 2.12). The wings remain fully extended throughout the wingbeat, but rotate and twist at the end of each half stroke. Hummingbirds flap their wings almost horizontally (Figure 2.13 left) and produce lift also during upstroke, about 25%-33%. The flapping plane of two-winged insects can be slightly inclined (Figure 2.13 right); nevertheless, the upstroke generates up to 50% (Warrick et al., 2005, 2012).

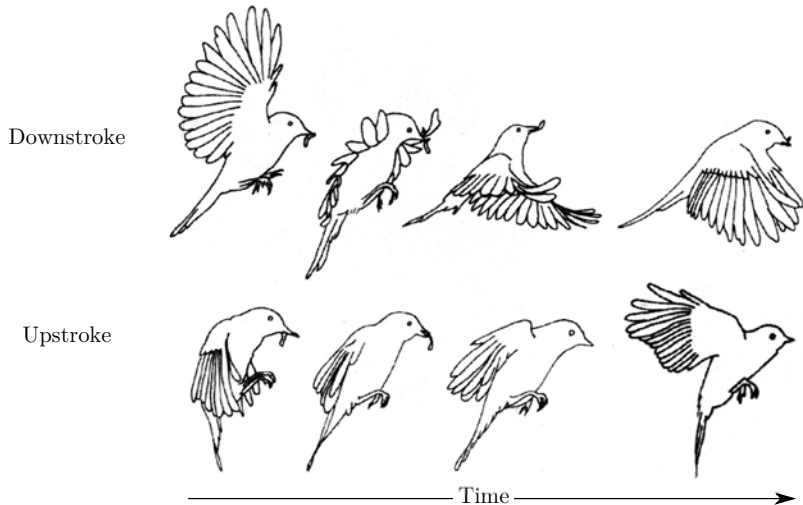


**Figure 2.11:** Asymmetric hovering typical for birds and bats. Adapted from Azuma (2006).

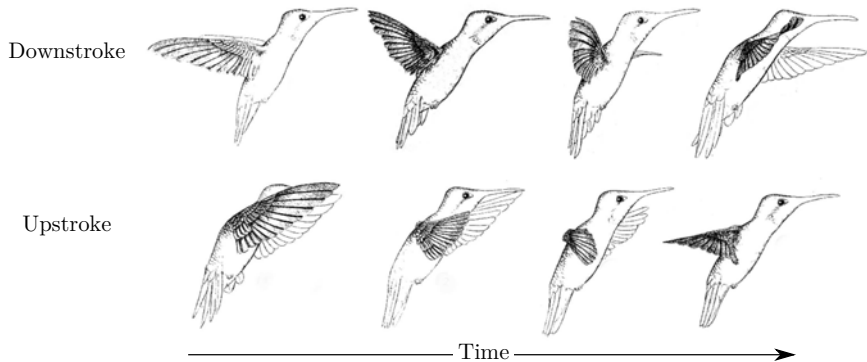


**Figure 2.12:** Symmetric hovering typical for hummingbirds (left) and insects (right). Adapted from Greenewalt (1990).

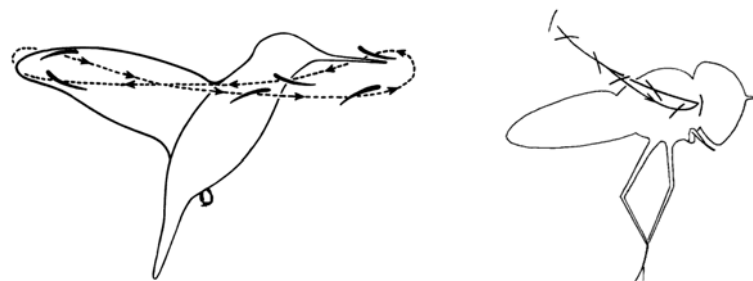


**Figure 2.13:** Wingtip trajectory in hovering hummingbirds and insects. Adapted from Ellington (1984a,b).

Hummingbird wing morphology differs from other birds as the upper arm and forearm bones are significantly shorter (Figure 2.14) and so the “hand” part of the wing, called the handwing, is much larger: over 75% of wing area in hummingbirds compared to about 50% in most birds (Warrick et al., 2012). On top of that the wrist and the elbow cannot articulate; all the motion comes from the very mobile shoulder. The wing is being moved by a pair of powerful muscles: a depressor muscle powers the downstroke and an elevator the upstroke. The depressor is twice as heavy as the elevator, which corresponds to the uneven lift production between downstroke and upstroke mentioned earlier. The hummingbird muscles form up to 30% of the body weight (Greenewalt, 1990, p116).

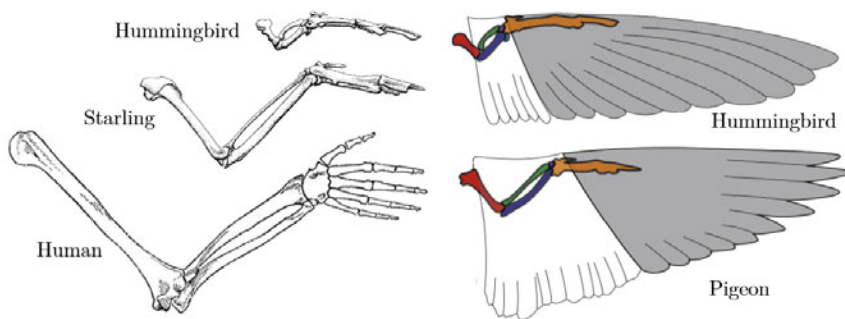


**Figure 2.14:** Wing morphology: size of forelimb bones with human arm as a reference (left) and handwing size (right, handwing in grey). The handwing is significantly larger in hummingbirds. Adapted from Dial (1992); Warrick et al. (2012) and [www.aokainc.com](http://www.aokainc.com).

There are two ways how flapping motion is produced in insects (Dudley, 2002). Phylogenetically older insects use direct muscles to flap their wings (Figure 2.15 left). They have two groups of muscles, the depressors and the elevators, that contract to move the wing in downstroke and in upstroke, respectively. Direct drive is typical for four-winged insects like dragonflies and damselflies. The brain controls each wing independently, which makes their flight very agile, but it also limits their flapping frequency, which is relatively low.

In phylogenetically modern insects, e.g. flies and bees, the wings are driven indirectly by the deformation of thorax and by displacing the dorsal part of the thorax called the notum (Figure 2.15 right). The upstroke is effected by contracting the vertical muscles and lowering the notum. Longitudinal muscles are contracted in downstroke to deform the thorax in longitudinal direction and subsequently raise the notum. The thorax acts as a resonant system, so the animals can flap at much higher frequencies, with greater amplitudes and the wings are always synchronized.

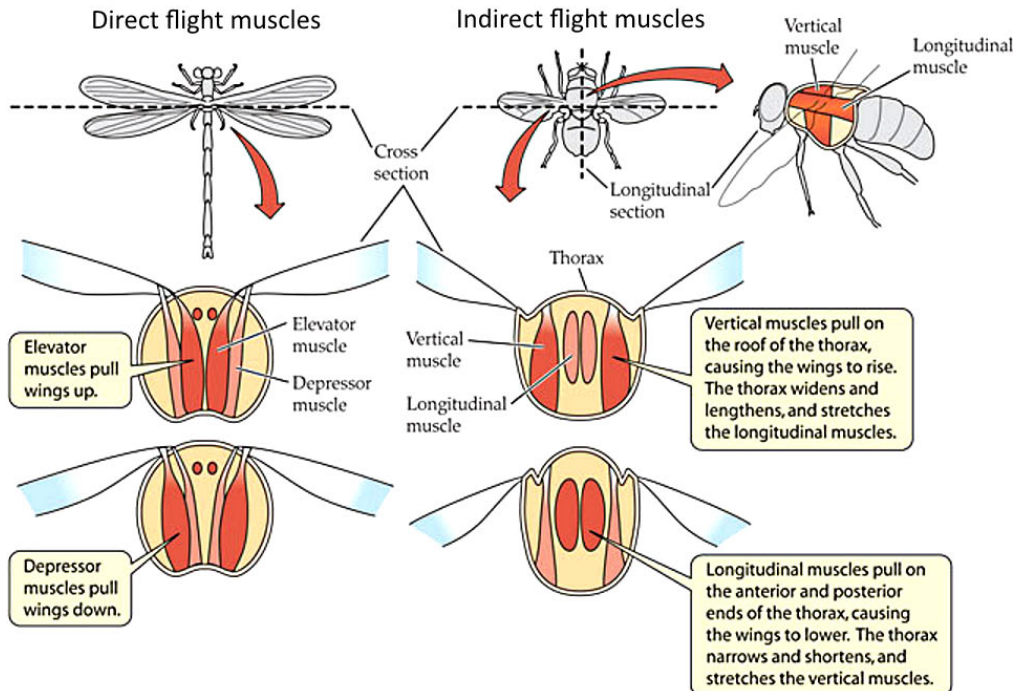


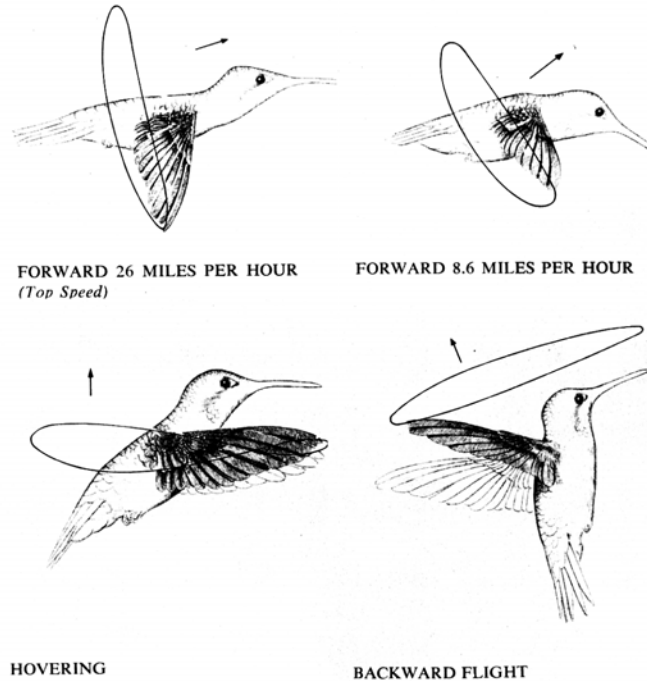
**Figure 2.15:** Direct (left) and indirect insect flight muscles (right). From Hill et al. (2012).

Surprisingly, the maximum lift to muscle-weight ratio is constant among insects and birds, despite their different evolution paths (Marden, 1987).

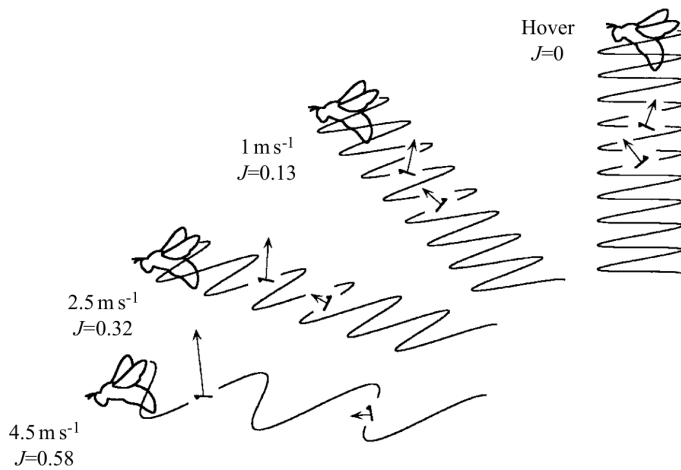
Hummingbirds and insects can combine precise hovering flight with fast cruising as well as with backward flight. Figure 2.16 shows wing-tip path and body positions of a hummingbird in all the mentioned flight modes. As in other birds, the flapping plane is nearly vertical in cruising. It inclines backwards as the flight speed decreases becoming approximately horizontal when hovering. It inclines further back to fly backwards. The wing-tip follows an oval pattern in most situations, but a figure-of-eight pattern is used near hovering.

Figure 2.17 shows wing-tip paths of a bumblebee flying at different speeds. The paths in this figure combine the flapping velocity with the downwash (the air moved by the interaction with the flapping wings). The shape of these paths can be characterized by a dimensionless ratio between the flight velocity and the (average) flapping velocity called the *advance ratio* (Ellington, 1984b)

$$J = \frac{U}{2\Phi f R}, \quad (2.5)$$



**Figure 2.16:** Wing-tip paths of a hummingbird in forward, hovering and backward flight. Adapted from Greenewalt (1990).



**Figure 2.17:** Wing-tip paths of a bumblebee at different flight speeds composed of flapping velocity and downwash. The arrows represent the generated forces. The imbalance between upstroke and downstroke path lengths and forces is characterized by the advance ratio  $J$ . Figure from Ellington (1999).

where  $\Phi$  is the flapping amplitude,  $f$  the flapping frequency and  $R$  the wing length. Ellington defines hovering as flight with advance ratio  $J$  below 0.1, where both upstroke and downstroke produce approximately equal amount of lift. We can observe that as the advance ratio increases, the upstroke paths become more vertical and shorter while downstroke paths more horizontal and longer. This signifies that for higher advance ratios downstroke generates higher force, which is directed upwards to provide lift, while the force during upstroke is smaller and is directed forwards to provide thrust.

## 2.3 Hovering flapping flight aerodynamics

Because of the scope of this work, only symmetric hovering flight (ie. flight with an advanced ratio  $J$  less than 0.1) with a single pair of flapping wings is considered further.

### 2.3.1 Dynamic scaling

The flow patterns over flapping wings can be characterized by several dimensionless numbers (Shyy et al., 2013). The most important is the *Reynolds number* which relates the inertial and viscous forces. For hovering flight it is defined as

$$Re_{hover} = \frac{U_{ref} L_{ref}}{\nu} = \frac{2\Phi f R \bar{c}}{\nu} = \frac{4\Phi f R^2}{\nu A}, \quad (2.6)$$

where  $\nu$  is the kinematic viscosity of air, the mean tip velocity, calculated as  $2\Phi f R$ , is taken as the reference speed  $U_{ref}$  and mean chord  $\bar{c}$  as the reference length  $L_{ref}$ . The definition was also rewritten using the wing aspect ratio  $A = \frac{2R}{\bar{c}}$ . We can see that for flyers with similar flapping amplitudes  $\Phi$  and aspect ratios  $A$  the Reynolds number is proportional to  $f R^2$ . Typical Reynolds numbers for hovering flapping flight lie between  $\sim 10$  and  $\sim 10\,000$ .

For forward flight the forward velocity  $U_\infty$  is usually taken as the reference velocity and the definition becomes independent of flapping

$$Re_{forward} = \frac{U_\infty \bar{c}}{\nu}. \quad (2.7)$$

Another dimensionless quantity, characterizing an oscillating flow, is the *Strouhal number*. It relates the oscillatory and forward motion and is thus only applicable to forward flight. It is defined as

$$St = \frac{f L_{ref}}{U_{ref}} = \frac{\Phi f R}{U_\infty}, \quad (2.8)$$

where the reference length is the distance travelled by the wing tip over one half-stroke  $\Phi R$ . The Strouhal numbers typical for most swimming and flying animals are between 0.2 and 0.4 (Taylor et al., 2003).

The level of unsteadiness associated with flapping wings in hover can be characterized by the *reduced frequency* used for pitching and plunging airfoils. It is defined as

$$k_{\text{hover}} = \frac{2\pi f L_{\text{ref}}}{U_{\text{ref}}} = \frac{\pi f \bar{c}}{2\Phi f R} = \frac{\pi}{\Phi \mathcal{R}}, \quad (2.9)$$

where the reference velocity is again the mean tip velocity and the reference length is half of the mean chord  $\bar{c}/2$ . The higher is the value of reduced frequency the greater is the role of the unsteady effects on the aerodynamic force production. Morphological data and dimensionless numbers of several hovering animals are in Table 2.1.

	<b>Chalcid wasp</b>	<b>Fruit fly</b>	<b>Hawkmoth</b>	<b>Rufous hummingbird</b>	<b>Giant hummingbird</b>
$m$ [g]	2.6e-7	0.002	1.6	3.4	20
$R$ [mm]	0.7	2.39	48.3	47	130
$\bar{c}$ [mm]	0.33	0.78	18.3	12	43
$f$ [Hz]	370	218	26.1	43	15
$\Phi$ [ $^{\circ}$ ]	120	140	115	116	120
$\mathcal{R}$ [-]	4.2	6.1	5.3	7.8	6
$Re$ [-]	23	126	5885	6249	22353
$k$ [-]	0.35	0.21	0.30	0.20	0.25

**Table 2.1:** Morphological parameters and dimensionless numbers of hovering flapping flight in nature. Data taken from Shyy et al. (2010); Weis-Fogh (1973).

### 2.3.2 Lift enhancing aerodynamic mechanisms

When researchers tried to model insect aerodynamics using traditional, steady state formulations in a quasi steady manner the models would grossly under-predict the generated lift; some of the animals would hardly be able to take-off (Ellington, 1984a). This induced further research that revealed that the produced forces are enhanced by flow patterns of highly unsteady nature. The flow structures around the wings involve periodic formation and shedding of vortices; they are still under active research. Many key mechanisms were observed and identified both experimentally and numerically, including the delayed stall of leading edge vortex, Kramer effect, wake capture and clap-and-fling (Sane, 2003; Lehmann, 2004).

*Delayed stall of the leading edge vortex* is the most important feature of the flow around flapping wings. Insects operate their wings at very high angles of attack. As it was described in Section 2.1 a fixed 2D airfoil operated at high angles of attack stalls. The flow separates on the upper surface of the airfoil and the airfoil loses lift due to smaller pressure difference between the regions above and below the wing.

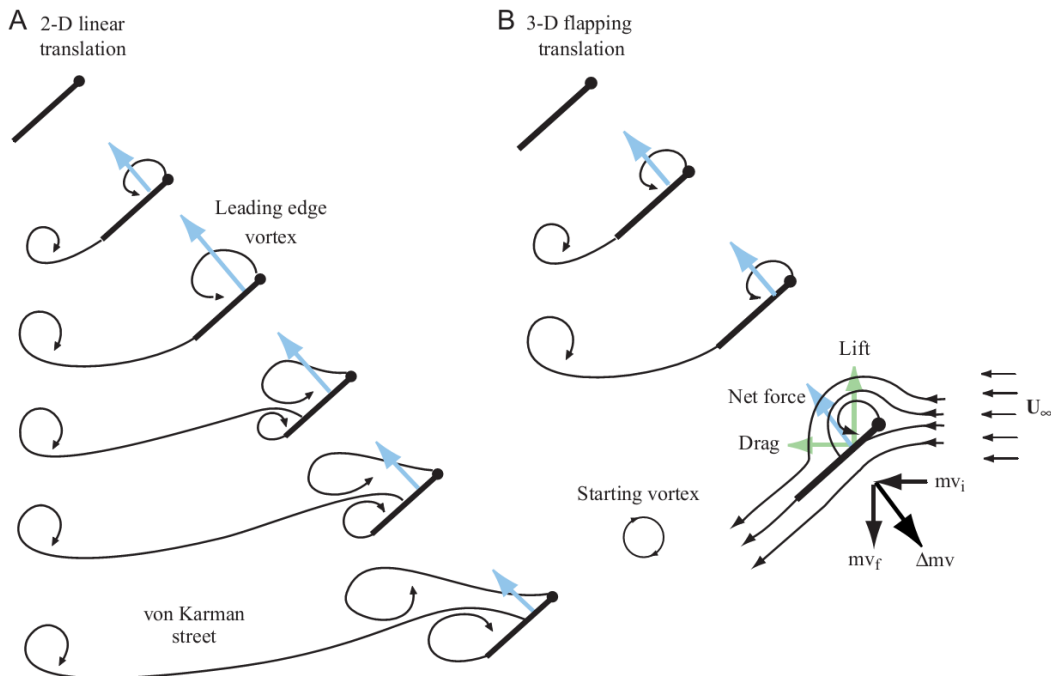


**Figure 2.18:** Difference between a 2D translating wing (left) and 3D flapping wing in the translation phase (right), from Sun and Wu (2003).

However, if an airfoil is started from still the leading edge vortex remains attached during the first couple of chord lengths, which results in very high lift. This mechanism, first identified by Walker (1932), is called the delayed stall. A fixed wing operated at low Reynolds numbers, which are typical for insects, would then start to alternately shed trailing edge and leading edge vortices forming a wake pattern known as the von Karman vortex street (Figure 2.18 left).

On the contrary, for a flapping wing the leading edge vortex remains stably attached (Figure 2.18 right) as was first shown by Ellington et al. (1996) and confirmed by Dickinson et al. (1999). The stability of the leading edge vortex is attributed to the observed axial flow from the wing root to the wing tip (Ellington et al., 1996; van den

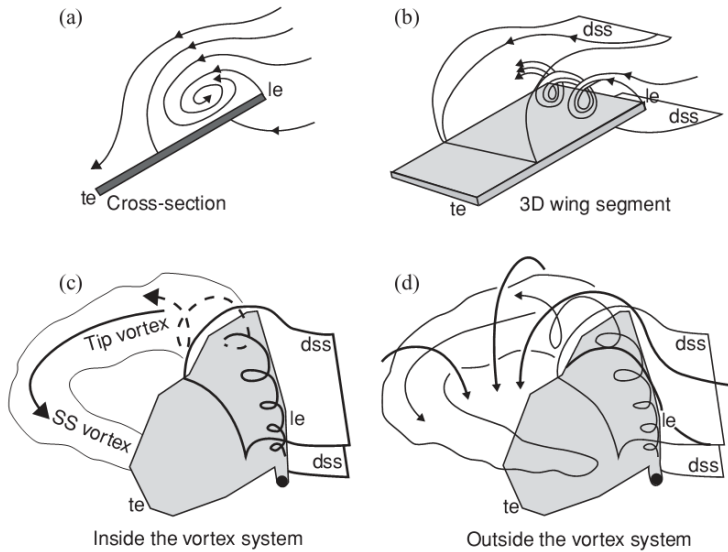


**Figure 2.19:** Leading edge vortex stabilized by axial flow, from van den Berg and Ellington (1997)

Berg and Ellington, 1997; Usherwood and Ellington, 2002), see Figure 2.19, similarly to low aspect ratio delta wings. This flow tends to be important for higher Reynolds numbers, while being rather weak for lower Reynolds numbers (Birch et al., 2004), nevertheless this seems to be sufficient for the leading edge vortex stability (Shyy and Liu, 2007).

The leading edge vortex enhances not only the lift but also the drag force. It contributes by about 7 to 16% to the bound circulation of a hummingbird wing (Warrick et al., 2009) and by up to 40% to the circulation of slow flying bats (Muijres et al., 2008).

The second mechanism that can enhance the lift production is the *Kramer effect*, sometimes called the rapid pitch rotation (Shyy et al., 2010) or rotational forces (Sane and Dickinson, 2002). As it was first demonstrated by Kramer (1932) in the context of wing flutter, the lift of a fixed wing in steady flow will increase if the wing rotates from low to high angle of attack. The span-wise rotation of the wing causes that the stagnation point moves away from the trailing edge and as a result additional circulation is generated to restore the Kutta condition. Depending on the sense of rotation, this circulation is added to or subtracted from the bound vortex circulation which results into positive or negative change of lift force, respectively.

Similar mechanism occurs in flapping wings at the reversal point between strokes, where the wing rotates rapidly along its span-wise axis. Studies of this phenomena carried out by Dickinson et al. (1999); Sane and Dickinson (2002) showed that an advanced rotation will enhance the lift force whereas a delayed rotation will cause the lift to drop. Insects take advantage of this phenomena by timing the rotation during manoeuvres (Dickinson et al., 1993).

Another mechanism related to the stroke reversal is the *wake capture*, sometimes also called the wing-wake interaction. It was first demonstrated by Dickinson et al. (1999) and further investigated by Birch and Dickinson (2003). As the wing reverses it interacts with the shed vortices from the previous strokes (Figure 2.20). This increases the relative flow speed and the transferred momentum results in higher aerodynamic force just after reversal. The magnitude of this enhancement depends strongly on the wing kinematics just before and just after the reversal.

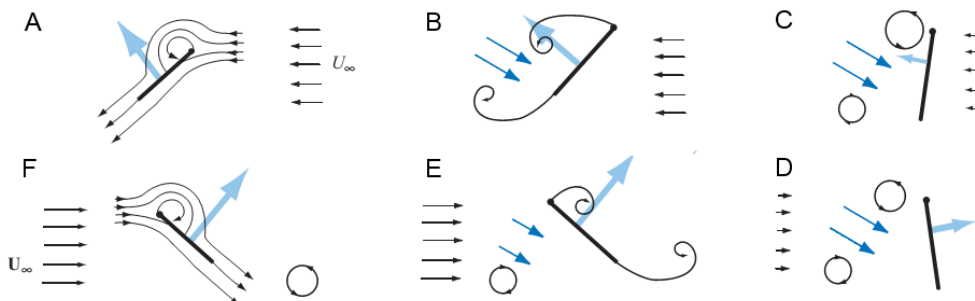


**Figure 2.20:** Wake capture mechanism. Light blue arrows represent the generated force, dark blue arrows show the flow direction, from Sane (2003)

The last aerodynamic mechanism enhancing the lift is called the *clap-and-fling* or clap-and-peel (Weis-Fogh, 1973; Ellington, 1984b). It occurs only in animals that touch their wings dorsally at the end of upstroke. In the 'clap' phase the wings touch first with their leading edges and keep rotating until also the trailing edges touch, pushing the trapped air downwards, which generates additional thrust (Figure 2.21). Once the wings start to 'fling' apart a gap opens between the leading edges. The air is sucked in which boosts the circulation build-up around the wings. Also, the starting vortices eliminate each other which further enhances the circulation development.

Clap-and-fling mechanism was observed in multiple insect species (e.g. Weis-Fogh (1973); Ellington (1984b); Zanker (1990)) and can enhance the lift by up to 25% (Marden, 1987).

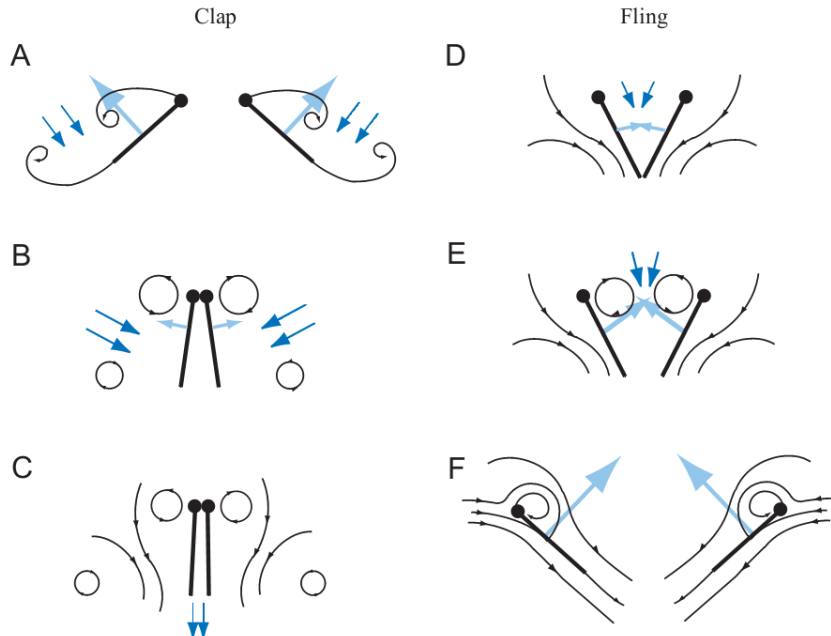


**Figure 2.21:** Clap and fling mechanism. Light blue arrows represent the generated force, dark blue arrows show the flow direction, from Sane (2003).

Apart from purely aerodynamic mechanisms, the interaction of the flow and the wing structure can also have a positive effect on the lift production (Shyy et al., 2013; Tanaka et al., 2013). For example, an appropriate combination of chord- and span-wise flexibility leads to a relative phase-advance of the wing rotation, resulting into lift increase due to Kramer effect.

### 2.3.3 Flight stability

While lift generation is of a primary importance for flying animals they also need to balance their body when facing perturbations coming from the wind or when manoeuvring. Many works tried to identify whether this stability is inherent or whether it is augmented by the sensory systems. To control the flight, insects can rely on their vision (compound eyes and ocelli) as well as on airflow sensors (antennae and wind sensitive hairs) and on inertial sensors (halteres), see Taylor and Krapp (2008). Studying passive stability experimentally is complicated as breaking the feedback loops by “deactivation” of the sensory systems leads to abnormal behaviour of the animal. Thus, numerical treatment was preferred by most authors.

The numerical studies employed aerodynamic models with various complexities (CFD, quasi-steady aerodynamics). The studies considered hovering or forward flight and covered both longitudinal and lateral directions of various insect species differing in size and in wing kinematics (Sun et al., 2007; Xiong and Sun, 2008; Zhang and Sun, 2010; Faruque and Humbert, 2010a,b; Orlowski and Girard, 2011; Cheng and Deng, 2011). While minor differences in the predicted behaviour exist especially in the lateral direction (Karasek and Preumont, 2012), the common conclusion is that the hovering flapping flight is inherently unstable and needs to be actively controlled.

Experimental studies of near-hover flapping flight stability are sparse. Taylor and Thomas (2003) performed experiments on a desert locust in forward flight and found that it was unstable. However, the animal was tethered and it could use its sensory systems. Hedrick et al. (2009) studied yaw turns in animals ranging from fruit flies to large birds. They showed that the deceleration phase of a yaw turn can be accomplished passively, without any active control of the animal, thanks to damping coming from the flapping motion, which they termed Flapping Counter Torque.

Recent works of Ristroph et al. (2010, 2013) studied the response of free flying fruit-flies to an external disturbance in yaw and pitch, respectively. Tiny ferromagnets were glued to the fly's body so that it could be reoriented by a magnetic field while being recorded by three high speed cameras. They observed that the fly used the same wing kinematic changes as it would use for a voluntary manoeuvre, suggesting it employs active auto-stabilization.

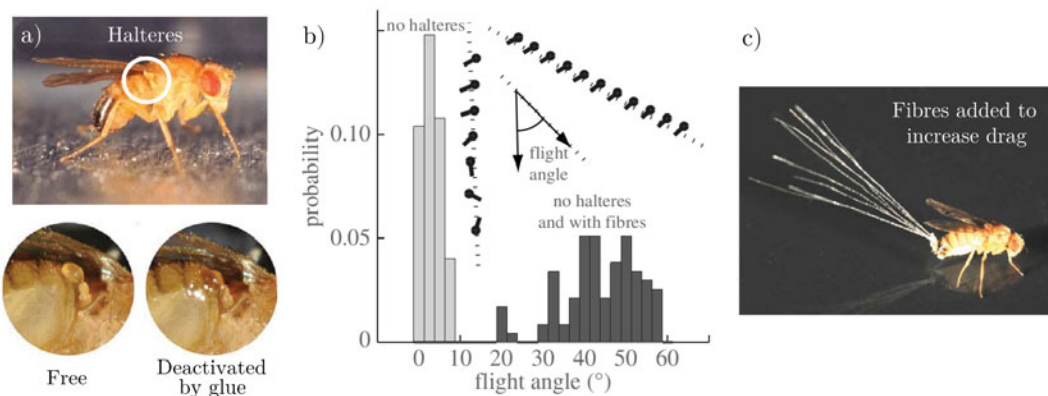


**Figure 2.22:** Demonstration of insect flight inherent instability: a) Halteres, biological vibrating gyroscopes in fruit-flies sensing the angular rates, before and after their deactivation, b) histogram of flight trajectory angles of flies without halteres, before and after increasing the passive damping, c) passive damping increased by fibres. From Ristroph et al. (2013).

In the next experiment they deactivated the halteres (insect gyroscopes), leaving the fly with only the visual feedback, whose reaction is about four times slower. This made the fly unable to fly as it fell nearly straight down, suggesting that the flight is indeed inherently unstable. Nevertheless, it was possible to restore the insects stability by attaching light dandelion fibres to its abdomen. This generated sufficient damping, so that the insect could keep more or less the same orientation, see Figure 2.22.

### 2.3.4 Attitude stabilization

Due to the inherent instability of flapping flight, hovering animals need to balance their bodies actively. The attitude stabilization requires independent control of body rotation around the roll (longitudinal) and pitch (lateral) axis. On top of that, turning requires control of rotation around the yaw (vertical) body axis. The necessary moments are produced by introducing small asymmetries into otherwise symmetric wing motion.

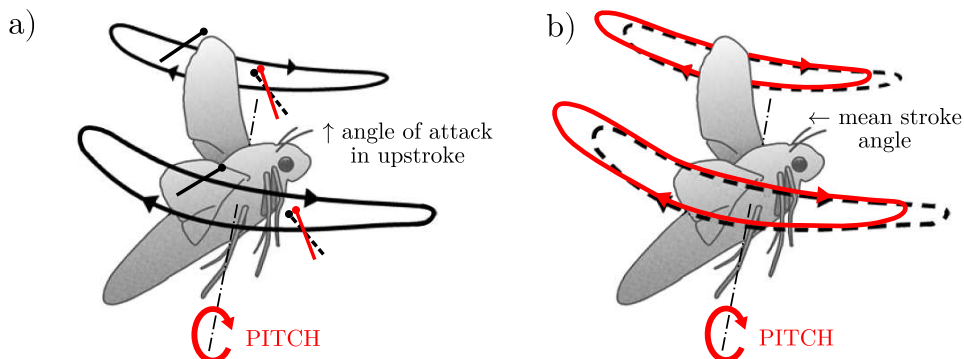


**Figure 2.23:** Pitch moment generation in insects: a) via angle of attack asymmetry, b) via mean wing position. Adapted from Conn et al. (2011).

For pitching the animal needs to shift the centre of lift in fore/aft direction (Ellington, 1999). This shift can be realized by moving the maximal/minimal wing stroke positions (the mean stroke angle) and/or by a difference in the angle of attack during upstroke and downstroke (Dudley, 2002), see Figure 2.23. The former was observed in free flying fruit flies during the auto-stabilization after an externally triggered pitch perturbation (Ristroph et al., 2013) and also in tethered fruit flies (Zanker, 1988).

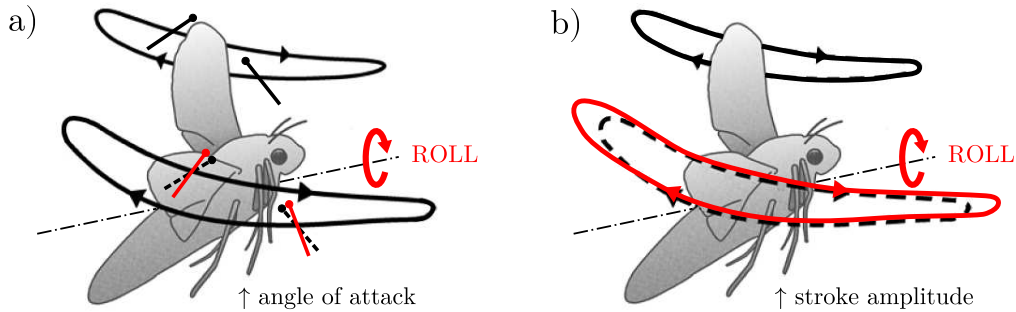


**Figure 2.24:** Roll moment generation in insects: a) via angle of attack difference, b) via flapping amplitude difference. Adapted from Conn et al. (2011).

Roll can be initiated by introducing an asymmetry between the lift of the left and right wing. Insects achieve this by increasing the flapping amplitude and/or by modifying the angle of attack on one wing (Ellington, 1999), as it was observed in tethered fruit-flies (Hengstenberg et al., 1986), see Figure 2.24.

Finally yawing can be effected by increasing the drag force on one of the wings. A difference in angle of attack while yawing was observed by Ellington (1999), see Figure 2.25. The same was reported for fruitflies by Bergou et al. (2010), together with significant asymmetry of mean stroke angles. Nevertheless, they attributed 98% of the yaw moment to the angle of attack difference. Interestingly, a different strategy in fruit-fly yaw turns was reported by Fry et al. (2003). They observed a backward tilt of stroke plane together with an increase of amplitude on the outside wing.

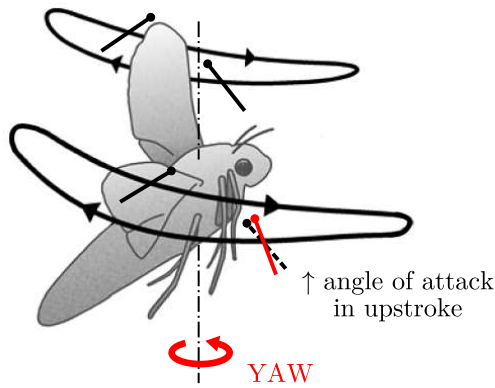


**Figure 2.25:** Yaw moment generation in insects via angle of attack asymmetry. Adapted from Conn et al. (2011).

Apart from wings also other body parts contribute to the overall torques produced. Zanker (1988) observed lateral deflection of the abdomen that should increase the drag on one side during visually simulated yaw turns in tethered fruit-flies. A (smaller) dorso-ventral deflection was reported while pitching. The drag can be increased further by hindlegs (Zanker et al., 1991). Video footages of flying hummingbirds also reveal that many species use their tail, in addition to wing motion and stroke plane changes, to control their body rotation when manoeuvring, see Figure 2.26.



**Figure 2.26:** Rufous hummingbird flying backwards. The interval between the displayed positions is 3 wingbeats, each position is a composite of two frames to show the wing limit positions and the stroke plane direction. Original video footage, <http://youtu.be/Cly6Y69WOYk>, courtesy of JCM Digital Imaging (<http://jcmdi.com>).

### 2.3.5 Flight control

Flying animals control their speed by modulating the thrust force. Hummingbirds can increase the produced thrust by increasing the stroke amplitude and at a smaller rate also the flapping frequency, as it was documented by Altshuler and Dudley (2003) by load lifting. The same was observed by Chai et al. (1996) by reducing the air pressure. Insects on the other hand are operating their wings at an approximately constant frequency (Dudley, 2002), because their thorax works as a resonant system. The thrust modulation is thus achieved through changes of flapping amplitude. Some insects can however further enhance the thrust by employing the clap and fling mechanism (Ellington, 1999), which can provide an additional boost of up to 25% (Marden, 1987). The maximal amplitudes of both hummingbirds and insects are mechanically limited by their morphology.

Flying forward and sideways is usually achieved by tilting the mean thrust vector into the desired direction, resulting into a horizontal force component that accelerates the flight. This strategy is similar to helicopters. In steady flight, the animals do this by tilting the stroke plane together with the body along the pitch or along the roll axis for forward/backward or sideways flight respectively (Vogel, 1967; Dudley and Ellington, 1990; Dudley, 2002; Tobalske et al., 2007). However, the relative angle between the body axis and stroke plane can slightly change when manoeuvring, see Figure 2.26. The same was observed in hawkmoths even in steady flight (Willmott and Ellington, 1997).

A strategy that generates directly a longitudinal or lateral force by modulating the drag forces was observed recently. Forward flight was induced by a paddling motion in fruit-fly (Ristroph et al., 2011), as the fly used different angles of attack during upstroke and downstroke. A lateral force resulting into sideways flight can be generated by differential timing of wing rotation in the same species (Ristroph et al., 2009).

## 2.4 References

- D. L. Altshuler and R. Dudley. Kinematics of hovering hummingbird flight along simulated and natural elevational gradients. *Journal of Experimental Biology*, 206: 3139–3147, 2003. doi:10.1242/jeb.00540.
- A. Azuma. *The Biokinetics of Flying and Swimming*. AIAA Education Series. AIAA, 2nd edition edition, 2006.

- A. J. Bergou, L. Ristroph, J. Guckenheimer, I. Cohen, and Z. J. Wang. Fruit flies modulate passive wing pitching to generate in-flight turns. *Physical review letters*, 104(14):1–4, 2010. doi:10.1103/PhysRevLett.104.148101.
- J. M. Birch and M. H. Dickinson. The influence of wingwake interactions on the production of aerodynamic forces in flapping flight. *Journal of Experimental Biology*, 206:2257–2272, 2003. doi:10.1242/jeb.00381.
- J. M. Birch, W. B. Dickson, and M. H. Dickinson. Force production and flow structure of the leading edge vortex on flapping wings at high and low reynolds numbers. *Journal of Experimental Biology*, 207:1063–1072, 2004. doi:10.1242/jeb.00848.
- P. Chai, R. Harrykissoon, and R. Dudley. Hummingbird hovering performance in hyperoxic heliox: effects of body mass and sex. *Journal of Experimental Biology*, 199:2745–2755, 1996.
- B. Cheng and X. Deng. Translational and rotational damping of flapping flight and its dynamics and stability at hovering. *IEEE Transactions on Robotics*, 27(5):849–864, Oct. 2011. doi:10.1109/TRO.2011.2156170.
- A. T. Conn, C. S. Ling, and S. C. Burgess. Biomimetic analysis of insect wing kinematics for flapping MAVs. *International Journal of Micro Air Vehicles*, 3(1):1–11, 2011. doi:10.1260/1756-8293.3.1.1.
- K. Dial, A. Biewener, B. Tobalske, and D. Warrick. Mechanical power output of bird flight. *Nature*, 390(6655):67–70, 1997.
- K. P. Dial. Avian forelimb muscles and nonsteady flight: Can birds fly without using the muscles in their wings? *The Auk*, 109(4):874–885, 1992.
- M. H. Dickinson, F.-O. Lehmann, and K. G. Gtz. The active control of wing rotation by drosophila. *Journal of Experimental Biology*, 182:173–189, 1993.
- M. H. Dickinson, F.-O. Lehmann, and S. P. Sane. Wing rotation and the aerodynamic basis of insect flight. *Science*, 284(5422):1954–1960, Jun. 1999. doi:10.1126/science.284.5422.1954.
- R. Dudley. *The Biomechanics Of Insect Flight: Form, Function, Evolution*. Princeton University Press, 2002.
- R. Dudley and C. P. Ellington. Mechanics of forward flight in bumblebees: I. kinematics and morphology. *Journal of Experimental Biology*, 148(1):19–52, 1990.

- C. P. Ellington. The aerodynamics of hovering insect flight. I. the quasi-steady analysis. *Philosophical Transactions of the Royal Society of London. Series B, Biological Sciences*, 305(1122):1–15, Feb. 1984a.
- C. P. Ellington. The aerodynamics of hovering insect flight. III. kinematics. *Philosophical Transactions of the Royal Society of London. Series B, Biological Sciences*, 305(1122):41–78, Feb. 1984b.
- C. P. Ellington. The aerodynamics of hovering insect flight. IV. aerodynamic mechanisms. *Philosophical Transactions of the Royal Society of London. Series B, Biological Sciences*, 305(1122):79–113, Feb. 1984c.
- C. P. Ellington. The novel aerodynamics of insect flight: application to micro-air vehicles. *Journal of Experimental Biology*, 202:3439–3448, 1999.
- C. P. Ellington, C. van den Berg, A. P. Willmott, and A. L. R. Thomas. Leading-edge vortices in insect flight. *Nature*, 384:626–630, 1996. doi:10.1038/384626a0.
- I. Faruque and J. S. Humbert. Dipteran insect flight dynamics. Part 1: Longitudinal motion about hover. *Journal of Theoretical Biology*, 264(2):538–552, May. 2010a. doi:10.1016/j.jtbi.2010.02.018.
- I. Faruque and J. S. Humbert. Dipteran insect flight dynamics. Part 2: Lateral-directional motion about hover. *Journal of Theoretical Biology*, 265(3):306–313, Aug. 2010b. doi:10.1016/j.jtbi.2010.05.003.
- Flugtechnik & Leichtbau. Eta glider. <http://www.leichtwerk.de/eta/de/flugerprobung/leistung.html>, 2001. Accessed: 18/08/2014.
- S. N. Fry, R. Sayaman, and M. H. Dickinson. The aerodynamics of free-flight maneuvers in drosophila. *Science*, 300(5618):495–498, Apr. 2003.
- C. H. Greenewalt. *Hummingbirds*. Dover Publications, 1990.
- T. L. Hedrick, B. Cheng, and X. Deng. Wingbeat time and the scaling of passive rotational damping in flapping flight. *Science*, 324(5924):252–255, Apr. 2009. doi:10.1126/science.1168431.
- R. Hengstenberg, D. Sandeman, and B. Hengstenberg. Compensatory head roll in the blowfly calliphora during flight. *Proceedings of the Royal society of London. Series B. Biological sciences*, 227(1249):455–482, 1986.
- R. W. Hill, G. A. Wyse, and M. Anderson. *Animal Physiology*, companion website: [sites.sinauer.com/animalphys3e](http://sites.sinauer.com/animalphys3e). Sinauer Associates, Inc., 2012.

- M. Karasek and A. Preumont. Flapping flight stability in hover: A comparison of various aerodynamic models. *International Journal of Micro Air Vehicles*, 4(3):203–226, 2012. doi:10.1260/1756-8293.4.3.203.
- M. Kramer. Die zunahme des maximalauftriebes von tragflügeln bei plötzlicher anstellwinkel vergrösserung. *Zeitschrift für Flugtechnik und Motorluftschiffahrt*, 23:185–189, 1932.
- F.-O. Lehmann. The mechanisms of lift enhancement in insect flight. *Naturwissenschaften*, 91(3):101–122, 2004. doi:10.1007/s00114-004-0502-3.
- J. H. Marden. Maximum lift production during takeoff in flying animals. *Journal of Experimental Biology*, 130(1):235–258, 1987.
- F. T. Muijres, L. Johansson, R. Barfield, M. Wolf, G. Spedding, and A. Hedenstrom. Leading-edge vortex improves lift in slow-flying bats. *Science*, 319(5867):1250–1253, 2008.
- G. Neuweiler. *The Biology of Bats*. Oxford University Press, 2000.
- U. M. Norberg. Evolution of vertebrate flight: an aerodynamic model for the transition from gliding to active flight. *American Naturalist*, 126(3):303–327, 1985.
- U. M. L. Norberg. Structure, form, and function of flight in engineering and the living world. *Journal of morphology*, 252(1):52–81, 2002. doi:10.1002/jmor.10013.
- C. T. Orlowski and A. R. Girard. Stability derivatives for a flapping wing MAV in a hover condition using local averaging. In *2011 American Control Conf.*, pages 1604–1609, San Francisco, California, Jun. - Jul. 2011.
- C. Pennycuick. Gliding flight of the white-backed vulture *gyps africanus*. *Journal of Experimental Biology*, 55(1):13–38, 1971.
- L. Ristroph, G. J. Berman, A. J. Bergou, Z. J. Wang, and I. Cohen. Automated hull reconstruction motion tracking (HRMT) applied to sideways maneuvers of free-flying insects. *Journal of Experimental Biology*, 212(9):1324–1335, 2009. doi:10.1242/jeb.025502.
- L. Ristroph, A. J. Bergou, G. Ristroph, K. Coumes, G. J. Berman, J. Guckenheimer, Z. J. Wang, and I. Cohen. Discovering the flight autostabilizer of fruit flies by inducing aerial stumbles. *Proceedings of the National Academy of Sciences*, 107(11):4820–4824, 2010. doi:10.1073/pnas.1000615107.
- L. Ristroph, A. J. Bergou, J. Guckenheimer, Z. J. Wang, and I. Cohen. Paddling mode of forward flight in insects. *Physical review letters*, 106(17):178103, 2011. doi:PhysRevLett.106.178103.

- L. Ristroph, G. Ristroph, S. Morozova, A. J. Bergou, S. Chang, J. Guckenheimer, Z. J. Wang, and I. Cohen. Active and passive stabilization of body pitch in insect flight. *Journal of The Royal Society Interface*, 10(85):1–13, 2013. doi:10.1098/rsif.2013.0237.
- S. P. Sane. The aerodynamics of insect flight. *Journal of Experimental Biology*, 206: 4191–4208, 2003. doi:doi:10.1242/jeb.00663.
- S. P. Sane and M. H. Dickinson. The aerodynamic effects of wing rotation and a revised quasi-steady model of flapping flight. *Journal of Experimental Biology*, 205:1087–1096, 2002.
- W. Shyy and H. Liu. Flapping wings and aerodynamic lift: the role of leading-edge vortices. *AIAA Journal*, 45(12):2817–2819, 2007.
- W. Shyy, H. Aono, S. Chimakurthi, P. Trizila, C.-K. Kang, C. Cesnik, and H. Liu. Recent progress in flapping wing aerodynamics and aeroelasticity. *Progress in Aerospace Sciences*, 46(7):284–327, Oct. 2010. doi:<http://dx.doi.org/10.1016/j.paerosci.2010.01.001>.
- W. Shyy, H. Aono, C.-K. Kang, and H. Liu. *An Introduction to Flapping Wing Aerodynamics*. Cambridge University Press, 2013.
- M. Sun and J. H. Wu. Aerodynamic force generation and power requirements in forward flight in a fruit fly with modeled wing motion. *Journal of Experimental Biology*, 206:3065–3083, 2003. doi:doi:10.1242/jeb.00517.
- M. Sun, J. Wang, and Y. Xiong. Dynamic flight stability of hovering insects. *Acta Mech. Sinica*, 23(3):231–246, Jun. 2007. doi:10.1007/s10409-007-0068-3.
- H. Tanaka, H. Suzuki, I. Kitamura, M. Maeda, and H. Liu. Lift generation of hummingbird wing models with flexible loosened membranes. In *2013 IEEE/RSJ International Conference on Intelligent Robots and Systems (IROS)*, pages 3777–3783, 2013.
- G. K. Taylor and H. G. Krapp. Sensory systems and flight stability: what do insects measure and why? *Advances in insect physiology*, 34(231-316), 2008. doi:10.1016/S0065-2806(07)34005-8.
- G. K. Taylor and A. L. R. Thomas. Dynamic flight stability in the desert locust *schistocerca gregaria*. *Journal of Experimental Biology*, 206(16):2803–2829, Aug. 2003. doi:10.1242/jeb.00501.
- G. K. Taylor, R. L. Nudds, and A. L. R. Thomas. Flying and swimming animals cruise at a Strouhal number tuned for high power efficiency. *Nature*, 425:707–711, Oct. 2003. doi:10.1038/nature02000.

- B. W. Tobalske and K. P. Dial. Flight kinematics of black-billed magpies and pigeons over a wide range of speeds. *Journal of Experimental Biology*, 1999(2):263–280, 1996.
- B. W. Tobalske, W. L. Peacock, and K. P. Dial. Kinematics of flap-bounding flight in the zebra finch over a wide range of speeds. *Journal of Experimental Biology*, 202(13):1725–1739, 1999.
- B. W. Tobalske, D. R. Warrick, C. J. Clark, D. R. Powers, T. L. Hedrick, G. A. Hyder, and A. A. Biewener. Three-dimensional kinematics of hummingbird flight. *Journal of Experimental Biology*, 210(13):2368–2382, Jul. 2007. doi:10.1242/jeb.005686.
- J. R. Usherwood and C. P. Ellington. The aerodynamics of revolving wings: I. model hawkmoth wings. *Journal of Experimental Biology*, 205:1547–1564, 2002.
- C. van den Berg and C. P. Ellington. The vortex wake of a hoveringmodel hawkmoth. *Philosophical Transactions of the Royal Society of London. Series B: Biological Sciences*, 352:317–328, 1997.
- S. Vogel. Flight in drosophila II. variations in stroke parameters and wing contour. *Journal of Experimental Biology*, 46(2):383–392, 1967.
- P. Walker. Experiments on the growth of circulation about a wing and an apparatus for measuring fluid motion. Technical Report 1402, Air ministry, Aeronautical Research Committee, Reports and memoranda, 1932.
- D. Warrick, T. Hedrick, M. J. Fernndez, B. Tobalske, and A. Biewener. Hummingbird flight. *Current Biology*, 22(12):472–477, 2012.
- D. R. Warrick, B. W. Tobalske, and D. R. Powers. Aerodynamics of the hovering hummingbird. *Nature*, 435:1094–1097, 2005. doi:10.1038/nature03647.
- D. R. Warrick, B. W. Tobalske, and D. R. Powers. Lift production in the hovering hummingbird. *Proceedings of the Royal Society B*, 276:3747–3752, 2009. doi:10.1098/rspb.2009.1003.
- T. Weis-Fogh. Quick estimates of flight fitness in hovering animals, including novel mechanisms for lift production. *Journal of Experimental Biology*, 59(1):169–230, 1973.
- R. Whitford. *Design for air combat*. Jane’s Publishing Company Limited, 1987.
- A. P. Willmott and C. P. Ellington. The mechanics of flight in the hawkmoth *manduca sexta* I. Kinematics of hovering and forward flight. *Journal of Experimental Biology*, 200:2705–2722, 1997.

- Y. Xiong and M. Sun. Dynamic flight stability of a bumblebee in forward flight. *Acta Mech. Sinica*, 24(1):25–36, Feb. 2008. doi:DOI 10.1007/s10409-007-0121-2.
- J. Zanker. The wing beat of drosophila melanogaster. I. Kinematics. *Philosophical Transactions of the Royal Society of London. Series B, Biological Sciences*, 327 (1238):1–18, 1990.
- J. M. Zanker. How does lateral abdomen deflection contribute to flight control of drosophila melanogaster? *Journal of Comparative Physiology A*, 162(5):581–588, 1988.
- J. M. Zanker, M. Egelhaaf, and A.-K. Warzecha. On the coordination of motor output during visual flight control of flies. *Journal of Comparative Physiology A*, 169(2):127–134, 1991.
- Y. Zhang and M. Sun. Dynamic flight stability of a hovering model insect: lateral motion. *Acta Mech. Sinica*, 26(2):175–190, May. 2010. doi:10.1007/s10409-009-0303-1.

## Chapter 3

# Mathematical modelling

In this chapter a dynamic model of hovering flapping flight is introduced. This model serves as a basis for stability study of flapping flight as well as for control design and flight simulations of the designed hummingbird robot. Its goal is to provide reasonable estimates of the generated aerodynamic forces and moments rather than a detailed analysis of the flow around the flapping wings. Thus, a computationally efficient model with low complexity was selected. The robot is modelled as a rigid body and a quasi-steady modelling approach is used to evaluate the aerodynamic forces of the flapping wings.

### 3.1 Flapping flight aerodynamics

The unsteady nature of the flow mechanisms in flapping flight has already been discussed in the previous chapter. Hence, proper modelling of flapping flight requires a numerical solution of Navier-Stokes equations. Such a solution is usually very complex due to moving boundaries and 3D geometry. On top of that real wings are being twisted and flexed under the aerodynamic loads, which means the Navier-Stokes model should be coupled with a model of structural dynamics.

Many CFD simulations were used to study the aerodynamics of hovering insects of different sizes, some considering also flexible wings. A thorough review of published results was carried out by Shyy et al. (2013). However, these models require significant computational power and their implementation is very complex, which limits their use in flight simulations and in control design.

An alternative to complex models can be the quasi steady modelling approach (Sane and Dickinson, 2002). Unlike in a proper unsteady treatment, the quasi-steady model assumes that the instantaneous forces depend only on the wing motion at

the given instant. The model was derived from steady flow thin airfoil theory and from theory originally developed for flutter analyses (Sedov, 1965; Fung, 1969). It consists of relatively simple analytic equations with force coefficients from Dickinson et al. (1999) that partially include the effect of delayed stall, which was discussed in Section 2.3.2. It is thus possible to predict the time history of wing forces for any kinematic pattern with low demands on computation power. Despite many simplifications, it will be demonstrated that this model provides cycle-averaged results comparable to a CFD simulation when assessing hovering flight stability.

### 3.1.1 Wing kinematics

The flapping motion of hummingbird and insect wings has three DOFs (Figure 3.1). The principal motion is an oscillatory motion with frequency  $f$  (the wingbeat frequency) occurring in the stroke plane  $x_{SP}y_{SP}$ . The stroke plane is inclined from the

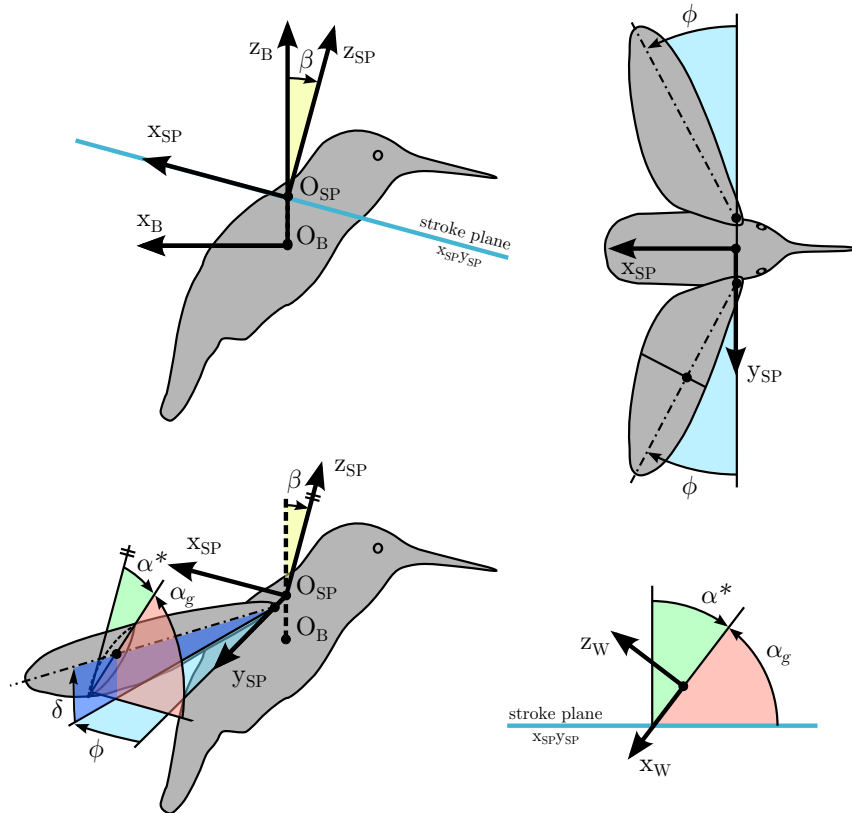


**Figure 3.1:** Angles defining the wing position.

body horizontal plane  $x_{BYB}$  by angle  $\beta$ . The wing position inside the stroke plane is defined by the sweep angle  $\phi$ . One stroke consists of two consecutive half-strokes: the *downstroke* (dorso-ventral motion,  $\dot{\phi} < 0$ ) and the *upstroke* (ventro-dorsal motion,  $\dot{\phi} > 0$ ). At the reversal between each half-stroke the wing rotates along its longitudinal axis, its orientation is given by the wing inclination angle  $\alpha^*$  measured between the wing chord and the normal to the stroke plane. The geometric angle of attack  $\alpha_g$ , measured from the stroke plane, is thus defined as  $\alpha_g = \pi/2 - |\alpha^*|$ . The rotation is termed *pronation* and *supination* on the dorsal and ventral side, respectively. The wings can also deviate from the stroke plane by the deviation angle  $\delta$ , which is measured with respect to wing longitudinal axis.

The wing motion can be parametrised, similar to Berman and Wang (2007), in the following way:

$$\begin{aligned}\phi &= \phi_0 + \frac{\phi_m}{\arcsin(k_\phi)} \arcsin [k_\phi \cos (2\pi ft)] \\ \alpha^* &= \alpha_0 + \frac{\pi/2 - \alpha_m}{\tanh(k_\alpha)} \tanh [k_\alpha \sin(2\pi ft - \varphi_\alpha)] \\ \delta &= \delta_{m1} \sin(2\pi ft) + \delta_{m2} \sin(4\pi ft),\end{aligned}\quad (3.1)$$

$t$  is time,  $\phi_0$  sweep offset (mean position),  $\phi_m$  sweep (flapping) amplitude,  $\alpha_m$  geometric angle of attack around mid-stroke,  $\alpha_0$  inclination offset,  $\varphi_\alpha$  the phase shift between the sweep and the inclination,  $\delta_1$  deviation amplitude of an oval pattern and  $\delta_2$  deviation amplitude of a figure-of-eight pattern. The parameter  $k_\phi$  defines the shape of sweep angle function  $\phi(t)$  from harmonic ( $k_\phi \rightarrow 0$ ) to triangular ( $k_\phi = 1$ ). Similarly, the parameter  $k_\alpha$  changes the shape of the inclination angle function  $\alpha^*(t)$  from harmonic ( $k_\alpha \rightarrow 0$ ) to square wave ( $k_\alpha \rightarrow \infty$ ). The parameter effects are demonstrated in Figures 3.2 and 3.3.

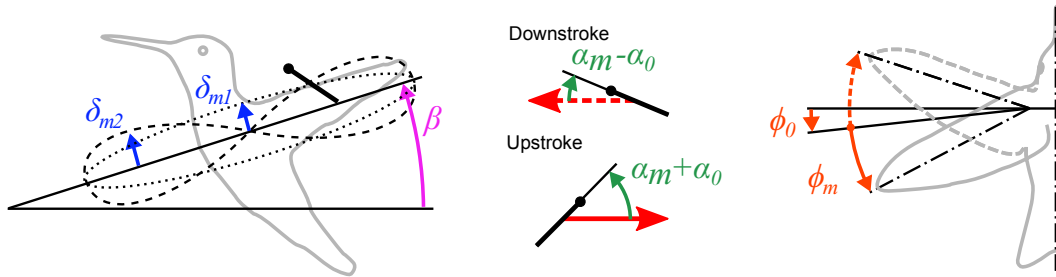
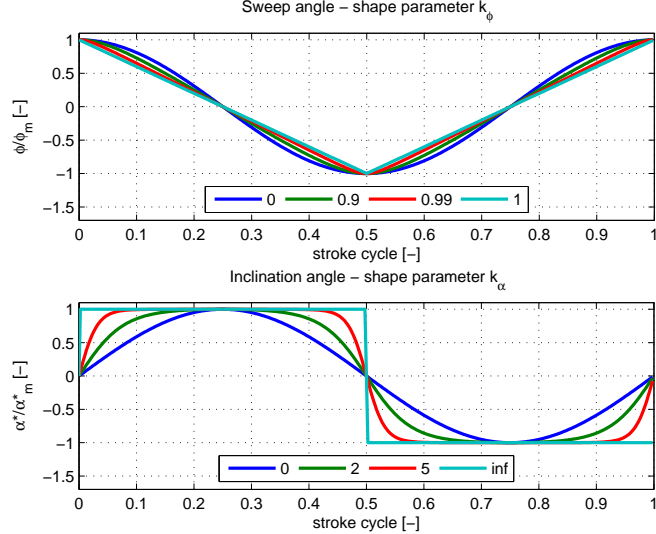


Figure 3.2: Parameters defining the wing kinematics.



**Figure 3.3:** Parameters  $k_\phi$  and  $k_\alpha$  defining the shape of sweep and inclination angle functions.

### 3.1.2 Quasi-steady aerodynamics

The quasi-steady model consists of three force components: force due to wing translation with normal and tangential part  $F_{Ntr}$  and  $F_{Ttr}$ , force due to wing rotation  $F_{Nr}$  and force due to the inertia of added mass of the fluid  $F_{Na}$ . The directions of the normal and tangential force components and their relation to the lift and drag are shown in Figure 3.4.

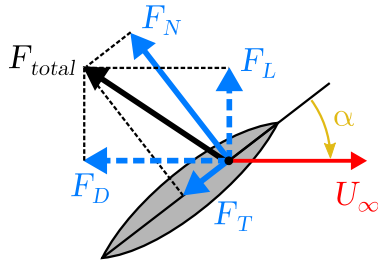


**Figure 3.4:** Different components of the total aerodynamic force.

In this work a flat and rigid wing of an arbitrary form is assumed. The important wing geometry parameters are displayed in Figure 3.5.  $R$  is the wing length,  $\bar{c}$  is the mean chord length,  $S = R\bar{c}$  is the surface of a single wing. A chord section at the distance  $r$  from the wing root has a length  $c$ .  $\hat{x}_0$  is the non-dimensional position of the rotational axis. The aspect ratio of the wing is defined as  $\mathcal{A}R = \frac{2R^2}{S} = \frac{2R}{\bar{c}}$ .

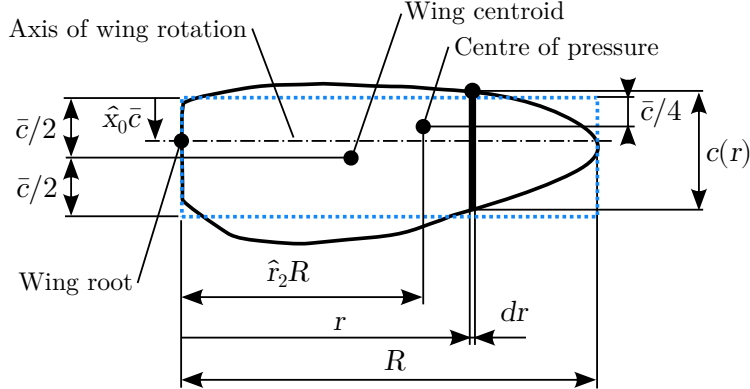


**Figure 3.5:** Wing geometry parameters

### 3.1.2.1 Force due to wing translation

The lift force due to translation of a 2D airfoil can be expressed according to an equation for fixed wing in steady flow as

$$F'_{Ltr} = \frac{1}{2} \rho C_L(\alpha) c U_\infty^2, \quad (3.2)$$

where  $\rho$  is the air density and  $C_L$  is the lift coefficient.

If we consider hovering flapping flight and wing motion with 2 DOF the section speed can be expressed as  $U_\infty(r) = r\dot{\phi}$ . For a wing with length  $R$  and mean chord  $\bar{c}$  we introduce the non-dimensional section position and the non-dimensional chord length as  $\hat{r} = \frac{r}{R}$  and  $\hat{c} = \frac{c}{\bar{c}}$ , respectively (Ellington, 1984a). The force of the whole wing is given by an integral of the section force over the wing span

$$\begin{aligned} F_{Ltr} &= \int_0^R F'_{Ltr}(r) dr = \\ &= \frac{1}{2} \rho C_L(\alpha) \dot{\phi}^2 \int_0^R c(r) r^2 dr = \\ &= \frac{1}{2} \rho C_L(\alpha) \dot{\phi}^2 R^3 \bar{c} \int_0^1 \hat{c}(\hat{r}) \hat{r}^2 d\hat{r} = \\ &= \frac{1}{2} \rho C_L(\alpha) S \hat{r}_2^2 R^2 \dot{\phi}^2, \end{aligned} \quad (3.3)$$

where  $\hat{r}_2^2 = \int_0^1 \hat{c}(\hat{r}) \hat{r}^2 d\hat{r}$  is the non-dimensional radius of the second moment of inertia. It defines the span-wise position of the centre of pressure where the forces with

circulatory origin act. Its chord-wise position is assumed, similar to other studies, to be at one quarter of the chord from the leading edge (Figure 3.5), which is a simplification as Dickson et al. (2006) showed experimentally on a model wing that the location of the centre of pressure depends on the angle of attack.

The lift can also be formulated as a function of the centre of pressure speed  $U_{CP} = \hat{r}_2^2 R^2 \dot{\phi}^2$  as

$$F_{Ltr} = \frac{1}{2} \rho C_L(\alpha) S U_{CP}^2. \quad (3.4)$$

Similar formulation can be written for the drag force

$$F_{Dtr} = \frac{1}{2} \rho C_D(\alpha) S U_{CP}^2. \quad (3.5)$$

Since the remaining force components to be introduced in the next sections are all of a pressure origin and thus act normally to the wing chord it is convenient to transform the above lift and drag forces also into normal and tangential component (Deng et al., 2006)

$$F_{Ntr} = \frac{1}{2} \rho C_N(\alpha) S U_{CP}^2 \quad (3.6)$$

$$F_{Ttr} = \frac{1}{2} \rho C_T(\alpha) S U_{CP}^2. \quad (3.7)$$

The normal and tangential force coefficients  $C_N$  and  $C_T$  were obtained by transformation of the empirical coefficients of Dickinson et al. (1999), which include the effect of the delayed stall of the leading edge vortex, and have the following form

$$C_N(\alpha) = 3.4 \sin(\alpha) \quad (3.8)$$

$$C_T(\alpha) = \begin{cases} 0.4 \cos^2(2\alpha) & 0 \leq |\alpha| < \frac{\pi}{4} \\ 0 & \frac{\pi}{4} \leq |\alpha| < \frac{3\pi}{4} \\ -0.4 \cos^2(2\alpha) & \frac{3\pi}{4} \leq |\alpha| < \pi. \end{cases} \quad (3.9)$$

### 3.1.2.2 Force due to wing rotation

Another force component that contributes to the total force generated by a flapping wing is the force due to wing rotation. It was derived from quasi-steady equations used for flutter analysis (e.g. Fung, 1969). A translating wing that also starts to rotate will develop additional circulation around itself to satisfy the Kutta condition (Ellington, 1984b). With the notation of Figure 3.5 this circulation can be expressed as

$$\Gamma_r = \pi \dot{\alpha} c^2 \left( \frac{3}{4} - \hat{x}_0 \right). \quad (3.10)$$

For a 2D airfoil the force is defined as

$$F'_{Nr}(r) = \rho U_\infty \Gamma_r = \pi \rho c^2 \left( \frac{3}{4} - \hat{x}_0 \right) U_\infty \dot{\alpha}. \quad (3.11)$$

As a force of circulatory origin it acts at the centre of pressure and normally to the wing.

The total wing force is again obtained by integration over the wingspan while substituting  $U_\infty(r) = r\dot{\phi}$  and introducing the non-dimensional position  $\hat{r}$  and chord  $\hat{c}$

$$\begin{aligned} F_{Nr} &= \int_0^R F'_{Nr} dr = \\ &= \pi \rho \left( \frac{3}{4} - \hat{x}_0 \right) \dot{\alpha} \dot{\phi} R^2 \bar{c}^2 \int_0^1 \hat{c}^2(r) \hat{r} d\hat{r}. \end{aligned} \quad (3.12)$$

This can be rewritten further using the centre of pressure speed  $U_{CP}$  as

$$F_{Nr} = \rho \pi \left( \frac{3}{4} - \hat{x}_0 \right) \dot{\alpha} U_{CP} \frac{R \bar{c}^2}{\hat{r}_2} \int_0^1 \hat{c}^2(r) \hat{r} d\hat{r}. \quad (3.13)$$

### 3.1.2.3 Force due to the inertia of added mass

The force due to the inertia of the added mass off the fluid can be formulated with the help of equations originally introduced for flutter analysis. According to Fung (1969) this force consists of two components: a force due to the acceleration of an apparent mass and a centrifugal force.

The apparent mass acceleration force acts at the mid-chord (Figure 3.6). It is defined as the apparent mass of a cylindrical section  $\rho \pi \frac{c^2}{4}$  times the normal acceleration

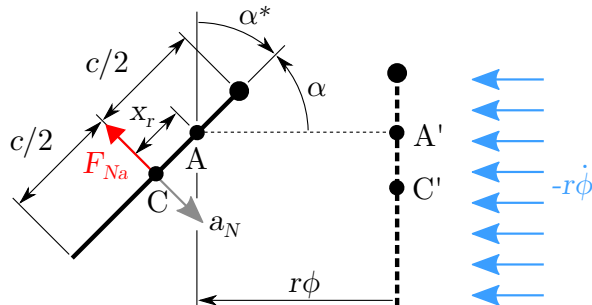


**Figure 3.6:** Wing section and parameters for calculation of the added mass force.

$a_N$  of the mid-chord. Assuming hovering flight and wing motion with 2 DOF the acceleration of a wing section at a distance  $r$  from the wing root can be written as

$$a_N(r) = x_r \ddot{\alpha} - r \ddot{\phi} \sin \alpha, \quad (3.14)$$

where  $x_r$  is the distance of the axis of rotation A to the mid-chord C (Figure 3.6). Assuming further that this distance is equal to a quarter chord ( $x_r = \frac{c}{4}$ ) the force becomes

$$F'_{Na}(r) = \rho \pi \frac{c^2(r)}{4} a_N(r) = \rho \pi \frac{c^2(r)}{4} \left( \frac{c(r)}{4} \ddot{\alpha} - r \ddot{\phi} \sin \alpha \right). \quad (3.15)$$

The centrifugal force is a force of circulatory origin and is located at 3/4 of the chord from the leading edge. It is defined as the apparent mass times  $U\dot{\alpha}$ , where  $U$  is the component of relative wind speed in chord direction. For hovering flight with 2 DOF the wing section force can be written as

$$F'_{Nc}(r) = \rho \pi \frac{c^2(r)}{4} \left( -r \dot{\phi} \cos \alpha \right) \dot{\alpha}. \quad (3.16)$$

The total force is obtained by integration of the section forces over the wingspan while also introducing the non-dimensional position  $\hat{r}$  and chord  $\hat{c}$

$$\begin{aligned} F_{Na} &= \int_0^R [F'_{Na}(r) + F'_{Nc}(r)] dr = \\ &= -\frac{1}{4} \rho \pi R^2 \bar{c}^2 \left( \ddot{\phi} \sin \alpha + \dot{\phi} \dot{\alpha} \cos \alpha \right) \int_0^1 \hat{c}^2 \hat{r} d\hat{r} + \frac{1}{16} \rho \pi R \bar{c}^3 \ddot{\alpha} \int_0^1 \hat{c}^3 d\hat{r}. \end{aligned} \quad (3.17)$$

This formulation was presented by Maybury and Lehmann (2004), which is the formulation from Sane and Dickinson (2001) with additional corrections. Compared to Maybury and Lehmann (2004) the terms including derivations of sweep angle  $\phi$  in our formulation differ in sign. This is due to an opposite definition of the positive direction of  $\phi$ .

### 3.1.2.4 Total force

Since the effects of the added mass inertia are relatively small compared to the other two components it will be neglected further in the text for simplicity. However, its effects will be demonstrated at the end of this section. Thus, the total force of the flapping wing is a sum of forces due to translation and rotation

$$\begin{aligned} F_N &= F_{Ntr} + F_{Nr} = \frac{1}{2} \rho C_N(\alpha) S U_{CP}^2 + \rho \pi \left( \frac{3}{4} - \hat{x}_0 \right) \dot{\alpha} U_{CP} \frac{R \bar{c}^2}{\hat{r}_2} \int_0^1 \hat{c}^2(\hat{r}) \hat{r} d\hat{r} \\ F_T &= F_{Tr} = \frac{1}{2} \rho C_T(\alpha) S U_{CP}^2. \end{aligned} \quad (3.18)$$

For a wing with given form the force varies only with the velocity of the centre of pressure  $U_{CP}$  and with the angle of attack  $\alpha$ . The angle of attack is defined in Figure 3.7 as the angle between the negative  $x_W$  axis of the wing and the  $U_{CP}$  velocity vector. It can be either positive or negative, with values from the interval  $(-\pi, \pi)$ . The normal component  $F_N$  acts in  $z_W$  direction (thus for hovering flight we get positive values in downstroke and negative in upstroke) and the tangential component  $F_T$  acts in  $x_W$  direction (in hover it is always positive or zero). The expressions for the centre of pressure velocity and for the angle of attack for arbitrary flight conditions will be derived in the following section.

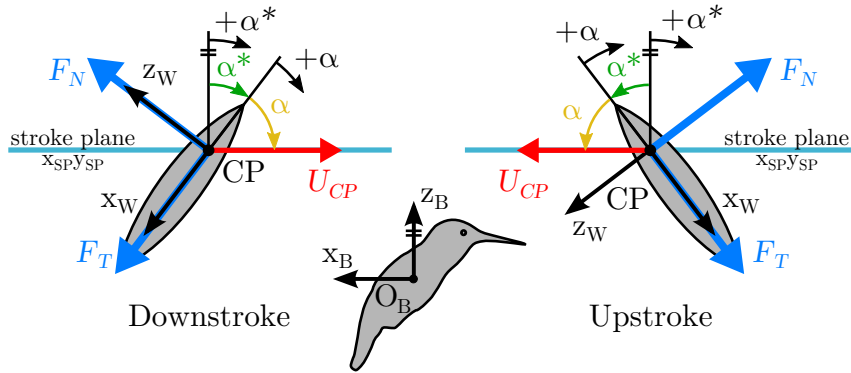


**Figure 3.7:** Angle of attack  $\alpha$  and orientation of normal,  $F_N$ , and tangential,  $F_T$ , force component in upstroke and downstroke (hovering flight). The figure displays right wing section and considers  $\beta = 0$  and  $\delta = 0$  for clarity.

### 3.1.3 Centre of pressure velocity and angle of attack

For hovering flight (body velocities and angular velocities are zero) and zero deviation from the stroke plane the aerodynamic angle of attack can be approximated as  $\alpha = \text{sign}(U_{CP})\pi/2 - \alpha^*$  (see Figure 3.7). Assuming further that the centre of pressure (CP) lies on the span-wise rotation axis, its velocity is given by relation  $U_{CP} = \dot{r}_2 R \phi$ .

For a general case, when the body is in motion, the CP velocity is modified. Since not only the magnitude but also the direction of CP velocity changes, the aerodynamic angle of attack is also affected as can be seen in Figure 3.8 a). Situations, where angle of attack is negative or greater than  $90^\circ$  are sketched in 3.8 b) and 3.8 c) respectively. Things get even more complicated when the wing deviates from the stroke plane and the rotation axis is not going through the CP.

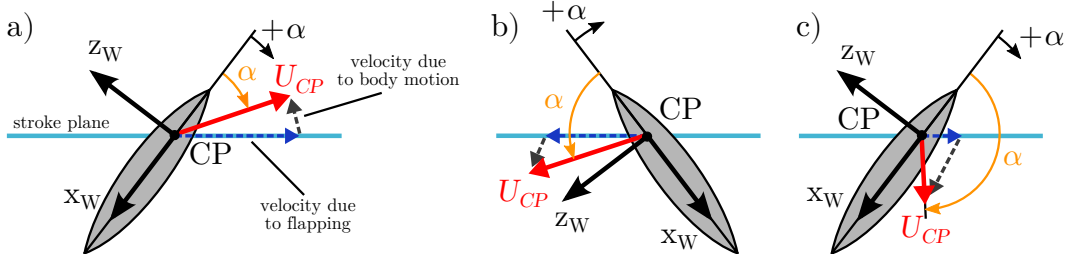


**Figure 3.8:** Influence of body motion on the angle of attack; the figures represent the right wing cross-section and consider  $\beta = 0$  and  $\delta = 0$  for clarity. a) Decomposition of the wing velocity into components due to flapping and due to body motion. b) Situation with negative angle of attack. c) Situation with angle of attack greater than  $90^\circ$ .

The motion of the wing with respect to the surrounding air can be decomposed into a series of simultaneous motions. For their description we introduce three coordinate frames displayed in Figure 3.9 a) - global (inertial) frame G, body-fixed frame B and wing-fixed frame W. A left superscript with the frame letter will be used to indicate the coordinate system in which a vector or matrix is expressed. The origin of the B frame is in the centre of gravity of the bird. In hover its axes are parallel to global frame axes with  $z_B$  axis pointing towards the sky,  $x_B$  axis in the backward flight direction and  $y_B$  axis in the direction of the right wing. The origin of the wing frame W is placed into the wing-root. The  $y_W$  axis is aligned with the wing spanwise rotation axis,  $x_W$  axis is parallel to the chord and pointing towards the trailing edge of the wing and  $z_W$  axis is normal to the wing surface, positive on the dorsal side of the wing.

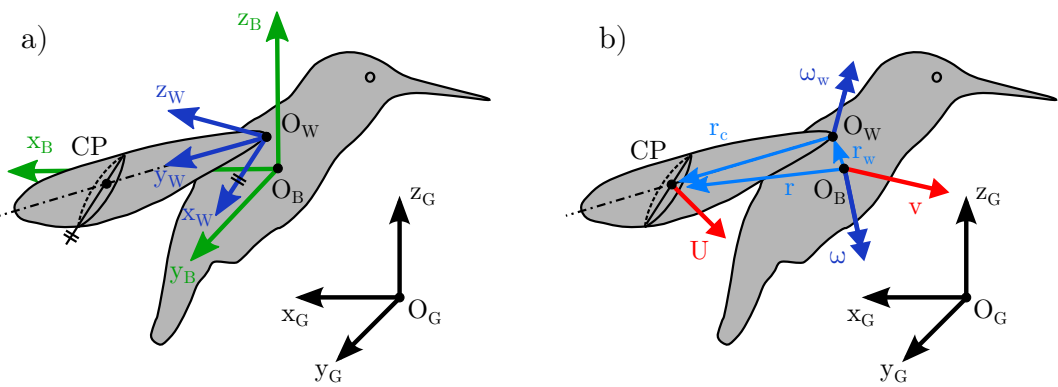


**Figure 3.9:** Wing kinematics description. a) Introduced coordinate frames: global frame G, body-fixed frame B and wing-fixed frame W. b) Centre of pressure position and velocity as a result of simultaneous motions.

Any vector in the W frame can be transformed to the B frame by the rotation matrix  $\mathbf{R}$ , which is a function of the wing position angles from Section 3.1.1. For the right wing the matrix is defined as

$$\mathbf{R} = \mathbf{R}_y(-\beta)\mathbf{R}_z(-\phi)\mathbf{R}_x(\delta)\mathbf{R}_y\left(\frac{\pi}{2} - \alpha^*\right). \quad (3.19)$$

The opposite vector transformation (from B frame to W frame) is given by a transpose of the above matrix  $\mathbf{R}^T$ . The angular velocity between the wing and the body is, in skew-symmetric form, given by the derivation of the rotation matrix

$$\boldsymbol{\Omega}_w = \begin{bmatrix} 0 & -\omega_{wz} & \omega_{wy} \\ \omega_{wz} & 0 & -\omega_{wx} \\ -\omega_{wy} & \omega_{wx} & 0 \end{bmatrix} = \dot{\mathbf{R}}. \quad (3.20)$$

For wings flapping in a horizontal flapping plane with no deviation ( $\beta = 0$ ,  $\delta = 0$ ) we obtain

$$\mathbf{R} = \begin{bmatrix} \cos \phi \sin \alpha^* & \sin \phi & \cos \phi \cos \alpha^* \\ -\sin \phi \sin \alpha^* & \cos \phi & -\sin \phi \cos \alpha^* \\ -\cos \alpha^* & 0 & \sin \alpha^* \end{bmatrix} \quad (3.21)$$

$$\boldsymbol{\omega}_w = \begin{bmatrix} \omega_{wx} \\ \omega_{wy} \\ \omega_{wz} \end{bmatrix} = \begin{bmatrix} \dot{\phi} \cos \alpha^* \\ -\dot{\alpha}^* \\ -\dot{\phi} \sin \alpha^* \end{bmatrix}. \quad (3.22)$$

The CP velocity is a resultant of body absolute motion (with velocity  $\mathbf{v} = [u, v, w]$  and angular velocity  $\boldsymbol{\omega} = [p, q, r]$ ) and the wing rotation relative to the body  $\boldsymbol{\omega}_w$ , see Figure 3.9 b). By using the theory for simultaneous motion we can express the velocity of CP of the wing in W frame as

$$\mathbf{U} = \mathbf{R}^T (\mathbf{v} + \boldsymbol{\omega} \times \mathbf{r}) + \boldsymbol{\omega}_w \times \mathbf{r}_c, \quad (3.23)$$

where  $\mathbf{r}_c = \left[ \left( \frac{1}{4} - \hat{x}_0 \right) \bar{c}, \pm \hat{r}_2 R, 0 \right]^T$  is the position of the CP in the right/left wing frame, respectively, and  $\mathbf{r}$  is the CP position in the body frame defined as

$$\mathbf{r} = \mathbf{r}_w + \mathbf{R} \mathbf{r}_c, \quad (3.24)$$

where  $\mathbf{r}_w = [x_w, \pm e/2, z_w]^T$  is the right/left shoulder position in the body frame, respectively.  $e$  is the width of the chest, i.e. the distance between the shoulders.

The angle of attack of the wing is measured between the wing chord and the relative velocity vector of the wing with respect to the surrounding air (Figure 3.8). Here the angle of attack is approximated to be constant along the wingspan and the value

for the CP is used. The magnitude of the CP velocity vector in xwzw plane of the wing is

$$U_{CP} = \sqrt{U_x^2 + U_z^2}. \quad (3.25)$$

The effect of the spanwise component  $U_y$  on the aerodynamics is not considered.

According to Figure 3.8 the angle of attack can be computed as

$$\alpha = \text{atan2}(-U_z, -U_x), \quad (3.26)$$

where the atan2 is a four-quadrant inverse tangent function returning values between  $-\pi$  and  $\pi$  (MathWorks, 2014). The time derivative of the angle of attack can be derived from the above equation as

$$\dot{\alpha} = \frac{\dot{U}_z U_x - U_z \dot{U}_x}{U_x^2 + U_z^2}. \quad (3.27)$$

The velocity derivations in the formula represent the change of CP velocity vector in the wing frame and thus need to be carried out in that frame.

### 3.1.4 Comparison with CFD

To justify the use of quasi-steady aerodynamics and to show the importance of the force component due to rotation, the instantaneous forces calculated by our model are compared to CFD data. Lift, drag and side force curves from CFD study by Zhang and Sun (2010a) are plotted in Figure 3.10 together with the curves resulting from the quasi-steady model. To demonstrate the degree of importance of the quasi-steady model components, first only the force due to translation (3.6-3.7) is considered and the model is called ASL (tr). In model ASL (tr+rot) the force due to rotation (3.13) is also included. Finally in model ASL (tr+rot+add) the last component due to the inertia of the added mass, similar to (3.17), is considered. The details on the wing kinematics and morphology used are in (Karasek and Preumont, 2012).

The forces are presented in the form of non-dimensional force coefficients defined as  $C_L = F_L/(0.5\rho S \bar{U}_{CP}^2)$  and similarly for  $C_D$  and  $C_Y$ .  $\bar{U}_{CP}$  is the mean CP velocity defined as  $\bar{U}_{CP} = 4\phi_m f \hat{r}_2 R$ . Lift  $F_L$  is the force that is normal to the stroke plane. Drag  $F_D$  lies inside the stroke plane and represents the force in an opposite direction to the wing instantaneous motion. Finally the side force  $F_Y$  represents the  $y_B$  axis component of the drag force. The curves start at cycle time  $t^+ = 0$ , which is the point of reversal between upstroke and downstroke, the cycle is completed at  $t^+ = 1$ .

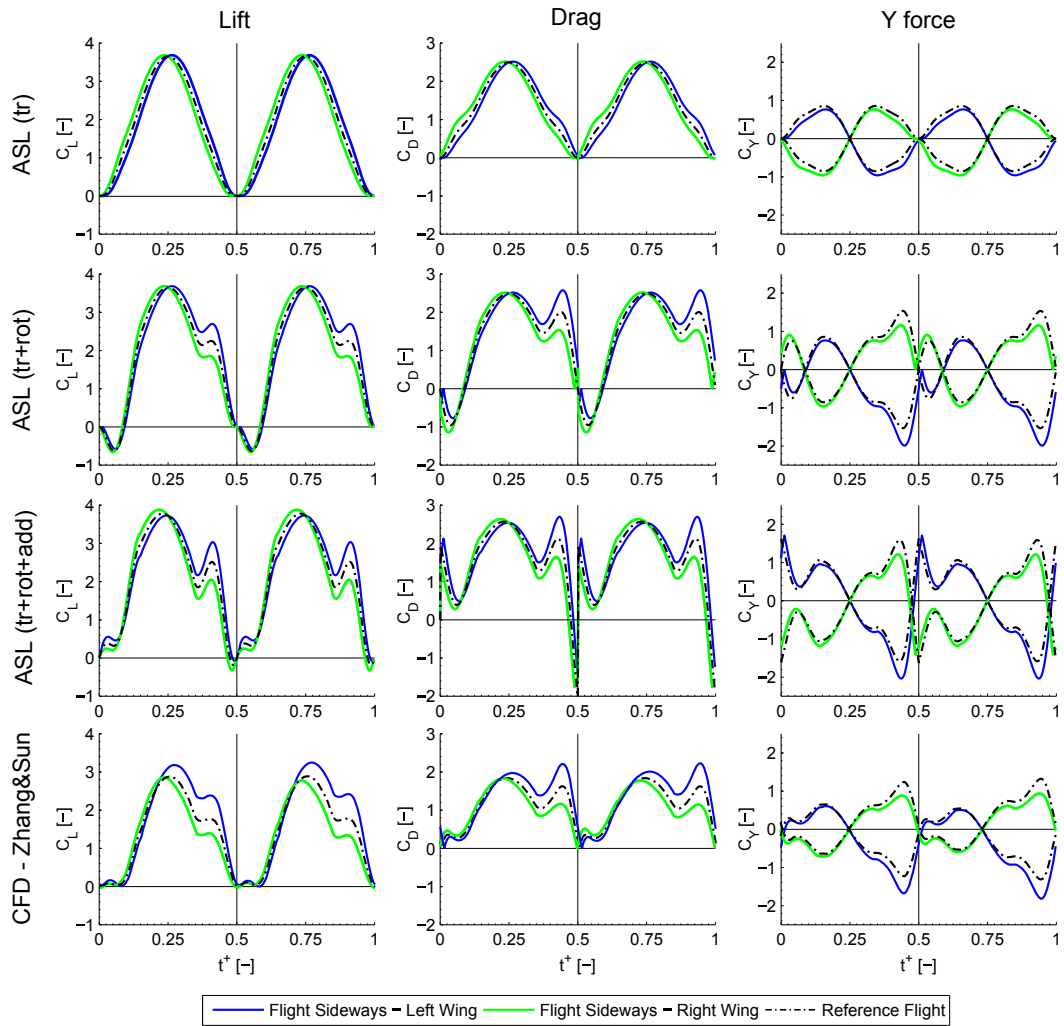


**Figure 3.10:** Instantaneous forces over one flapping cycle predicted with quasi-steady model with increasing number of components and compared to CFD results of Zhang and Sun (2010a).

Apart from the wing forces in hovering conditions (dash-dotted line, lift and drag identical for both wings), the left and right wing forces in sideways-flight with speed  $v = 0.15 \bar{U}_{CP}$  are also displayed. Good agreement of the force traces when the system is slightly deviated from its equilibrium is important for assessing the system stability, which will be studied in the following section.

When we compare the CFD results (Figure 3.10, 4th row) to the force curves from the translational component model ASL (tr) (Figure 3.10, 1st row) it is clear, that such a model is insufficient. On the contrary, the curves obtained by the ASL (tr+rot) model (Figure 3.10, 2nd row) show much better agreement with the CFD results. The rotational force component is responsible for the positive lift peak before and negative lift peak after the stroke reversal. Similar peaks can be observed in drag and in the side force (both positive). Major differences occur after the reversal, where the forces predicted by the ASL (tr+rot) model drop, while positive peaks can be observed in the CFD force traces. The differences might be, at least partially, explained by the wake capture mechanism that is included only in the CFD model.

The addition of the added mass inertia component increases the magnitude of the curves and further modifies the behaviour around the stroke reversal (Figure 3.10, 3rd row). The accordance with the CFD results is slightly improved in some parts (lift peak and side force sign after the reversal) while in other parts the accordance gets worse (non-zero lift and drag force at the reversal). Thus, the overall improvement over the ASL (tr+rot) model force traces is insignificant, if any.

All the quasi-steady models over predict the CFD force magnitudes by about 20%. Considering that the used quasi-steady force coefficients were determined empirically for a wing with different geometry and under different conditions, this difference is still acceptable. Regardless the magnitudes, the shape of the force traces and the trend of their changes, important for studying the stability and control of flapping flight, are captured with good accordance when the force due to rotation is used.

## 3.2 Body dynamics

The dynamics of the flying robot can be described, under rigid body assumption, by Newton-Euler motion equations. Similar to an aircraft we obtain 12 ordinary differential equations with 12 unknown coordinates - velocity ( $u, v, w$ ), angular velocity ( $p, q, r$ ), position ( $x, y, z$ ) and orientation expressed by Roll-Pitch-Yaw angles ( $\varphi, \theta, \psi$ ) - see Figure 3.11. By omitting the equations for position and heading (yaw)

angle  $\psi$  the system is reduced to 8 equations

$$\begin{aligned}
 \dot{u} &= -(wq - vr) + X/m + g \sin \vartheta \\
 \dot{v} &= -(ur - wp) + Y/m - g \cos \vartheta \sin \varphi \\
 \dot{w} &= -(vp - uq) + Z/m - g \cos \vartheta \cos \varphi \\
 I_{xx}\dot{p} &= (I_{yy} - I_{zz}) qr + I_{xz}(\dot{r} + pq) + L \\
 I_{yy}\dot{q} &= (I_{zz} - I_{xx}) pr + I_{xz}(r^2 - p^2) + M \\
 I_{zz}\dot{r} &= (I_{xx} - I_{yy}) pq + I_{xz}(\dot{p} - qr) + N \\
 \dot{\varphi} &= p + q \sin \varphi \tan \vartheta + r \cos \varphi \tan \vartheta \\
 \dot{\vartheta} &= q \cos \varphi - r \sin \varphi,
 \end{aligned} \tag{3.28}$$

where  $m$  is the body mass and  $I_{xx}$ ,  $I_{yy}$ ,  $I_{zz}$  and  $I_{xz}$  are the non-zero moments and product of inertia in body frame (products  $I_{xy}$  and  $I_{yz}$  are both zero due to body symmetry). Aerodynamic forces and moments are represented by vectors ( $X$ ,  $Y$ ,  $Z$ ) and ( $L$ ,  $M$ ,  $N$ ) respectively.

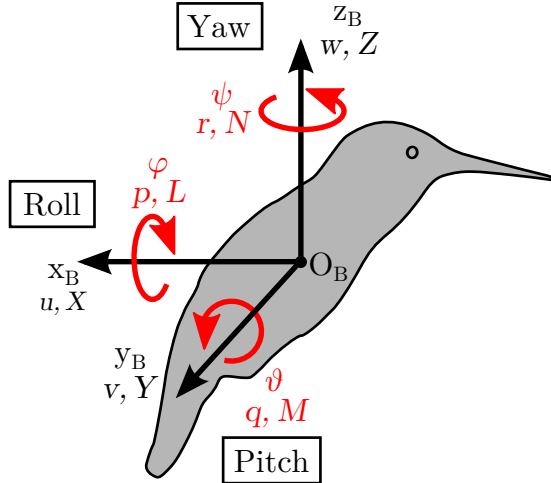


**Figure 3.11:** Definition of body coordinates

There are two main types of aerodynamic forces to be considered: wing forces and drag of body, legs and tail. According to Ristroph et al. (2013) the body drag force becomes important only in milligram-scale insects and legs and tail need to be considered only in specific species. Xiong and Sun (2008) showed, that the body effects become significant only for higher forward speeds. Thus, all drag-type forces are neglected and only the wing forces are considered further.

The wing forces (3.18) are transformed into the body frame as follows

$$[X, Y, Z]^T = \sum_i [X_i, Y_i, Z_i]^T = \sum_i \mathbf{R}_i [F_{Ti}, 0, F_{Ni}]^T \quad (3.29)$$

$$[L, M, N]^T = \sum_i \mathbf{r}_{ci} \times [X_i, Y_i, Z_i]^T, \quad (3.30)$$

where index  $i$  stands for the left and the right wing.

### 3.2.1 System linearisation

The mathematical model introduced in the previous sections is nonlinear and was used in flight simulations. For stability studies and control design a linear model is preferred.

The system dynamics (3.28) include aerodynamic forces and moments (3.29, 3.30) that are functions of wing motion parameters  $\mathbf{p} = [f, \beta_L, \phi_{mL}, \phi_{0L}, \alpha_{mL}, \alpha_{0L}, \varphi_{\alpha L}, \delta_{m1L}, \delta_{m2L}, \beta_R, \dots, \delta_{m2R}]^T$ , system state  $\mathbf{x} = [u, v, w, p, q, r, \varphi, \vartheta]^T$  and time  $t$ . Assuming the flapping frequency is much higher than the bandwidth of the system, the aerodynamic forces can be replaced by their cycle averaged values (mean values over one wingbeat), e.g.

$$\bar{X} = \int_0^{\frac{1}{f}} X(\mathbf{x}, \mathbf{p}, t) dt = \bar{X}(\mathbf{x}, \mathbf{p}), \quad (3.31)$$

that depend only on  $\mathbf{x}$  and  $\mathbf{p}$ . Small perturbation theory is used to rewrite the states and wing motion parameters as

$$\mathbf{x} = \mathbf{x}_e + \delta\mathbf{x}, \quad \mathbf{p} = \mathbf{p}_e + \delta\mathbf{p}, \quad (3.32)$$

where subscript  $e$  signifies the equilibrium values and  $\delta$  symbol stands for the perturbation. The aerodynamic forces and moments are approximated by the linear terms of Taylor's expansion. For the x-axis force we obtain

$$\bar{X}(\mathbf{x}, \mathbf{p}) = \bar{X}_e(\mathbf{x}_e, \mathbf{p}_e) + \sum_{i=1}^6 \frac{\partial \bar{X}}{\partial x_i}(\mathbf{x}_e, \mathbf{p}_e) \delta x_i + \sum_{j=1}^n \frac{\partial \bar{X}}{\partial p_j}(\mathbf{x}_e, \mathbf{p}_e) \delta p_j, \quad (3.33)$$

where  $\bar{X}_e$  is the cycle averaged force generated in equilibrium and  $n$  is the number of wing kinematic parameters. The terms of the first summation are the derivatives with respect to body velocities and angular velocities called the *stability derivatives*. If taken with an opposite sign they represent aerodynamic damping. The second summation terms are the derivatives with respect to changes in wing motion. They

are called the *control derivatives*. Further the overbar notation for cycle averages is dropped and the notation of the derivatives is shortened in the following manner

$$\frac{\partial \bar{X}}{\partial u} = X_u, \quad \frac{\partial \bar{X}}{\partial v} = X_v, \quad \dots, \quad \frac{\partial \bar{X}}{\partial f} = X_f, \quad \frac{\partial \bar{X}}{\partial \beta} = X_\beta, \quad \dots \quad (3.34)$$

Since only the near hover flight is considered, all the equilibrium states are zero ( $u_e = v_e = w_e = p_e = q_e = r_e = \varphi_e = \vartheta_e = 0$ ) and the perturbed states are equal to their absolute values ( $\delta\mathbf{x} = \mathbf{x}$ ). The wing motion parameters  $\mathbf{p}_e$  must ensure that the z-force is in balance with the gravity force ( $Z_e = mg$ ), while the remaining forces and moments are zero ( $X_e = Y_e = L_e = M_e = N_e = 0$ ).

First it is supposed that the wing kinematics does not change ( $\delta\mathbf{p} = \mathbf{0}$ ). Instead, an arbitrary external force [ $X_{ext}, Y_{ext}, Z_{ext}$ ] or moment [ $M_{ext}, N_{ext}, L_{ext}$ ] can be applied on the body. According to previous works on passive stability, e.g. Taylor and Thomas (2003); Zhang and Sun (2010a), as well as to our results there exists no aerodynamic coupling between the longitudinal and lateral system. By neglecting the second order terms, the equations can be rewritten as two linear subsystems represented in state space as

$$\begin{bmatrix} \dot{u} \\ \dot{w} \\ \dot{q} \\ \dot{\vartheta} \end{bmatrix} = \mathbf{A}_{\text{long}} \begin{bmatrix} u \\ w \\ q \\ \vartheta \end{bmatrix} + \mathbf{B}_{\text{long}} \begin{bmatrix} X_{ext} \\ Z_{ext} \\ M_{ext} \end{bmatrix} \quad (3.35)$$

$$\begin{bmatrix} \dot{v} \\ \dot{p} \\ \dot{r} \\ \dot{\varphi} \end{bmatrix} = \mathbf{A}_{\text{lat}} \begin{bmatrix} v \\ p \\ r \\ \varphi \end{bmatrix} + \mathbf{B}_{\text{lat}} \begin{bmatrix} Y_{ext} \\ L_{ext} \\ N_{ext} \end{bmatrix}, \quad (3.36)$$

where the system matrices are

$$\mathbf{A}_{\text{long}} = \begin{bmatrix} \frac{X_u}{m} & \frac{X_w}{m} & \frac{X_q}{m} & g \\ \frac{Z_u}{m} & \frac{Z_w}{m} & \frac{Z_q}{m} & 0 \\ \frac{M_u}{I_{yy}} & \frac{M_w}{I_{yy}} & \frac{M_q}{I_{yy}} & 0 \\ 0 & 0 & 1 & 0 \end{bmatrix} \quad (3.37)$$

$$\mathbf{A}_{\text{lat}} = \begin{bmatrix} \frac{Y_v}{m} & \frac{Y_p}{m} & \frac{Y_r}{m} & -g \\ \frac{L_v I_{zz} + N_v I_{xz}}{I_{xx} I_{zz} - I_{xz}^2} & \frac{L_p I_{zz} + N_p I_{xz}}{I_{xx} I_{zz} - I_{xz}^2} & \frac{L_r I_{zz} + N_r I_{xz}}{I_{xx} I_{zz} - I_{xz}^2} & 0 \\ \frac{L_v I_{xz} + N_v I_{xx}}{I_{xx} I_{zz} - I_{xz}^2} & \frac{L_p I_{xz} + N_p I_{xx}}{I_{xx} I_{zz} - I_{xz}^2} & \frac{L_r I_{xz} + N_r I_{xx}}{I_{xx} I_{zz} - I_{xz}^2} & 0 \\ 0 & 1 & 0 & 0 \end{bmatrix} \quad (3.38)$$

and the control matrices are

$$\mathbf{B}_{\text{long}} = \begin{bmatrix} \frac{1}{m} & 0 & 0 \\ 0 & \frac{1}{m} & 0 \\ 0 & 0 & \frac{1}{I_{yy}} \\ 0 & 0 & 0 \end{bmatrix} \quad (3.39)$$

$$\mathbf{B}_{\text{lat}} = \begin{bmatrix} \frac{1}{m} & 0 & 0 \\ 0 & \frac{I_{zz}}{I_{xx}I_{zz}-I_{xz}^2} & \frac{I_{xz}}{I_{xx}I_{zz}-I_{xz}^2} \\ 0 & \frac{I_{xz}}{I_{xx}I_{zz}-I_{xz}^2} & \frac{I_{xx}}{I_{xx}I_{zz}-I_{xz}^2} \\ 0 & 0 & 0 \end{bmatrix}. \quad (3.40)$$

In reality, the control forces and moments will be generated by the wings. From the approximation in (3.33) a relation between the vector of cycle averaged forces and moments and the modifications of wing kinematics parameters  $\Delta\mathbf{p}$  can be written as

$$[X, Y, Z, L, M, N]^T = \mathbf{J}\Delta\mathbf{p}, \quad (3.41)$$

where  $\mathbf{J}$  is the matrix of control derivatives defined as

$$\mathbf{J} = \begin{bmatrix} X_{p_1} & X_{p_2} & \cdots & X_{p_n} \\ Y_{p_1} & Y_{p_2} & \cdots & Y_{p_n} \\ \vdots & \vdots & \ddots & \vdots \\ N_{p_1} & N_{p_2} & \cdots & N_{p_n} \end{bmatrix}. \quad (3.42)$$

The kinematic parameters modifications that should produce desired forces/moments are estimated by a pseudoinverse of the previous relation

$$\Delta\mathbf{p} = \mathbf{J}^+[X, Y, Z, L, M, N]^T. \quad (3.43)$$

### 3.2.2 Stability and control derivatives

The stability and control derivatives are computed numerically. For example, the value of  $X_u$  can be obtained from the mean force  $\bar{X}$  computed for small positive and for small negative forward velocity  $\Delta u$  and  $-\Delta u$ , respectively, while keeping other states  $\mathbf{x}$  and wing motion parameters in their equilibrium values  $\mathbf{x}_e$  and  $\mathbf{p}_e$ .

$$X_u = \frac{\partial \bar{X}}{\partial u} \cong \frac{\bar{X}(\mathbf{x}_e + \Delta\mathbf{u}, \mathbf{p}_e) - \bar{X}(\mathbf{x}_e - \Delta\mathbf{u}, \mathbf{p}_e)}{2\Delta u}, \quad (3.44)$$

where  $\Delta\mathbf{u} = [\Delta u, 0, 0, 0, 0, 0]$ . Other stability and control derivatives are obtained in a similar manner.

### 3.3 Reduced model of a flapping wing MAV

In hovering flapping flight, many of the stability derivatives can be dropped. Assuming symmetric wing motion and wing shoulders placed in the z<sub>BYB</sub> plane of the body, derivatives  $X_w$ ,  $Z_u$ ,  $Z_q$  and  $M_w$  will be zero in the longitudinal system and  $Y_r$ ,  $L_r$ ,  $N_v$  and  $N_p$  in the lateral system. This simplifies the system matrices  $\mathbf{A}_{\text{long}}$  and  $\mathbf{A}_{\text{lat}}$  substantially as many of the cross-coupling terms disappear.

In natural fliers the forward flight is the preferred motion. Thus, even in hovering their body posture stays inclined slightly forward with respect to the vertical axis. Due to the definition of the body axes (Figure 3.11) the product of inertia  $I_{xz}$  is non-zero and is responsible for the coupling of roll and yaw. Most hovering MAVs, on the other hand, are designed so that hovering is the nominal operating point and so their body posture is vertical and  $I_{xz} = 0$ , which decouples yaw from the rest of the system.

Thus, the flapping MAV dynamics can be modelled by four subsystems:

- the pitch dynamics ( $u, q, \vartheta$ )

$$\begin{bmatrix} \dot{u} \\ \dot{q} \\ \dot{\vartheta} \end{bmatrix} = \begin{bmatrix} \hat{X}_u & \hat{X}_q & g \\ \hat{M}_u & \hat{M}_q & 0 \\ 0 & 1 & 0 \end{bmatrix} \begin{bmatrix} u \\ q \\ \vartheta \end{bmatrix} + \begin{bmatrix} 1 & 0 \\ 0 & 1 \\ 0 & 0 \end{bmatrix} \begin{bmatrix} \hat{X}_{ext} \\ \hat{M}_{ext} \end{bmatrix} \quad (3.45)$$

- the vertical dynamics ( $w$ )

$$\dot{w} = \hat{Z}_w w + \hat{Z}_{ext} \quad (3.46)$$

- the roll dynamics ( $v, p, \varphi$ )

$$\begin{bmatrix} \dot{v} \\ \dot{p} \\ \dot{\varphi} \end{bmatrix} = \begin{bmatrix} \hat{Y}_v & \hat{Y}_p & -g \\ \hat{L}_v & \hat{L}_p & 0 \\ 0 & 1 & 0 \end{bmatrix} \begin{bmatrix} v \\ p \\ \varphi \end{bmatrix} + \begin{bmatrix} 1 & 0 \\ 0 & 1 \\ 0 & 0 \end{bmatrix} \begin{bmatrix} \hat{Y}_{ext} \\ \hat{L}_{ext} \end{bmatrix} \quad (3.47)$$

- the yaw dynamics ( $r$ )

$$\dot{r} = \hat{N}_r r + \hat{N}_{ext}, \quad (3.48)$$

where the following shortened notation was used:  $\hat{X}_u = X_u/m$ , etc. for force derivatives,  $\hat{M}_u = M_u/I_{yy}$ , etc. for moment derivatives,  $\hat{X}_{ext} = X_{ext}/m$ , etc. for external forces and  $\hat{L}_{ext} = L_{ext}/I_{xx}$  for external moments.

### 3.4 Stability predicted by various aerodynamic models

The objective of this section is to compare the pole locations of various models, including CFD, to justify the use of quasi-steady aerodynamics and cycle-averaging approximations near hovering. This section is based on the results published in (Karasek and Preumont, 2012).

Similar to the model developed in the preceding sections, all the models considered in the comparison employ the *rigid body assumption*: the periodic effects due to flapping are neglected and only the cycle averaged forces are applied on a rigid body, whose equations of motion are linearised, subsequently. The validity of the rigid body assumption was confirmed by Zhang and Sun (2010b) who coupled Navier-Stokes equations with equations of motion and, for small amplitude disturbances, observed no major difference from the cycle-averaged linearised model even for a hawkmoth with relatively low flapping frequency (26.1 Hz).

Because the studied systems (3.35-3.36) are reachable and, assuming all the states being accessible, also observable, the poles and respective modes of motion of the insect can be computed as eigenvalues and eigenvectors of the linearised system matrices  $\mathbf{A}_{\text{long}}$  (3.37) and  $\mathbf{A}_{\text{lat}}$  (3.38). The stability derivatives that appear in the linearised model are calculated based on the wing aerodynamics in all the models; the body drag is not considered as it was found to be negligible near hover (Sun and Xiong, 2005).

It is difficult to measure the stability derivatives directly on flying animals as it would require “deactivation” of all their control system to obtain correct data (Taylor and Thomas, 2003). Thus, most of the published data come from numerical studies. The model animal that will be studied in this section was chosen to be a drone-fly, because CFD-based results are available both for longitudinal (Wu and Sun, 2009) and lateral dynamics (Zhang and Sun, 2010a) for this insect. The important morphological and wing kinematics parameters are in Table 3.1.

Models from Cheng and Deng (2011) and Orlowski and Girard (2011) based on quasi-steady aerodynamics are also included in the comparison. They consider only the force component due to translation, equivalent to (3.6-3.7), but provide analytic expressions of the stability derivatives that can be evaluated for any animal or MAV. Similar to the comparison of force traces in Section 3.1.4 the quasi-steady model from this chapter is represented three times: ASL (tr) includes only the force due to translation (3.6-3.7), ASL (tr+rot) adds the force due to rotation (3.13) and finally ASL (tr+rot+add) adds also the component due to the inertia of the added mass, which is similar to (3.17).

$f$ (Hz)	$\phi_m$ (°)	$m$ (mg)	$I_{xx}$ (kg.m <sup>2</sup> )	$I_{yy}$ (kg.m <sup>2</sup> )	$I_{zz}$ (kg.m <sup>2</sup> )	$I_{xz}$ (kg.m <sup>2</sup> )	$R$ (mm)	$\mathcal{R}$ (-)
164	53.55	87.76	6.58e-10	1.31e-9	8.35e-10	-5.50e-10	11.2	7.52

**Table 3.1:** Dronefly wing and morphological parameters.

### 3.4.1 Stability derivatives

The stability derivatives resulting from all the considered models are summarised in Table 3.2 for longitudinal and in Table 3.3 for lateral system. As in the case of the reduced MAV model from the previous section, many of the derivatives are zero or negligible (compared to derivatives of the same type, i.e. with the same units) no matter what aerodynamic model is used, namely  $\hat{X}_w$ ,  $\hat{Z}_u$ ,  $\hat{Z}_q$  and  $\hat{M}_w$  in the longitudinal system and  $\hat{Y}_r$ ,  $\hat{L}_r$ ,  $\hat{N}_v$  and  $\hat{N}_p$  in the lateral system. Thus, the vertical motion  $w$  is aerodynamically decoupled from the rest of the longitudinal system ( $u$ ,  $q$ ,  $\vartheta$ ) and the yaw rotation  $r$  is aerodynamically decoupled from the rest of the lateral system ( $v$ ,  $p$ ,  $\varphi$ ). Nevertheless, there still exists coupling of roll  $p$  and yaw  $r$  through the inertia product  $I_{xz}$ . All the coordinates were defined in Figure 3.11.

Model	$\hat{X}_u$ (s <sup>-1</sup> )	$\hat{X}_q$ (ms <sup>-1</sup> )	$\hat{Z}_w$ (s <sup>-1</sup> )	$\hat{M}_u$ (m <sup>-1</sup> s <sup>-1</sup> )	$\hat{M}_q$ (s <sup>-1</sup> )
Wu and Sun (2009) (CFD) <sup>*</sup>	-2.22	0.0095	-2.03	-638	-1.65
ASL (tr+rot+add)	-3	-0.0641	-4.7	-691	-9.94
ASL (tr+rot)	-3	-0.0539	-4.7	-607	-9.58
ASL (tr)	-3	-0.00549	-4.7	-369	-3.18
Cheng and Deng (2011)	-2.67	0	-3.63	-328	-2.87
Orlowski and Girard (2011)	-2.74	0	-3.8	-243	-3.11

**Table 3.2:** Stability derivatives - longitudinal system. \*Further non-zero derivatives were found by the CFD study of Wu and Sun (2009):  $\hat{X}_w = 0.179$  s<sup>-1</sup>,  $\hat{Z}_u = -0.108$  s<sup>-1</sup>,  $\hat{Z}_q = 0.0012$  ms<sup>-1</sup>,  $\hat{M}_w = 43.0$  m<sup>-1</sup>s<sup>-1</sup>.

When comparing the stability derivatives from the quasi-steady models to the CFD results the conclusions are ambiguous: for some derivatives we get the same sign and similar magnitude for all the models (e.g.  $\hat{X}_u$ ,  $\hat{Y}_v$ ,  $\hat{N}_r$ ) while for many others there exists no clear correspondence as the magnitudes and sometimes even the signs differ. On the other hand, not all the stability derivatives affect the stability (system poles) in the similar manner. As has been shown in Sun et al. (2007) and Zhang and Sun (2010a) the most important derivatives with respect to stability are  $\hat{X}_u$ ,  $\hat{Z}_w$ ,  $\hat{M}_u$ ,  $\hat{M}_q$  (longitudinal system) and  $\hat{L}_v$ ,  $\hat{L}_p$ ,  $\hat{N}_r$  (lateral system).

Model	$\hat{Y}_v$ (s <sup>-1</sup> )	$\hat{Y}_p$ (ms <sup>-1</sup> )	$\hat{L}_v$ (m <sup>-1</sup> s <sup>-1</sup> )	$\hat{L}_p$ (s <sup>-1</sup> )	$\hat{N}_r$ (s <sup>-1</sup> )
Zhang and Sun (2010a) <sup>*</sup> (CFD)	-1.57	0.0043	-575	-19.7	-25.8
ASL (tr+rot+add)	-1.26	-0.0606	-692	-21.4	-29.6
ASL (tr+rot)	-1.26	-0.0609	-429	-20.8	-29.2
ASL (tr)	-1.26	0.00228	310	-37.6	-29.2
Cheng and Deng (2011)	-1.11	0	272	-20.6	-21.5

**Table 3.3:** Stability derivatives - lateral system. \*Further non-zero derivatives were found by the CFD study of Zhang and Sun (2010a):  $\hat{L}_r = 0.0493 \text{ s}^{-1}$ ,  $\hat{N}_v = -21.4 \text{ m}^{-1}\text{s}^{-1}$ ,  $\hat{N}_p = -1.54 \text{ s}^{-1}$ .

### 3.4.2 Longitudinal system poles

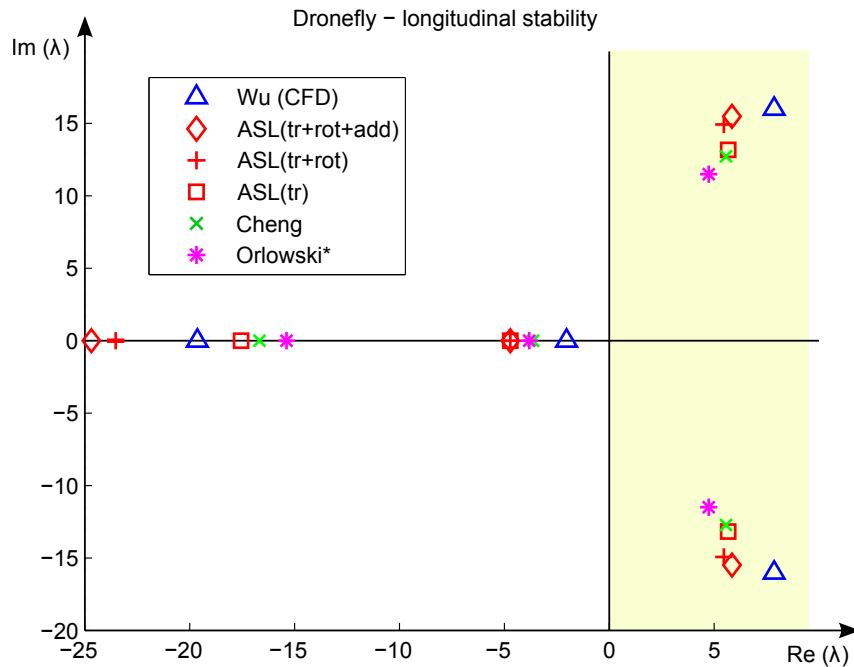
If it was difficult to make some conclusions from the control derivatives values, the pole maps make the situation much easier to understand. The longitudinal system poles are given in Table 3.4. The pole map in Figure 3.12 shows that although the pole locations vary among the different models, the general distribution remains the same: we always see a pair of complex conjugate poles with positive real part, resulting into an unstable oscillatory natural mode, and two negative real poles, representing fast and slow stable natural modes, called subsidence modes by Wu and Sun (2009).

It can be observed that even the simplest models, Cheng & Deng, Orlowski & Girard and ASL (tr), with only translational component give us poles which are reasonably close to the CFD study. If we add the components due to rotation and added mass inertia, the oscillatory mode poles move towards the CFD poles, on the other hand the fast stable mode pole moves away from its CFD counterpart.

Model	Longitudinal system		
	$\lambda_{1,2}$ (Mode 1)	$\lambda_3$ (Mode 2)	$\lambda_4$ (Mode 3)
Wu and Sun (2009)	$7.88 \pm 16i$	-19.6	-2.03
ASL (tr+rot+add)	$5.87 \pm 15.5i$	-24.7	-4.7
ASL (tr+rot)	$5.47 \pm 14.9i$	-23.5	-4.7
ASL (tr)	$5.68 \pm 13.2i$	-17.5	-4.7
Cheng and Deng (2011)	$5.57 \pm 12.7i$	-16.7	-3.63
Orlowski and Girard (2011)	$4.76 \pm 11.5i$	-15.4	-3.8

**Table 3.4:** Poles of the longitudinal system

The eigenvectors (Table 3.6) further show that all the natural modes are estimated reasonably well both in amplitude as well as in phase for all the models. The slow stable subsidence mode (Mode 3), representing the motion in vertical direction  $w$ , is decoupled from the rest. The remaining two modes are dominated by horizontal motion  $u$  coupled with pitch rotation  $q$ . These two motions are in phase for Mode 2 (fast subsidence), but almost in anti-phase (phase difference always greater than  $120^\circ$ ) for Mode 1 (unstable oscillatory).

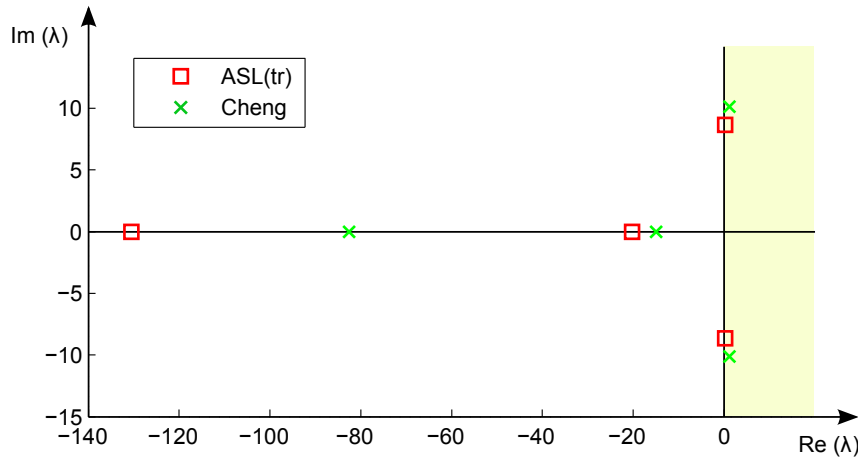
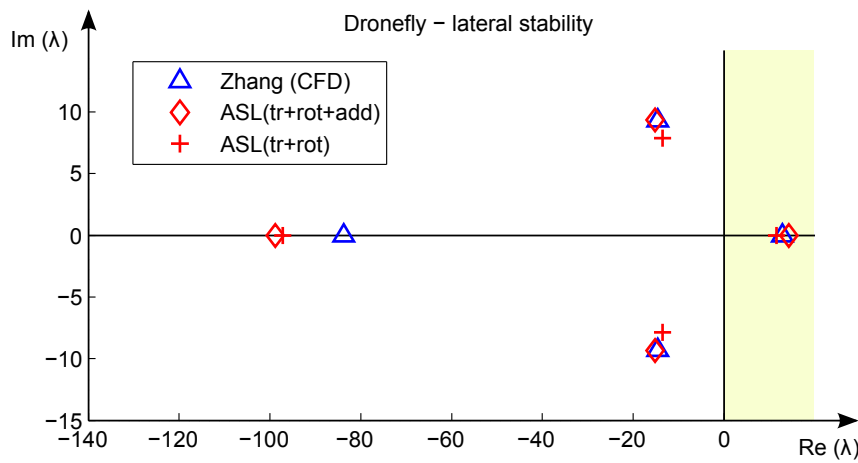


**Figure 3.12:** Pole map - longitudinal system. All the models show similar dynamic behaviour.

### 3.4.3 Lateral system poles

In the lateral direction the situation is different, see Table 3.5 and Figure 3.13. The quasi steady based models with only translational force, Cheng & Deng and ASL (tr), predict one pair of complex conjugate poles with positive real part, resulting into unstable oscillatory mode, and two negative real poles, representing fast and slow stable subsidence modes. On the contrary the models where rotational force is included as well as the CFD model predict a positive real pole, representing a slow unstable divergence mode, a pair of complex conjugate poles with negative real parts (a stable oscillatory mode) and a negative real pole (fast subsidence mode). This shows the importance of the rotational force component on the stability results.

Model	Lateral system		
	$\lambda_{5(5,6)}$ (Mode 4)	$\lambda_{6,7(7)}$ (Mode 5)	$\lambda_8$ (Mode 6)
Zhang and Sun (2010a)	12.9	$-14.6 \pm 9.32i$	-83.7
ASL (tr+rot+add)	14.3	$-15.1 \pm 9.33i$	-98.8
ASL (tr+rot)	11.5	$-13.5 \pm 7.87i$	-97.2
ASL (tr)	$0.274 \pm 8.64i$	-20.3	-130
Cheng and Deng (2011)	$1.25 \pm 10.1i$	-14.9	-82.5

**Table 3.5:** Poles of the lateral system**Figure 3.13:** Pole map - lateral dynamics. Results divided into two figures according to the pole location structure: CFD study Zhang and Sun (2010a) and quasi-steady models that include rotational force (top) and quasi-steady models based only on translational force (bottom).

		Wu and Sun (2009), Zhang and Sun (2010a)	ASL (tr+rot+add)	ASL (tr+rot)	ASL (tr)	Cheng and Deng (2011)	Orlowski and Girard (2011)
Mode 1	$u$	0.522 (56.9°)	0.531 (66.3°)	0.556 (65.3°)	0.619 (57.1°)	0.647 (57.1°)	0.715 (56.9°)
	$w$	0.004 (-49.1°)	0 (0°)	0 (0°)	0 (0°)	0 (0°)	0 (0°)
	$q$	17.859 (-63.8°)	16.578 (-69.3°)	15.910 (-69.9°)	14.369 (-66.7°)	13.901 (-66.4°)	12.444 (-67.5°)
	$\vartheta$	1 (0°)	1 (0°)	1 (0°)	1 (0°)	1 (0°)	1 (0°)
Mode 2	$u$	0.553 (180°)	0.526 (180°)	0.540 (180°)	0.682 (180°)	0.701 (180°)	0.777 (180°)
	$w$	0.002 (180°)	0 (0°)	0 (0°)	0 (0°)	0 (0°)	0 (0°)
	$q$	19.626 (180°)	24.667 (180°)	23.513 (180°)	17.527 (180°)	16.668 (180°)	15.373 (180°)
	$\vartheta$	1 (0°)	1 (0°)	1 (0°)	1 (0°)	1 (0°)	1 (0°)
Mode 3	$u$	3.965 (180°)	0 (0°)	0 (0°)	0 (0°)	0 (0°)	0 (0°)
	$w$	58.792 (180°)	1 (0°)	1 (0°)	1 (0°)	1 (0°)	1 (0°)
	$q$	2.034 (180°)	0 (0°)	0 (0°)	0 (0°)	0 (0°)	0 (0°)
	$\vartheta$	1 (0°)	0 (0°)	0 (0°)	0 (0°)	0 (0°)	0 (0°)
Mode 4	$v$	0.675 (180°)	0.686 (180°)	0.821 (180°)	1.118 (100°)	0.945 (103°)	-
	$p$	12.888 (0°)	14.310 (0°)	11.534 (0°)	8.644 (88.2°)	10.186 (82.9°)	-
	$r$	2.972 (180°)	3.076 (180°)	2.152 (180°)	1.603 (20°)	2.743 (38°)	-
	$\varphi$	1 (0°)	1 (0°)	1 (0°)	1 (0°)	1 (0°)	-
Mode 5	$v$	0.616 (35.3°)	0.533 (37.6°)	0.619 (35.8°)	0.519 (0°)	0.710 (0°)	-
	$p$	17.325 (147°)	17.775 (148°)	15.623 (150°)	20.263 (180°)	14.926 (180°)	-
	$r$	11.892 (74.6°)	12.120 (83.8°)	9.158 (92.9°)	30.264 (180°)	22.222 (180°)	-
	$\varphi$	1 (0°)	1 (0°)	1 (0°)	1 (0°)	1 (0°)	-
Mode 6	$v$	0.124 (0°)	0.039 (0°)	0.041 (0°)	0.078 (0°)	0.121 (0°)	-
	$p$	83.682 (180°)	98.839 (180°)	97.176 (180°)	130.466 (180°)	82.518 (180°)	-
	$r$	77.503 (0°)	92.924 (0°)	91.553 (0°)	110.773 (0°)	73.580 (0°)	-
	$\varphi$	1 (0°)	1 (0°)	1 (0°)	1 (0°)	1 (0°)	-

**Table 3.6:** Eigenvectors of the longitudinal (Modes 1-3) and lateral system (modes 4-6) showing the amplitude and phase (in parenthesis). Longitudinal system values are normalized by pitch  $\vartheta$ , lateral by roll  $\varphi$ .

The addition of the third component due to added mass inertia further moves the complex pair of poles towards the CFD results.

From the eigenvectors in Table 3.6 we see that the dominant motion in Mode 4 is the sideways motion  $v$ . For the first three models it is in anti-phase with roll  $p$  but in phase with yaw  $r$ . In the remaining models, ASL(tr) and Cheng & Deng, the sideways motion and roll are nearly in phase, the phase difference from yaw is smaller than  $90^\circ$ . Mode 5 is a combination of the three motions  $v, p, r$ . In the first three models the sideways motion and roll are out of phase by about  $110^\circ$  and the yaw phase lies approximately in between. In the remaining models the sideways motion is in anti-phase with roll and yaw rotation. Mode 6, similar in all the models, represents the out of phase coupling of roll and yaw.

#### 3.4.4 Effect of derivatives $\hat{X}_q$ and $\hat{Y}_p$

In Section 3.4.1 it was shown that various models predict very similar dynamic behaviour, even though the sign of stability derivatives  $\hat{X}_q$  and  $\hat{Y}_p$  varies among the models. This suggests that these derivatives have very small effect on the dynamics. The comparison of pole positions for the full system and for the system with  $\hat{X}_q = 0$  and  $\hat{Y}_p = 0$  is in Table 3.7. The differences are indeed very small and, therefore, the derivatives  $\hat{X}_q$  and  $\hat{Y}_p$  can be neglected in the preliminary analyses.

Model	Longitudinal system			Lateral system	
	$\lambda_{1,2}$	$\lambda_3$	$\lambda_{5(5,6)}$	$\lambda_{6,7(7)}$	$\lambda_8$
Wu&Sun (2009) /	$7.88 \pm 16i$	-19.6	12.9	$-14.6 \pm 9.32i$	-83.7
Zhang&Sun (2010a)	<b><math>7.94 \pm 15.9i</math></b>	<b>-19.7</b>	<b>12.9</b>	<b><math>-14.6 \pm 9.28i</math></b>	<b>-83.7</b>
ASL (tr+rot+add)	$5.87 \pm 15.5i$	-24.7	14.3	$-15.1 \pm 9.33i$	-98.8
	<b><math>5.39 \pm 16i</math></b>	<b>-23.7</b>	<b>13.8</b>	<b><math>-15.3 \pm 9.9i</math></b>	<b>-98</b>
ASL (tr+rot)	$5.47 \pm 14.9i$	-23.5	11.5	$-13.5 \pm 7.87i$	-97.2
	<b><math>5.1 \pm 15.3i</math></b>	<b>-22.8</b>	<b>11.2</b>	<b><math>-13.6 \pm 8.32i</math></b>	<b>-96.7</b>
ASL (tr)	$5.68 \pm 13.2i$	-17.5	$0.274 \pm 8.64i$	-20.3	-130
	<b><math>5.65 \pm 13.2i</math></b>	<b>-17.5</b>	<b><math>0.266 \pm 8.64i</math></b>	<b>-20.3</b>	<b>-130</b>

**Table 3.7:** Effect of derivatives  $\hat{X}_q$  and  $\hat{Y}_p$  on the system poles: complete system (black),  $\hat{X}_q$  and  $\hat{Y}_p$  neglected (red). Only the poles and models that were affected are displayed.

#### 3.4.5 Effect of inertia product $I_{xz}$

While in longitudinal system the vertical dynamics is decoupled from the pitch, a coupling between yaw and roll exists in the lateral system due to the inertia product

$I_{xz}$ . Assuming the dronefly body posture in hovering is vertical (as in most hovering MAVs), the inertia product  $I_{xz}$  becomes zero and the coupling disappears. The resulting pole locations are shown in Figure 3.14 and listed in Table 3.8.

We can observe some differences compared to the nominal body posture (inclined by  $48^\circ$  from the vertical axis), nevertheless the pole distribution remains the same. The biggest difference is in the fastest stable real pole, which after decoupling represents the yaw dynamics. On the other hand, the remaining poles (now representing the roll and lateral dynamics) represent still a good approximation of the original system. Hence, the roll and lateral dynamics can be in the first approximation treated independently of yaw, which greatly simplifies the problem of stability and control design, as will be shown in the next chapter.

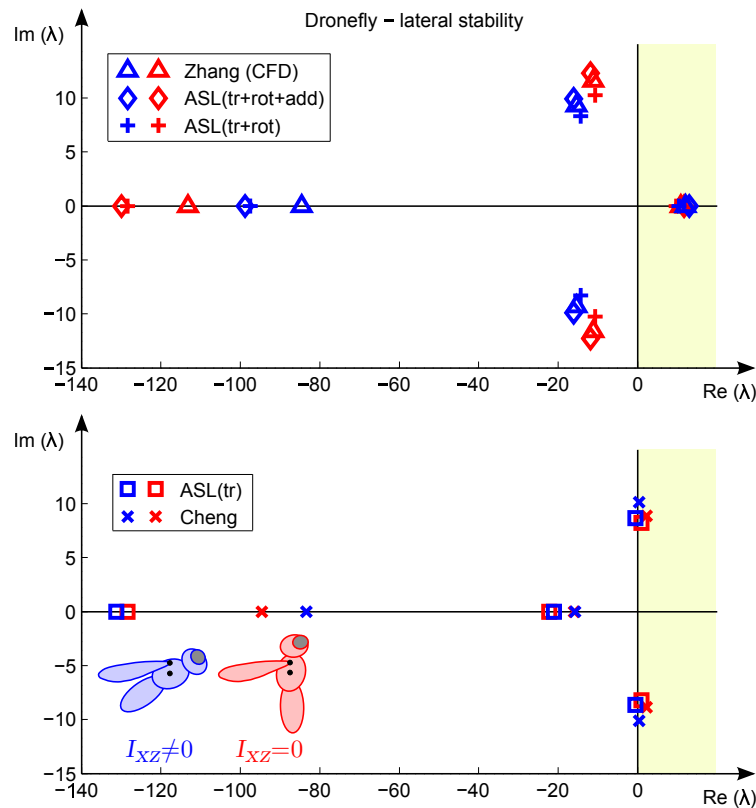


**Figure 3.14:** Effect of inertia product  $I_{xz}$  on the lateral poles: nominal body posture ( $I_{xz} \neq 0$ ) in blue, vertical posture ( $I_{xz} = 0$ ) in red. Results split into two parts according to the pole location structure: CFD study Zhang and Sun (2010a) and quasi-steady models that include rotational force (top), quasi-steady models based only on translational force (bottom).

Model	Lateral system		
	$\lambda_{5(5,6)}$	$\lambda_{6,7(7)}$	$\lambda_8$
Zhang and Sun (2010a)	12.9 10.9	-14.6 $\pm$ 9.32i -11.2 $\pm$ 11.6i	-83.7 -113
ASL (tr+rot+add)	14.3 11.7	-15.1 $\pm$ 9.33i -11.9 $\pm$ 12.3i	-98.8 -130
ASL (tr+rot)	11.5 9.65	-13.5 $\pm$ 7.87i -10.7 $\pm$ 10.3i	-97.2 -128
ASL (tr)	0.274 $\pm$ 8.64i 1 $\pm$ 8.23i	-20.3 -22.3	-130 -128
Cheng and Deng (2011)	1.25 $\pm$ 10.1i 2.26 $\pm$ 8.88i	-14.9 -16	-82.5 -94.6

**Table 3.8:** Effect of inertia product  $I_{xz}$  on the system poles: original body posture ( $I_{xz} \neq 0$ , black), vertical body posture ( $I_{xz} = 0$ , red).

### 3.4.6 Conclusion

It was shown that the stability of the flapping flight in hover can be successfully estimated while using a quasi-steady based model that includes components due to rotation and translation. Despite the simplifications used (the effective angle of attack and relative wing velocity were considered constant along the wingspan, the centre of pressure was placed on the wing spanwise rotation axis) the results are comparable to the ones obtained by CFD modelling, while the necessary computation power is significantly reduced. Therefore such a quasi-steady model can be advantageously used in flapping-wing MAV parameter and control design. However, the model, assuming rigid wings, will still remain a rather gross approximation as the wings of many natural fliers as well as of most MAVs are flexible.

The linearised model was further reduced by neglecting the inertia product  $I_{xz}$  and derivatives  $\dot{X}_q$  and  $\dot{Y}_p$ , whose effects on the pole locations were shown to be very small. Thus, the dynamics of hovering flapping flight can be described by only 8 stability derivatives and splits into 4 subsystems (pitch, roll, yaw and vertical dynamics) that can be treated separately in the control design.

## 3.5 References

- G. J. Berman and Z. J. Wang. Energy-minimizing kinematics in hovering insect flight. *Journal of Fluid Mechanics*, 582:153–168, Jun. 2007.

- doi:10.1017/S0022112007006209.
- B. Cheng and X. Deng. Translational and rotational damping of flapping flight and its dynamics and stability at hovering. *IEEE Transactions on Robotics*, 27(5): 849–864, Oct. 2011. doi:10.1109/TRO.2011.2156170.
- X. Deng, L. Schenato, W. C. Wu, and S. S. Sastry. Flapping flight for biomimetic robotic insects: part I-system modeling. *IEEE Transactions on Robotics*, 22(4): 776–788, Aug. 2006. doi:10.1109/TRO.2006.875480.
- M. H. Dickinson, F.-O. Lehmann, and S. P. Sane. Wing rotation and the aerodynamic basis of insect flight. *Science*, 284(5422):1954–1960, Jun. 1999. doi:10.1126/science.284.5422.1954.
- W. B. Dickson, A. D. Straw, C. Poelma, and M. H. Dickinson. An integrative model of insect flight control. *44th AIAA Aerospace Sciences Meeting and Exhibit; Reno, NV; USA; 9-12 Jan*, pages 1–19, 2006.
- C. P. Ellington. The aerodynamics of hovering insect flight. II. Morphological parameters. *Philosophical Transactions of the Royal Society of London. Series B, Biological Sciences*, 305(1122):17–40, Feb. 1984a. doi:10.1098/rstb.1984.0050.
- C. P. Ellington. The aerodynamics of hovering insect flight. IV. aerodynamic mechanisms. *Philosophical Transactions of the Royal Society of London. Series B, Biological Sciences*, 305(1122):79–113, Feb. 1984b.
- Y. C. Fung. *An introduction to the theory of aeroelasticity*. Dover, New York, 1969.
- M. Karasek and A. Preumont. Flapping flight stability in hover: A comparison of various aerodynamic models. *International Journal of Micro Air Vehicles*, 4(3): 203–226, 2012. doi:10.1260/1756-8293.4.3.203.
- MathWorks. Matlab documentation: atan2 function. <http://www.mathworks.com/help/matlab/ref/atan2.html>, 2014. Accessed: 18/08/2014.
- W. J. Maybury and F.-O. Lehmann. The fluid dynamics of flight control by kinematic phase lag variation between two robotic insect wings. *Journal of Experimental Biology*, 207:4707–4726, 2004. doi:10.1242/jeb.01319.
- C. T. Orlowski and A. R. Girard. Stability derivatives for a flapping wing MAV in a hover condition using local averaging. In *2011 American Control Conf.*, pages 1604–1609, San Francisco, California, Jun. - Jul. 2011.
- G. D. Padfield. *Helicopter Flight Dynamics: The Theory and Application of Flying Qualities and Simulation Modeling*. Blackwell Science Ltd., 2nd edition, 2007.

- L. Ristroph, G. Ristroph, S. Morozova, A. J. Bergou, S. Chang, J. Guckenheimer, Z. J. Wang, and I. Cohen. Active and passive stabilization of body pitch in insect flight. *Journal of The Royal Society Interface*, 10(85):1–13, 2013. doi:10.1098/rsif.2013.0237.
- S. P. Sane and M. H. Dickinson. The control of flight force by a flapping wing: lift and drag production. *Journal of Experimental Biology*, 204:2607–2626, 2001.
- S. P. Sane and M. H. Dickinson. The aerodynamic effects of wing rotation and a revised quasi-steady model of flapping flight. *Journal of Experimental Biology*, 205:1087–1096, 2002.
- L. I. Sedov. *Two-dimensional problems in hydromechanics and aerodynamics*. Interscience publishers, New York, 1965.
- W. Shyy, H. Aono, C.-K. Kang, and H. Liu. *An Introduction to Flapping Wing Aerodynamics*. Cambridge University Press, 2013.
- M. Sun and Y. Xiong. Dynamic flight stability of a hovering bumblebee. *Journal of Experimental Biology*, 208:447–459, 2005.
- M. Sun, J. Wang, and Y. Xiong. Dynamic flight stability of hovering insects. *Acta Mech. Sinica*, 23(3):231–246, Jun. 2007. doi:10.1007/s10409-007-0068-3.
- G. K. Taylor and A. L. R. Thomas. Dynamic flight stability in the desert locust *schistocerca gregaria*. *Journal of Experimental Biology*, 206(16):2803–2829, Aug. 2003. doi:10.1242/jeb.00501.
- J. Wu and M. Sun. Control for going from hovering to small speed flight of a model insect. *Acta Mech. Sinica*, 25(3):295–302, Jun. 2009. doi:10.1007/s10409-009-0241-y.
- Y. Xiong and M. Sun. Dynamic flight stability of a bumblebee in forward flight. *Acta Mech. Sinica*, 24(1):25–36, Feb. 2008. doi:DOI 10.1007/s10409-007-0121-2.
- Y. Zhang and M. Sun. Dynamic flight stability of a hovering model insect: lateral motion. *Acta Mech. Sinica*, 26(2):175–190, May. 2010a. doi:10.1007/s10409-009-0303-1.
- Y. Zhang and M. Sun. Dynamic flight stability of a hovering model insect: theory versus simulation using equations of motion coupled with navier-stokes equation. *Acta Mech. Sinica*, 26(4):509–520, 2010b. doi:10.1007/s10409-010-0360-5.

## Chapter 4

# Stability of near-hover flapping flight

This chapter studies the stability of the developed hummingbird-like MAV around hovering. The linearised model of near-hover flapping flight from the previous chapter is employed. The choice of wing position for an easily controllable MAV is discussed and a simplified solution of the pitch and roll stability problem is proposed.

### 4.1 Hummingbird robot parameters

Since the existing models predict that the hovering flapping flight of natural fliers is unstable, it is very unlikely that a passively stable MAV design would exist (without additional stabilizing surfaces like sails). However, the mathematical model can help us identify a design that would be easily controllable. In this section a 20 g hummingbird-like MAV with parameters according to Table 4.1 will be studied. The wing parameters were selected according to the robot prototype that will be presented in Chapter 6, the mass properties are an estimate based on a CAD model. Vertical body orientation is assumed while hovering so the inertia product  $I_{xz}$  is equal to zero.

$m$ (g)	$I_{xx}$ (kg.m <sup>2</sup> )	$I_{yy}$ (kg.m <sup>2</sup> )	$I_{zz}$ (kg.m <sup>2</sup> )	$e$ (mm)	$R$ (mm)	$\mathcal{R}$ (-)	$\hat{r}_2$ (-)	$\hat{x}_0$ (-)	$\int_0^1 c^2 \hat{r} d\hat{r}^*$ (-)
20	1e-5	1e-5	1e-3	31.6	90	9.33	0.531	0.25	0.418

**Table 4.1:** Hummingbird robot parameters, according to definitions in Chapter 3. \*Wing shape characteristic in equation (3.13).

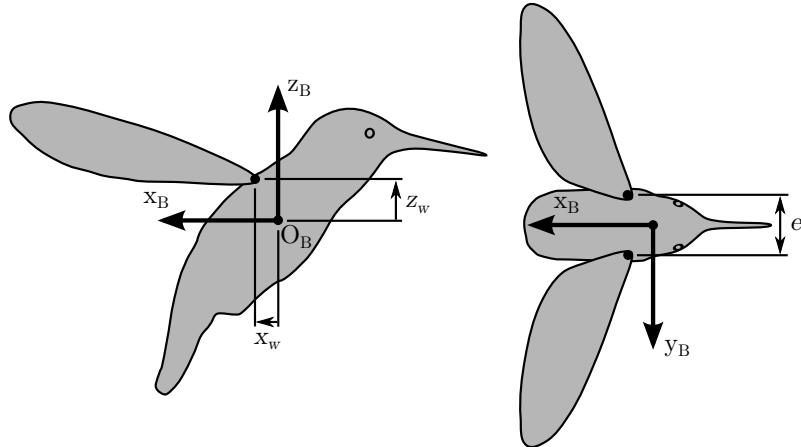


**Figure 4.1:** The position of the wing shoulders with respect to the COG.

Based on experiments that will be presented in Section 6.2 the wing operating conditions were estimated to a flapping amplitude  $\phi_m = 80^\circ$  and frequency  $f = 26$  Hz. The value of the angle of attack in mid-stroke that provides an equilibrium between the weight and the average lift force,  $\alpha_m = 33^\circ$ , was found by iterations. The last but very important design parameter is the position of the wings with respect to the centre of gravity (Figure 4.1). Our intuition tells us that the wings should be higher than the centre of gravity, which is also what can be observed in nature. To see its effect the vertical wing position  $z_w$  was kept as a free parameter. The longitudinal position of the wings was set to  $x_w = 0$ .

## 4.2 Pitch dynamics

The pitch dynamics is represented by the state space model

$$\begin{bmatrix} \dot{u} \\ \dot{q} \\ \dot{\vartheta} \end{bmatrix} = \begin{bmatrix} \hat{X}_u & \hat{X}_q & g \\ \hat{M}_u & \hat{M}_q & 0 \\ 0 & 1 & 0 \end{bmatrix} \begin{bmatrix} u \\ q \\ \vartheta \end{bmatrix} + \begin{bmatrix} 1 & 0 \\ 0 & 1 \\ 0 & 0 \end{bmatrix} \begin{bmatrix} \hat{X}_{ext} \\ \hat{M}_{ext} \end{bmatrix}. \quad (4.1)$$

The positive directions of the coordinates are displayed in Figure 4.2.

### 4.2.1 Pitch stability derivatives

The stability of the pitch dynamics is determined by the stability derivatives  $\hat{X}_u$ ,  $\hat{X}_q$ ,  $\hat{M}_u$  and  $\hat{M}_q$ . Their values can be evaluated numerically by the aerodynamic

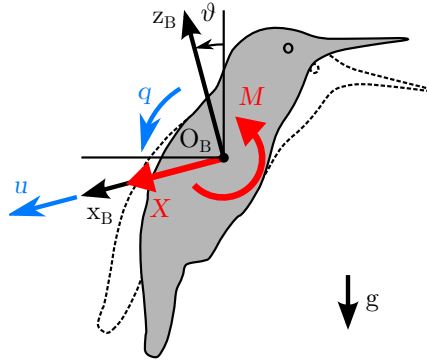


**Figure 4.2:** Coordinates of pitch dynamics.

model developed in the previous chapter. Such approach, however, does not provide much insight into the aerodynamic mechanisms that generate the damping effects. Here, first a simplistic approach is presented with the aim to find an (approximative) relationship between the stability derivatives (in particular their signs) and the vertical wing position  $z_w$ . The findings are then compared to the derivatives obtained numerically.

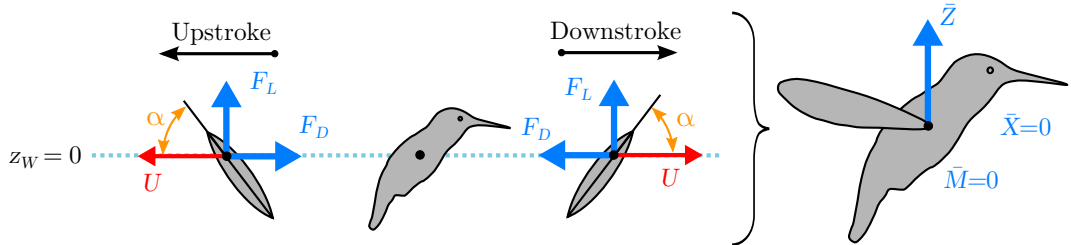


**Figure 4.3:** Symmetrical lift and drag forces generated in hover (left) and the resulting cycle averaged efforts (right).

Let's consider a wing that, in hovering, flaps with a constant CP speed  $U$  and a constant angle of attack  $\alpha$  (Figure 4.3). It is assumed that the wing lift and drag increase/decrease when either the wing speed  $U$  or angle of attack  $\alpha$  increase/decrease.

When the body moves backward with speed  $\Delta u$ , the wing speed decreases in down-stroke to  $U - \Delta u$ , but increases in up-stroke to  $U + \Delta u$ , which creates an imbalance in both lift and drag (Figure 4.4). While the average lift force  $\bar{Z}$  is not affected, the average longitudinal force  $\bar{X}$  opposes the motion  $u$ . Thus, the stability derivative  $\hat{X}_u$  should be negative, representing a damping term.

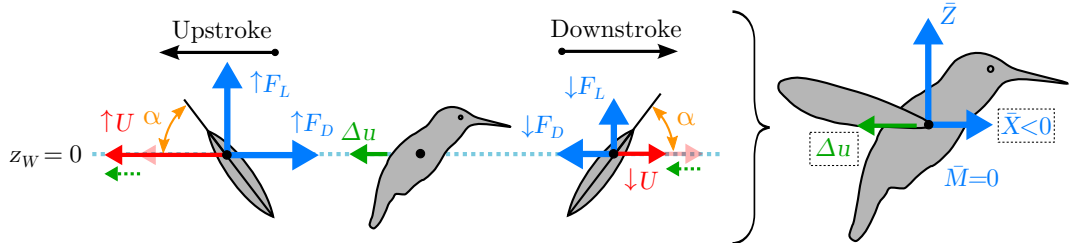


**Figure 4.4:** Effects of a disturbance in longitudinal direction  $\Delta u$  when the wing shoulders are placed at the COG ( $z_w = 0$ ). A wing speed difference between upstroke and downstroke induces a cycle-averaged damping force  $\bar{X}$  that opposes the disturbance.

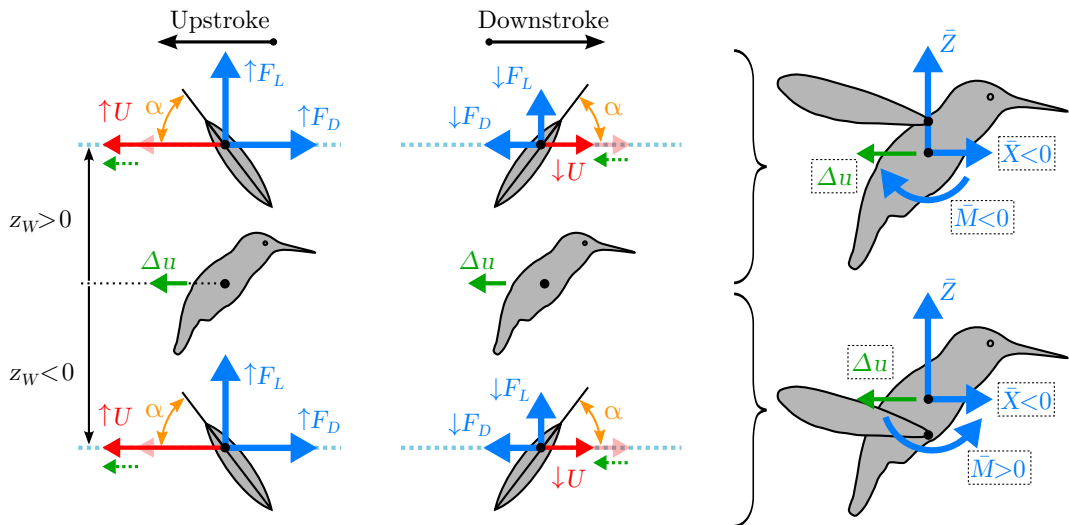


**Figure 4.5:** Effects of a disturbance in longitudinal direction  $\Delta u$  for a general wing shoulder position ( $z_w \neq 0$ ). The cycle-averaged drag force acts at a lever  $z_w$  and induces a pitch moment  $\bar{M}$ , whose sign is opposite to the sign of  $z_w$ .

For a general wing shoulder position ( $z_w \neq 0$ ) a pitch moment  $\bar{M} = \bar{X} z_w$  arises due to the lever arm from the wing shoulder to the COG (Figure 4.5). Therefore,  $\hat{M}_u$  should be positive below the COG and negative above the COG.

Rotating the body around the pitch axis with an angular rate  $\Delta q$  affects both the wing speed and the angle of attack. Considering first the wing shoulders placed at the COG ( $z_w = 0$ ), the principal effect is on the angle of attack  $\alpha$  (Figure 4.6). The angle increases for wing positions behind the body but decreases in front of the body because of a vertical velocity component due to the body rotation. The resulting difference in lift and drag averages out over one wingbeat, but the lift imbalance

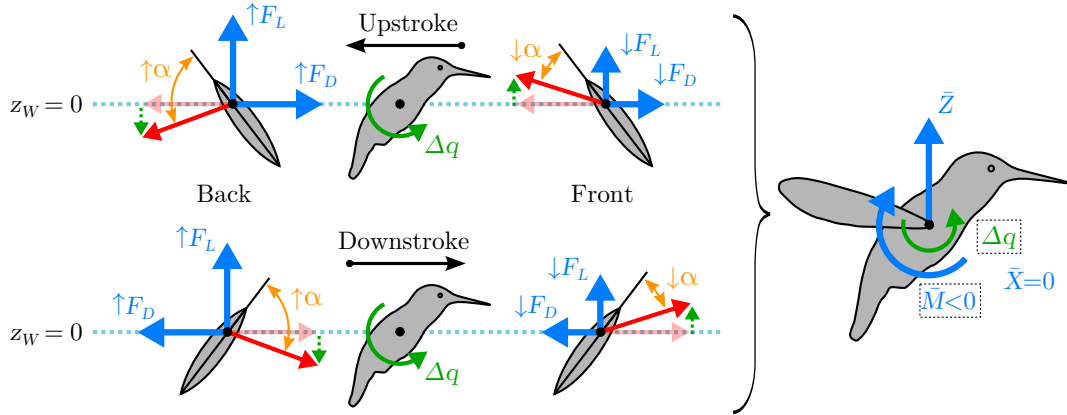


**Figure 4.6:** Effects of a pitch disturbance  $\Delta q$  when the wing shoulders are placed at the COG ( $z_w = 0$ ). The angle of attack increases behind the body, but decreases in front of the body, which causes an uneven distribution of the lift force and results into a cycle-averaged pitch moment  $\bar{M}$  that opposes the disturbance.

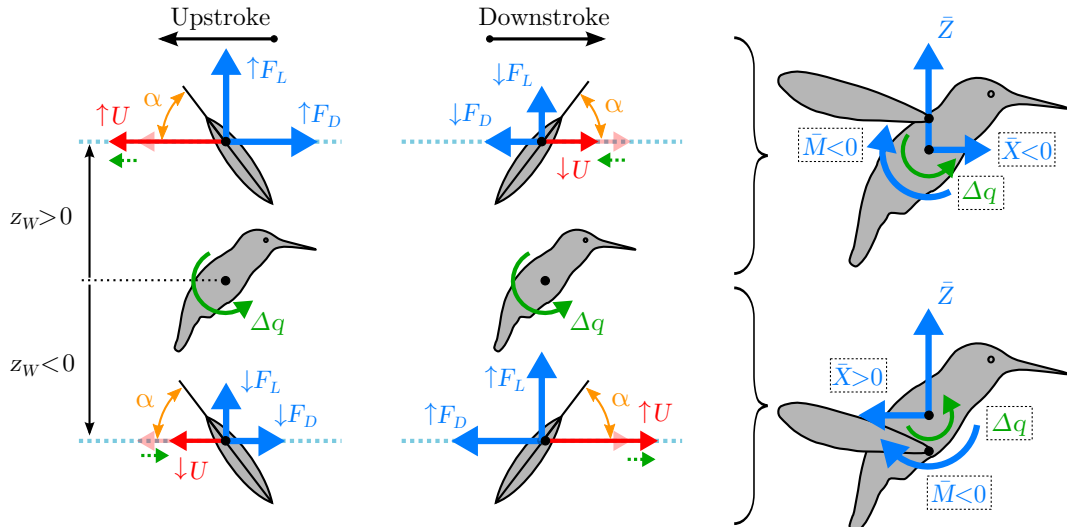


**Figure 4.7:** Effects of a pitch disturbance  $\Delta q$  for a general wing shoulder position ( $z_w \neq 0$ ). On top of the angle of attack changes the speed increases/decreases in upstroke and decreases/increases in downstroke when the wings shoulders are placed above/below the COG, respectively. This induces a non-zero cycle averaged force  $\bar{X}$ , whose sign is opposite to the sign of  $z_w$ , and decreases further the negative stabilizing pitch moment  $\bar{M}$  for both positive and negative  $z_w$ .

gives rise to a pitch moment  $M$  opposing the rotation  $\Delta q$ . Thus, the derivative  $\hat{M}_q$  should be negative.

If the wing shoulders are placed above or below the COG, the wing speed is also modified in the central wing position (Figure 4.7). The speed increases in upstroke and decreases in downstroke for  $z_w > 0$ ; the opposite is true for  $z_w < 0$ . This creates a drag asymmetry between upstroke and downstroke, which translates into the cycle averaged longitudinal force  $\bar{X}$ . Therefore, the derivative  $\hat{X}_q$  should be positive for  $z_w < 0$  and negative for  $z_w > 0$ . Further, the pitch moment gets modified to  $\bar{M} = \bar{M}_0 + \bar{X} z_w$ , where the first term represents the pitch damping moment for wing shoulders at COG ( $z_w = 0$ ). The second term is always smaller or equal to zero due to opposite signs of  $\bar{X}$  and  $z_w$ . Thus, the derivative  $\hat{M}_q$  should stay negative for any wing shoulder position.

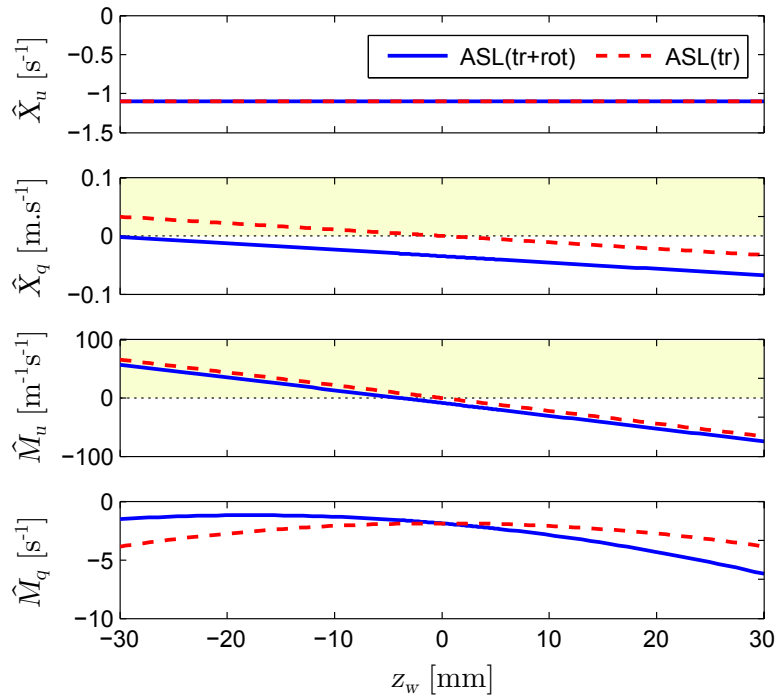


**Figure 4.8:** Stability derivatives of pitch dynamics for varying wing position  $z_w$ .

The stability derivatives given by the model presented in the previous chapter for robot parameters given in Section 4.1 are plotted in Figure 4.8. Two quasi-steady models were used, a simpler model including only the force due to translation, ASL (tr), and a more complex model that includes also the force due to rotation, ASL

(tr+rot). It has been shown in Section 3.4 that the latter gives comparable stability derivatives to a CFD model.

The simpler model ASL (tr) plotted in red dashed lines in Figure 4.8 is in complete agreement with the findings about the derivative signs based on Figures 4.4-4.7 made earlier. The derivative  $\hat{X}_u$  representing the damping of the forward translation is always negative and independent on the wing position. The derivative  $\hat{M}_q$ , the pitch rotation damping, remains always negative, varying with square of wing position  $z_w^2$  with a maximum at  $z_w = 0$ . The cross-coupling derivatives  $\hat{M}_u$  and  $\hat{X}_q$  are zero for  $z_w = 0$  and vary linearly, with a negative slope, with the wing position  $z_w$ .

The addition of the force due to rotation in ASL (tr+rot) has no effect on the derivative  $\hat{X}_u$  (blue solid lines in Figure 4.8). We can observe some differences among the other three derivatives, but the general behaviour remains similar. The pitch damping  $\hat{M}_q$  remains approximately quadratic function of  $z_w^2$ . Its maximum value, now at  $z_w \approx -18$  mm, slightly increases, but stays negative. The derivatives  $\hat{X}_q$  and  $\hat{M}_u$  are slightly offset from the simpler model, but keep the same slope.  $\hat{X}_q$  stays always negative in the studied range, while  $\hat{M}_u$  crosses zero at around -4 mm.

#### 4.2.2 System poles

Assuming a reachable and observable system with a system matrix  $\mathbf{A}$ , the system poles are defined as roots of the characteristic equation  $|\lambda\mathbf{I} - \mathbf{A}| = 0$ . For pitch dynamics, we obtain a cubic equation

$$\lambda^3 - (\hat{X}_u + \hat{M}_q)\lambda^2 + (\hat{X}_u\hat{M}_q - \hat{M}_u\hat{X}_q)\lambda - \hat{M}_u g = 0 \quad (4.2)$$

with three roots. Figure 4.9 shows position of the poles (root locus) for wing position  $z_w$  ranging from -30 mm to 30 mm, calculated from the stability derivatives shown in Figure 4.8. In both models, ASL (tr) in red-dashed lines and ASL (tr+rot) in blue lines, we can observe 3 different pole configurations. For positive values of  $z_w$  (wings placed above the centre of gravity), we have a pair of complex unstable poles and one real stable pole. For negative  $z_w$ , there is one stable real pole and an unstable pair of complex poles. Finally, there is a narrow transient region around the COG ( $z_w \approx 0$ ) for ASL (tr) and below the COG ( $z_w \approx -4$  mm) for ASL (tr+rot) where 3 real poles exist.

It can be demonstrated that the pole configuration is determined by the derivative  $\hat{M}_u$ . By neglecting the derivative  $\hat{X}_q$  (whose effect on the dynamics has been shown to be very small, see Section 3.4.4) the characteristic equation becomes

$$\lambda^3 - (\hat{X}_u + \hat{M}_q)\lambda^2 + \hat{X}_u\hat{M}_q\lambda - \hat{M}_u g = 0, \quad (4.3)$$

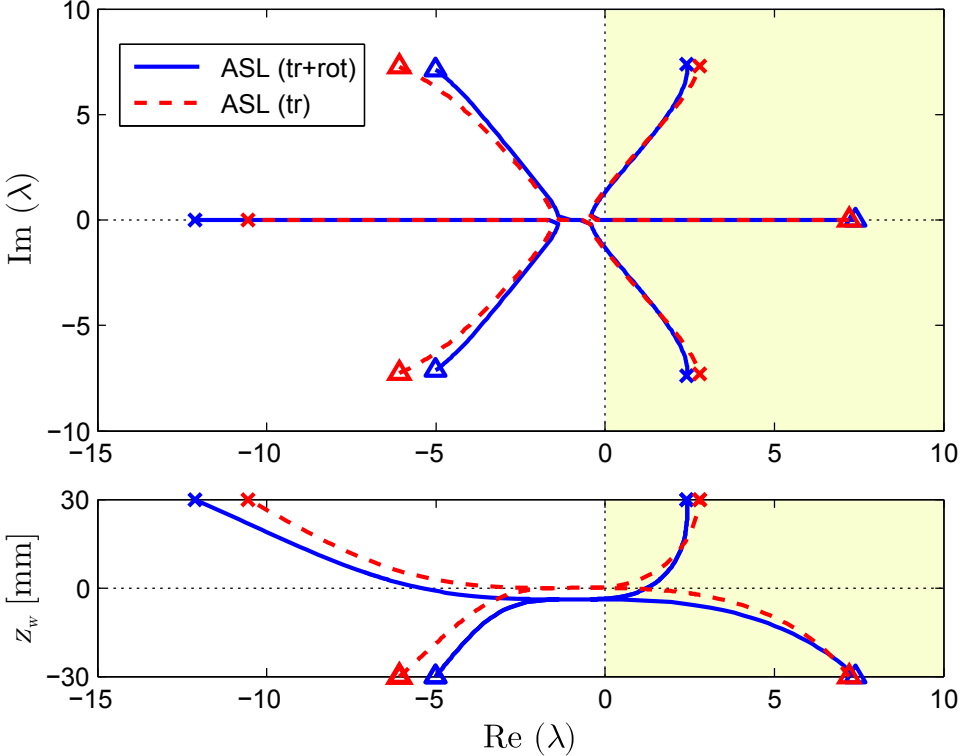


**Figure 4.9:** Influence of wing position  $z_w$  on the pitch dynamics: pole positions in complex plane (top) and real part of the poles against the wing position (bottom).

which can be rewritten as

$$\lambda \left( \lambda - \hat{X}_u \right) \left( \lambda - \hat{M}_q \right) - \hat{M}_u g = 0 \quad (4.4)$$

or

$$1 + \hat{M}_u \frac{-g}{\lambda \left( \lambda - \hat{X}_u \right) \left( \lambda - \hat{M}_q \right)} = 0. \quad (4.5)$$

The equation has the same form as a characteristic equation of system  $H(s) = -g / (\lambda(\lambda - \hat{X}_u)(\lambda - \hat{M}_q))$  in closed loop with a feedback gain  $\hat{M}_u$ . Thus, a root locus method can be used to study the effect of the derivative  $\hat{M}_u$  on the pitch dynamics poles.

The system  $H(s)$  has three poles, one at the origin and two on the real axis given by the derivatives  $\hat{X}_u$  and  $\hat{M}_q$ , respectively. Since  $H(s)$  has no zeros and a negative numerator, the root locus will follow asymptotes at  $\pm 60^\circ$  and  $180^\circ$  for  $\hat{M}_u \rightarrow -\infty$  and asymptotes at  $0^\circ$  and  $\pm 120^\circ$  for  $\hat{M}_u \rightarrow \infty$ . The start point of the asymptotes

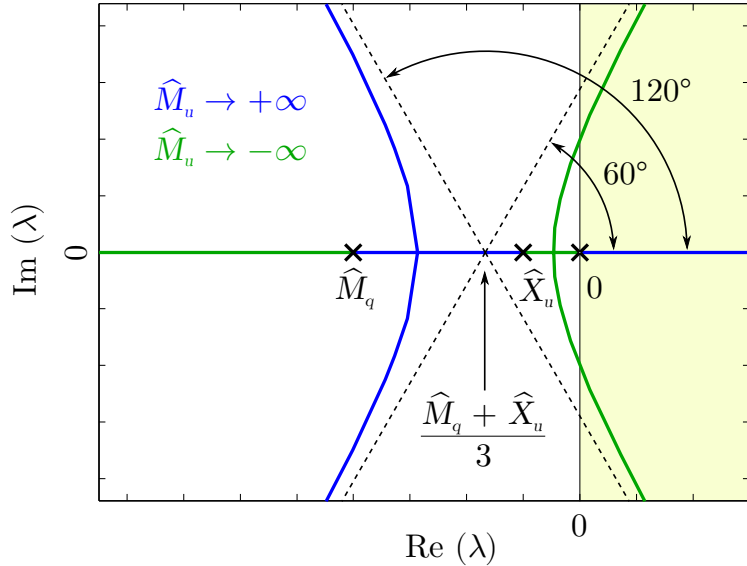


**Figure 4.10:** Root locus showing the effect of derivative  $\hat{M}_u$  on the system dynamics.

lies at  $(\hat{X}_u + \hat{M}_q)/3$ . The resulting root locus is shown in Figure 4.10 and looks very similar to the locus for varying wing position  $z_w$  (Figure 4.9): negative  $\hat{M}_u$  results into a pair of unstable complex poles and a stable real pole, while positive  $\hat{M}_u$  results into an unstable real pole and a pair of stable complex poles.

Provided that both  $\hat{X}_u$  and  $\hat{M}_q$  are negative, a small region of stability exists for small negative values of  $\hat{M}_u$ . This region, with one fast real pole and a pair of slow lightly damped complex poles, can only be enlarged by increasing the damping of forward translation or pitch rotation. This can be done either passively by adding some damping surfaces (tail, sails) or actively by feedback control.

#### 4.2.3 Active stabilization

Flying animals are equipped with sensory systems that provide feedback for active stabilization of their flight. As it has been mentioned already in Section 2.3.3, flies use two types of sensors to sense angular velocities: the compound eyes and the halteres. Compared to compound eyes, which are most sensitive to rates of the order of  $100^\circ/\text{s}$ , the halteres can sense rates up to  $1000^\circ/\text{s}$  (Taylor and Krapp, 2008) and their latency is about four times shorter (Ristroph et al., 2013). Sherman and Dickinson (2004) showed that the wing response simply follows a weighted sum of the two sensory signals. Thus, the aim of this section is to show under which conditions can the pitch dynamics be stabilized using a simple angular rate feedback with a gain  $k_q$ .

Such control will introduce a stabilizing moment  $\hat{M} = -k_q q$ . By plugging the moment into the state space model we get

$$\begin{bmatrix} \dot{u} \\ \dot{q} \\ \dot{\vartheta} \end{bmatrix} = \begin{bmatrix} \hat{X}_u & \hat{X}_q & g \\ \hat{M}_u & \hat{M}_q - k_q & 0 \\ 0 & 1 & 0 \end{bmatrix} \begin{bmatrix} u \\ q \\ \vartheta \end{bmatrix} + \begin{bmatrix} 1 & 0 \\ 0 & 1 \\ 0 & 0 \end{bmatrix} \begin{bmatrix} \hat{X}_{ext} \\ \hat{M}_{ext} \end{bmatrix}, \quad (4.6)$$

which yields the characteristic equation

$$\lambda^3 + \left( k_q - \hat{X}_u - \hat{M}_q \right) \lambda^2 + \left[ \hat{X}_u \left( \hat{M}_q - k_q \right) - \hat{M}_u \hat{X}_q \right] \lambda - \hat{M}_u g = 0. \quad (4.7)$$

The necessary (but not sufficient) condition for stability requires that all coefficients of the characteristic equation are positive. This already shows that the pitch rate feedback can stabilize the system only if the derivative  $\hat{M}_u$  is negative. By neglecting again the derivative  $\hat{X}_q$  and rewriting the characteristic equation into the root locus form with parameter  $\hat{M}_u$  we obtain

$$1 + \hat{M}_u \frac{-g}{\lambda (\lambda - \hat{X}_u) (\lambda + k_q - \hat{M}_q)} = 0. \quad (4.8)$$

We can observe, that the feedback gain moves the pole related to the pitch rate damping towards minus infinity (see Figure 4.11). This results into a shift of the

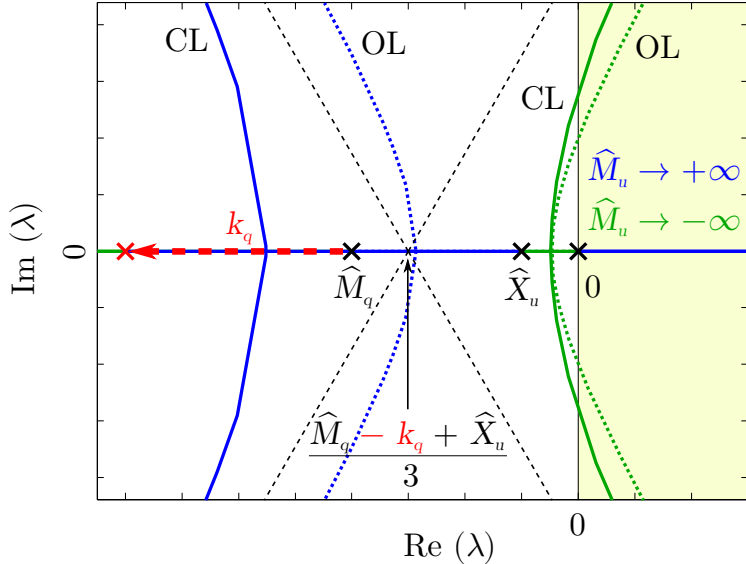


**Figure 4.11:** The effect of derivative  $\hat{M}_u$  on the pitch dynamics in open loop (OL) and in closed loop (CL) with pitch rate feedback  $k_q$ .

asymptotes origin to the left and causes an “opening” of the root locus for negative values of  $\hat{M}_u$ . Thus, the system becomes stable for a much larger interval of the stability derivative  $\hat{M}_u$ .

The minimal necessary gain for stability for a given  $\hat{M}_u$  can be expressed by using the Routh-Hurwitz stability criterion (e.g. Franklin et al., 2002, p. 158). The criterion yields three conditions

$$(k_q - \hat{X}_u - \hat{M}_q) [\hat{X}_u (\hat{M}_q - k_q) - \hat{M}_u \hat{X}_q] + \hat{M}_u g > 0 \quad (4.9)$$

$$k_q - \hat{X}_u - \hat{M}_q > 0 \quad (4.10)$$

$$-\hat{M}_u g > 0. \quad (4.11)$$

The third condition confirms that  $\hat{M}_u$  must be negative. The second condition is usually fulfilled as both derivatives  $\hat{X}_u$  and  $\hat{M}_q$  are typically negative (see Table 4.2). Thus, the minimal gain can be expressed from the first condition. Since the gain should be positive we obtain

$$k_{q,min} = \frac{\hat{M}_u \hat{X}_q - 2\hat{X}_u \hat{M}_q - \hat{X}_u^2 + \sqrt{(\hat{X}_u^2 + \hat{M}_u \hat{X}_q)^2 + 4\hat{X}_u \hat{M}_u g}}{-2\hat{X}_u}. \quad (4.12)$$

For a typical hovering animal the minimal necessary gain is much higher than the remaining terms in the brackets on the left side of relation (4.9), namely  $k_{q,min} \gg (-\hat{X}_u - \hat{M}_q)$  and  $k_{q,min} \gg \left(-\hat{M}_q + \frac{\hat{M}_u \hat{X}_q}{\hat{X}_u}\right)$ . By neglecting these terms, and keeping in mind that  $\hat{X}_u < 0$ , we obtain much simpler condition

$$k_q > \sqrt{\frac{\hat{M}_u}{\hat{X}_u} g}, \quad (4.13)$$

which can serve as a good first estimate of minimal necessary gain. Moreover, if  $\hat{M}_q < \frac{\hat{M}_u \hat{X}_q}{\hat{X}_u}$ , all the terms neglected on the left side of the relation (4.9) are positive. In that case the relation (4.13) becomes a sufficient condition for stability.

Table 4.3 shows the poles computed for several animals using stability derivatives from Table 4.2. It also compares the values of the minimal feedback gain  $k$  calculated with the exact formula (4.12) and the values estimated by relation (4.13). We can see that in most cases the approximative formula is very close to the exact solution.

<b>Animal</b>	<b>Model</b>	$\hat{X}_u$ (s <sup>-1</sup> )	$\hat{X}_q$ (ms <sup>-1</sup> )	$\hat{M}_u$ (s <sup>-1</sup> )	$\hat{M}_q$ (m <sup>-1</sup> s <sup>-1</sup> )	$\hat{Z}_w$ (s <sup>-1</sup> )
Bumblebee 1	CFD <sup>1</sup>	-1.35	0.00456	-1360	-3.34	-1.78
	quasi-steady	-3.08	0	-988	-3.17	-2.69
Bumblebee 2	morphology	-4.19	-0.0163	-445	-1.9	-
	CFD <sup>2</sup>	-3.61	0.0342	-908	-8.76	-2.05
Hawkmoth 1	quasi-steady	-3.02	0	-185	-1.79	-2.32
	morphology	-3.04	-0.0265	-151	-2.85	-
Rufous hummingbird	CFD <sup>1</sup>	-0.624	-0.00437	-9.01	-0.432	-
	quasi-steady	-0.717	-0.01	-8.43	-0.566	-
	morphology	-0.758	-0.00833	-5.61	-0.362	-
	Black-chinned hum.	-0.741	-0.00815	-13.6	-0.242	-

**Table 4.2:** Stability derivatives computed using CFD, quasi-steady modelling and estimated from animal morphology. Data taken from the following studies: CFD<sup>1</sup> - Sun and Xiong (2005) with correction from Xiong and Sun (2008), CFD<sup>2</sup> - Zhang and Sun (2010), quasi-steady - Cheng and Deng (2011), morphology - Ristroph et al. (2013).

<b>Animal</b>	<b>Model</b>	$\lambda_1$	$\lambda_{2,3}$	$k_{q,min}$	$k_{q,min}^*$
Bumblebee 1	CFD <sup>1</sup>	-25.2	$10.2 \pm 20.6$ i	92.9	99.2
	quasi-steady	-23.5	$8.6 \pm 18.4$ i	51.4	56.1
Bumblebee 2	morphology	-18.6	$6.3 \pm 14$ i	29.3	32.3
	CFD <sup>2</sup>	-24.6	$6.1 \pm 18.0$ i	34.8	49.7
Hawkmoth 1	quasi-steady	-13.9	$4.5 \pm 10.5$ i	21.2	24.5
	morphology	-13.6	$3.8 \pm 9.7$ i	18.5	22.1
Rufous hummingbird	CFD <sup>1</sup>	-4.8	$1.9 \pm 3.8$ i	11.2	11.9
	quasi-steady	-4.8	$1.8 \pm 3.8$ i	9.9	10.7
	morphology	-4.2	$1.5 \pm 3.3$ i	7.8	8.5
	Black-chinned hum.	-5.5	$2.2 \pm 4.4$ i	12.9	13.4

**Table 4.3:** System poles as roots of (4.2), minimal feedback gain for stability  $k_{q,min}$  from (4.12) and its estimate  $k_{q,min}^*$  according to (4.13). All the values computed for the data in Table 4.2.

### 4.3 Roll dynamics

The roll dynamics is represented by the state space model

$$\begin{bmatrix} \dot{v} \\ \dot{p} \\ \dot{\varphi} \end{bmatrix} = \begin{bmatrix} \hat{Y}_v & \hat{Y}_p & -g \\ \hat{L}_v & \hat{L}_p & 0 \\ 0 & 1 & 0 \end{bmatrix} + \begin{bmatrix} 1 & 0 \\ 0 & 1 \\ 0 & 0 \end{bmatrix} \begin{bmatrix} \hat{Y}_{ext} \\ \hat{L}_{ext} \end{bmatrix}. \quad (4.14)$$

The positive directions of the coordinates are shown in Figure 4.12. The system has the same structure as the pitch dynamics (4.1). Both systems have 3 DOF and coupling exists between the translation and rotation rate. The different sign next to the gravity acceleration  $g$  comes from the frame orientation, the effect on the dynamics remains the same as in pitch.

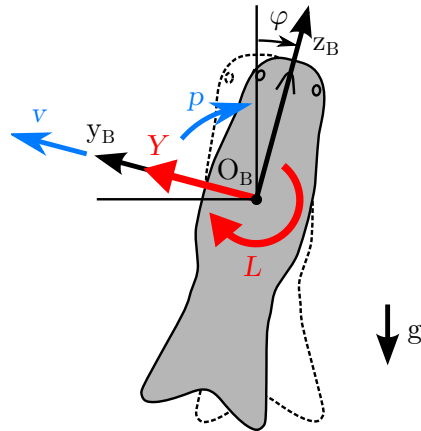


**Figure 4.12:** Coordinates of roll dynamics.

#### 4.3.1 Roll stability derivatives

The roll dynamics stability is determined by the stability derivatives  $\hat{Y}_v$ ,  $\hat{Y}_p$ ,  $\hat{L}_v$  and  $\hat{L}_p$ . As in previous section, a simplistic approach is used to approximate the relationship between the signs of the stability derivatives and the vertical wing position  $z_w$ . The findings are again compared to the derivatives obtained numerically.

In the simplistic model the wing forces depend on the angle of attack  $\alpha$  and the CP velocity  $U$ , which is the velocity component tangential to the flapping motion. It is assumed, that the velocity component in the direction of the wing longitudinal axis has no effect on the produced forces.

A lateral body motion  $\Delta v$  affects the velocity  $U$  mostly close to the extremal wing positions (Figure 4.13).  $U$  is reduced when the wing moves in the direction of lateral disturbance, but it is increased when moving in the opposite direction. This affects the drag force distribution over the cycle; its dominant direction determines the cycle averaged lateral force  $\bar{Y}$ , which is negative and opposes the disturbance  $\Delta v$ .

For a general wing position ( $z_w \neq 0$ ) the averaged drag force, acting at the wing shoulder, also produces a roll moment  $\bar{L} = \bar{Y} z_w$  (Figure 4.14). Therefore, the derivative  $\hat{Y}_v$  should be negative and independent on  $z_w$ .  $\hat{L}_v$  should be positive for wing shoulders placed below the COG and negative for wing shoulders above the COG.

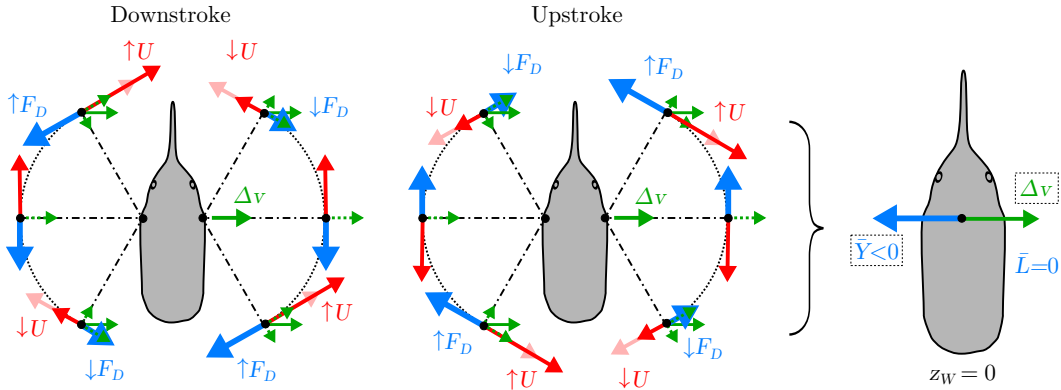


**Figure 4.13:** Effects of a disturbance in lateral direction  $\Delta v$  when the wing shoulders are placed at the COG ( $z_w = 0$ ). The tangential component of the wing speed  $U$  increases when the wing moves in the same direction as the body, but decreases when the wing moves opposite to the body. This induces an asymmetry in the drag forces and results into a cycle-averaged damping force  $\bar{Y}$  that opposes the lateral disturbance.

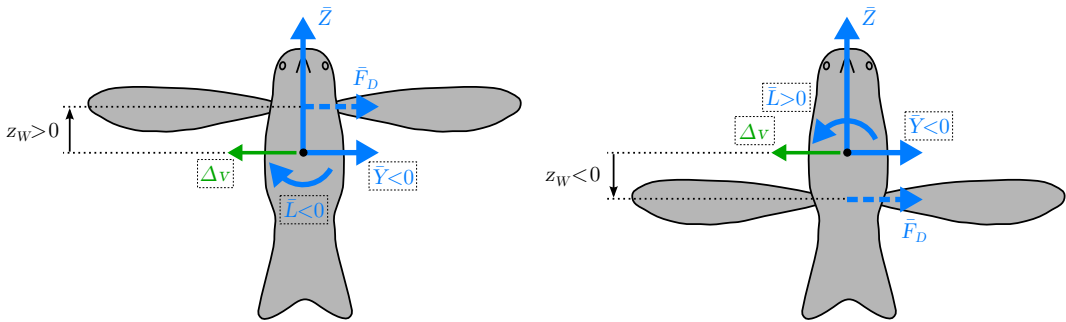


**Figure 4.14:** Effects of a disturbance in lateral direction  $\Delta v$  for a general wing shoulder position ( $z_w \neq 0$ ). The cycle-averaged drag force acts at a lever  $z_w$  and induces a roll moment  $\bar{L}$ , whose sign is opposite to the sign of  $z_w$ .

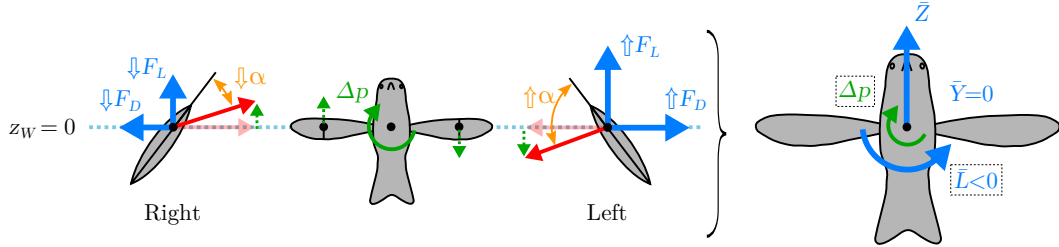


**Figure 4.15:** Effects of a roll disturbance  $\Delta p$  when the wing shoulders are placed at the COG ( $z_w = 0$ ). The angle of attack decreases on the right wing and increases on the left wing, causing a lift asymmetry and resulting into a roll moment  $\bar{L}$  opposing the roll rotation.

A roll disturbance  $\Delta p$  has a dominant effect on the angle of attack, which increases on the left wing and decreases on the right wing. This causes a lift difference resulting into a cycle-averaged roll moment  $\bar{L}$  opposing the disturbance direction (Figure 4.15). Therefore, the derivative  $\hat{L}_p$  should be negative.

For a general wing position ( $z_w \neq 0$ ), the body roll introduces also a speed component in the lateral direction (Figure 4.16). Similar to the lateral disturbance, the drag distribution is modified resulting into a cycle averaged lateral force  $\bar{Y}$ . Thus, the derivative  $\hat{Y}_p$  should be positive for wing shoulders above the COG and negative for wing shoulders below the COG. On top of that, the lateral force modifies further the roll moment to  $L = L_0 + Y z_w m / I_{xx}$ , where  $L_0$  is the roll moment at  $z_w = 0$  and the second term is always smaller or equal to zero due to opposite signs of  $Y$  and  $z_w$ . Therefore, the derivative  $\hat{L}_p$  should always stay negative.

The roll stability derivatives given by the model from the previous chapter are plotted in Figure 4.17. Again two quasi-steady models were used, a simpler model including only the force due to translation ASL (tr) and a more complex model that includes also the force due to rotation, ASL (tr+rot).

As in pitch dynamics, the simpler model ASL (tr) plotted in red dashed lines in Figure 4.17 is coherent with the findings based on Figures 4.13-4.16. The derivative  $\hat{Y}_v$  is negative and thus represents the lateral motion damping. It is independent on the wing position  $z_w$ . The derivative  $\hat{L}_p$  stays also negative and represents the damping of the roll rotation. Its maximum is at  $z_w = 0$  and it decreases with a square of wing position  $z_w^2$ . The derivatives  $\hat{L}_v$  and  $\hat{Y}_p$  represent the cross-coupling terms. They are zero at  $z_w = 0$  and vary linearly, with a positive slope, with the wing position  $z_w$ .

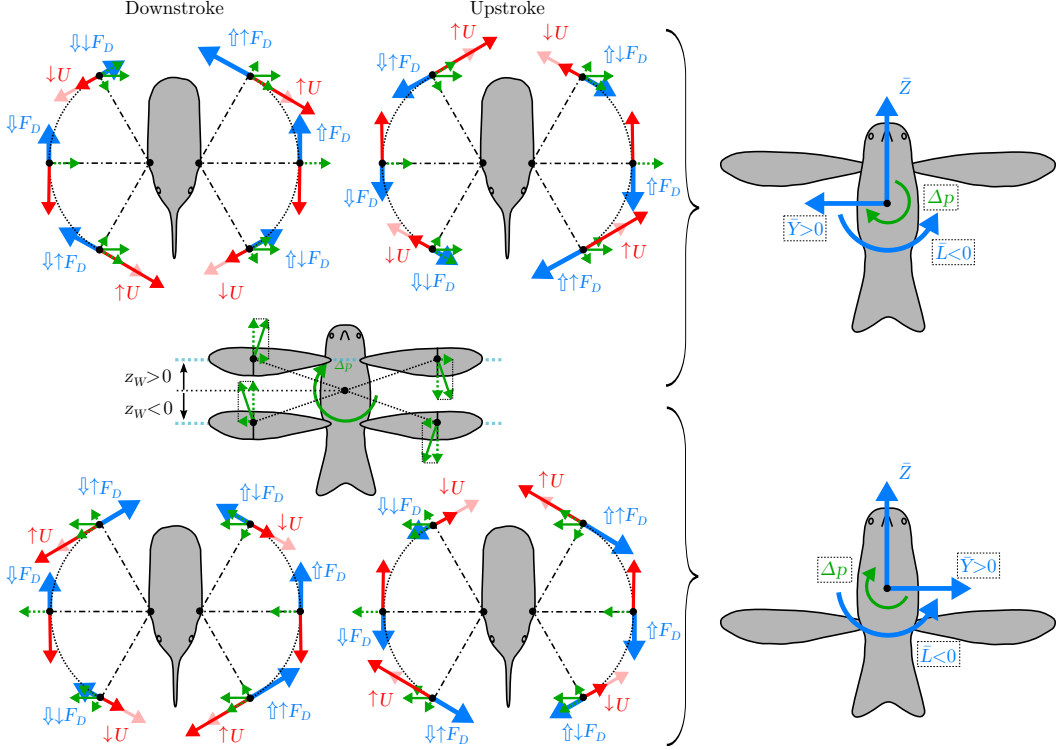


**Figure 4.16:** Effects of a roll disturbance  $\Delta p$  for a general wing shoulder position ( $z_w \neq 0$ ). On top of the angle of attack changes, the wing speed due to body rotation has a lateral component, which is negative/positive for wing shoulders above/below the COG, respectively. This component introduces a drag force asymmetry similar to the lateral disturbance  $\Delta v$  and results into a lateral force with the same sign as  $z_w$ . Moreover, the roll moment decreases further for both positive and negative  $z_w$ .

The more complex model ASL (tr+rot), which includes also the force due to rotation, is plotted in blue lines in Figure 4.17. There is no change in the derivative  $\hat{Y}_v$ . The roll damping  $\hat{L}_p$  keeps its quadratic form, but the maximum slightly increases and moves to  $z_w \approx 22\text{mm}$ , while staying negative. The cross/coupling derivatives  $\hat{L}_v$  and  $\hat{Y}_p$  keep the same slope, but are offset. The former crosses zero at around 5 mm, the latter stays negative in the studied range.

We can observe that while the aerodynamic mechanisms behind the stability derivatives of pitch and roll dynamics are different, they follow the same trends with respect to wing shoulder position  $z_w$ . The translation derivatives  $\hat{X}_u$  and  $\hat{Y}_v$  are both negative and constant, the rotation derivatives  $\hat{M}_q$  and  $\hat{L}_p$  are also negative and vary with the square of wing position  $z_w^2$ , and the cross-terms  $\hat{M}_u$ ,  $\hat{X}_q$  and  $\hat{L}_v$ ,

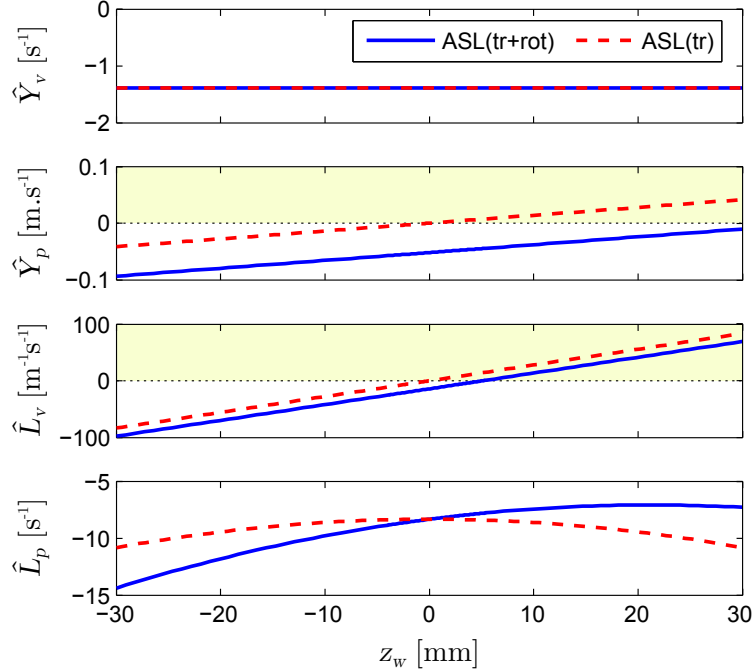


**Figure 4.17:** Stability derivatives of roll dynamics for varying wing position  $z_w$ .

$\hat{Y}_p$  all vary with wing position  $z_w$ . The different slope directions are caused by frame definitions, the effects on the system are the same. Thus, the conclusions made about stability of the pitch dynamics closely apply also to the roll system.

### 4.3.2 System poles

System poles of roll dynamics are given by characteristic equation

$$\lambda^3 - (\hat{Y}_v + \hat{L}_q) \lambda^2 + (\hat{Y}_v \hat{L}_p - \hat{L}_v \hat{Y}_p) \lambda + \hat{L}_v g = 0. \quad (4.15)$$

As expected, the observed root locus (Figure 4.18) is very similar to the one of pitch dynamics. Again, 3 different pole configurations exist in both models, ASL(tr) in red dashed lines and ASL(tr+rot) in blue lines. A pair of unstable complex conjugate poles and one stable real pole exists for wing positions well above the COG. Wing positions well below the COG yield a pair of stable complex conjugate poles and one unstable real pole. A transient region with 3 real poles exists around the COG ( $z_w \approx 0$ ) for ASL(tr) and slightly above the COG (approximately for  $z_w \in (3, 5)$  mm) for ASL(tr+rot).

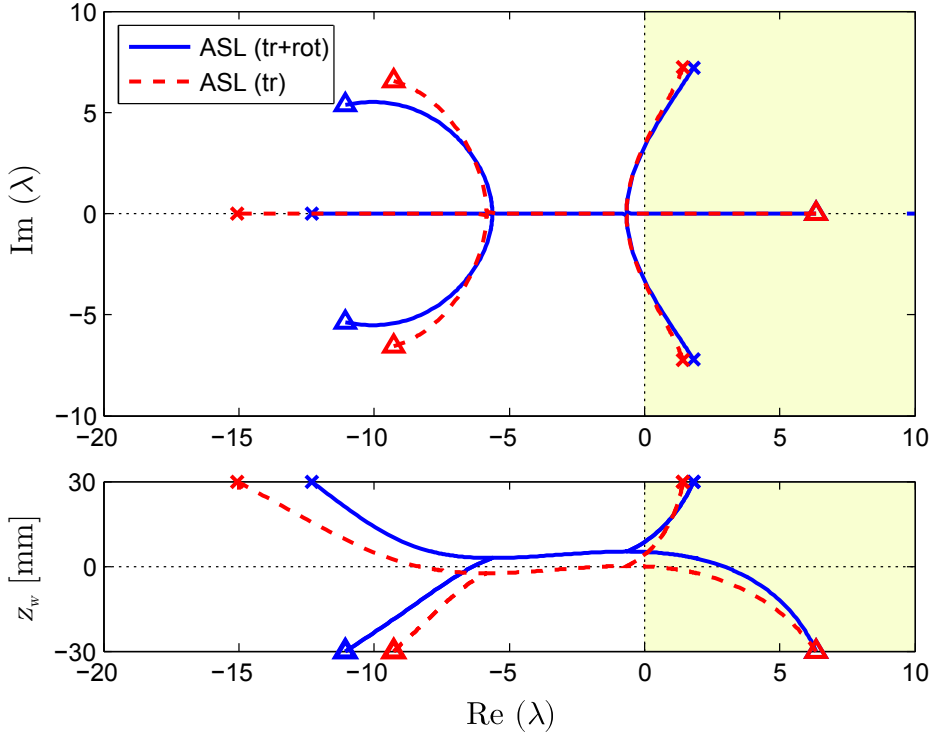


**Figure 4.18:** Influence of wing position  $z_w$  on the roll dynamics: pole positions in complex plane (top) and real part of the poles against the wing position (bottom).

The pole configuration in the pitch dynamics was determined by the derivative  $\hat{M}_u$ , the pitch moment induced by longitudinal translation. In roll the important derivative is  $\hat{L}_v$ , the roll moment induced by the lateral translation. Assuming the derivative  $\hat{Y}_p$  is negligible and following the same steps as in pitch, the characteristic equation can be rewritten to

$$1 + \hat{L}_v \frac{g}{\lambda (\lambda - \hat{Y}_v) (\lambda - \hat{L}_p)} = 0, \quad (4.16)$$

which is a root locus form with virtual feedback gain  $\hat{L}_v$ . The root locus is shown in Figure 4.19. Because the numerator of the virtual open loop system is positive, the situation is opposite to the pitch dynamics. We observe a pair of unstable complex poles and a stable real pole for positive  $\hat{L}_v$ , while negative  $\hat{L}_v$  results into an unstable real pole and a pair of stable complex poles.

However, because positive wing shoulder positions  $z_w > 0$  yield positive  $\hat{L}_v$ , but negative  $\hat{M}_u$ , the difference in the root locus positive directions of pitch and of roll

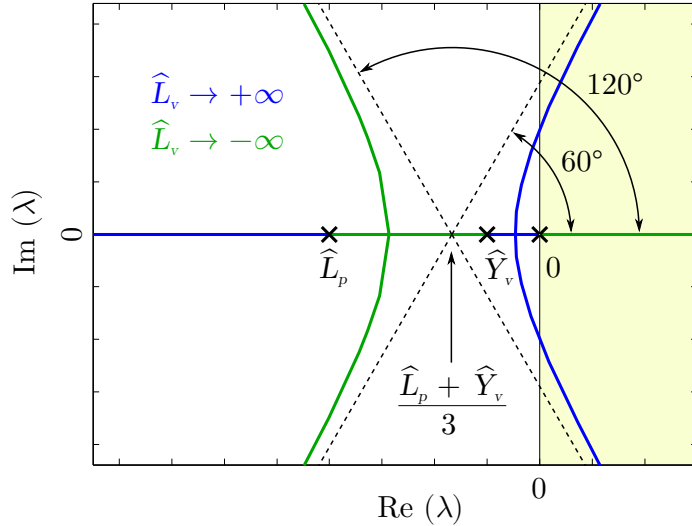


**Figure 4.19:** Root locus showing the effect of derivative  $\hat{L}_v$  on the roll dynamics.

is compensated; for a given wing position  $z_w$  the two systems behave similarly. A small region of stability exists in roll for small positive values of  $\hat{L}_v$ , provided that the derivatives  $\hat{Y}_v$  and  $\hat{L}_p$  remain negative. The stable region (with one fast real pole and a pair of slow lightly damped complex poles) can be enlarged by increasing the damping of lateral translation or roll rotation. The roll can be damped similar to pitch: either passively by damping surfaces (tail, sails) or by an active feedback.

Due to the different predictions of the derivative  $\hat{L}_v$  by the two models ASL(tr) and ASL(tr+rot) there exists an interval of positive wing positions, where ASL(tr) already predicts an unstable pair of complex poles and a stable real pole, while ASL(tr+rot) still gives a stable pair of complex poles and an unstable real pole. This can explain the discrepancy in the dronefly stability results (Section 3.4.3) among the considered models. Although the more complex models predict the pole configuration with an unstable real pole, the following section will show that the other configuration with an unstable complex pole-pair is more probable as it is easier to control.

### 4.3.3 Active stabilization

The active stabilization of roll via rate feedback is analogous to pitch. A proportional gain  $k_p$  introduces a stabilizing moment  $\hat{L} = -k_p p$ . The characteristic equation becomes

$$\lambda^3 + \left(k_p - \hat{Y}_v - \hat{L}_p\right)\lambda^2 + \left[\hat{Y}_v \left(\hat{L}_p - k_p\right) - \hat{L}_v \hat{Y}_p\right]\lambda + \hat{L}_v g = 0 \quad (4.17)$$

and can be rewritten further while neglecting  $\hat{Y}_p$  as

$$1 + \hat{L}_v \frac{g}{\lambda (\lambda - \hat{Y}_v) (\lambda + k_p - \hat{L}_p)} = 0. \quad (4.18)$$

The feedback gain moves the pole related to the roll rate damping towards minus infinity which “opens” the root locus for positive values of  $\hat{L}_v$  and enlarges the interval of stability.

The Routh-Hurwitz stability criterion yields three conditions

$$(k_p - \hat{Y}_v - \hat{L}_p) [\hat{Y}_v (\hat{L}_p - k_p) - \hat{L}_v \hat{Y}_p] - \hat{L}_v g > 0 \quad (4.19)$$

$$k_p - \hat{Y}_v - \hat{L}_p > 0 \quad (4.20)$$

$$\hat{L}_v g > 0. \quad (4.21)$$

The third condition requires that  $\hat{L}_v$  must be positive. The second condition is usually met as both derivatives  $\hat{Y}_v$  and  $\hat{L}_p$  are typically negative. Finally, the first condition can be used to express the minimum gain value for stability. Assuming the gain is positive we obtain

$$k_{p,min} = \frac{\hat{L}_v \hat{Y}_p - 2\hat{Y}_v \hat{L}_p - \hat{Y}_v^2 + \sqrt{(\hat{Y}_v^2 + \hat{L}_v \hat{Y}_p)^2 - 4\hat{Y}_v \hat{L}_v g}}{-2\hat{Y}_v}. \quad (4.22)$$

#### 4.4 Vertical and yaw dynamics stability

The vertical and yaw dynamics are decoupled from the rest of the dynamics (as long as  $I_{xz} = 0$ ) and each can be treated separately. They are modelled by two first-order differential equations

$$\dot{w} = \hat{Z}_w w + \hat{Z}_{ext} \quad (4.23)$$

$$\dot{r} = \hat{N}_r r + \hat{N}_{ext} \quad (4.24)$$

with coordinates according to Figure 4.20. The system poles can be expressed directly from the characteristic equation as

$$\lambda_w = \hat{Z}_w \quad (4.25)$$

$$\lambda_r = \hat{N}_r. \quad (4.26)$$

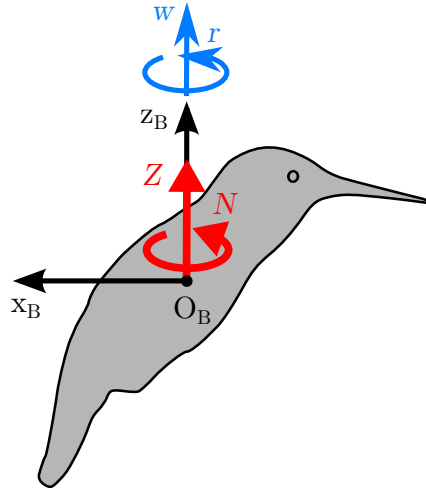


**Figure 4.20:** Coordinates of vertical and yaw dynamics.

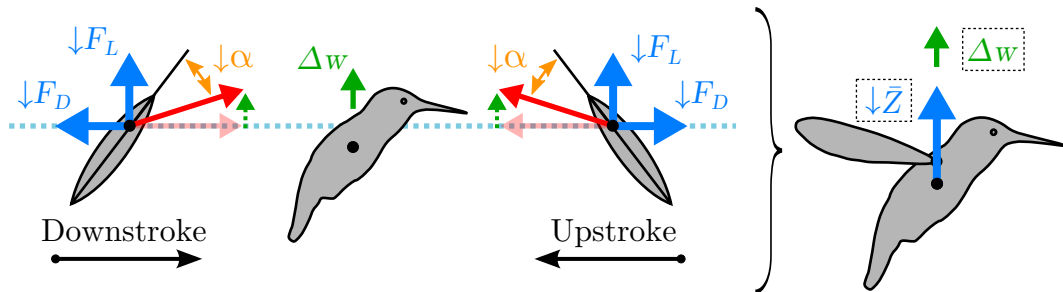


**Figure 4.21:** Effects of a disturbance in vertical direction  $\Delta w$ . A decreased angle of attack in both upstroke and downstroke causes the cycle-averaged vertical force  $\bar{Z}$  to drop, opposing the disturbance.

For a stable system, the stability derivatives  $\hat{Z}_w$  and  $\hat{N}_r$  need to be negative.

Figure 4.21 shows that a vertical disturbance  $\Delta w$  decreases the angle of attack in both upstroke and downstroke resulting into a drop of cycle-averaged vertical force  $\bar{Z}$ . Thus, the derivative  $\hat{Z}_w$  should be negative, representing a damping of the vertical motion.

The effect of a yaw disturbance  $\Delta r$  on the wing aerodynamic forces is captured in Figure 4.22. In downstroke, the right wing moves in the sense of the disturbance, which increases the wing velocity and results into an increase of drag. The left wing moves against the disturbance, which reduces the wing velocity and subsequently the drag. Opposite situation can be observed in upstroke. Overall, the drag produced

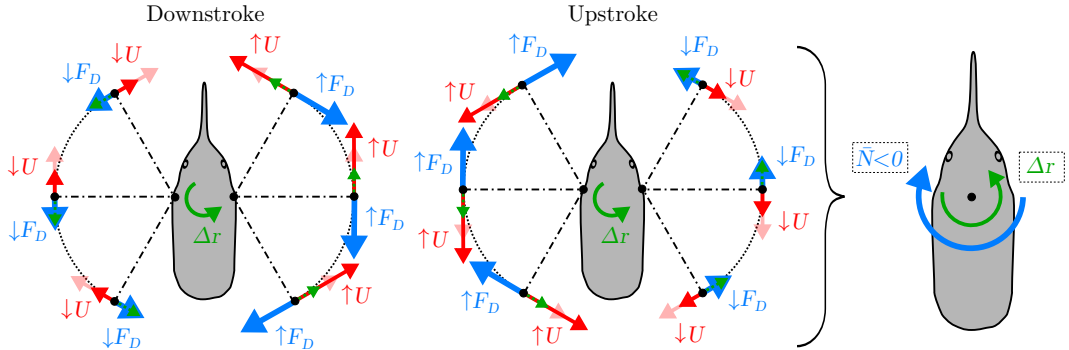


**Figure 4.22:** Effects of a yaw disturbance  $\Delta r$ . In downstroke, the wing speed of the right wing increases as it moves in the sense of the disturbance, while the speed of the left wing decreases as it moves against the disturbance. The opposite is true for the upstroke. The drag force distribution over the cycle is affected, resulting into a negative cycle-averaged yaw moment  $\bar{N}$  that counteracts the disturbance.

in the direction opposing the disturbance dominates, which results into a negative cycle-averaged yaw moment  $\bar{N}$ . Thus, the derivative  $\hat{N}_r$  should also be negative meaning the yaw disturbance is being damped passively.

Because both considered disturbances are related to the vertical body axis  $z_B$ , the derivatives  $\hat{Z}_w$  and  $\hat{N}_r$  should stay independent of wing position  $z_w$ . Indeed, the models ASL (tr) and ASL (tr+rot) give the same and constant values for any wing position of the robot with parameters from Section 4.1:  $\hat{Z}_w = -1.37 \text{ s}^{-1}$  and  $\hat{N}_r = -54.9 \text{ m}^{-1}\text{s}^{-1}$ . Thus, both vertical and yaw motion should be passively stable.

## 4.5 Wing position choice

In the previous paragraphs it has been shown that out of the four subsystems (pitch, roll, yaw and vertical dynamics) only the vertical and yaw dynamics are inherently stable for any wing position  $z_w$ . Moreover, the latter is true only for flyers with a vertical posture in hovering, as the system gets coupled with the roll dynamics via non-zero inertia product  $I_{xz}$  otherwise.

While there exists an interval of theoretical stability in both pitch and roll dynamics, the intervals of wing positions are very small and in general do not intersect. Therefore, it is impossible to find a wing position where the hummingbird robot would be, even theoretically, passively stable. The wing position could be chosen from one of the two intervals, which would mean that only one of the systems needs

to be stabilized actively. However, even if the model predictions were correct, the poles would still lie very close to the imaginary axis so some stability augmentation would be necessary.

Since the flight needs to be stabilized in any case, a wing position should be chosen so that the controller can be as simple as possible yet robust. It has been shown that if  $\hat{M}_u$  is positive and  $\hat{L}_v$  is negative, both pitch and roll systems have a pair of complex unstable poles and a real stable pole. Such a system can be easily stabilized by a simple rate feedback. On the other hand, negative  $\hat{M}_u$  and positive  $\hat{L}_v$  yields a pair of stable complex poles and an unstable real pole, a configuration that will remain unstable even with the rate feedback.

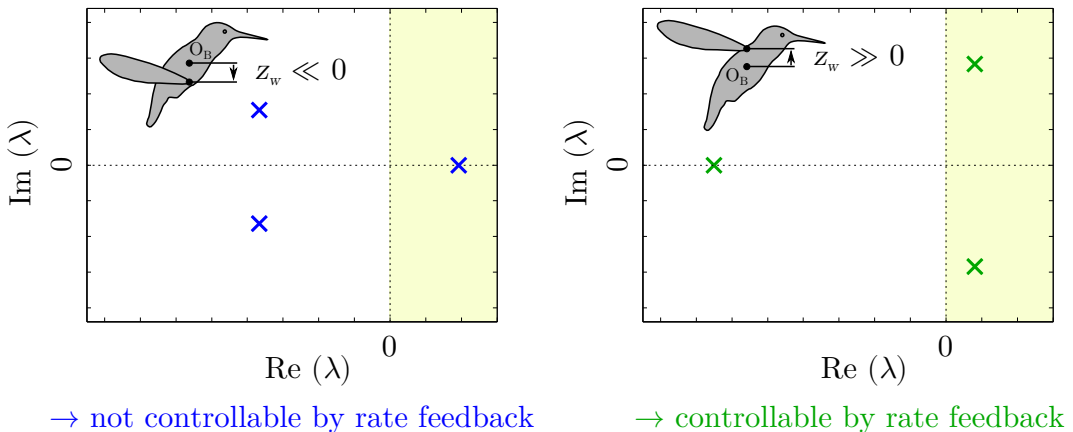


**Figure 4.23:** Pole configurations observed in both pitch and roll systems: situation for  $\hat{M}_u \gg 0$  or  $\hat{L}_v \ll 0$  (wing positions well below the COG) cannot be stabilized by rate feedback (left); situation for  $\hat{M}_u \ll 0$  or  $\hat{L}_v \gg 0$  (wing positions well above the COG) is controllable by rate feedback (right).

The quasi-steady based aerodynamic model predicts that positive  $\hat{M}_u$  and negative  $\hat{L}_v$  can only be obtained if the wing shoulders are placed (sufficiently high) above the COG. For the MAV considered in this chapter the wings should be placed above  $z_w > 5$  mm (see Figures 4.8 and 4.17). To keep a certain safety margin,  $z_w = 10$  mm was selected.

## 4.6 Rate feedback gains

The minimal necessary gains for stable pitch and roll rate feedback can be computed from equations (4.12) and (4.22), respectively. Considering  $z_w = 10$  mm we

will obtain  $k_{q,min} \approx 13.8$  and  $k_{p,min} \approx 1.5$ . As expected, the pitch dynamics require slightly higher gain as the chosen wing position is further from the passively stable interval in pitch than in roll.

The root locus can be obtained by rewriting the characteristic equations 4.7 and 4.17 (while neglecting  $\hat{X}_q$  and  $\hat{Y}_p$ ) into the following form

$$1 + k_q \frac{\lambda(\lambda - \hat{X}_u)}{\lambda(\lambda - \hat{X}_u)(\lambda - \hat{M}_q) - \hat{M}_u g} = 0 \quad (4.27)$$

$$1 + k_p \frac{\lambda(\lambda - \hat{Y}_v)}{\lambda(\lambda - \hat{Y}_v)(\lambda - \hat{L}_p) + \hat{L}_v g} = 0. \quad (4.28)$$

where the terms multiplied by the gains  $k_q$  and  $k_p$  are the open-loop transfer functions  $Q(s)/\hat{M}(s)$  and  $P(s)/\hat{L}(s)$ , respectively. The root loci for gains  $k_q$  and  $k_p$  going from zero to infinity are plotted in Figure 4.24. We can observe that, no matter how big the gain is, the real part of the originally unstable pair of poles will always stay “trapped” between the pair of zeros, one at the origin and the other given by  $\hat{X}_u$  and  $\hat{Y}_v$  for pitch and roll, respectively. Thus, a more complex controller needs to be used if faster response is required. Alternatively, the derivatives  $\hat{X}_u$  and  $\hat{Y}_v$  could be decreased by adding passive damping surfaces. However, this would also influence the remaining stability derivatives that define the open loop poles, so the effect on the whole root locus is not apparent.

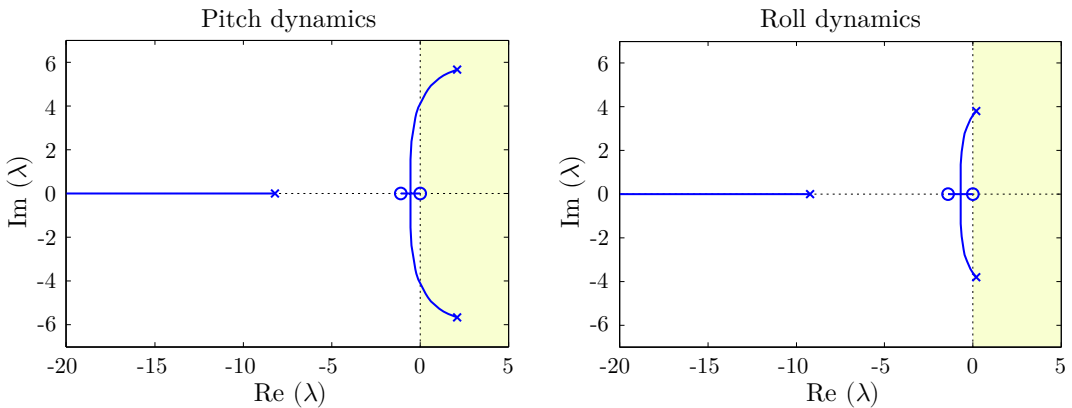


**Figure 4.24:** Root locus for a rate feedback gain in pitch (left) and in roll systems (right).

## 4.7 Conclusion

The inherent instability of pitch and roll dynamics was demonstrated through a simplistic approach, which is coherent with quasi-steady modelling results. The systems can be actively stabilized by a simple angular rate feedback, provided that the wing shoulders are placed sufficiently above the COG. This conclusion is in accordance with morphology of hovering animals as well as with observations of basic motoric response in fruit-flies. Of course a more sophisticated control law can be used (and is probably used to some extent also by flying animals). The design of a controller for the hummingbird robot will be described in more detail in the next chapter.

## 4.8 References

- B. Cheng and X. Deng. Translational and rotational damping of flapping flight and its dynamics and stability at hovering. *IEEE Transactions on Robotics*, 27(5):849–864, Oct. 2011. doi:10.1109/TRO.2011.2156170.
- G. F. Franklin, J. Powel, and A. Emami-Naeini. *Feedback Control of Dynamic Systems*. Prentice Hall, 4th edition, 2002.
- L. Ristroph, G. Ristroph, S. Morozova, A. J. Bergou, S. Chang, J. Guckenheimer, Z. J. Wang, and I. Cohen. Active and passive stabilization of body pitch in insect flight. *Journal of The Royal Society Interface*, 10(85):1–13, 2013. doi:10.1098/rsif.2013.0237.
- A. Sherman and M. H. Dickinson. Summation of visual and mechanosensory feedback in drosophila flight control. *Journal of Experimental Biology*, 207(1):133–142, 2004. doi:10.1242/jeb.00731.
- M. Sun and Y. Xiong. Dynamic flight stability of a hovering bumblebee. *Journal of Experimental Biology*, 208:447–459, 2005.
- G. K. Taylor and H. G. Krapp. Sensory systems and flight stability: what do insects measure and why? *Advances in insect physiology*, 34(231-316), 2008. doi:10.1016/S0065-2806(07)34005-8.
- Y. Xiong and M. Sun. Dynamic flight stability of a bumblebee in forward flight. *Acta Mech. Sinica*, 24(1):25–36, Feb. 2008. doi:DOI 10.1007/s10409-007-0121-2.
- Y. Zhang and M. Sun. Dynamic flight stability of a hovering model insect: theory versus simulation using equations of motion coupled with navier-stokes equation. *Acta Mech. Sinica*, 26(4):509–520, 2010. doi:10.1007/s10409-010-0360-5.



# Chapter 5

## Flapping flight control

Since the hovering flapping flight is inherently unstable, it needs to be stabilized passively (by additional damping surfaces like tails or sails) or actively (by wing motion). In this chapter an active attitude controller is developed based on the linearised cycle-averaged model from the previous chapter. On top of that, a 4 DOF flight controller is added to control the heading and the flight velocity in any direction. Wing motion parameters suitable for thrust and control moment modulation are selected. Finally, the controller performance is demonstrated through simulations with the full non-linear model from Chapter 3.

### 5.1 Control design

Many strategies of tail-less flapping flight control can be found in the literature. It has been demonstrated on a real insect-sized MAV that a simple angular rate feedback succeeds to stabilize the attitude (Fuller et al., 2014), confirming the previous chapter conclusions. For flight control, most works use design techniques based on output or state feedback with decentralized (Doman et al., 2010) or centralized architectures (Deng et al., 2006b,a; Rifai et al., 2009; Rakotomamonjy et al., 2010; Ma et al., 2013). Nevertheless, more elaborate control techniques have also been employed (Chung and Dorothy, 2010). Most of the controllers were tested numerically in non-linear simulations, often based on quasi-steady aerodynamics. However, the controller of Ma et al. (2013) succeeded to control near hover flight of a real insect-sized MAV inside a flight arena with a position tracking system.

The control design presented here uses the linearised model developed in the previous chapters. The controllers are chosen and tuned by pole placement method. The MAV parameters were given in Section 4.1. According to the conclusions of the previous chapter, the wing shoulders are placed at  $z_w = 10$  mm. Nevertheless, the

described approach should be applicable to any MAV with vertical body posture in hovering ( $I_{xz} = 0$ ) and with wing shoulders placed sufficiently high above the COG.

The dynamics of such an MAV splits into 4 subsystems (pitch, roll, yaw and vertical dynamics) that can be treated separately. Pitch and roll dynamics are unstable, therefore the attitude is stabilized first. The second step is to control the flight velocity ( $u, v, w$ ) and the steering ( $r$ ). In this section it is assumed that an arbitrary external moment and force can be applied on the MAV body. The generation of these control moments and forces by wing motion will be discussed in Section 5.2. From now on, the subscript  $ext$  of external efforts will be dropped, i.e.  $L_{ext} = L$ , etc.

### 5.1.1 Pitch dynamics

The pitch dynamics has 2 DOFs: the pitch angle  $\vartheta$  and the longitudinal velocity  $u$ . However, they do not need to be controlled independently. Similar to quadrocopters, e.g. Michael et al. (2010), the flight speed can be controlled by pitching the body forward and backward, which modulates the longitudinal component of the total thrust vector. Thus, the pitch dynamics can be controlled through a single input, the pitch moment  $M$ , and the state space model (3.45) can be rewritten as a set of transfer functions

$$\frac{U(s)}{\hat{M}(s)} = \frac{\hat{X}_q s + g}{s^3 - (\hat{X}_u + \hat{M}_q)s^2 + (\hat{X}_u \hat{M}_q - \hat{M}_u \hat{X}_q)s - \hat{M}_u g} \quad (5.1)$$

$$\frac{\Theta(s)}{\hat{M}(s)} = \frac{s - \hat{X}_u}{s^3 - (\hat{X}_u + \hat{M}_q)s^2 + (\hat{X}_u \hat{M}_q - \hat{M}_u \hat{X}_q)s - \hat{M}_u g}. \quad (5.2)$$

The system poles are given by the denominator roots. For wings placed above the COG ( $z_w > 0$ ), the derivative  $\hat{M}_u$  is negative, which results into a stable real pole and an unstable pair of complex-conjugate poles (see previous chapter). The zeros are given by the numerator roots and are different for the two transfer functions:  $z = -g/\hat{X}_q$  for forward motion and  $z = \hat{X}_u$  for pitch (another zero at  $z = 0$  would appear for transfer function to pitch rate  $q$  due to derivation).

For the hummingbird robot parameters and  $z_w = 10$  mm we get the poles  $\lambda_1 = -8.2$  and  $\lambda_{2,3} = 2.11 \pm 5.65i$  and zeros  $z = 215$  for forward motion and  $z = -1.1$  for pitch. The open loop pole-zero maps are displayed in Figure 5.1.

The proposed controller uses a cascade structure according to Figure 5.2. The innermost loop 1 controls the pitch rate  $q$ , the middle loop 2 controls the pitch angle  $\vartheta$  and the outer loop 3 controls the forward speed  $u$ . The first two loops can be implemented on-board of an MAV equipped with an Inertial Measurement Unit (IMU),

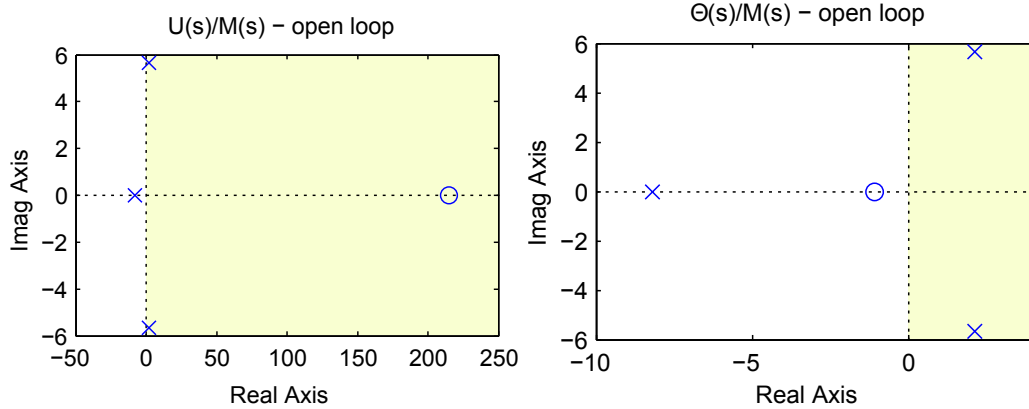


**Figure 5.1:** Open loop pole-zero maps of pitch dynamics: forward motion (left) and pitch angle (right).

which senses the attitude and angular velocities. The third loop represents the pilot operating the MAV or an autopilot, if an external measurement system like motion tracking or GPS is available. Each loop compensator was tuned by pole-placement, starting from the innermost loop. As it will be shown in Section 5.3, the output of the full non-linear model needs to be cycle-averaged to remove the oscillation due to flapping from the feedback. This introduces a time delay not included in the linearised model. Thus, an emphasis was put on keeping the phase margin large in order to make the controller more robust.

It has been shown in the previous chapter that the pitch rate can be stabilized by a rate feedback. However, much better performance is achieved by adding an integrator (cancelling the system zero at the origin) and a negative zero, i.e. a PI controller. The resulting root-locus and Bode plot for the selected gain are shown in Figure 5.3. Such a compensator reduces the steady state error and has a relatively high phase margin of  $77^\circ$ . The step response of the linear system is plotted in Figure 5.6 (left). The steady state error is still present but it will be compensated by the outer loops.

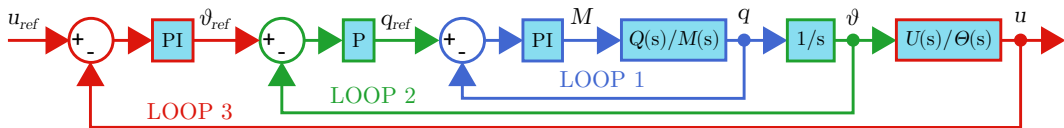


**Figure 5.2:** Cascade control of pitch dynamics: loop 1 controls the pitch rate  $q$ , loop 2 the pitch angle  $\vartheta$  and loop 3 the longitudinal velocity  $u$ .

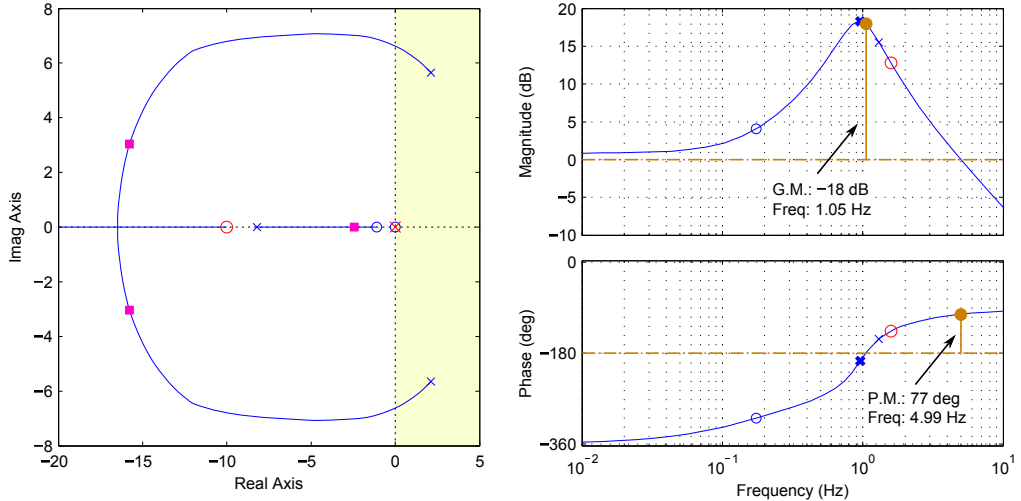


**Figure 5.3:** Loop 1 - pitch rate  $q$ : root locus (left) and Bode plot<sup>1</sup> for the selected gain (right).

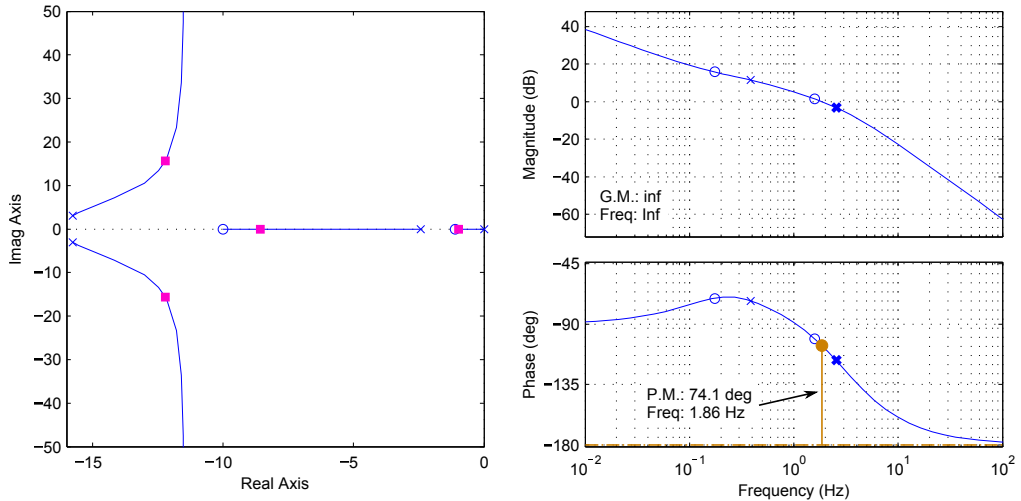


**Figure 5.4:** Loop 2 - pitch angle  $\vartheta$ : root locus (left) and Bode plot for the selected gain (right).

<sup>1</sup>In non-minimum phase systems (with poles/zeros in the right hand plane) the Bode plot follows less common rules and the stability condition gets modified. If an increasing gain brings the unstable system to stability and if its magnitude crosses 0 dB once, the stability criterion requires that magnitude is greater than 0 dB at  $-180^\circ$  phase. The definitions of the gain and phase margins are modified accordingly.

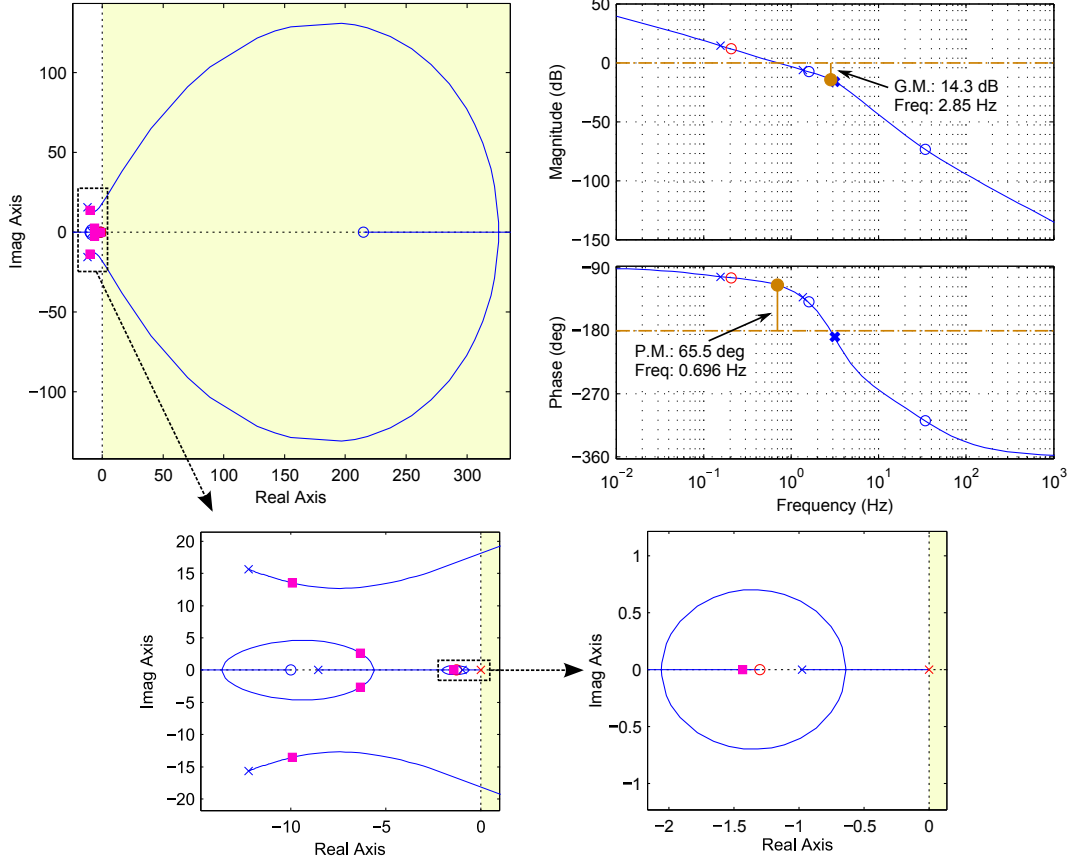


**Figure 5.5:** Loop 3 - longitudinal velocity  $u$ : root locus (top, left) with detail views (bottom) and Bode plot for the selected gain (top, right).

The output of the first closed loop is integrated to obtain the pitch angle  $\vartheta$ , which results into an additional system pole at the origin. The second loop is controlled by a simple proportional feedback. The root locus and the Bode plot are shown in Figure 5.4. The phase margin is  $74.1^\circ$  and the step response (Figure 5.6 centre) shows that closed loop system converges quickly to the desired value.

The output of the second closed loop is multiplied by the transfer function  $U(s)/\Theta(s) = (\hat{X}_q s + g)/(s - \hat{X}_u)$  to get the longitudinal speed  $u$ . Thus, the small negative zero of the pitch motion is cancelled and a large positive zero of forward motion is added. A PI controller (an integrator and a negative zero) is used to control  $u$  in the last loop. The root locus and bode plot is shown in Figure 5.5. The chosen controller gain results into a phase margin of  $65.5^\circ$ . The step response is displayed in Figure 5.6 (right) showing a good performance with very little overshoot.

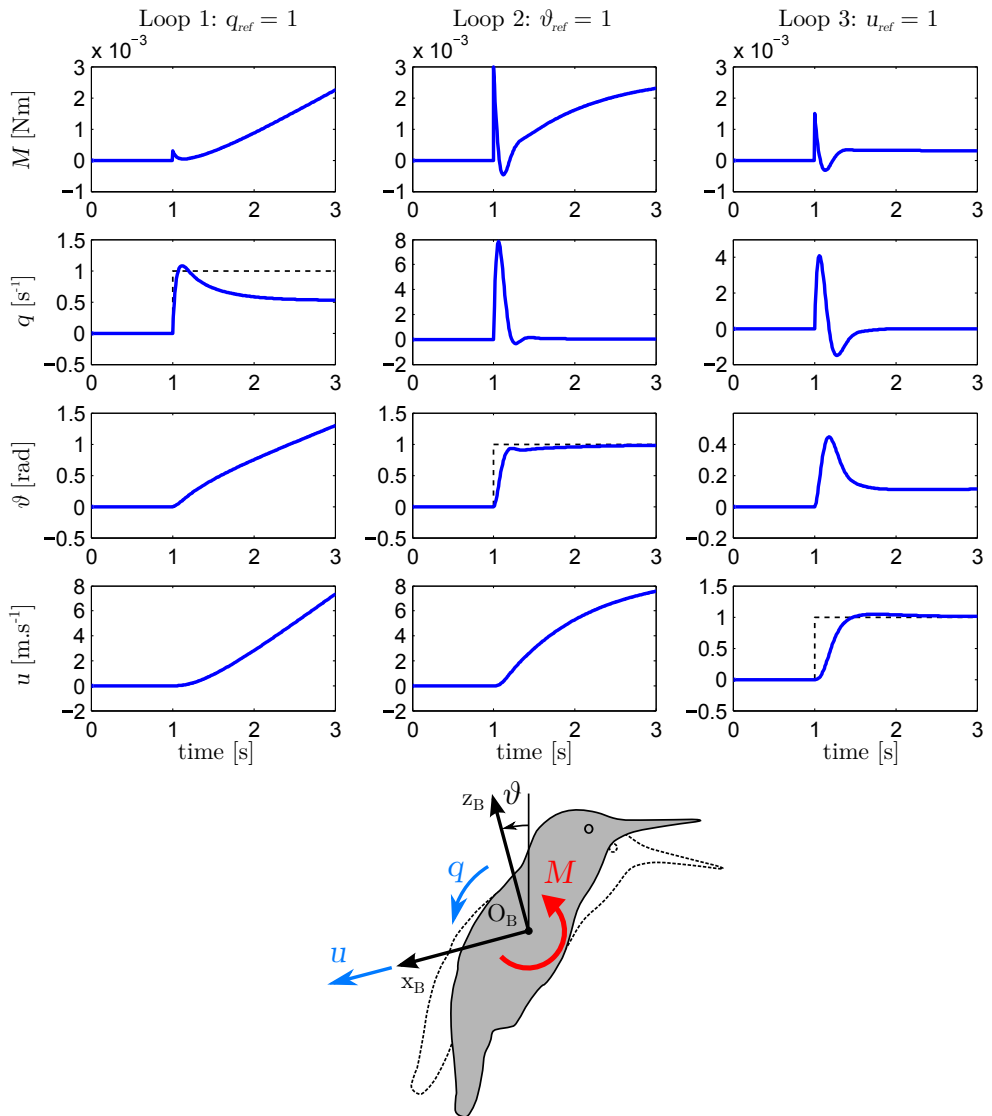


**Figure 5.6:** Step response of the linearized pitch dynamics in closed loop: loop 1 - pitch rate control (left), loop 2 - pitch angle control (center) and loop 3 - longitudinal speed control (right).

### 5.1.2 Roll dynamics

The control of the roll dynamics is nearly identical to pitch. The lateral flight speed is controlled by rolling the body left or right. Thus, only one input, the roll moment  $L$ , is considered. The system can be represented by a pair of transfer functions

$$\frac{V(s)}{\hat{L}(s)} = \frac{\hat{Y}_p s - g}{s^3 - (\hat{Y}_v + \hat{L}_p)s^2 + (\hat{Y}_v\hat{L}_p - \hat{L}_v\hat{Y}_p)s + \hat{L}_v g} \quad (5.3)$$

$$\frac{\Phi(s)}{\hat{L}(s)} = \frac{s - \hat{Y}_v}{s^3 - (\hat{Y}_v + \hat{L}_p)s^2 + (\hat{Y}_v\hat{L}_p - \hat{L}_v\hat{Y}_p)s + \hat{L}_v g}. \quad (5.4)$$

For wings well above the COG the denominator roots give one stable real pole and an unstable pair of complex-conjugate poles. Unlike in longitudinal direction, the lateral motion zero is negative, placed at  $z = g/\hat{Y}_p$  (derivative  $\hat{Y}_p$  is always negative). The roll motion zero lies at  $z = \hat{Y}_v$  (another zero would lie at  $z = 0$  for transfer function to roll rate  $p$ ). For the hummingbird robot parameters we get the system poles  $\lambda_1 = -9.2$  and  $\lambda_{2,3} = 0.2 \pm 3.8i$  and zeros  $z = -258$  for lateral motion and  $z = -1.4$  for roll. The open loop pole-zero maps are shown in Figure 5.7.

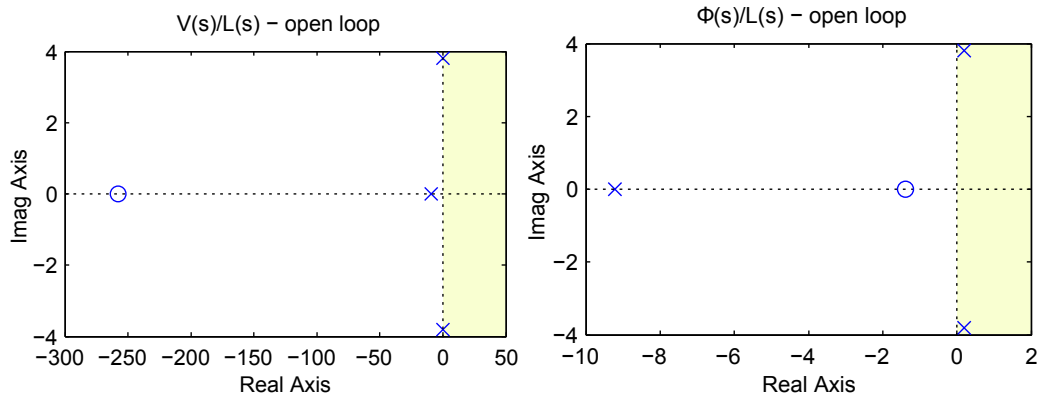


**Figure 5.7:** Open loop pole-zero maps of roll dynamics: sideways motion (left) and roll angle (right).

Again a cascade controller is used, where the innermost loop 1 controls the roll rate  $p$ , the middle loop 2 controls the roll angle  $\varphi$  and the outer loop 3 controls the lateral speed  $v$  (Figure 5.8). The compensators were chosen the same as in the pitch system: PI for loops 1 and 3 and P for loop 2. They were tuned by pole placement.

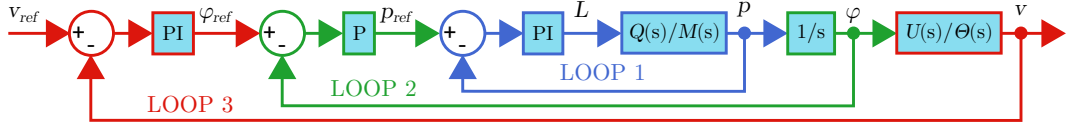


**Figure 5.8:** Cascade control of roll dynamics: loop 1 controls the roll rate  $p$ , loop 2 the pitch angle  $\varphi$  and loop 3 the lateral velocity  $v$ .

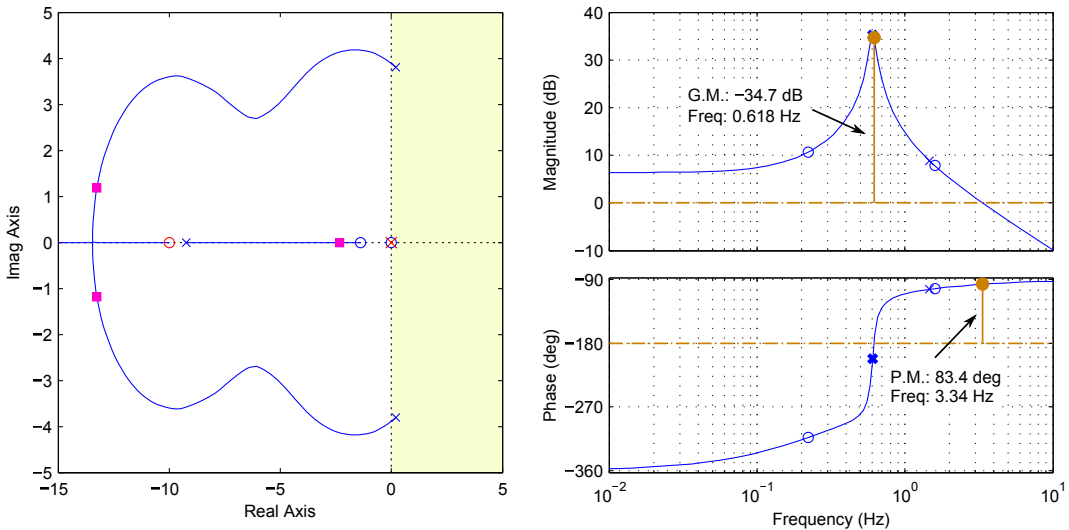


**Figure 5.9:** Loop 1 - roll rate  $p$ : root locus (left) and Bode plot for the selected gain (right).

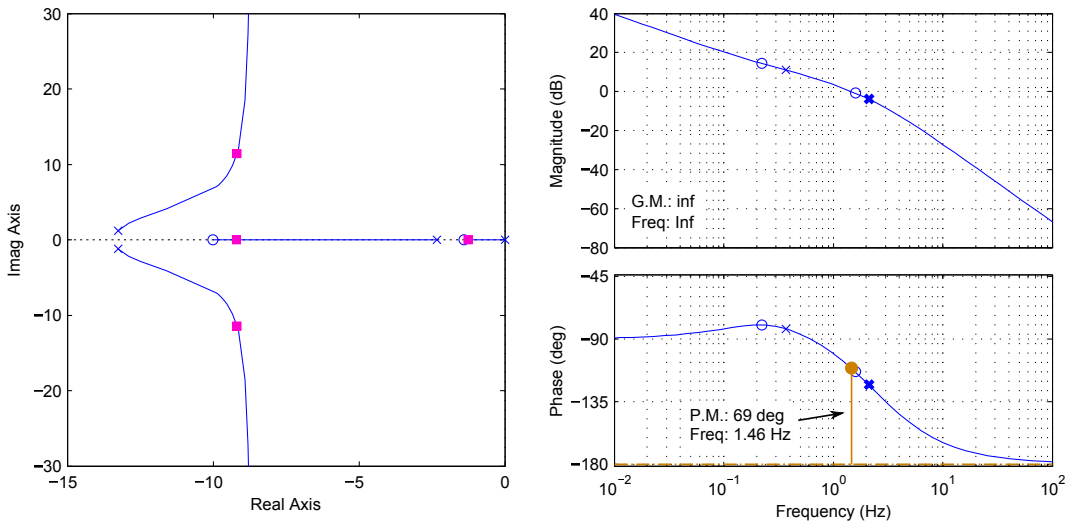


**Figure 5.10:** Loop 2 - roll angle  $\varphi$ : root locus (left) and Bode plot for the selected gain (right).

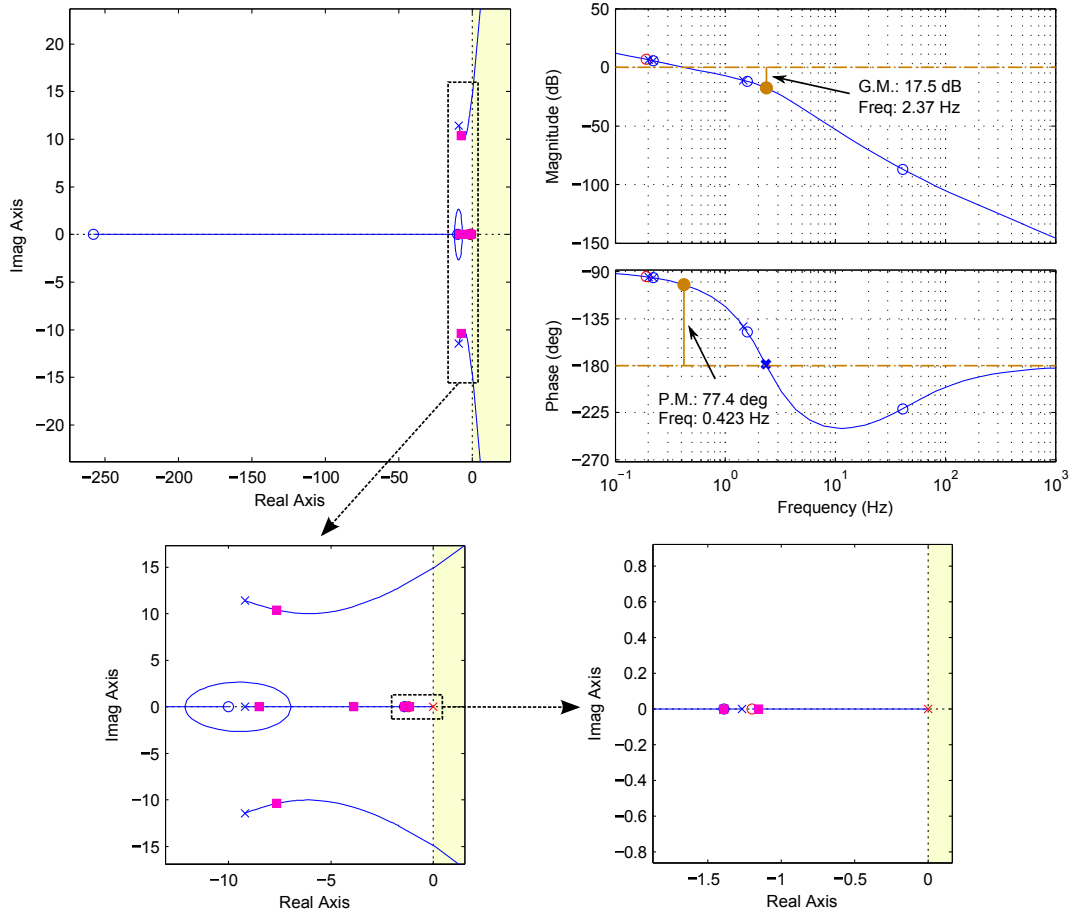


**Figure 5.11:** Loop 3 - lateral velocity  $v$ : negative root locus (top, left) with detail views (bottom) and Bode plot for the selected gain (top, right).

The root loci and the bode plots for the three loops are shown in Figures 5.9–5.11. The plots of loops 1 and 2 are equivalent to those in pitch. The loop 3, however, is different. A negative gain is required because the body needs to roll in negative  $\varphi$  direction to move in positive  $v$  direction and also both system zeros are negative. The phase margins of the loops 1, 2 and 3 are  $83.4^\circ$ ,  $69^\circ$  and  $77.4^\circ$ , respectively.

The step responses for all three compensators are plotted in Figure 5.12. The performance is comparable to the pitch system. The lateral speed response is slightly slower due to a smaller gain, because a higher phase margin was preferred.

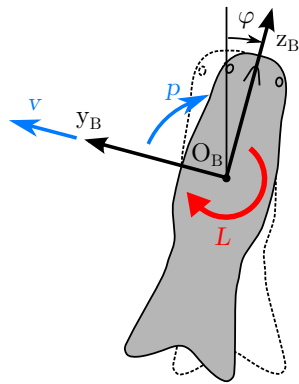
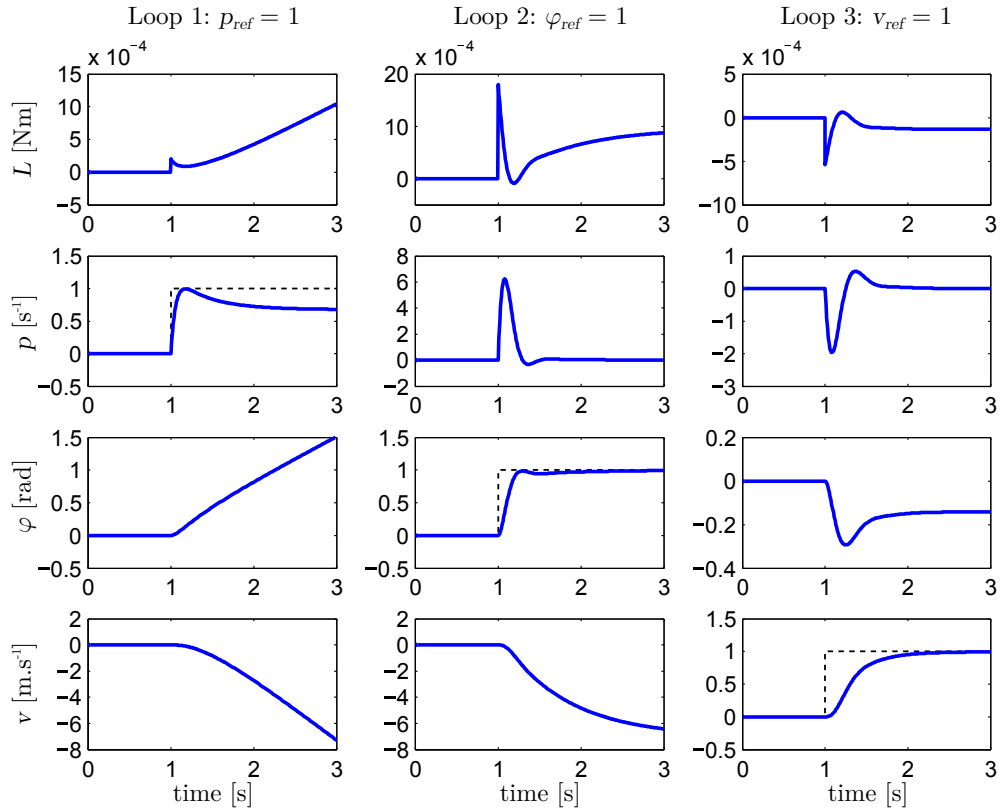


**Figure 5.12:** Step response of the linearized roll dynamics in closed loop: loop 1 - roll rate control (left), loop 2 - roll angle control (center) and loop 3 - lateral speed control (right).

### 5.1.3 Yaw and vertical dynamics

The yaw dynamics is a SISO (single input single output) system that can be represented by the transfer function from yaw moment  $N$  to yaw rate  $r$

$$\frac{R(s)}{\hat{N}(s)} = \frac{1}{s - \hat{N}_r}. \quad (5.5)$$

Because  $\hat{N}_r$  is negative, the system pole  $\lambda = \hat{N}_r$  is always stable (see Section 4.4). For the considered MAV parameters we get  $\lambda = -54.9$ . While the yaw could be controlled by a simple proportional feedback, a pure integral feedback results into a zero steady state error. The root locus showing the selected gain and the closed loop step response are displayed in Figure 5.13 (left).

The vertical dynamics is also a SISO system with a transfer function from vertical force  $Z$  to vertical speed  $w$

$$\frac{W(s)}{\hat{Z}(s)} = \frac{1}{s - \hat{Z}_w}. \quad (5.6)$$

The system is also passively stable, because the derivative  $\hat{Z}_w$  is negative, but the aerodynamic damping is much smaller than in yaw ( $\lambda = -0.027$  for the considered MAV). Thus, a PI compensator is used for vertical speed control. The root locus and step response are shown in Figure 5.13 (right).

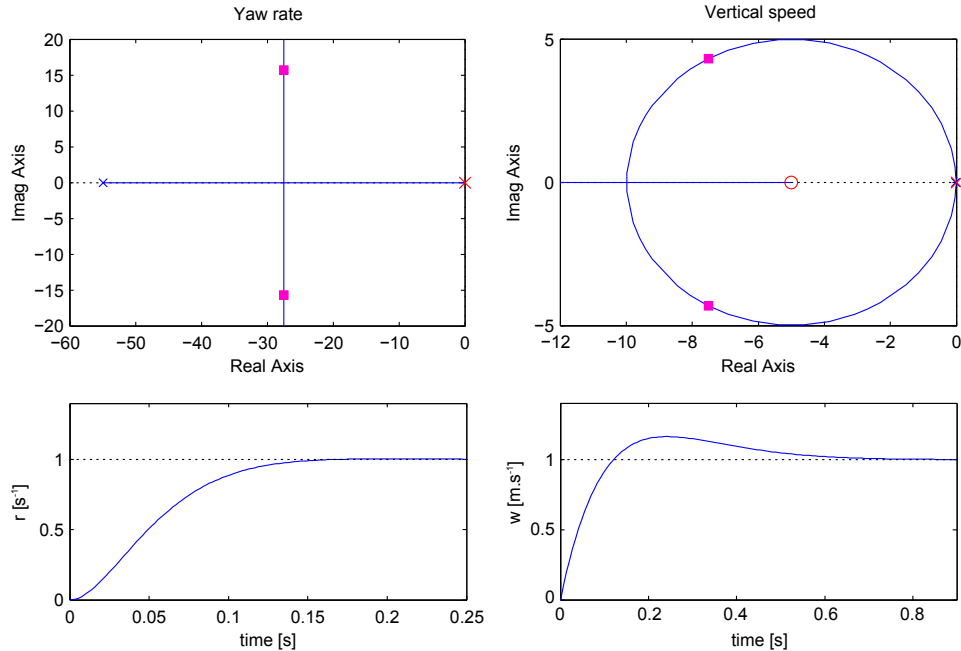


**Figure 5.13:** Root locus (top row) and step response (bottom row) of the yaw rate (left) and vertical speed (right) controllers. The vertical speed system pole is very close to the origin and so it is overlapped by the integrator pole in the root locus.

### 5.1.4 Complete controller

The scheme of the complete controller with all 4 subsystems is shown in Figure 5.14. The right dashed rectangle highlights the attitude controller, the velocity controller is inside the dashed rectangle on the left and represents the (auto)pilot. The compensator parameters are summarized in Table 5.1.

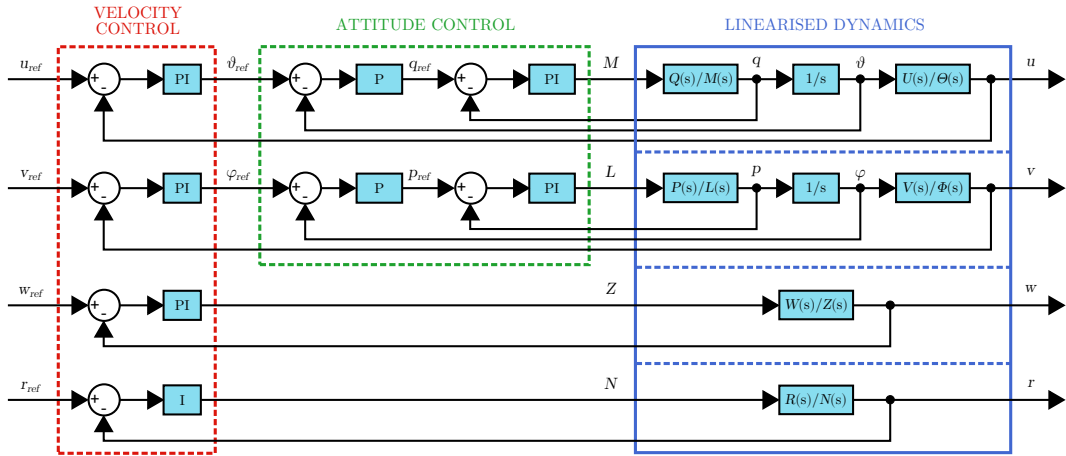


**Figure 5.14:** Cascade control of the linearised system.

		Transfer function	$K_P$	$K_I$
Pitch dynamics	$q$	$0.0003 \frac{s+10}{s}$	0.0003	0.003
	$\vartheta$	10	10	-
	$u$	$0.5 \frac{s+1.3}{s}$	0.5	0.65
Roll dynamics	$p$	$0.0002 \frac{s+10}{s}$	0.0002	0.002
	$\varphi$	9	9	-
	$v$	$-0.3 \frac{s+1.2}{s}$	-0.3	-0.36
Yaw dynamics	$r$	$0.003 \frac{1}{s}$	-	0.003
Vertical dynamics	$w$	$0.3 \frac{s+5}{s}$	0.3	1.5

**Table 5.1:** Control parameters: the compensator transfer function and an equivalent PI controller with a proportional gain  $K_P$  and an integral gain  $K_I$ .

## 5.2 Control moment generation

The proposed controller can stabilize the attitude and control the flight in 4 DOF by modulating an external vertical force  $Z$  and moments around the three body axes  $L$ ,  $M$  and  $N$ . In reality, these control efforts need to be generated through changes of wing kinematics.

### 5.2.1 Control derivatives

As it was already presented in Section 3.2.1, the effects of the wing motion parameter changes  $\Delta\mathbf{p}$  on the generated efforts are given by the control derivatives matrix  $\mathbf{J}$  defined as

$$\mathbf{J} = \begin{bmatrix} X_{p_1} & X_{p_2} & \cdots & X_{p_n} \\ Y_{p_1} & Y_{p_2} & \cdots & Y_{p_n} \\ \vdots & \vdots & \ddots & \vdots \\ N_{p_1} & N_{p_2} & \cdots & N_{p_n} \end{bmatrix}. \quad (5.7)$$

Each matrix element represents a partial derivative of a cycle averaged force / moment component with respect to one of the wing motion parameters,  $p_i$ . The derivatives are calculated in the equilibrium with states  $\mathbf{x}_e$  and wing motion parameters  $\mathbf{p}_e$ ; a shortened notation is used as in the previous sections, i.e.  $X_{p_i} = \frac{\partial \bar{X}}{\partial p_i}(\mathbf{x}_e, \mathbf{p}_e)$ .

The wing motion parameter changes  $\Delta\mathbf{p}$ , necessary to generate the desired combination of forces and moments, can be computed by relation

$$\Delta\mathbf{p} = \mathbf{J}^+[X, Y, Z, L, M, N]^T, \quad (5.8)$$

where  $\mathbf{J}^+$  is a pseudo-inverse of the matrix  $\mathbf{J}$ . Finally, these changes are added to the equilibrium values

$$\mathbf{p} = \mathbf{p}_e + \Delta\mathbf{p}. \quad (5.9)$$

The control derivatives were evaluated numerically using the approach described in Section 3.2.2, assuming the set of wing kinematics parameters  $\mathbf{p}$  according to Section 3.1.1. The results are split into two parts. First, we change the parameters symmetrically, i.e. the parameter changes made on both wings are equal and have identical signs. Second, we change the parameters asymmetrically, i.e. the changes done on the two wings have equal magnitudes but opposite signs.

When applying the wing kinematic changes symmetrically (subscript S) only the longitudinal system efforts ( $X$ ,  $Z$  and  $M$ ) are modified. The linearised relationship can be written as

$$[X, Z, M]^T = \mathbf{J}_S [\phi_{mS}, \phi_{0S}, \alpha_{mS}, \alpha_{0S}, \varphi_{\alpha S}, \delta_{m1S}, \delta_{m2S}, \beta_S, f_S]^T. \quad (5.10)$$

The matrix  $\mathbf{J}_S$  was normalized to have comparable values between the forces and moments: the row belonging to the moment  $M$  was divided by a characteristic length  $R_{CP} = R\hat{r}_2$  (the CP position on the wing). The normalized matrix with units mN/ $^\circ$ , or mN/Hz in case of the flapping frequency, was evaluated as

$$\tilde{\mathbf{J}}_S = \begin{matrix} & \phi_{mS} & \phi_{0S} & \alpha_{mS} & \alpha_{0S} & \varphi_{\alpha S} & \delta_{m1S} & \delta_{m2S} & \beta_S & f_S \\ \begin{matrix} X \\ Z \\ \frac{M}{R_{CP}} \end{matrix} & \left[ \begin{array}{ccccccccc} 0 & 0.59 & 0 & -4.8 & 0 & 0.29 & 0 & -3.4 & 0 \\ 4.9 & 0 & 1.4 & 0 & -0.6 & 0 & 4.3 & 0 & 15 \\ 0 & -2.5 & 0 & -0.41 & 0 & 2.9 & 0 & -0.44 & 0 \end{array} \right] \end{matrix}. \quad (5.11)$$

For asymmetric changes of wing kinematics (subscript A) only the lateral system force and moments  $Y$ ,  $L$  and  $N$  are affected. The relationship can be written as

$$[Y, L, N]^T = \mathbf{J}_A [\phi_{mA}, \phi_{0A}, \alpha_{mA}, \alpha_{0A}, \varphi_{\alpha A}, \delta_{m1A}, \delta_{m2A}, \beta_A]^T, \quad (5.12)$$

where the control derivatives matrix, normalized as before, is

$$\tilde{\mathbf{J}}_A = \begin{matrix} & \phi_{mA} & \phi_{0A} & \alpha_{mA} & \alpha_{0A} & \varphi_{\alpha A} & \delta_{m1A} & \delta_{m2A} & \beta_A \\ \begin{matrix} Y \\ \frac{L}{R_{CP}} \\ \frac{N}{R_{CP}} \end{matrix} & \left[ \begin{array}{ccccccccc} -0.66 & 0 & 0.31 & 0 & 1.9 & 0 & -0.29 & 0 \\ -4.3 & 0 & -2 & 0 & 0.47 & 0 & -7.2 & 0 \\ 0 & 0.2 & 0 & -7.8 & 0 & 0.094 & 0 & -3.8 \end{array} \right] \end{matrix}. \quad (5.13)$$

By studying the matrices  $\tilde{\mathbf{J}}_S$  and  $\tilde{\mathbf{J}}_A$  we can identify two groups of parameters according to their effect on the generated forces and moments. The first group includes flapping frequency  $f$ , sweep amplitude  $\phi_m$ , angle of attack amplitude  $\alpha_m$ , phase shift  $\varphi_\alpha$  and amplitude of figure eight-like deviation  $\delta_{m2}$  (Figure 5.15 left). If we modify these parameters symmetrically on both wings, we control the vertical force  $Z$ . If we modify these parameters, excluding the flapping frequency, asymmetrically (with positive sign on the left wing and negative on the right wing) we modulate the roll moment  $L$  and lateral force  $Y$ .

The second group includes sweep angle offset  $\phi_0$ , angle of attack offset  $\alpha_0$ , amplitude of oval-like deviation  $\delta_{m1}$  and mean stroke plane inclination  $\beta$  (Figure 5.15 right). Symmetric changes of these parameters result into pitch moment  $M$  and longitudinal force  $X$  modulation. Same parameters taken asymmetrically modify the yaw moment  $N$ .

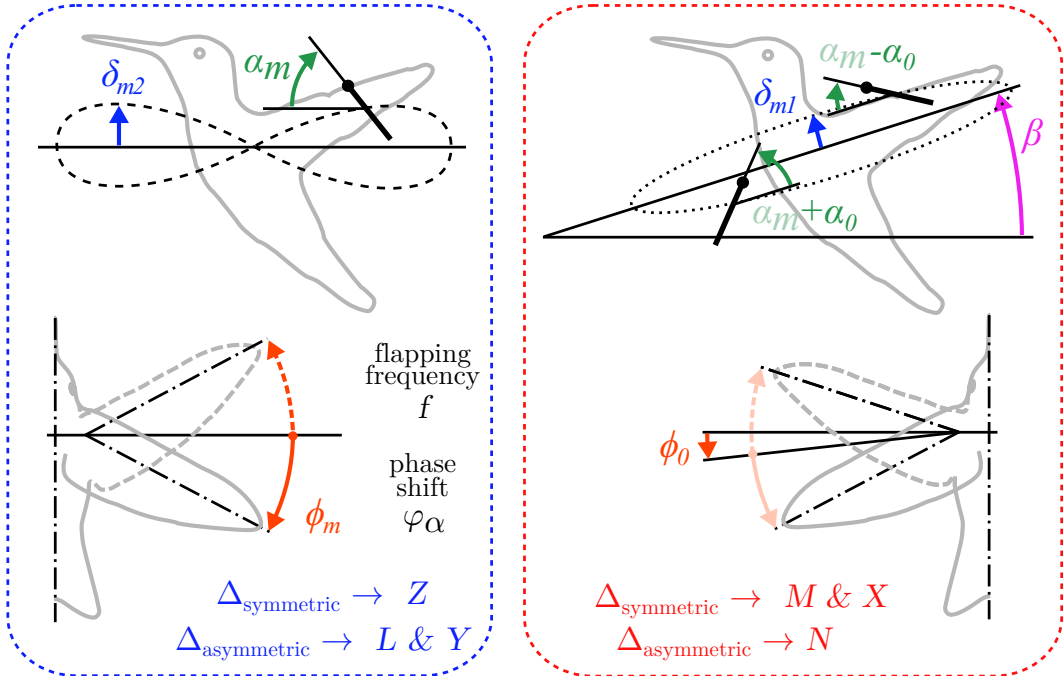


**Figure 5.15:** Wing kinematics parameters, split into two groups according to their effect on the cycle averaged forces: parameters affecting  $Z$ ,  $L$  and  $Y$  (left) and  $M$ ,  $X$  and  $N$  (right).

### 5.2.2 Choice of control parameters

In the MAV design the number of parameters needed for control needs to be minimized. The matrices (5.11) and (5.13) show that two parameters modified symmetrically and two modified asymmetrically are sufficient to generate independently the four control forces/moments  $Z$ ,  $L$ ,  $M$  and  $N$ . While this leaves no control of the "parasite" forces  $X$  and  $Y$ , it allows a simpler design of the MAV wing motion control mechanism. Another two parameters, one symmetric and one asymmetric, would be necessary to assure that  $X$  and  $Y$  is zero.

For the selected 4 parameters ( $p_{S1}$  controlling  $Z$ ,  $p_{S2}$  controlling  $M$ ,  $p_{A1}$  controlling  $L$  and  $p_{A2}$  controlling  $N$ ) the control derivatives matrix reduces to  $\mathbf{J}_{\text{red}}$  and the control force and moments can be expressed as

$$\begin{bmatrix} Z \\ M \\ L \\ N \end{bmatrix} = \mathbf{J}_{\text{red}} \begin{bmatrix} \Delta p_{S1} \\ \Delta p_{S2} \\ \Delta p_{A1} \\ \Delta p_{A2} \end{bmatrix} = \begin{bmatrix} Z_{p_{S1}} & 0 & 0 & 0 \\ 0 & 0 & L_{p_{A1}} & 0 \\ 0 & M_{p_{S2}} & 0 & 0 \\ 0 & 0 & 0 & N_{p_{A2}} \end{bmatrix} \begin{bmatrix} \Delta p_{S1} \\ \Delta p_{S2} \\ \Delta p_{A1} \\ \Delta p_{A2} \end{bmatrix}. \quad (5.14)$$

The relationship shows that the control system is, in theory, fully decoupled. Finally, the control force and moments are transformed into the wing kinematic parameters as

$$[\Delta p_{S1}, \Delta p_{S2}, \Delta p_{A1}, \Delta p_{A2}]^T = \mathbf{J}_{red}^{-1}[X, L, M, N]^T. \quad (5.15)$$

There are many possible choices of the control parameters set. Since the effect on  $X$  and  $Y$  forces is ignored, a successful control is not guaranteed. Thus, the control performance of each selected combination needs to be tested in a non-linear simulation. Finally, the choice of the control parameters is heavily constrained by the design feasibility of the wing motion control mechanism.

Because the designed MAV is powered by a DC motor, the flapping frequency can be controlled easily. It was chosen as the symmetric parameter controlling the vertical force  $Z$ . The choice of the remaining parameters reflects the control mechanism that will be presented in Section 7.2 and is sketched in Figure 5.16. The roll moment  $L$  is controlled by asymmetric modulation of the flapping amplitude  $\phi_m$ , the pitch moment  $M$  by symmetric modulation of the mean wing position (offset)  $\phi_0$  and the yaw moment by asymmetric modulation of the offset  $\phi_0$ .

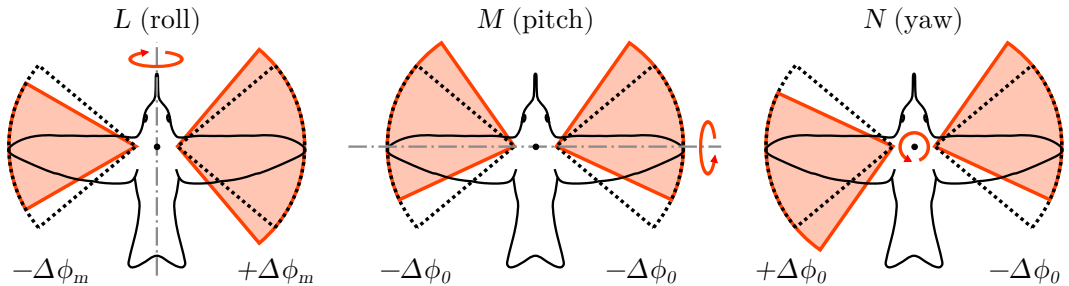


**Figure 5.16:** Control moments generated through wing kinematics parameters  $\phi_m$  and  $\phi_0$ .

### 5.3 Simulation results

Figure 5.17 shows the control scheme with the full, non-linear model that has been implemented in Matlab/Simulink. The model includes the non-linear aerodynamics and body dynamics from Chapter 3. A moving average over the last wingbeat is used to remove the periodic oscillation due to flapping from the feedback. To test the controller performance, a trajectory with step commands in all four controlled DOFs (velocities  $u, v, w$ , angular velocity  $r$ ) was used. First a step input was applied successively on each DOF, one at a time, to show the control performance with the coupling effects of the rest of the nonlinear system. Then, the step input was applied to all the 4 DOFs at once to reveal any control cross-coupling effects and evaluate

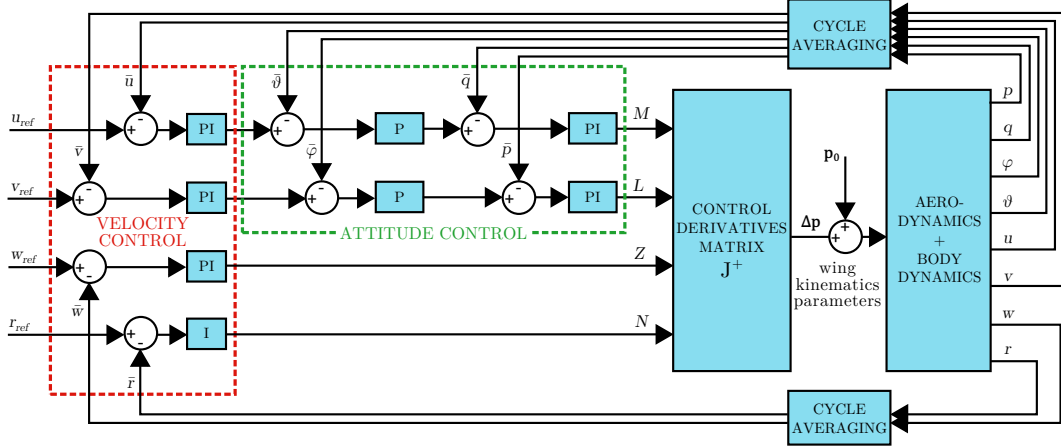


**Figure 5.17:** Cascade control of the full non-linear system.

the potential decrease of control performance. The control commands were set to 0.1 m/s and 10°/s for the linear and angular velocities, respectively, representing slow flight around hovering.

The simulation results are shown in Figure 5.18 where the green solid lines represent the full non-linear model, the black dotted lines the linearised model and the red dashed lines the command. Unlike in the linearised model, there exists small coupling between the pitch and vertical dynamics and between the roll and yaw dynamics in the non-linear model. Nevertheless, the longitudinal (pitch + vertical dynamics) and lateral (roll + yaw dynamics) systems stay independent.

The high frequency oscillation in the longitudinal DOFs ( $u, w, \vartheta$ ) of the non-linear system is caused by the periodic aerodynamic forces due to the wing flapping. The mean values, however, are closely following the linear results. In the lateral DOFs ( $v, r, \varphi$ ) the oscillation appears only when the left and right wing kinematics or flow conditions differ. It is in particular pronounced during the lateral motion, where an asymmetrically varying wing drag induces high yaw oscillation (see Figure 4.13). Yet again, the non-linear system response is reasonably close to the linearised model.

The time behaviour of the control parameters (Figure 5.19) shows that the necessary changes in the wing kinematics are very small. The vertical flight controller varies the flapping frequency  $f$  by approximately ±2 Hz. The lateral flight control requires changes of flapping amplitude  $\phi_m$  by only ±0.5°. The wing offset  $\phi_0$  is used for both longitudinal flight and yaw control. While variation of ±1.5° is enough for longitudinal speed control, up to ±4° is required for yaw rotation. This is in

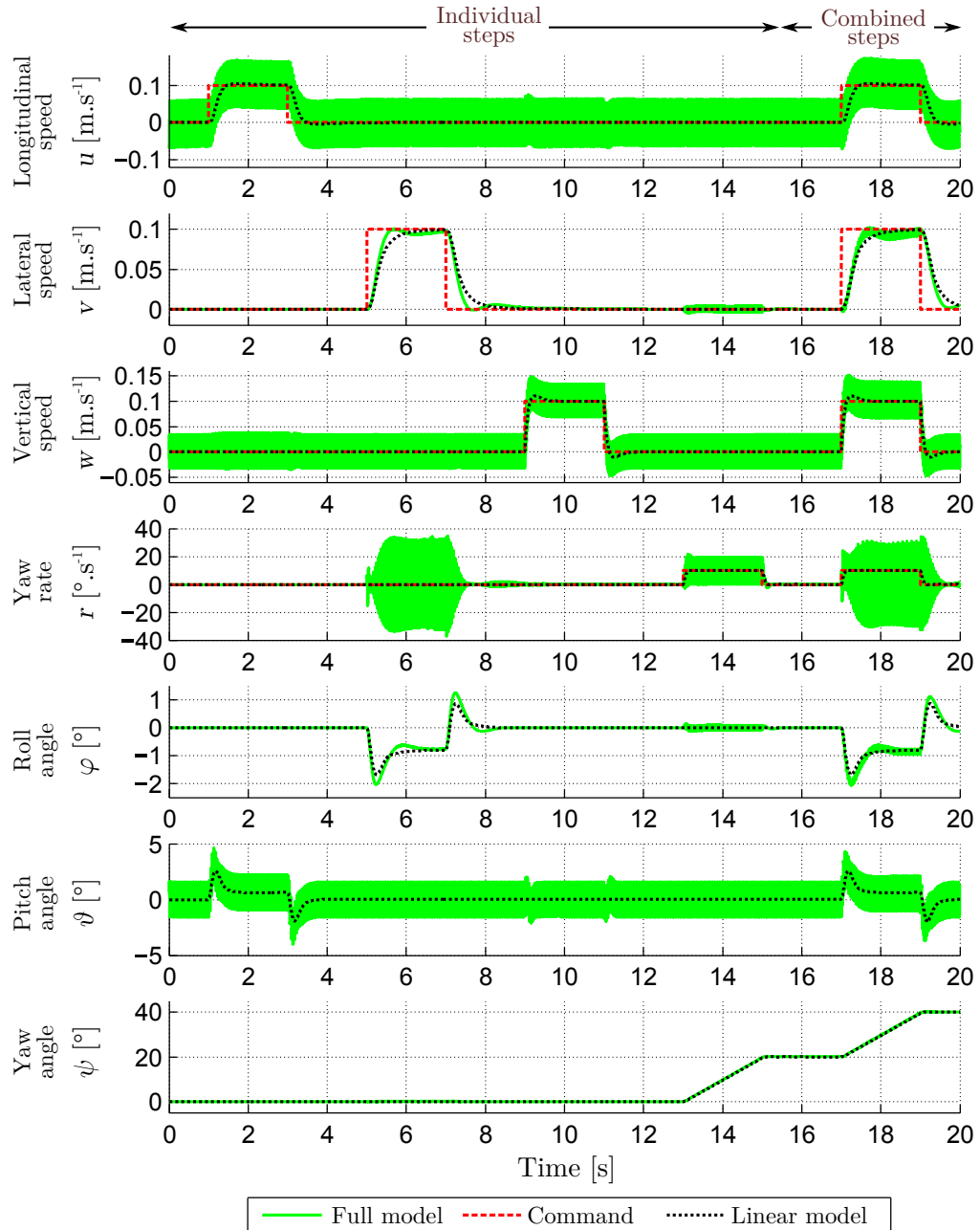


**Figure 5.18:** Simulation results: response to a sequence of step inputs and a combined step in the 4 controlled DOFs ( $u$ ,  $v$ ,  $w$  and  $r$ ). Comparison of the full, non-linear model with the cycle-averaged linearised model.

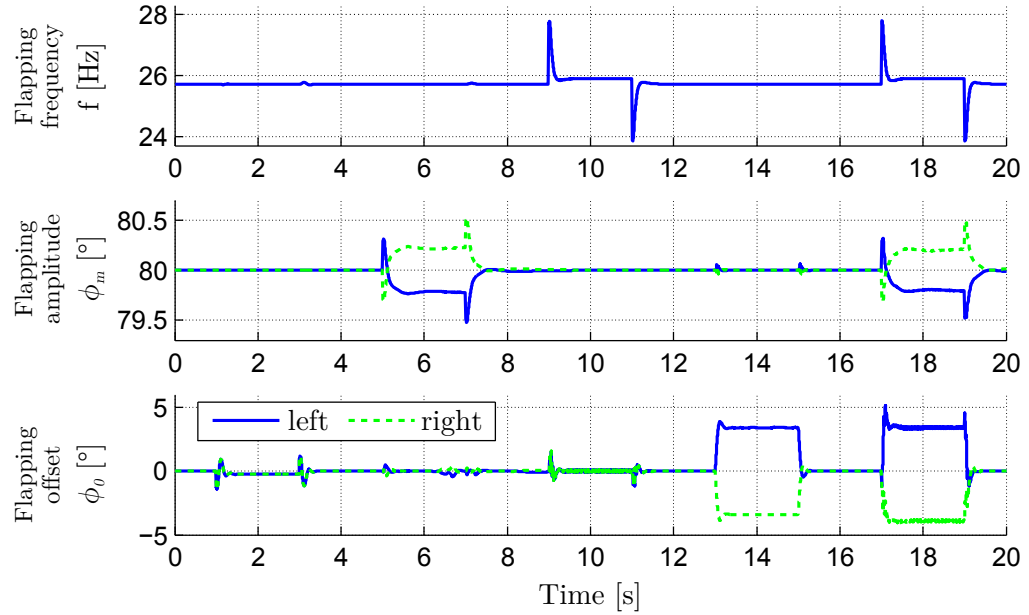


**Figure 5.19:** Simulation results: wing kinematic parameters controlling the flight during the test sequence in Figure 5.18.

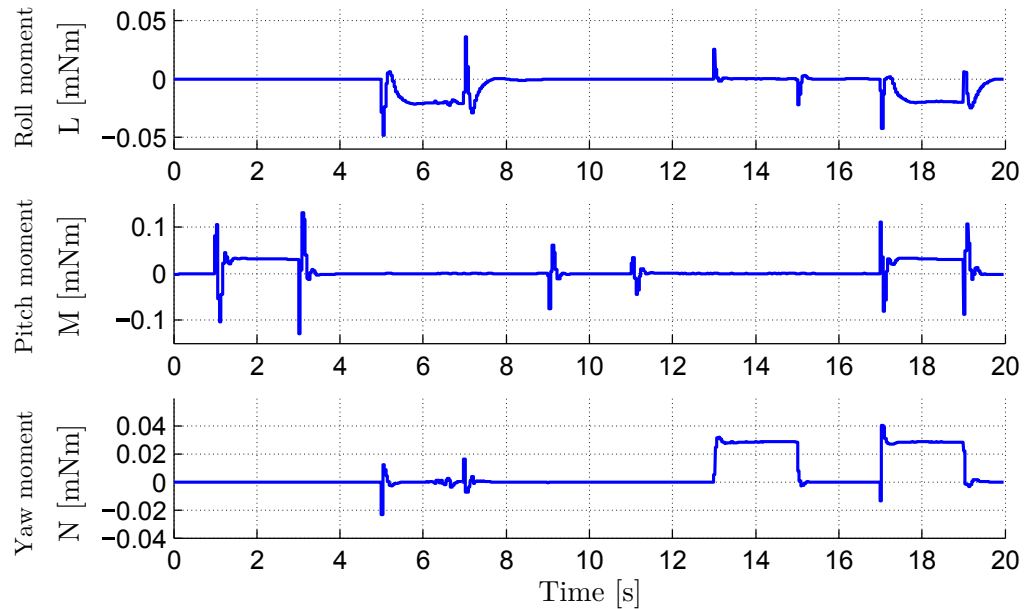


**Figure 5.20:** Simulation results: estimates of cycle averaged control moments generated by the wings during the test sequence in Figure 5.18.

accordance with the control derivatives matrix (5.13), which shows that the effect of  $\phi_0$  on yaw moment  $N$  is relatively low. A more effective parameter for yaw control could be chosen, but a solution using the same parameter for both pitch and roll was preferred as it reduces the MAV design complexity. No significant change in the overall performance is observed in the combined command and also the wing kinematics parameters remain in a similar range.

Figure 5.20 displays the control moments generated by the wings with the modified wing kinematics. They were obtained by averaging the wing aerodynamic efforts over each flapping cycle while removing the component due to aerodynamic damping (estimated by the linearised model). Their maximum absolute values are  $|L|_{max} \approx 0.05$  mNm (roll),  $|M|_{max} \approx 0.13$  mNm (pitch) and  $|N|_{max} \approx 0.04$  mNm (yaw).

## 5.4 Conclusion

The controller of near-hover flapping flight presented in this chapter can stabilize and control the flight in 4 DOF by altering 4 parameters: the flapping frequency, the difference between the left and right wing flapping amplitude and, independently, the left and right wing offset. The controller was tuned for the linearised, cycle-averaged model. Its performance was tested in a non-linear simulation that showed good agreement between the two models. The study provides an initial estimate of the necessary wing kinematics changes as well as of control moments these changes should generate. A prototype designed based on these results will be presented in the following chapters.

## 5.5 References

- S. Chung and M. Dorothy. Neurobiologically inspired control of engineered flapping flight. *Journal of Guidance, Control, and Dynamics*, 33(2):440–453, 2010.
- X. Deng, L. Schenato, and S. Sastry. Flapping flight for biomimetic robotic insects: part II-flight control design. *IEEE Transactions on Robotics*, 22(4):789–803, Aug. 2006a. doi:10.1109/TRO.2006.875483.
- X. Deng, L. Schenato, W. C. Wu, and S. S. Sastry. Flapping flight for biomimetic robotic insects: part I-system modeling. *IEEE Transactions on Robotics*, 22(4):776–788, Aug. 2006b. doi:10.1109/TRO.2006.875480.
- D. B. Doman, M. W. Oppenheimer, and D. O. Sigthorsson. Wingbeat shape modulation for flapping-wing micro-air-vehicle control during hover. *Journal of Guidance, Control, and Dynamics*, 33(3):724–739, 2010. doi:10.2514/1.47146.

- G. F. Franklin, J. Powel, and A. Emami-Naeini. *Feedback Control of Dynamic Systems*. Prentice Hall, 4th edition, 2002.
- S. B. Fuller, M. Karpelson, A. Censi, K. Y. Ma, and R. J. Wood. Controlling free flight of a robotic fly using an onboard vision sensor inspired by insect ocelli. *Journal of The Royal Society Interface*, 11(97), 2014. doi:10.1098/rsif.2014.0281.
- K. Y. Ma, P. Chirarattananon, S. B. Fuller, and R. J. Wood. Controlled flight of a biologically inspired, insect-scale robot. *Science*, 340:603–607, 2013. doi:10.1126/science.1231806.
- N. Michael, D. Mellinger, Q. Lindsey, and V. Kumar. The GRASP Multiple Micro UAV Testbed. *IEEE Robotics and Automation*, 17(3):56–65, 2010. doi:10.1109/MRA.2010.937855.
- T. Rakotomamonjy, M. Ouladsine, and T. L. Moing. Longitudinal modelling and control of a flapping-wing micro aerial vehicle. *Control engineering practice*, 18 (7):679–690, Jul. 2010. doi:10.1016/j.conengprac.2010.02.002.
- H. Rifai, J.-F. Guerrero-Castellanos, N. Marchand, and G. Poulin. Bounded attitude control of a flapping wing micro aerial vehicle using direct sensors measurements. In *2009 IEEE International Conference on Robotics and Automation, Kobe, Japan*, pages 3644–3650. 2009 IEEE International Conference on Robotics and Automation, Kobe, Japan, 2009.



# Chapter 6

## Flapping mechanism

While the theoretical basis of the hovering flapping flight has been introduced in the previous text, the remaining chapters are dedicated to the robotic hummingbird design. Our project aims at a tail-less flapping wing MAV with a wingspan of around 20 cm and a mass around 20 g. This chapter presents the development of an uncontrolled robot prototype generating the lift force, consisting of a flapping mechanism and a pair of wings. Details are given on its design as well as on conducted experiments that lead to a successful tethered take-off demonstration.

### 6.1 Flapping mechanism concept

The lift production is crucial for any air vehicle. The designed hummingbird-like robot generates the lift by flapping its wings. They need to be driven at a frequency that is high enough to counteract the gravity and stay airborne. There are many ways how to obtain the flapping motion - the design of the transmission mechanism depends strongly on the actuator choice. The vast majority of existing MAV designs employed rotary electric motors (e.g. de Croon et al., 2009; Keenon et al., 2012). However, other actuators were also used, including piezo-actuators (Wood, 2008), SMA actuators (Furst et al., 2013), magnetic actuators (Vanneste et al., 2011) and even combustion engines (Zdunich et al., 2007).

In this project an electric DC motor was chosen for three main reasons:

1. There is a relatively wide choice of electric motors in the 2 g to 7 g range (10 % to 35 % of expected total weight).
2. DC motors can be directly powered by off-the-shelf speed controllers and Li-Po batteries.

3. The motors should have enough power to lift our robot as they are being used in Radio Controlled (RC) helicopters and multicopters of similar sizes and weights.

Employing a rotary actuator requires a transmission mechanism that transforms the rotating motion into the flapping motion of the wings. A linkage mechanism has been developed for this purpose. It consists of two stages: a slider crank based mechanism that generates a rocker motion of (low) amplitude  $\Psi$ , and a four-bar linkage that amplifies the motion to the desired amplitude of  $\Phi = 120^\circ$  (Figure 6.1). While a single stage mechanism could also be used to achieve such an amplitude, the speed profile of the resulting motion would not be symmetric. Also, such a mechanism would operate close to its singular positions, which in reality could result in mechanism blocking due to compliance and backlashes. The advantage of using two stages is that the asymmetries coming from individual stages can be compensated by an appropriate choice of dimensions and at the same time mechanism singularities can be further away from the working range.

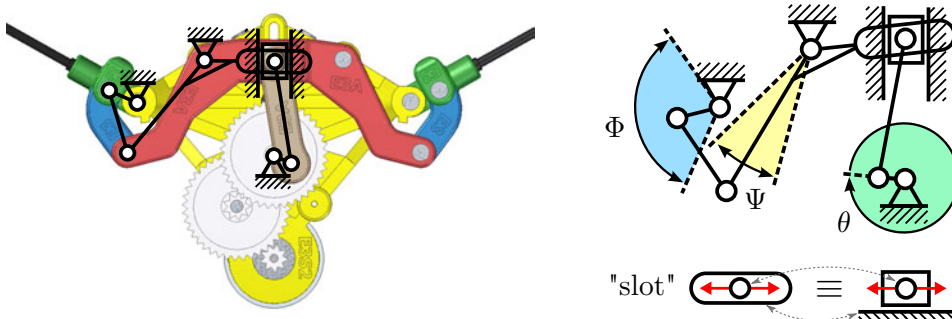


**Figure 6.1:** The flapping mechanism is composed of two stages: slider crank with a rocker producing oscillating motion and a four-bar mechanism for motion amplification. Mechanism model (left) and scheme displaying the motor input  $\theta$ , intermediate amplitude  $\Psi$  and flapping amplitude  $\Phi$  at the output (right).

### 6.1.1 Kinematics

The kinematics of the proposed mechanism can be treated separately for each mechanism stage. Using the notation of Figure 6.2 the kinematics of the first stage can be expressed analytically as

$$\psi_3 = \arctan \left( \frac{A_1 - L_1 \cos \theta - \sqrt{L_2^2 - L_1^2 \sin^2 \theta}}{L_3} \right) + \frac{\pi}{2}, \quad (6.1)$$

where  $\theta$  is the input angle and  $\psi_3$  is the angle of the intermediary link 3-4. The analytic solution of the second (amplification) stage is a classical solution of a four bar mechanism

$$\phi = \arctan\left(\frac{a}{b}\right) - \arccos\left(\frac{c}{\sqrt{a^2 + b^2}}\right), \quad (6.2)$$

where

$$\begin{aligned} a &= -2L_4L_6 \sin(\psi_3 - \alpha_{34}) \\ b &= 2A_2L_6 - 2L_4L_6 \cos(\psi_3 - \alpha_{34}) \\ c &= L_5^2 - A_2^2 - L_4^2 - L_6^2 + 2A_2L_4 \cos(\psi_3 - \alpha_{34}). \end{aligned} \quad (6.3)$$

The dimensions were optimized numerically by minimizing a cost function, which consisted of a difference from the desired amplitude and a difference between upstroke and downstroke velocity profiles; the final dimensions are in Table 6.1. The relationship of the output angle  $\phi$  on the input angle  $\theta$  is very close to a harmonic function (Figure 6.3).

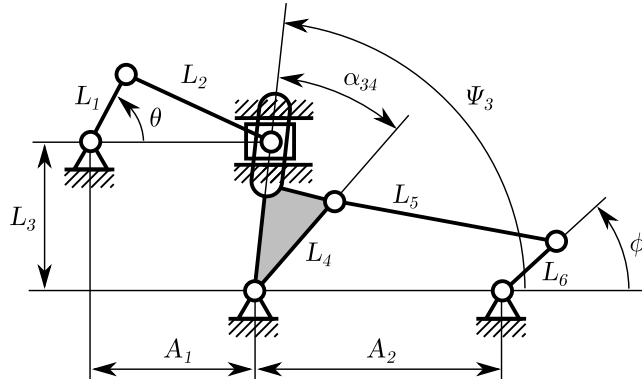


**Figure 6.2:** Kinematic scheme of the flapping mechanism.

$L_1$	$L_2$	$L_3$	$L_4$	$L_5$	$L_6$	$A_1$	$A_2$	$\alpha_{34}$
2.25	12.00	8.00	14.00	7.53	3.57	11.00	-9.20	-70

**Table 6.1:** Mechanism dimensions (lengths in mm, angles in °)

The final structure of the flapping mechanism was rearranged (compared to Figure 6.2) to minimize the overall mechanism dimensions. The mutual orientation of the two stages was adapted as is shown in Figure 6.1 and the wing bar was connected

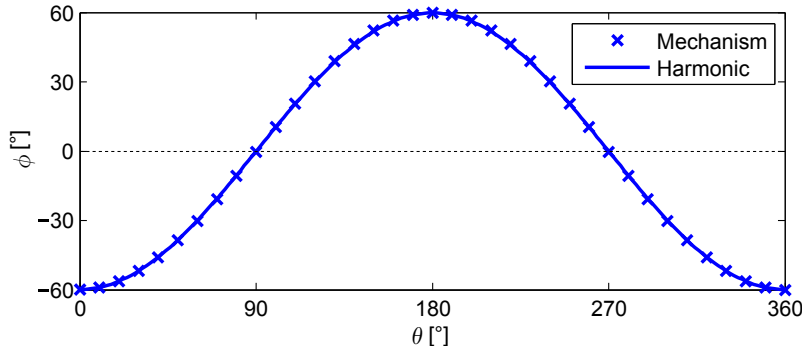


**Figure 6.3:** Kinematics of the flapping mechanism compared to a harmonic function.

to the output link at an angle so that the mean wing position is parallel with the lateral body axis.

### 6.1.2 Mechanism design

The design of the flapping mechanism has undergone a lot of development. Some of the prototype versions are listed in Table 6.2 and displayed in Figure 6.4. The frame and the links are all 3D printed. Several technologies (FDM, SLS, PolyJet) and various materials were tested. Finally, the PolyJet technology was chosen because the parts do not require any further processing thanks to its fine resolution ( $42 \mu\text{m}$  in xy,  $16 \mu\text{m}$  in z - Objet Eden series). The originally used material, DurusWhite, was replaced by the Digital ABS composite photo-polymer, which is considerably stronger. The links are connected together and to the frame by steel and aluminium rivets.

The first mechanism generations (A to E) were designed for bench tests. They were easy to repair in case of a failure as all the links were accessible. However, the position of the motor was not ideal for flight because the COG of the system was not on the axis between the shoulders. Moving the motor above the mechanism in later generations (G to J) allowed its placement exactly in the centre. Although this solution is more complex, harder to repair and means an extra penalty in weight, the frame is stronger and the wing shoulders are more robust thanks to ball bearings (version G) or brass bearings (version J) that were integrated into the shoulder design. On top of that, this configuration allows a relatively easy access to the mechanism from below, which is necessary for control mechanism implementation (Chapter 7).

Several DC motors of diameters between 6 mm and 8.5 mm were used to drive the mechanism, see Table 6.3. The majority of them are brushed pager motors adopted

Ver.	Date	Material	Motor <sup>a</sup>	Motor Weight [g]	Mechanism Weight [g]	Total Weight [g]	Max. Lift [g]	Wing Length [mm]	Flapping Frequency [Hz]
<b>A</b>	2/2012	FDM ABS	A-6	1.77	3.43	5.2	-	-	-
<b>C2</b>	5/2012	DurusWhite	A-6	1.77	4.03	5.8	6.4	70	21.1
<b>E2</b>	10/2012	DurusWhite	D-7	2.78	4.72	7.5	9.6	70	23.5
<b>E4</b>	1/2014	Digital ABS	F-8	5.20	4.90	10.1	16.1	90	26.2
<b>G2</b>	4/2013	DurusWhite	A-7	2.69	6.28	9.0	9.6	70	24.5
<b>J2</b>	1/2014	Digital ABS	F-8	5.20	7.30	12.5	16	90	23.8

Table 6.2: Evolution of the flapping mechanism. <sup>a</sup>See Table 6.3 for motor details.

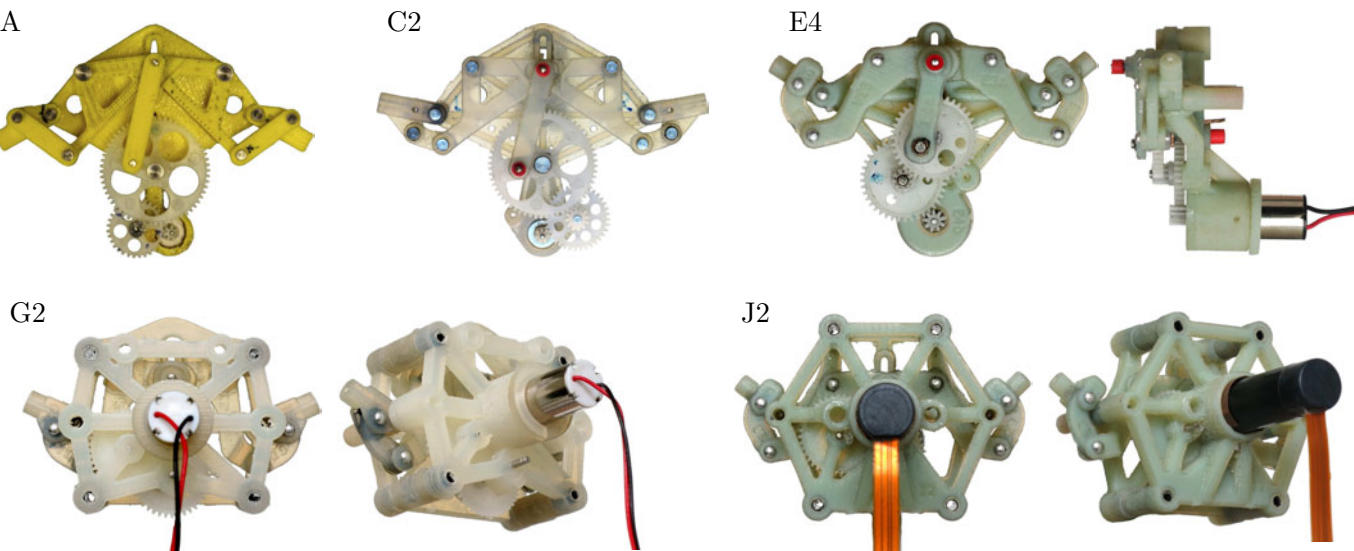


Figure 6.4: Evolution of the flapping mechanism - generations A (2/2012) to J (1/2014).

by RC modellers (BR DC), but professional brushless motors (BL DC) were also successfully used. The factors limiting the maximal speed of small DC motors are usually the temperature (the motor is heated by current and friction) and, in case of brushed motors, the wear of the brushes. It is the latter case that also limits the lifetime of the brushed motors.

The highest lift was obtained with the 8mm BL DC from Faulhaber. Its advantage is that the performance remains constant over time, but it needs to be driven by a speed controller whose stock version (SC 1801P) is too large and heavy (23 mm x 32 mm, 3.6 g). Thus, a smaller and lighter speed controller needs to be either found on the market or developed to use this motor in flight. An alternative motor, giving nearly the same performance, is the 8.5 mm BR DC from AEO-RC. The performance, however, decreases with time as the motor heats up. The motor lasts only about 5 minutes when operated at the maximal flapping frequency before its brushes wear out. Currently, the BL motor is used for bench tests and the BR motor for take-off demonstrations.

A two stage gearbox is used to reduce the motor speed. The limited space requires that gears with a small module of 0.3 mm are used. The choice of the reduction ratio was limited by the gears available on the market. The final gearbox consists of a 9t pinion, 40t/9t double spur gear and 40t spur gear giving a reduction ratio of approximately 19.75:1. A custom built gear set with a gear ratio optimized for the load and motor characteristic combination is being considered.

An exploded view of the most recent flapping mechanism (version J) is shown in Figure 6.5. Its weight, without the motor, is 7.3 g.

### 6.1.3 Wing design

The design of the wings is inspired by the Nano Hummingbird (Keenon et al., 2012) and by the DelFly (de Croon et al., 2009). The wing is made of a thin flat membrane. It has two sleeves, one on the leading edge and one on the root edge (close to the body), that accommodate the leading edge and root edge CFRP (carbon-fibre-reinforced polymer) bars. Since the angle between the sleeves is greater than the angle between the bars the wing becomes cambered and twisted after the assembly (Figure 6.6). The camber is bistable - it flips passively from one side to another depending on the direction of motion, as can be seen in Figure 6.7.

The wings are hand built - a reasonable accuracy and repeatability is achieved by printing the desired shape on a sheet of paper that is attached under the membrane

Motor	Type	$m$ [g]	$D$ [mm]	$L$ [mm]	$k_V$ [rpm/V]	$R$ [ $\Omega$ ]	$P_{max}^+$ [W]
A-6 BR*	AE0-RC GPS6	1.77	6	14	13000	2.8	1.2
A-7 BR*	AE0-RC GPS7	2.69	7	16	11000	2.1	1.5
A-8 BR*	AE0-RC EPS8	4.85	8.5	20	12600	0.7	2.5
D-7 BR*	Didel MK07-1.7	2.78	7	17	11000	2.1	1.6
F-8 BL	Faulhaber 0824-006B	5.20	8	24	5753	3.1	> 2.5

**Table 6.3:** DC motors used along the project. BR = brushed motor, BL = brushless motor. All motors have output shaft of 1 mm in diameter. \*No data-sheets provided, parameters estimated experimentally. <sup>+</sup>Maximal output power achieved during experiments with flapping prototype E4 without motor overheating (approximate values).

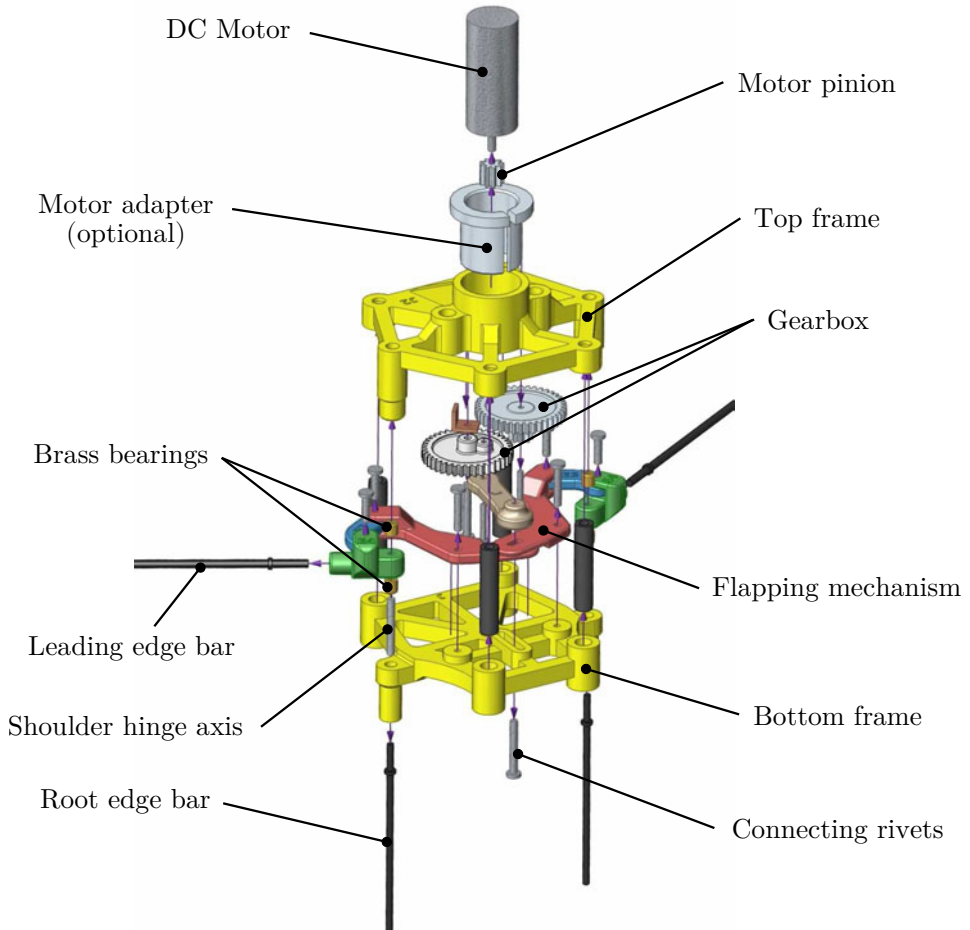


**Figure 6.5:** Exploded view of the flapping mechanism J2.

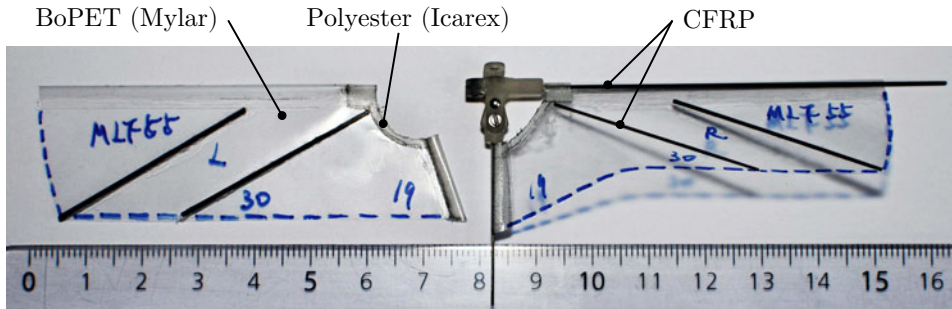


**Figure 6.6:** Polyester film wing becomes cambered after assembly.

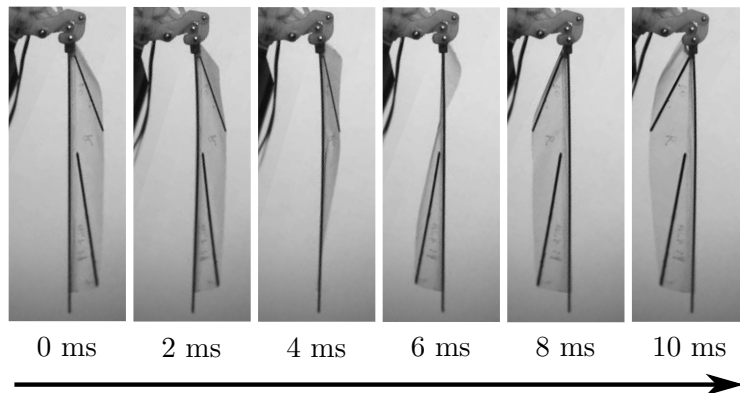


**Figure 6.7:** High speed camera sequence of a wing flipping at the stroke reversal (top view) while flapping at 15 Hz. The whole sequence represents about 15 % of the flapping cycle.

and used as a template for cutting. The best results (in terms of lift and durability) were obtained with a 15 micron thick polyester film. 1 mm x 0.12 mm CFRP bands are used as stiffeners. The sleeves at the leading edge and at the root edge are reinforced with Icarex to increase their durability. They allow an easy assembly and disassembly as well as free rotation around the 0.8 mm leading edge and 0.5 mm root edge CFRP bars.

In the early prototypes the whole wing frame, including the leading edge and root edge bars, was mobile, as displayed in Figure 6.8 (left). An adapted version of this solution has an adjustable angle between the leading edge and root edge bars (Figure 6.8 centre) and is used to find an optimal angle between the sleeves. Finally the design was simplified and the mass being moved reduced by fixing the root bar directly to the frame, making it coincident with the wing shoulder axis (Figure 6.8 right).

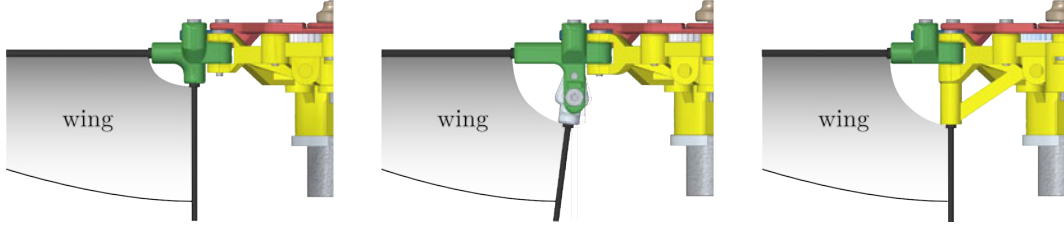


**Figure 6.8:** Different solutions of the wing frame: mobile root bar (left), mobile root bar with adjustable angle (center), fixed root bar (right).

## 6.2 Experiments

Many tests were carried out throughout the development process. While the main goal was to maximize the generated lift force by mechanism and wing design optimisations, mechanism reliability and wing robustness were also important factors. A high speed camera (Photron FASTCAM SA3, resolution 1024 x 1024 pixels) was used to observe the wing behaviour throughout the cycle and to track the mechanism and wing kinematics. The generated forces were measured on a custom built force balance.

### 6.2.1 Wing kinematics

While the flapping mechanism was designed for a nominal flapping amplitude  $\Phi_0 = 120^\circ$ , the amplitude will increase with frequency due to compliance of the wing bars and of the mechanism itself. The high speed camera was employed to quantify these

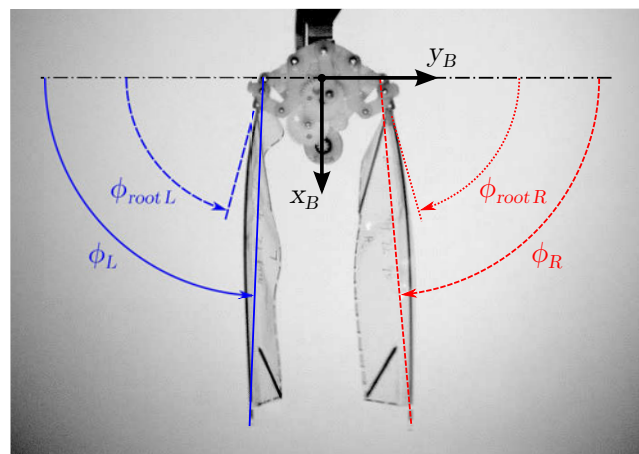


**Figure 6.9:** Definition of the tracked angles.

effects as well as to identify any imperfections compared to the mechanism theoretical kinematics.

The sweep angle was tracked at the wing root ( $\phi_{root}$ ) and at the wing tip ( $\phi_{tip}$ , see Figure 6.9). The camera was set to record at 2000 fps with a shutter speed of 10 000 fps to remove any motion blur. The amplitude was subsequently calculated as  $\Phi = \phi_{max} - \phi_{min}$  and offset as  $\phi_0 = (\phi_{max} + \phi_{min})/2$ , where  $\phi_{max}$  and  $\phi_{min}$  are the maximal and minimal observed angles  $\phi$ , respectively.

Figure 6.10 shows the traces of wing angles of prototype E4 over two wingbeats at a flapping frequency of 25Hz. The increase of the tracked flapping amplitude compared to the theoretical model is significant. The amplitude measured at the wing roots includes the effect of backlashes in the linkage mechanism as well as the compliance of its links. The compliance of the leading edge bars results into a further amplification of the amplitude, measured at the wing tip. It can be observed that the bars flex in particular during the stroke reversal when the accelerations are high. Thus, the sweep angle at the wing tip becomes more triangular compared to the theoretical, nearly harmonic curve.

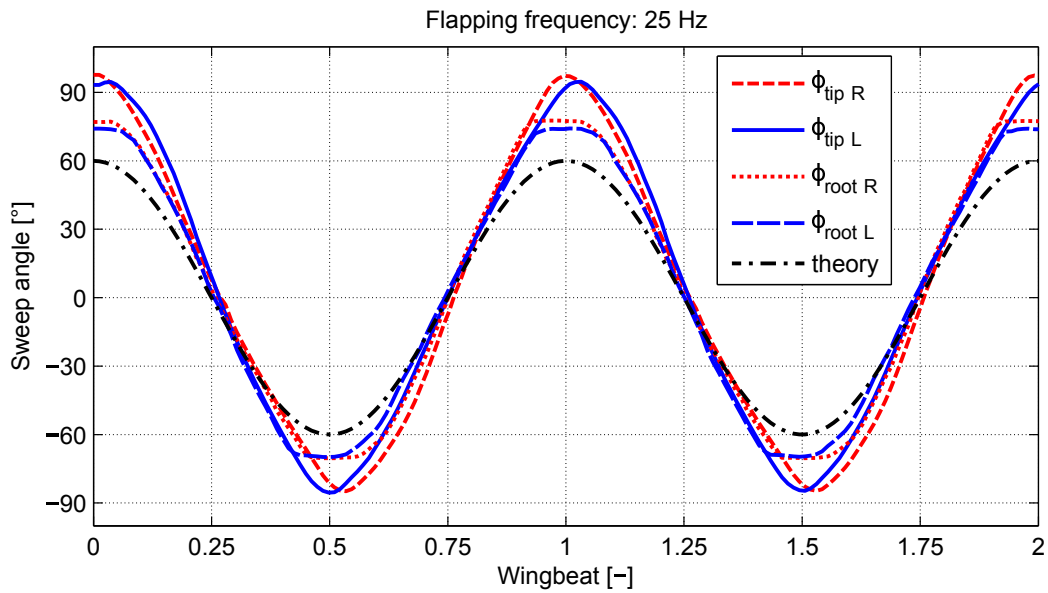


**Figure 6.10:** Tracked wing kinematics of prototype E4 at  $f = 25$  Hz. Left wing traces are in blue, right wing traces in red. The sweep angle was measured at the wing tip ( $\phi_{tip}$ ) and at the output of the mechanism ( $\phi_{root}$ ). Black dash-dotted line represents the theoretical kinematics, without compliance and backlashes.

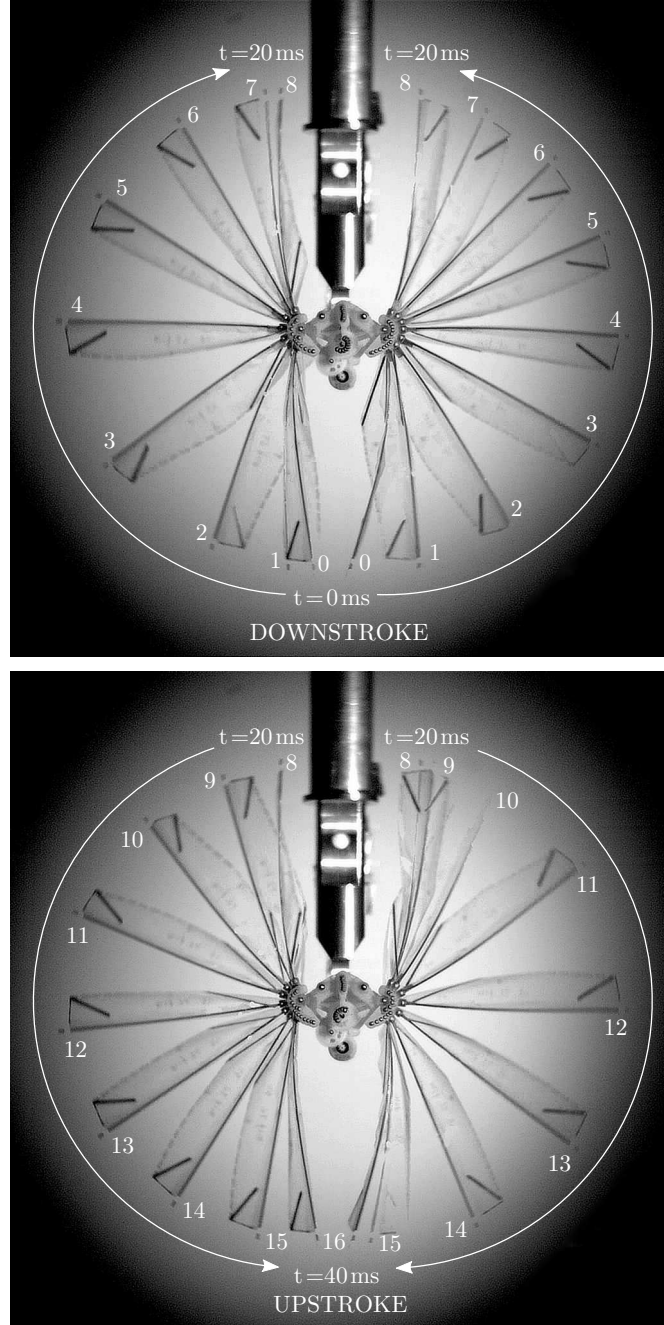


**Figure 6.11:** High speed camera measurement: the image displays the wings every 2.5 ms over one complete cycle at 25 Hz. The sequence is split into the downstroke (frames 0 → 8, top) and the upstroke (frames 8 → 16, bottom).

The small differences in the left and right wing amplitudes are caused by the mechanism imperfections. There is, however, a small difference in the timing of the wing reversal, which is an inherent property coming from the design of the joints between the slider crank stage and the amplification stages. The right wing reverses before the left wing when behind the body ( $\phi > 0$ ), while the opposite happens in front of the body ( $\phi < 0$ ). This can produce a small oscillation around the yaw axis, nevertheless, the effects should average out over one wingbeat.

A composite image of high speed camera frame sequence showing the wing positions every 2.5 ms over the full wingbeat is shown in Figure 6.11. We can observe the leading edge bar deformation close to the reversal, the differences between upstroke and downstroke of left and right wing as well as the positions of mechanism joints throughout the wingbeat.

The relationship between the flapping amplitude and offset and the flapping frequency is displayed in Figure 6.12. For the measured range of frequencies (15 to 25 Hz) the mechanism amplitude increases from above 140° to almost 150°. The increase of the wing tip amplitude is more significant, from below 160° to almost 180°. As will be shown in Section 6.2.3, this can be considered as beneficial, because an increase of flapping amplitude means a lower frequency is needed to take off and a lower frequency means lower accelerations and lower inertial forces on the mechanism links.

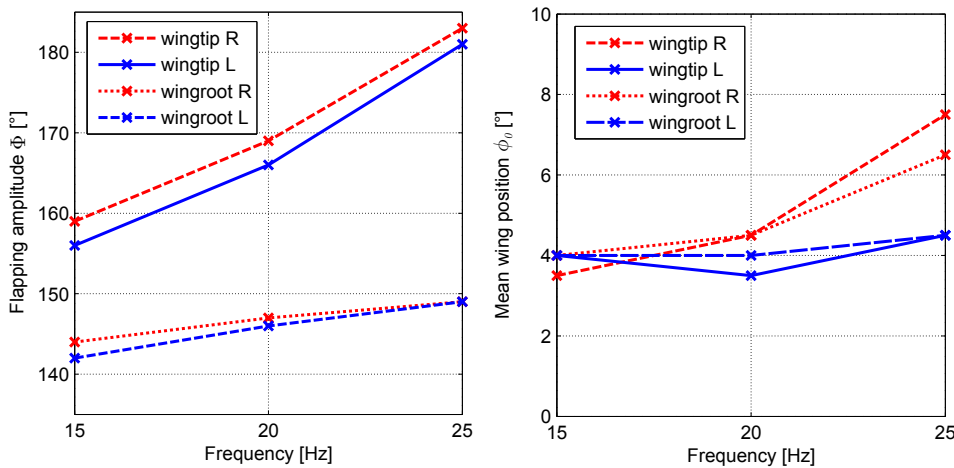


**Figure 6.12:** The tracked flapping amplitude (left) and offset (right) as a function of flapping frequency. Results measured for prototype E4.

The offset remains slightly positive and nearly constant in the studied range (around  $4^\circ$  on the left and between  $4^\circ$  and  $7^\circ$  on the right wing); there is almost no difference between the wing roots and tips. The small non-zero offset does not represent a major problem. The generated pitch moment can be compensated by a small shift of the prototype COG.

### 6.2.2 Force balance

Measuring the efforts of a flapping wing robot is a challenging task. The generated forces are relatively small (order of 0.01 N) which requires high sensitivity. On top of that these efforts are of a periodic nature where not only the flapping frequency but also the higher harmonics are present. Hence the sensor should have a high resonance frequency.

The most frequently used commercial 6DOF force-torque sensor in the flapping wing research is the Nano17 Titanium (ATI, 2014). It is the only sensor on the market that is compact and has a high sensitivity to forces (resolution up to  $1/682 \text{ N} \approx 0.15 \text{ g}$ ) and moments (resolution up to  $3/364 \text{ mNm} \approx 0.008 \text{ mNm}$ ) while keeping a high resonance frequency in all DOFs (3 kHz). However, its price was well above the project budget so a decision was made to build a custom force balance. To keep the design simple the balance should be able to measure only lift  $Z$  and pitch moment  $M$ . Moreover, only the cycle averaged efforts were of our primary interest.

In the past we already used a precision pocket scale to evaluate the mean lift with acceptable results. The sensors used in the scales are usually double beam cantilevers with strain gages in full bridge configuration. Their advantage is that they are insensitive to the axial force as well as to the bending moment. The experimentally determined resonance frequency of a sensor extracted from one of the scales was 210 Hz, roughly 8 times the flapping frequency of the robot prototype. That is not enough to measure the time histories within one flapping cycle, but sufficient to evaluate the cycle averaged values. Thus these sensors were selected as inexpensive yet reasonably precise base components for the designed force balance.

The balance uses two of these single axis force sensors in a configuration that is shown in Figure 6.13. Applying lift  $F_L$ , drag  $F_D$  and moment  $M$  on the balance results in the following sensor forces

$$\begin{aligned} S_1 &= (F_D H - M)/B - F_L/2 \\ S_2 &= (M - F_D H)/B - F_L/2 \\ R_x &= -F_D. \end{aligned} \tag{6.4}$$

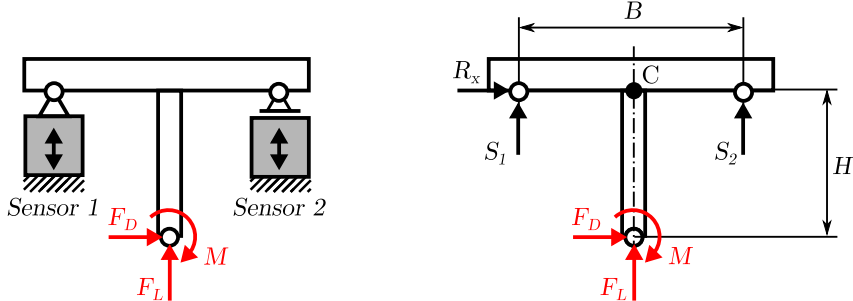


**Figure 6.13:** Schematics of the force balance (left) and its free body diagram (right).

Originally a third sensor was used to measure the drag force  $F_D$ . However, the first tests showed that the cycle averaged drag force was very low and its effect on the moment was negligible. Thus the third sensor has been dismounted for the measurements presented here. This allows to mount the robot closer to the rotation joints, which increases the resonant frequency of the whole system. The moment at the robot COG,  $M$ , is approximated by the moment at the centre between the two rotation joints,  $M_C$ . The measured efforts can be expressed as

$$\begin{aligned} F_L &= -S_1 - S_2 \\ M_C &= M - F_D H = (S_2 - S_1)B/2. \end{aligned} \quad (6.5)$$

The sensitivity of sensors 1 and 2 to the moment can be tuned by the selection of distance  $B$  between the two sensor joints. It was set to 50 mm, giving a good sensitivity yet enough space in between to fix the robot prototype. For small distance  $H$  and small cycle averaged drag force  $F_D$  the moment  $M_C$  is a good approximation of the true moment  $M$ , with an error that can be expressed from equation (6.5). This has no effect on the lift force precision.

The assembled force balance is shown in Figure 6.14. Each sensor is connected to a custom build electronic circuit that provides stabilized power to the bridge and amplifies the bridge output. The sensors have been calibrated one at a time. The rotational joints in the system should have as little friction as possible. The joint on the left is constructed as a blade inside a groove. The joint is held together by a magnetic force of a NdFeB cylindrical magnet that attracts the blade inside the groove. Both the blade and the groove are from soft magnetic steel. The joint on the right is built in a similar manner. Since it should also allow displacement to the sides to have an isostatic system, the blade was replaced by a steel ball that is touching a flat steel plate. Since the contact of the spherical ball and flat plate is only in one point, another magnet was attached on the top to increase the attractive force.

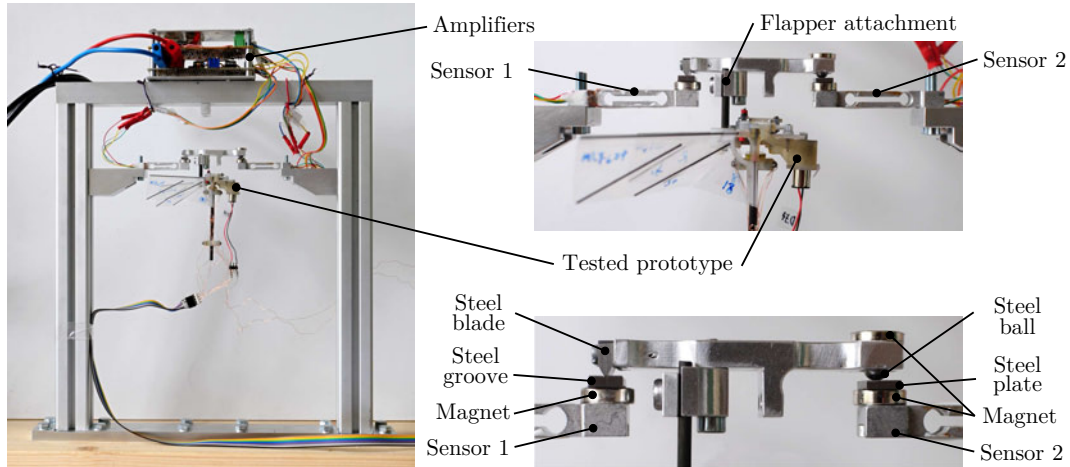


**Figure 6.14:** Force balance overview and detail views on sensors and magnetic joints

The force balance signals are processed with a dSpace 1103 digital signal processor, together with the voltage and current readings of the DC motor. The flapping frequency can be detected from the motor current, because the motor torque is constantly changing due to the periodic aerodynamic and inertial forces. Nevertheless, the setup is also equipped with an optional infrared barrier providing a trigger signal at every wing pass. In case of the brushless DC the frequency is calculated from the signals of Hall sensors, which are integrated in the motor.

The measured resonant frequency of the balance is 173 Hz for lift and 297 Hz for pitch moment (Figure 6.15). As expected, this is too low to measure detailed force and moment traces over a flapping cycle, but the system provides enough bandwidth to evaluate the cycle averages for the expected flapping frequencies (below 30 Hz).

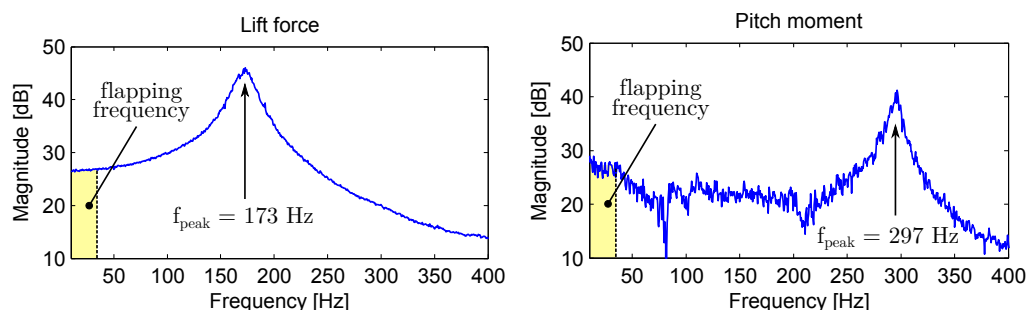


**Figure 6.15:** Force balance: measured frequency response gain magnitude of lift (left) and moment (right) showing the resonance frequencies.

The averaging is done online and is always calculated over a finite number of cycles. The averaging interval can be adjusted and was set to 3 seconds for the measurements presented here. The other readings (voltage, current, frequency) are averaged in the same way. The repeatability of the lift measurements is good, with a typical standard deviation below 1 mN. We observe a bigger dispersion in the moment measurements, where a typical standard deviation is 0.05 mNm. This includes random effects coming from both the measurement and processing system and from the tested prototypes.

### 6.2.3 Lift production

The mean lift force of flapping wings can be approximated by the classical theory for a fixed wing in steady flow while employing cycle-averaged quantities. A flat and rigid wing is assumed and, for simplicity, the centre of pressure is placed at the mid-length  $R_{CP} = R/2$ . When a wing flaps at a frequency  $f$  with an amplitude  $\Phi = 2\phi_m$  its CP moves with a mean velocity

$$\bar{U}_{CP} = 2\Phi f R_{CP} = \Phi f R. \quad (6.6)$$

Then, the cycle averaged lift force of a pair of wings can be written as

$$\bar{F}_L = \frac{1}{2} \rho \bar{C}_L (2S) \bar{U}_{CP}^2 = \rho \bar{C}_L S (\Phi f R)^2, \quad (6.7)$$

where  $S$  is the surface of a single wing and  $\bar{C}_L$  is the mean lift coefficient that, if we accept the quasi-steady assumption, depends on the wing geometry and the angle of attack variation over one wingbeat. By including the definition of the wing aspect ratio  $\mathcal{A}R = 2R^2/S$  we can rewrite the expression to

$$\bar{F}_L = \frac{1}{2} \rho \bar{C}_L \mathcal{A}R (S\Phi f)^2. \quad (6.8)$$

Since the real wing is flexible it deforms more under higher aerodynamic loads at higher frequencies and the deformation affects also the angle of attack, so the coefficient  $\bar{C}_L$  is not likely to stay constant. Nevertheless, we see that the lift force should primarily vary with the wing lift coefficient, the aspect ratio and with the squares of wing surface, flapping amplitude and frequency. The validity of this simplified relation was studied experimentally and will be discussed in the following text.

### 6.2.4 Wing design optimization

Many wing designs were tested in order to find the size and shape producing the highest lift force. The parameters studied included the material of the wing (5, 10

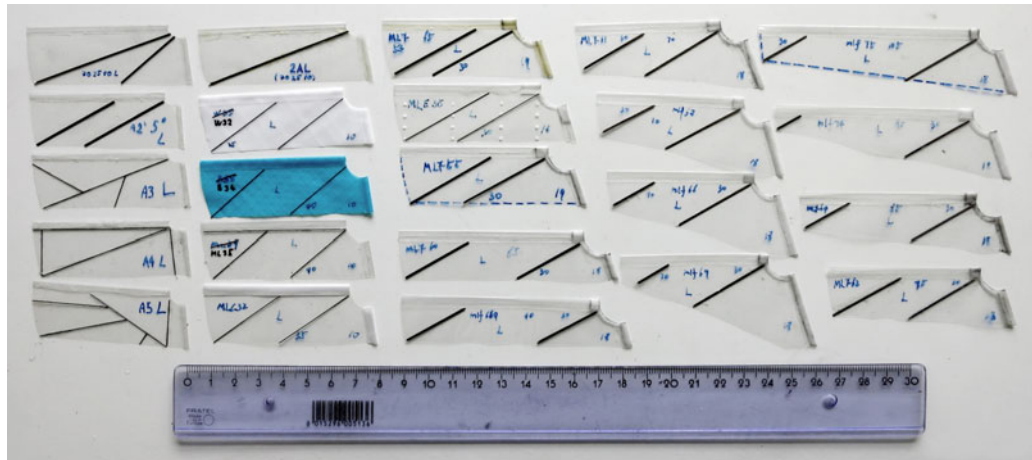


**Figure 6.16:** A sample of over 70 wing designs that were built and tested.

and 15 micron polyester film, Icarex, Chikara, ...), the stiffeners size and placement, the overall wing shape, the length  $L$ , the surface  $S$ , the aspect ratio  $\mathcal{A}$ , the taper or the angle between the sleeves  $\beta_W$ . Some of the tested designs are shown in Figure 6.16.

Several difficulties had to be faced during the experiments. The early prototypes suffered from short lifetime and performance variations due to wear. The same was true for the brushed motors used. As the flapping mechanism evolved, its reliability improved significantly and its performance got more constant over time. Using a quality brushless motor added further to a better consistency of the results.

Nevertheless, the lift force is always determined by the combination of the motor, the flapping mechanism and the wings. Any change in the whole chain of components resulted in a change of the maximal force. For these reasons results of each measurement set were related to the results of a nominal wing design (measured together with each set) rather than compared with absolute values of previous measurements.

Equation (6.8) showed that the mean lift force approximation depends on the wing geometry ( $\mathcal{R}, S^2, \bar{C}_L$ ) and also on the squares of flapping frequency  $f^2$  and amplitude  $\Phi^2$ . The flapping amplitude is determined by the flapping mechanism (although it can still be modified by the choice of the leading edge bars that flex while flapping), while the flapping frequency remains free. However, keeping it low was preferred in order to reduce the inertial effects in the flapping mechanism. This implies that wings with higher aspect ratio, higher surface and of course higher lift coefficients should be searched. Some examples of the conducted tests are given next.

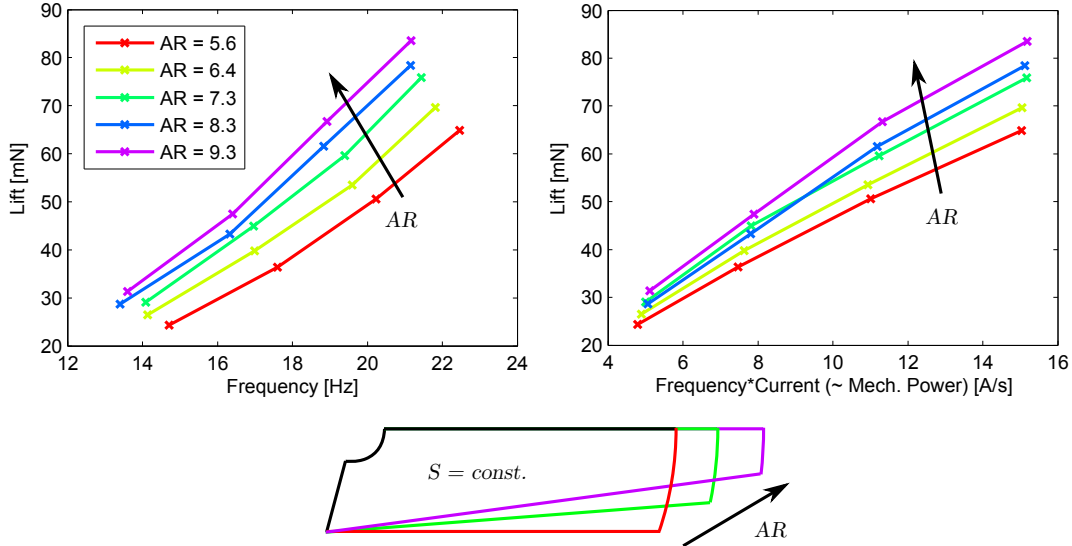


**Figure 6.17:** Lift force of wings with constant surface, but varying aspect ratio and taper (bottom), plotted against the flapping frequency (top-left) and against the motor current multiplied by the frequency (top-right) which can be related to the mechanical power driving the flapping mechanism. The tests were conducted with the prototype E4 and motor A-7.

Figure 6.17 displays the effect of the wing aspect ratio  $\mathcal{R}$  for wings with constant surface ( $S = 1750 \text{ mm}^2$ ). The wing length was being increased ( $R = 70 \rightarrow 90 \text{ mm}$ ) while decreasing the tip chord. The root chord was kept constant (25 mm) so the wing transformed from a rectangular towards a triangular shape. Figure 6.17 (top-left) shows the measured lift plotted against the flapping frequency. As predicted, the highest lift was produced with the highest aspect ratio wing, at any frequency.

The mechanical power on the motor output  $P_{\text{mech}}$  is defined as the output torque times the angular velocity of the output shaft,  $P_{\text{mech}} = T_m \omega_m$ . It represents the power consumption of the flapping mechanism and wings combination: it includes the effects of the wing drag, the gearbox efficiency, the mechanism inertia and friction, but excludes the motor itself. Because the torque on the motor output shaft  $T_m$  is proportional to the motor current  $I$ , the current multiplied by the flapping frequency  $f$  can be related to the motor output mechanical power that drives the flapping mechanism. Figure 6.17 (top-right) shows that the highest aspect ratio wing is also the most efficient, on the tested prototype, as it produces the highest lift per mechanical power unit.

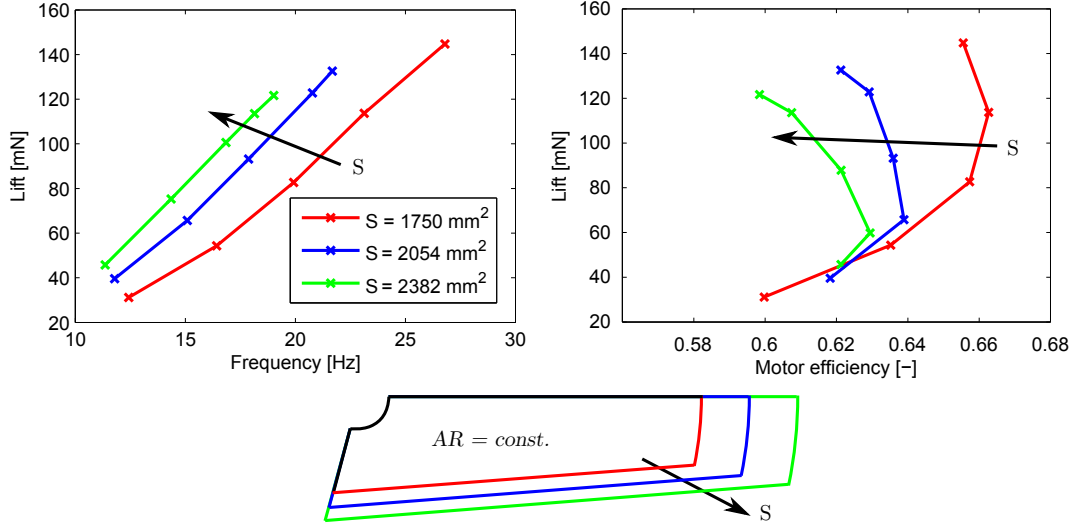


**Figure 6.18:** Lift force of wings with constant aspect ratio, but varying surface. The measured lift is plotted against the flapping frequency (top-left) and against the efficiency of the motor driving the flapping mechanism (top-right). The tests were terminated when the motor recommended heat limit was reached. The tests were conducted with the prototype E4 and motor F-8.

The effect of the wing area  $S$  on the lift force should be even more pronounced as it appears in the approximation in the second power. The experimental results for wings of constant aspect ratio ( $\mathcal{A}R = 9.3$ ) are shown in Figure 6.18. The surface was being increased while preserving the overall shape. Indeed, for a constant frequency, the highest lift was produced by the largest wing (Figure 6.18 top-left).

All the wings produce comparable amount of lift per mechanical watt. To include also the electric drive, the lift is this time plotted against the motor efficiency  $\eta_m$  defined as the ratio between the mechanical and electrical power

$$\eta_m = \frac{P_{mech}}{P_{el}} = \frac{T_m \omega_m}{UI}, \quad (6.9)$$

where  $U$  and  $I$  are the motor voltage and current, respectively. Figure 6.18 (top-right) shows that the most efficient wing with the used drive (BL DC Faulhaber 0824) is the smallest wing. On top of that, this allows to reach a higher mechanical power without a risk of motor overheating and thus also a higher absolute lift, although at a cost of increased flapping frequency. These results show that the wings need to be optimized for every new combination of motor and flapping mechanism in order to achieve maximal efficiency, which will be crucial for flight endurance.

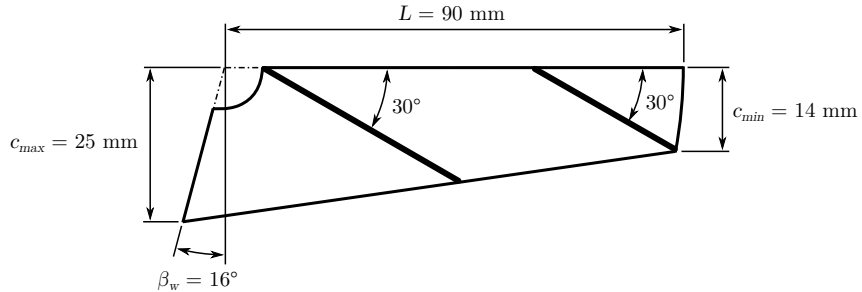


**Figure 6.19:** Shape and dimensions of the wing producing the highest lift. Its aspect ratio is  $\mathcal{R} = 9.3$ .

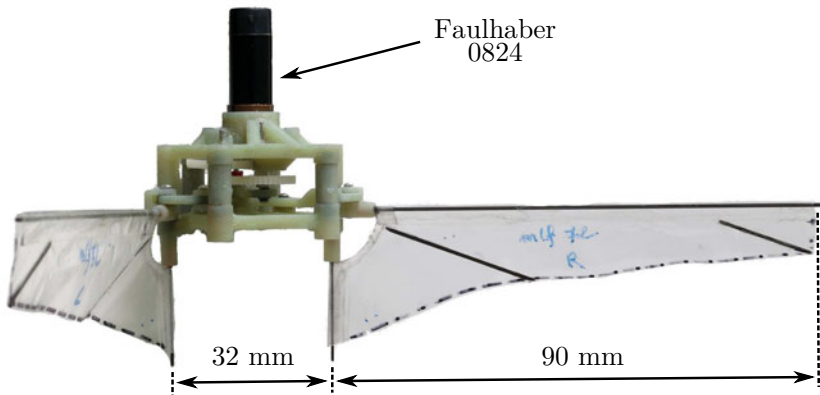


**Figure 6.20:** Prototype J2 with the best wing producing almost 160 mN of lift at 24 Hz.

It needs to be said that not all the tests were as conclusive as those presented here. The effects of the stiffeners placement were much more subtle. Some results would even contradict previous findings due to differences among the used motors and prototypes. Nevertheless, the experimental approach lead to a gradual lift increase.

The highest generated lift so far, almost  $160 \text{ mN} \approx 16 \text{ g}$ , was produced with the wings with dimensions shown in Figure 6.19 attached to the mechanism J2 driven by the 8 mm brushless motor F-8 (Figure 6.20). The measured lift curve is plotted in Figure 6.21. The grey dash-dotted line represents a trend-line assuming the lift force  $F_L$  is proportional to the second power of frequency  $f$ , while the lift coefficient  $\bar{C}_L$  and flapping amplitude  $\Phi$  in equation (6.8) remain constant. The real measured curve scales with slightly higher power, because the flapping amplitude also increases with frequency (see Figure 6.12) and the lift coefficient changes due to wing flexibility. Nevertheless, this shows that  $F_L \approx \text{const.} f^2$  can be used as a (conservative) rule of thumb when extrapolating the results.

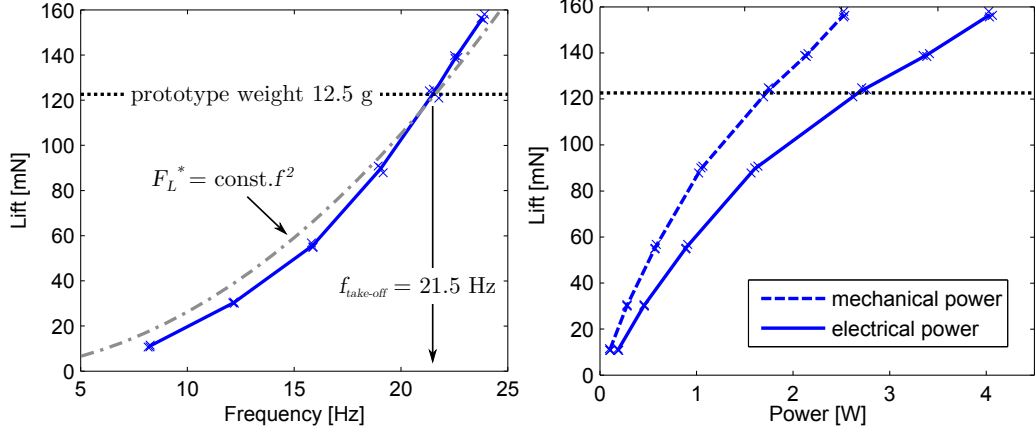


**Figure 6.21:** Measured lift of the best wing: relationship on the flapping frequency (left) and on the mechanical and electrical power of the motor (right). The black dotted line displays the prototype weight, grey dash-dotted line is a fitted curve assuming  $F_L = \text{const.}f^2$ . Individual measurements are plotted with crosses, the lines connect the average values.

The force necessary to lift the prototype weight (12.5 g) is displayed by the black dotted line, showing that the prototype would take-off around  $f = 21.5$  Hz. However, the power source is still off-board and the prototype lacks any control.

Due to the hovering flapping flight inherent instability, a take-off was demonstrated with a help of guide-wire that fixes the prototype attitude, but allows a free movement along the vertical axis as well as free yaw rotation (Figure 6.22). Older proto-

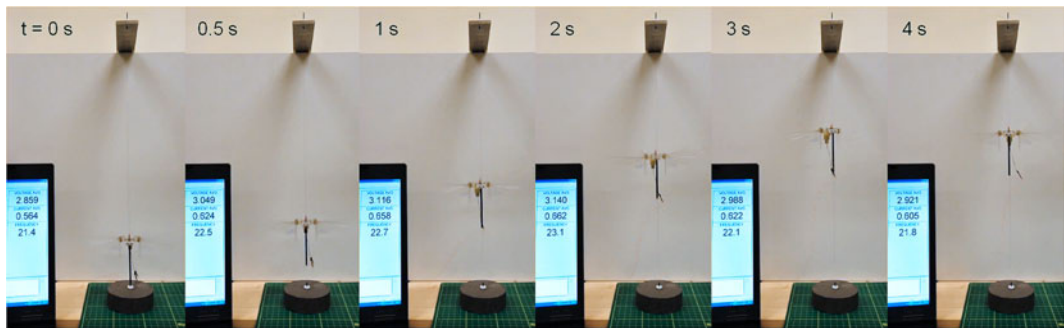


**Figure 6.22:** Take-off demonstration: a guide wire was used to stabilize the attitude of the uncontrolled prototype E4. Power was off-board, brought by 200 microns thin copper wires and controlled by hand to maintain a constant altitude after the take-off. Time of each frame is displayed in the upper left corner.

type E4 was used for this test, because it was easier to attach it to the guide wire. The power was still off-board and was brought by 200 microns thin copper wires. A control mechanism needed for active stabilization is being developed and will be described in the next chapter.

### 6.3 References

- ATI Industrial Automation. Nano17 titanium. [https://www.ati-ia.com/products/ft/ft\\_models.aspx?id=Nano17+Titanium](https://www.ati-ia.com/products/ft/ft_models.aspx?id=Nano17+Titanium), 2014. Accessed: 18/08/2014.
- G. de Croon, K. de Clerq, R. Ruijsink, B. Remes, and C. de Wagter. Design, aerodynamics, and vision-based control of the DelFly. *International Journal of Micro Air Vehicles*, 1(2):71–97, Jun. 2009. doi:10.1260/175682909789498288.
- S. J. Furst, G. Bunget, and S. Seelecke. Design and fabrication of a bat-inspired flapping-flight platform using shape memory alloy muscles and joints. *Smart Materials and Structures*, 22(1):014011, 2013. doi:10.1088/0964-1726/22/1/014011.
- M. T. Keenon, K. R. Klingebiel, H. Won, and A. Andriukov. Development of the nano hummingbird: A tailless flapping wing micro air vehicle. *AIAA paper 2012-0588*, pages 1–24, 2012.
- T. Vanneste, A. Bontemps, X. Q. Bao, S. Grondel, J.-B. Paquet, and E. Cattan. Polymer-based flapping-wing robotic insects: Progresses in wing fabrication, conception and simulation. In *ASME 2011 International Mechanical Engineering Congress and Exposition*, pages 771–778. American Society of Mechanical Engineers, 2011.
- R. J. Wood. The first takeoff of a biologically inspired at-scale robotic insect. *IEEE Transactions on Robotics*, 24(2):341–347, Apr. 2008. doi:10.1109/TRO.2008.916997.
- P. Zdunich, D. Bilyk, M. MacMaster, D. Loewen, J. DeLaurier, R. Kornbluh, T. Low, S. Stanford, and D. Holeman. Development and testing of the Mentor flapping-wing micro air vehicle. *Journal of Aircraft*, 44(5):1701–1711, 2007.

# Chapter 7

## Control mechanism

The primary role of the flapping wings is the thrust production. In a tail-less design the wings have a second, yet equally important, role: the active flight stabilization and control. To stabilize the body attitude and to steer, the wings need to generate moments around the three body axes: roll moment  $L$  around  $x_B$ , pitch moment  $M$  around  $y_B$  and yaw moment  $N$  around  $z_B$  axis.

To produce the control moments the robot needs to be able to modulate the mean lift and drag forces of each wing independently and also to control the placement of the cycle-averaged lift force with respect to the centre of gravity, see Figure 7.1. In such case the roll moment can be generated through a difference between the mean lift force of the left and of the right wing. The pitch moment can be produced by placing the mean lift force of both wings in front of or behind the centre of gravity. Finally, the yaw moment can be generated by a difference between the mean drag of the left and of the right wing.

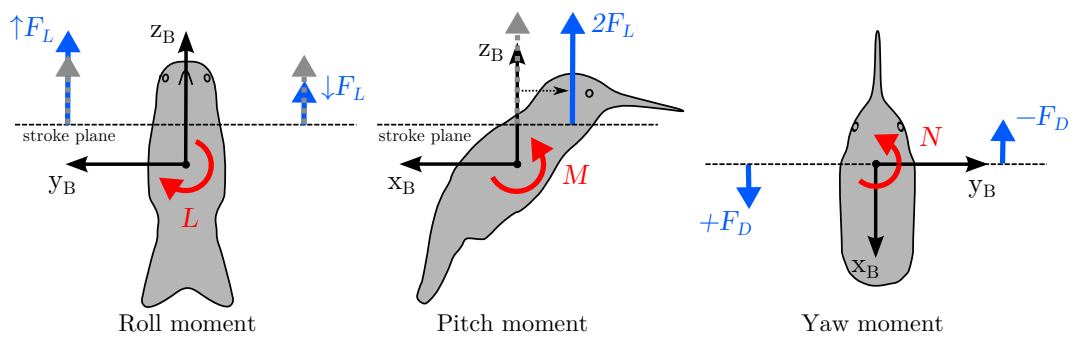


**Figure 7.1:** Principle of control moment generation.  $F_L$  and  $F_D$  are cycle averaged lift and drag forces, respectively, generated by a single wing.

Two possible solutions of the control mechanism, published in (Karasek et al., 2013, 2014), are presented in the following text. The first is based on the wing twist modulation according to Keenon et al. (2012). The second generates the necessary moments by modulating the wing flapping amplitude and offset (mean position), a strategy similar to Ma et al. (2013) and Truong et al. (2014).

## 7.1 Moment generation via wing twist modulation

The wing design presented in Section 6.1.3 consists of a membrane attached between the leading edge and root edge bars. At rest the membrane is slightly loose. The wing becomes cambered and twisted when moved due to a pressure difference. For a wing with specifically optimized geometry (Figure 7.2 left), the lift force can be increased by moving the root bar away from the membrane (membrane is stretched,  $\gamma > 0$ ) and decreased by moving it towards the membrane (membrane is loosened,  $\gamma < 0$  in Figure 7.2 right). This concept is used in the Nano Hummingbird and is called the Variable Wing Twist Modulation (Keenon et al., 2012).

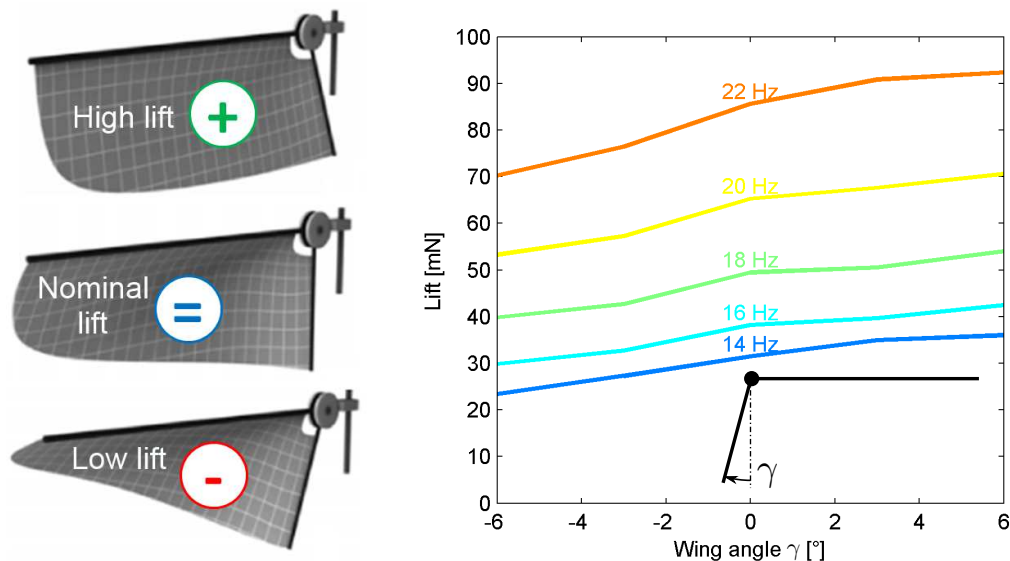


**Figure 7.2:** Wing twist modulation principle adapted from Keenon et al. (2012) (left) and measurement of lift as a function of angle  $\gamma$  for various flapping frequencies (right).

### 7.1.1 Moment generation principle

If the root bars are attached to the body frame and are displaced with respect to the frame the angle  $\gamma$  will not stay constant during the wingbeat. It will vary with the wing position given by the sweep angle  $\phi$ . Thanks to that not only the mean lift force but also its position can be controlled.

If the root bar end is displaced backwards the  $\gamma$  angle is negative (and the lift is reduced) when the wing is behind the body, but  $\gamma$  is positive (and the lift is increased) when in front of the body. If both left and right wing root bars are displaced in the same sense this results into a nose up pitch moment (Figure 7.3). If the root bars are displaced in the opposite sense a yaw moment is generated because the drag forces are also affected.

Lateral displacement of the root bars is used to generate a roll moment (Figure 7.4). A displacement of one of the bars towards the body causes a positive  $\gamma$  and thus a lift increase compared to the other wing, whose root bar is moved away from the body, which results into a lift reduction.

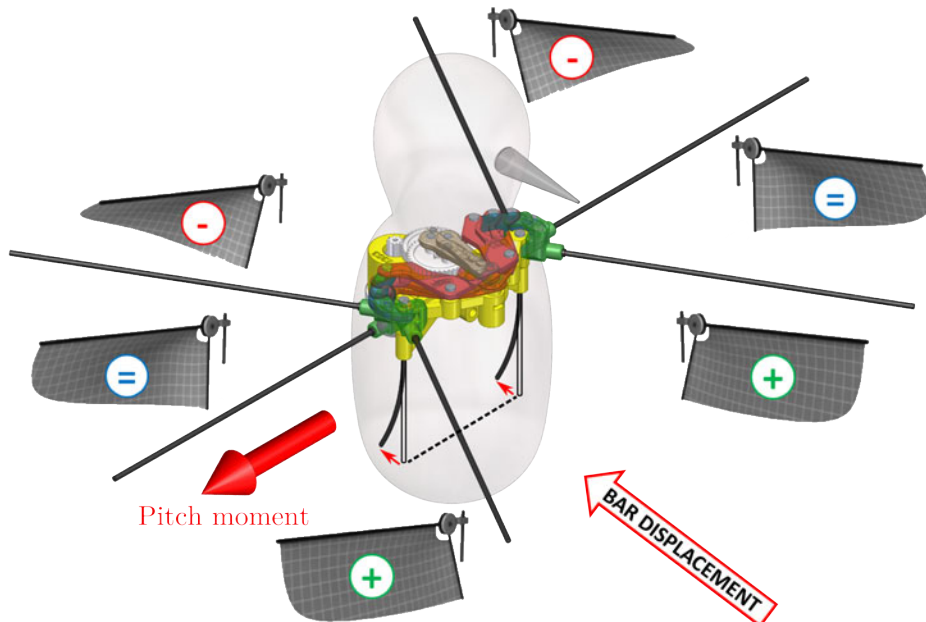


**Figure 7.3:** Pitch moment generation via wing twist modulation: displacing the bars longitudinally creates a front-back lift asymmetry.

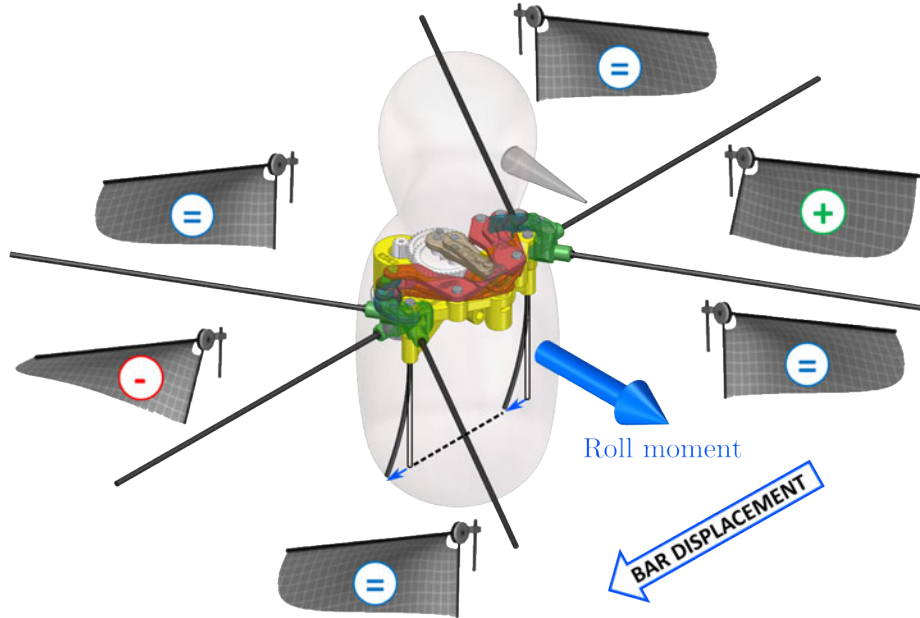


**Figure 7.4:** Roll moment generation via wing twist modulation: displacing the bars laterally creates a left-right lift asymmetry.

### 7.1.2 Manually operated control mechanism performance

To test the concept a plastic plate with a regular grid of holes was fixed below the flapping mechanism. The root bar ends could be manually placed and fixed in any of the equally spaced holes (Figure 7.5). Instead of a universal joint, which would give the root bars the necessary 2DOFs, flexible CFRP bars clamped in the body frame were used. This simplified the design substantially as no joints were necessary.

The bar ends were fixed in 5 positions at  $0$ ,  $\pm 2$  and  $\pm 4$  mm, measured from the central position where the root bars are straight. The fixing plate was 32 mm below the leading edge bars. The measurements were carried out at constant motor voltages (2, 2.5, 3 and 3.5 V) and repeated 3 times for each position.

The results for the pitch moment are plotted in Figure 7.6. The individual measurements are plotted as crosses, the lines represent the average values. The bar deformation has a negligible effect on the average lift force. The modulation of moment is approximately linear, but we can observe slightly different trend in the positive and negative directions. This might be caused by the asymmetric wing design where the stiffeners are glued only on one of the faces. When operating at

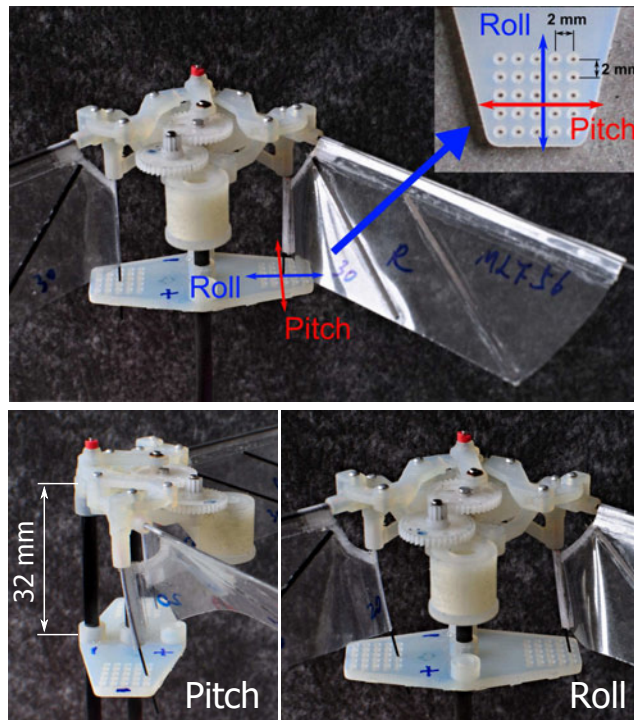


**Figure 7.5:** Testing prototype allowing fixing the bar ends in a grid of holes: hover position (top), pitch command (bottom-left) and roll command (bottom-right).

3.5 V, displacing the bars by  $\pm 4$  mm generates a pitch moment between -0.59 mNm and 0.5 mNm.

While our force balance cannot measure the roll moment, it was possible to estimate it indirectly (Figure 7.7). The roll moment is generated by increasing the lift force of one wing (by moving the root bar end towards the body) and decreasing the lift force of the other wing (by moving the bar end away from the body); the total lift should remain nearly constant. If both bars are moved symmetrically (e.g. towards the body) the roll moment is zero, but the total lift will change. Thus, the relationship between the bar deformation and the lift force can be evaluated and used to estimate the roll moment for asymmetric bar deformations.

The measured relationship between the total lift and the symmetric bar deformation is shown in Figure 7.7 a). Ideally, this relationship should be linear, however, the measurement shows a maximum at -2 mm and the lift starts to drop again for lower values. The linearity could be improved by a modified wing design.

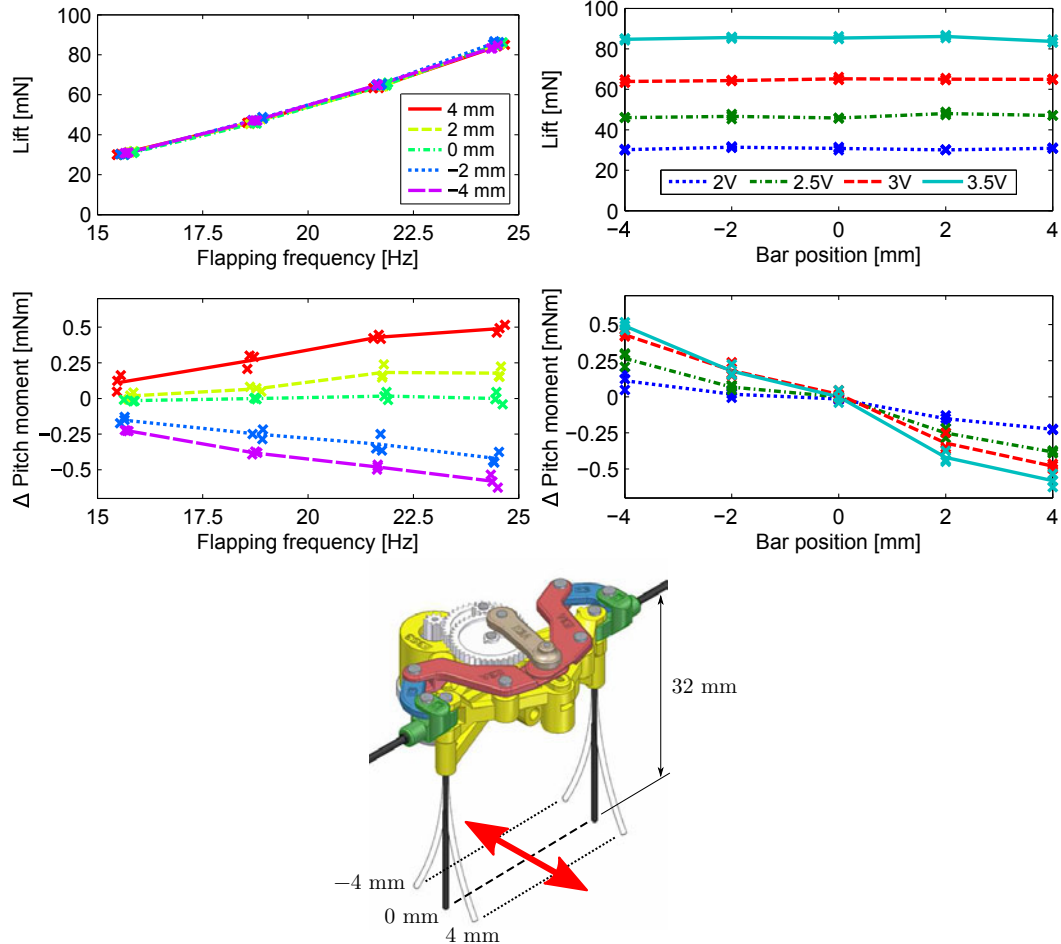


**Figure 7.6:** Lift and pitch moment at various positions of root bar ends. The bars were displaced manually.

The roll moment is estimated from the lift difference between positive and negative wing bar positions. The results, together with the estimated total lift, are plotted in Figure 7.7 c). The total lift decreases slightly with increasing absolute value of roll moment due to the nonlinear relation between the bar deformation and lift force mentioned earlier. The modulation of the roll moment is approximately linear (for higher motor voltages), although a small moment decrease can be observed in the extremities, again due the nonlinearity. At 3.5 V, a roll moment of  $\pm 0.43$  mNm is estimated for the maximal bar displacement of  $\pm 4$  mm.

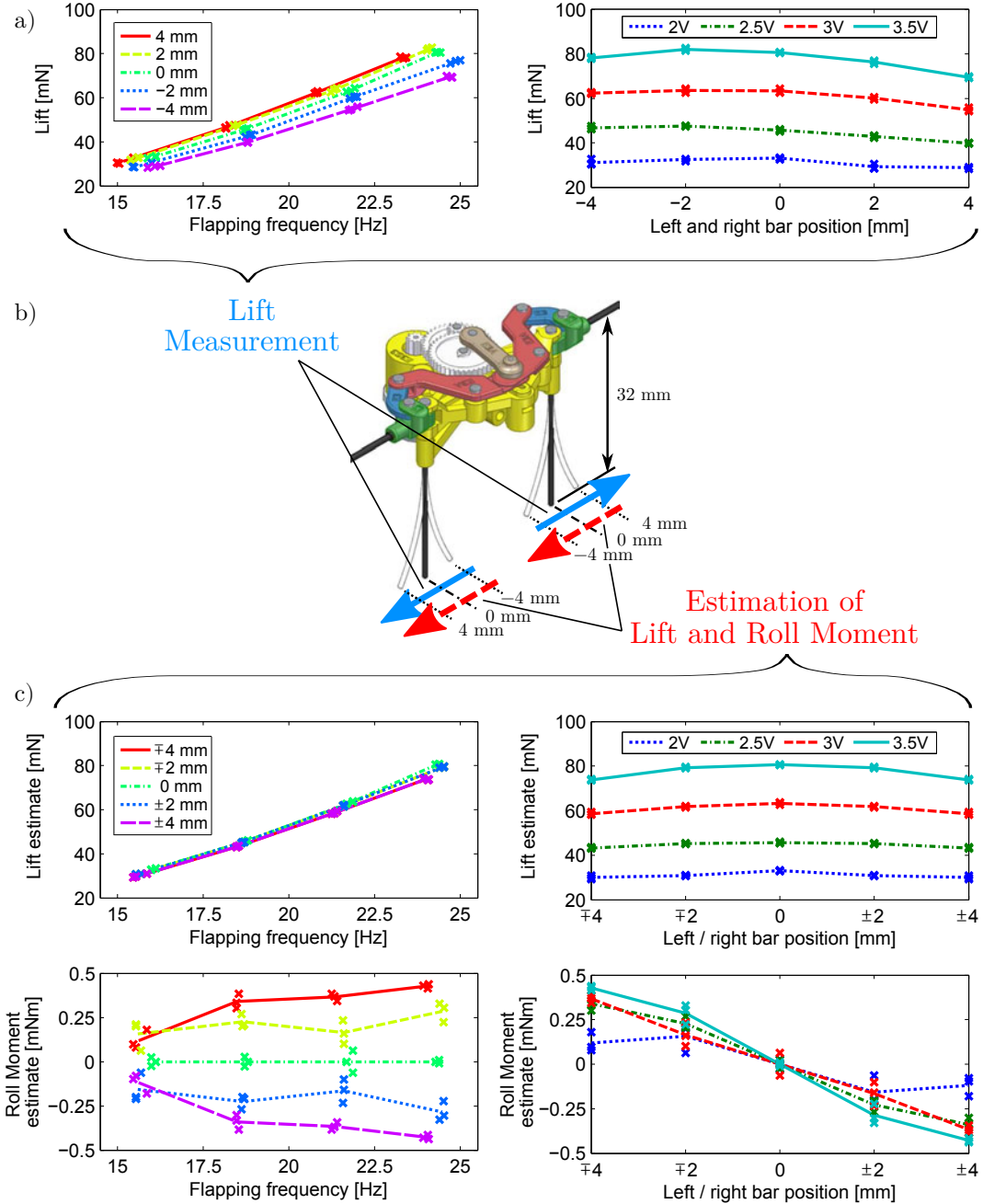


**Figure 7.7:** Roll moment indirect measurement: a) Lift measured for symmetric bar deformations, b) symmetric bar end positions during the lift measurement (blue arrows) and asymmetric positions for roll moment estimation (red arrows), c) estimated lift force and roll moment for asymmetric bar deformations.

### 7.1.3 SMA actuated control mechanism

One of the concepts considered for active displacement of the bar ends is using Shape Memory Alloys (SMA) wires as actuators. The material uses a shape memory effect: when heated above certain temperature the crystal structure changes and, if the material is under stress, we observe contraction of the wire. After cooling the original shape is restored (Lagoudas, 2008).

The use, advantages and limitations of SMAs were thoroughly reviewed by Mohd Jani et al. (2014). We chose this actuator because it is very lightweight and provides directly a displacement. It can be heated simply by Joule effect. But it also has some limitations that need to be considered in the design: the maximal stroke is only about 5% of the wire length. The necessary (passive) cooling reduces significantly the bandwidth. Moreover, the material has a hysteretic behaviour due to phase transformation: the heating follows different characteristics than the cooling. It can also suffer from fatigue, so operation at smaller strains (under 3.5%) and limited stresses (under 160MPa) is recommended (SAES Getters, 2009).

The use of flexible bars instead of joints not only reduces the control mechanism complexity, but the bar deformation also creates the stress necessary for SMA proper function. The small stroke achievable with an SMA wire can be overcome by the kinematics. The SMA wire is attached between two supports; the distance between these is just slightly shorter than the length of the SMA wire itself. Thus, a small contraction of the wire results in a relatively large displacement in the normal direction (Figure 7.8 left). The downside of this approach is that the maximal force is also reduced.

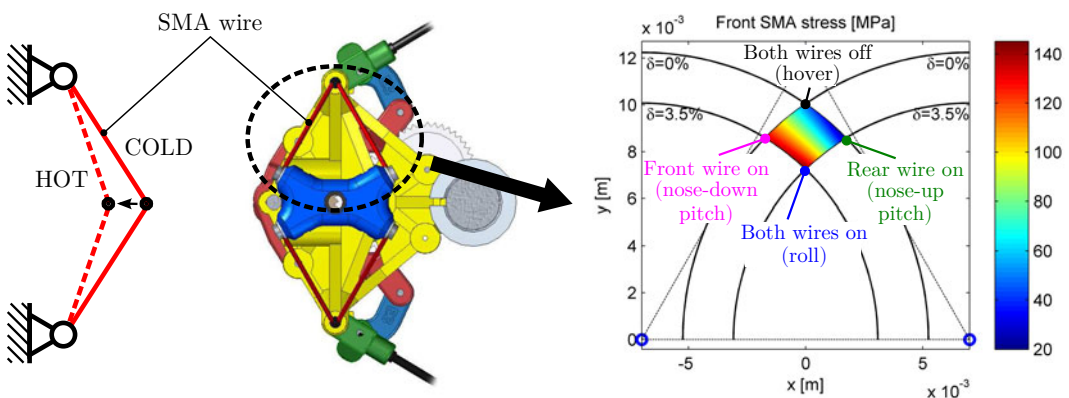


**Figure 7.8:** SMA driven control mechanism: kinematics for larger stroke (left), bottom view of the mechanism model (middle) with corresponding stress distribution for the front wire (right). The two supports are on top of each other in the bottom view.

The designed system uses one pair of SMAs per wing that can displace the bar end in both longitudinal and lateral directions (Figure 7.8 middle). If only one of the wires is heated the bar moves diagonally in forward or backward direction, heating the two wires at the same time moves the bar laterally closer to the body.

Heating the rear wires on both wings results into backward displacement of the bar ends and thus into a nose-up moment (as in Figure 7.3). Similarly heating the front wires on both wings results into a nose-down moment. Heating both wires on one wing while keeping them relaxed on the other wing results into a roll moment (similar to Figure 7.4).

The dimensions were selected to maximize the workspace while keeping the SMA wire stress under the maximal recommended value yet high enough to assure proper phase transformation (Figure 7.8 right).

An important aspect that determines the actuator bandwidth is the cycle time. While the heating phase can be accelerated by increasing the current, the cooling phase usually takes longer because the heat needs to be dissipated into the environment. The cooling is faster for wires with smaller diameter as the surface to volume ratio is higher. However, thinner wires mean also smaller maximal forces. The thinnest wire to withstand the estimated stress levels has a diameter of 50 microns.

The complete robot with the control mechanism is shown in Figure 7.9. The used SMA wires are SmartFlex®50 $\mu$ m, SAES Getters (2009). Their active section is 53

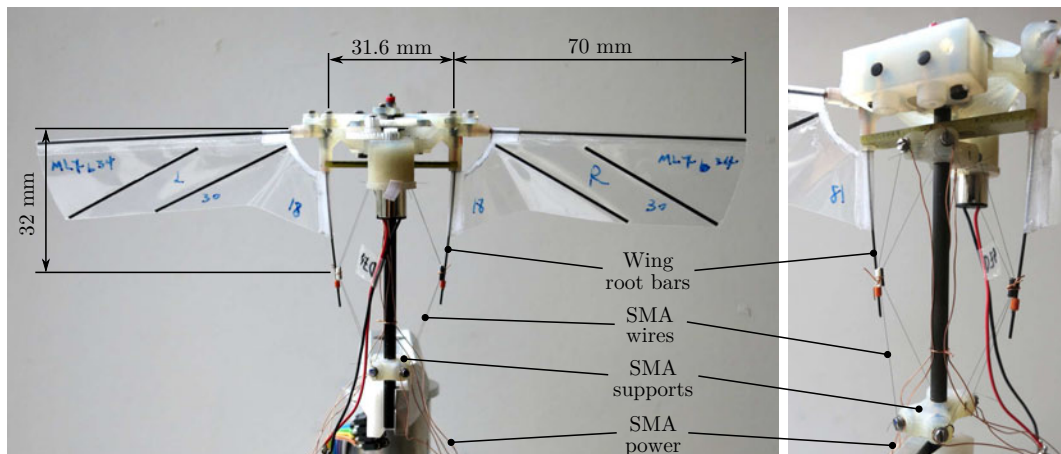


**Figure 7.9:** Robot prototype with SMA actuated control mechanism.

mm long, the distance between the supports is 47 mm. The system to attach the SMA wires consists of two washers under the head of a bolt. The SMA wire goes around the bolt and is pressed between the washers. The power is brought by another cable, pressed by the second washer to the support.

#### 7.1.4 SMA driven control mechanism performance

To determine the mechanism bandwidth the front and rear pair of wires were periodically heated and cooled in an alternating manner, i.e. the bars were alternating between the positions for nose-down and nose-up pitch moment. The achieved displacement was measured from a long exposure camera image. The duty cycle was 50 % and the frequency was being changed from 1 Hz to 5Hz. The current was constant during the heating phase, a value of 110 mA was identified as optimal (no overheating). The airflow from the wings accelerated the cooling process. The results presented in Figure 7.10 were measured at a moderate flapping frequency of about 16 Hz. The maximal displacement of 2.9 mm at 1 Hz decreases significantly as the command becomes faster. According to the results from the previous section the maximal displacement would generate a pitch moment of approximately  $\pm 0.2$  mNm.

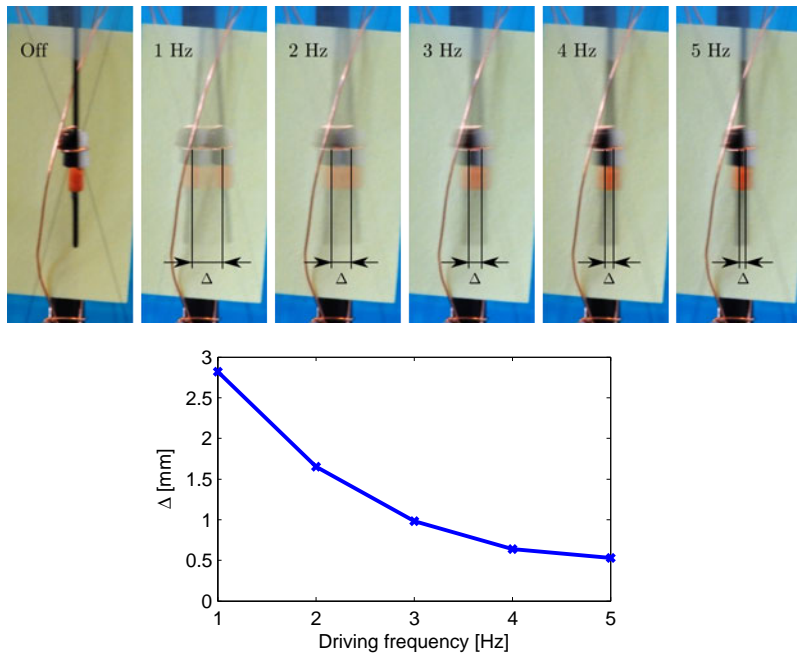


**Figure 7.10:** Long exposure images of root bar displacement by the SMA actuators driven at various frequencies (top) and processed results (bottom).

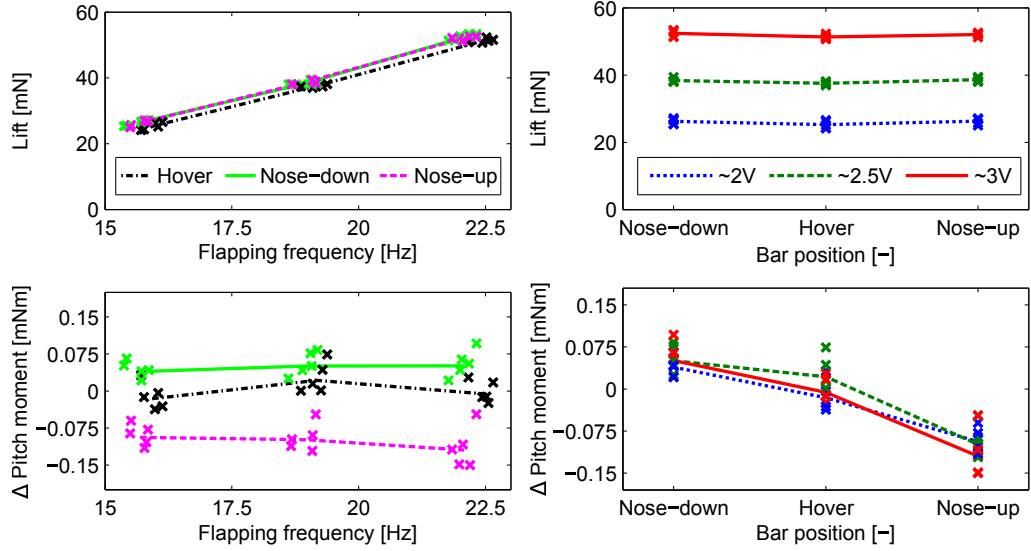


**Figure 7.11:** Lift and moment measurement results - SMA actuated bar displacement.

A direct pitch moment measurement was carried out in three (steady) positions according to Figure 7.8 (right): 1) in the hover position with all the wires relaxed, 2) in the nose-up moment position with the rear pair of wires heated and 3) in the nose-down moment position with the front pair of wires heated. The measurement was repeated five times in each position. The results are plotted in Figure 7.11; individual measurements are displayed as crosses and the lines represent the average values. The lift in hover position is slightly lower when compared to both nose-up and nose-down positions. This is in accordance with our expectations, because to generate a moment the wing root bar moves also in lateral direction which stretches the wing membrane and results in a lift increase.

The maximum generated pitch moment is approximately  $-0.11$  mNm (nose-up) and  $0.06$  mNm (nose-down), which is already at the limit of the resolution of the force balance. The moments are lower than  $\pm 0.2$  mNm estimated from the results in previous section, probably due to smaller bar displacements at higher flapping frequencies that involve higher stress and higher cooling rates. However, direct comparison is not completely correct as the wing design in the SMA actuated prototype had to be modified to compensate for the wing root bar deformation, that needs to be present even in hover position to create pre-stress. The asymmetry between nose-up and nose-down moments might come from imperfections of the hand built prototype (slight misalignment of the SMA supports, small variations of the SMA

wires lengths, ...). The indirect measurement of the roll moment estimated even lower moment values, which were already at the level of variation among individual measurements, because the SMA wires didn't provide enough displacement.

### 7.1.5 Conclusion on wing twist modulation

The presented concept, combining the wing twist modulation with flexible wing root bars, proved to be a feasible solution for generating the control moments. The experiments showed that a (manual) bar displacement of  $\pm 4$  mm can generate a pitch moment of  $\pm 0.5$  mNm and roll moment of  $\pm 0.4$  mNm, which is about 4 times and 8 times the necessary value, respectively, predicted by the flight simulation in Section 5.3. The maximal generated lift produced during the experiments (about 85 mN) was close to the maximal performance of the flapping mechanism at the time of the experiment. Because the control mechanism only acts on the root bar ends, it is completely independent on the flapping mechanism. The newest flapping mechanism version produces almost twice as much lift and so a similar increase in the pitch moment can be expected.

The actively controlled mechanism driven by SMA wires was attractive due to its low weight and relatively low complexity. However, several weak points of this solution were identified. Most importantly, the bandwidth as well as the achievable stroke (and thus the moments) were too low. Apart from that, it was cumbersome to adjust the initial stress in the SMA wires and many wire failures were experienced due to stress concentration in the attachment points. Thus, the full potential of the concept should be exploited by an alternative solution using actuators with larger stroke and higher bandwidth, such as micro-servomotors.

## 7.2 Moment generation via amplitude and offset modulation

The second concept generates the control moments by modulating the flapping amplitude and offset (mean wing position) according to Figure 7.12. This strategy was also used in the simulation presented in Chapter 5. Compared to wing twist modulation this strategy is more straight forward and works with any wing design. However, it requires a modification of the flapping mechanism. The roll moment is produced by increasing the amplitude of one wing and decreasing the amplitude of the other wing, which introduces a lift imbalance between the two wings. Moving the mean wing position of both wings forward or backward results into a nose-up or

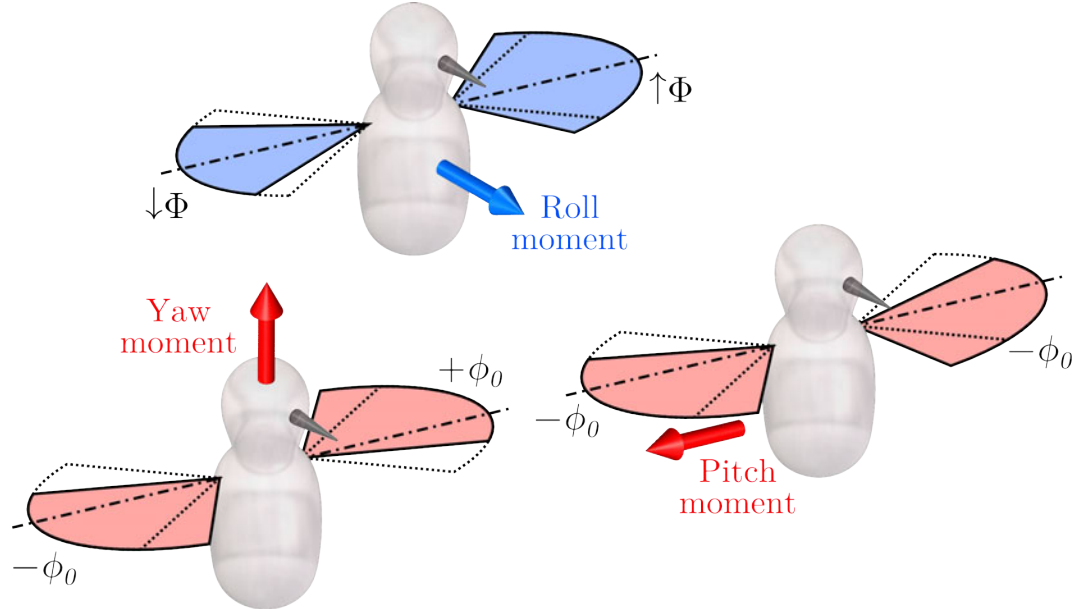


**Figure 7.12:** Moment generation via flapping amplitude and offset modulation.

nose-down pitch moment as the mean lift force origin moves forward or backward from the COG, respectively. Yaw moment generation is not so evident, but the mathematical model in Section 5.2 predicts that the necessary drag imbalance can also be introduced by changing the mean wing position asymmetrically, see equation (5.13).

### 7.2.1 Amplitude and offset modulation

During the flapping mechanism optimization process it has been found that both the flapping amplitude and the offset can be controlled by displacing the mechanism joints A and B, highlighted in Figure 7.13 a). The map in Figure 7.13 b) shows the relation between the position of the joint and the wing amplitude  $\Phi$  and offset  $\phi_0$ . The blue lines connect positions with constant offset and the red lines connect positions with constant amplitude. Thus, moving the joint along a blue line will modify the amplitude, but the offset will remain constant. Similarly a displacement along a red line will only affect the offset while keeping the amplitude constant.

It can be noticed that the two sets of curves cross each other at high angles (above  $70^\circ$ ) meaning the two parameters can be controlled independently. Moreover, the lines of constant offset are almost straight and nearly parallel; the curves of constant

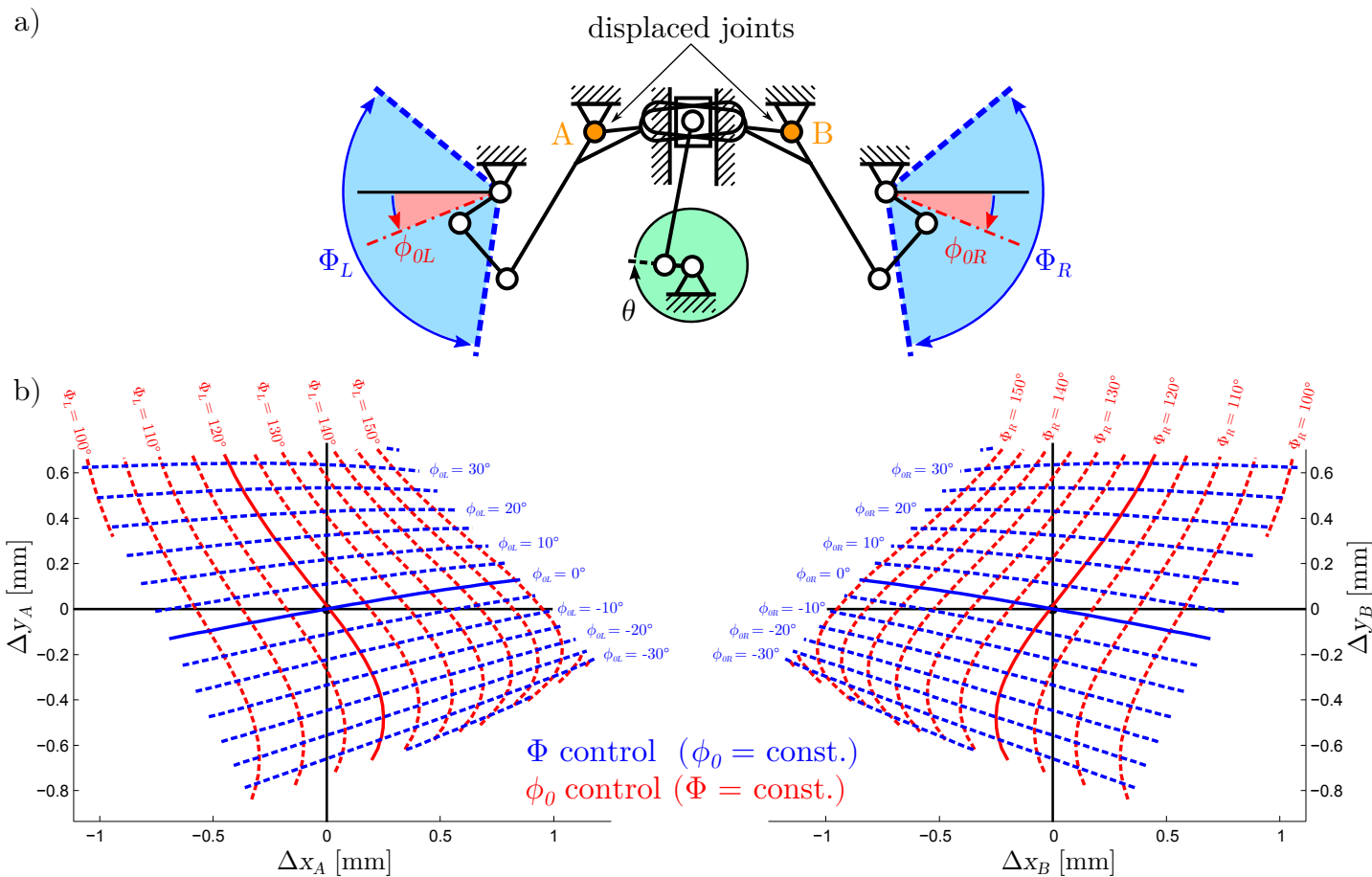


**Figure 7.13:** Amplitude and offset modulation via joint displacement: a) the flapping mechanism and the displaced joints A and B, b) lines of constant amplitude  $\Phi$  and offset  $\phi_0$  for varying joint position. Joint motion along the blue lines controls the amplitude  $\Phi$ , motion along the red lines controls the offset  $\phi_0$ .

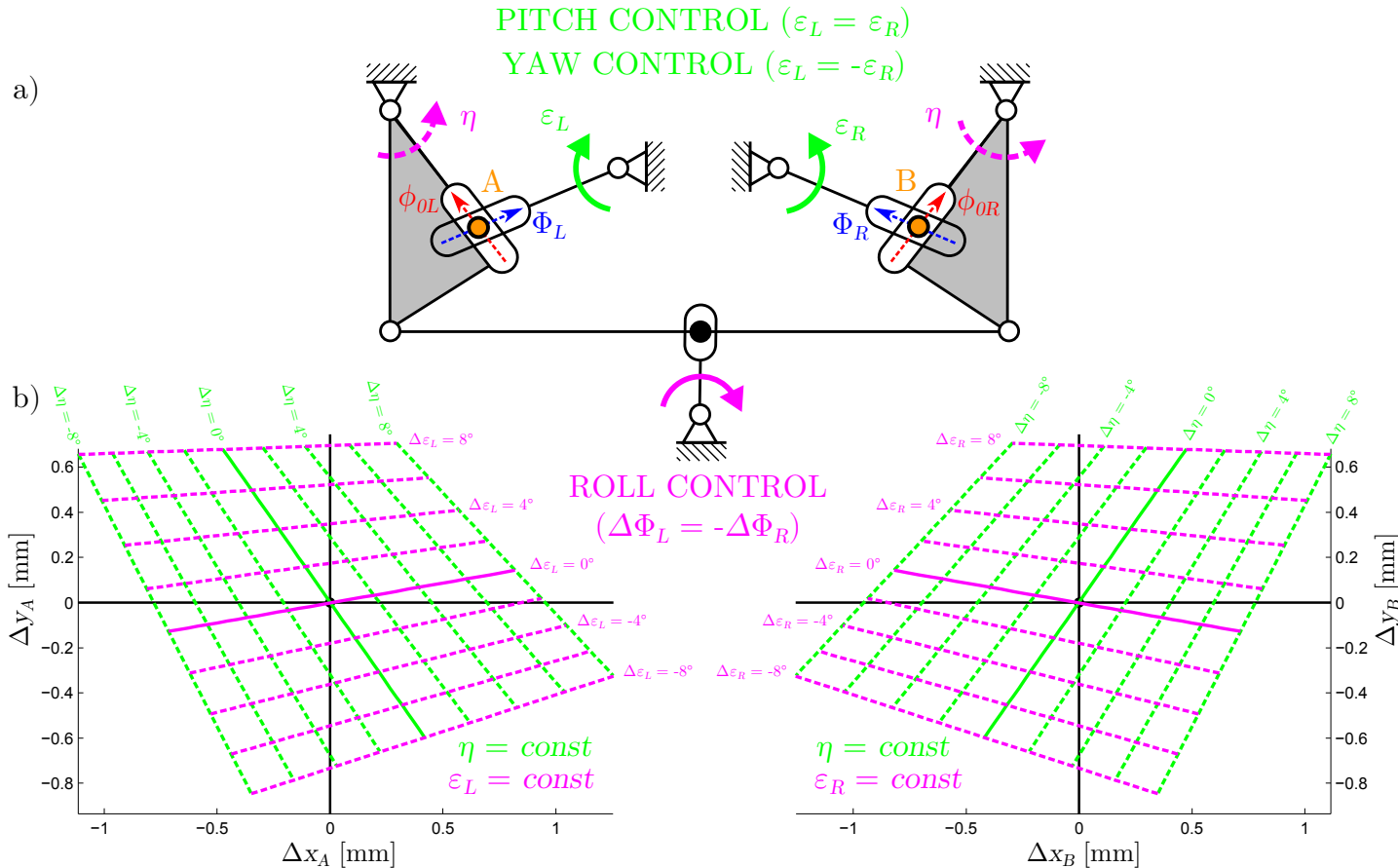


**Figure 7.14:** Amplitude and offset modulation via joint displacement: a) the control mechanism with 3DOF ( $\varepsilon_L, \varepsilon_R, \eta$ ) defining the position of joints A and B by an intersection of two mobile slots, b) lines of constant commands  $\epsilon$  and  $\eta$  approximating well the lines of constant amplitude  $\Phi$  and offset  $\phi_0$  in Figure 7.13 b). Joint motion along the magenta lines controls the roll moment, motion along the green lines controls the pitch ( $\Delta\varepsilon_L = \Delta\varepsilon_R$ ) or yaw ( $\Delta\varepsilon_L = -\Delta\varepsilon_R$ ) moments.

amplitude are also equally spaced and can be approximated by straight lines around the nominal position. This allows to design a joint displacement mechanism with two DOFs where the control is decoupled - one DOF controls directly the amplitude and the other controls the offset.

### 7.2.2 Control mechanism prototype

The scheme of the proposed mechanism for joint displacement is shown in Figure 7.14 a). Each joint is displaced by two arms with slots that rotate with respect to the frame by angles  $\epsilon$  and  $\eta$ , respectively. The joint position is defined by an intersection of the two slots. The arm hinges are located on the lines of nominal amplitude and of the nominal offset, respectively. If one of the arms is blocked and the other one is moving, the joint moves along a line defined by the slot of the blocked arm. If the hinges are placed far enough from the nominal position of the displaced joint ( $\Delta x = 0, \Delta y = 0$ ), these lines appear nearly parallel in the region of interest and the joint paths approximate well the theoretical curves of constant amplitude and offset, see Figure 7.14 b).

The control of left and right wing offset needs to be independent, operated by separate actuators: a symmetric offset change ( $\Delta\epsilon_L = \Delta\epsilon_R$ ) produces pitch moment while an asymmetric change ( $\Delta\epsilon_L = -\Delta\epsilon_R$ ) produces yaw moment. However, the amplitude can be controlled by a single actuator ( $\eta$ ) since only asymmetric amplitude changes are needed for roll. This can be achieved by a parallelogram linking the two arms responsible for amplitude control as is shown in Figure 7.14 a).

The final mechanical solution of the joint displacement mechanism is shown in Figure 7.15. The rivets of the joints to be displaced are fixed from the top to "anchors" that are free to slide in the horizontal plane of the frame. The displacement is limited to the zone considered in Figure 7.14 b) by the shape of the frame cut-out. All the parts were 3D printed, a photograph of an assembled prototype is shown in Figure 7.16. The mechanism is actuated by three micro servos (HobbyKing 5330) with a weight of 2.0 g each. The total weight of the controlled prototype including the servos (6.0 g) and the propulsion motor (5.2 g) is 21.4 g.

### 7.2.3 Wing kinematics

A high speed camera (Photron FASTCAM SA3) was used to study the changes in the wing kinematics of the control prototype. The wing motion was recorded at 500 fps under different control commands and the sweep angle  $\phi$  was tracked in the recordings (see Figure 6.9 in the previous chapter for its definition). As already mentioned in Section 6.2.1 the observed amplitudes were much larger than the design value of

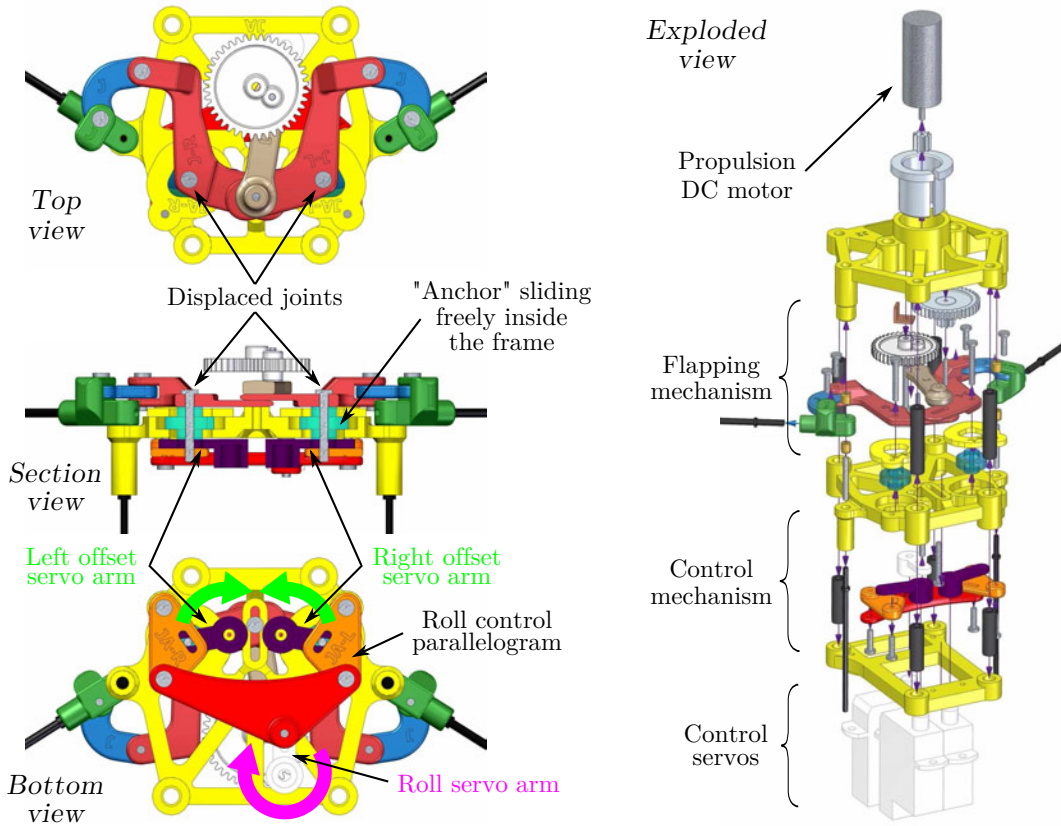


**Figure 7.15:** CAD model of the control prototype. Details of the flapping mechanism with the joint displacement system (left) and an exploded view of the whole prototype (right).

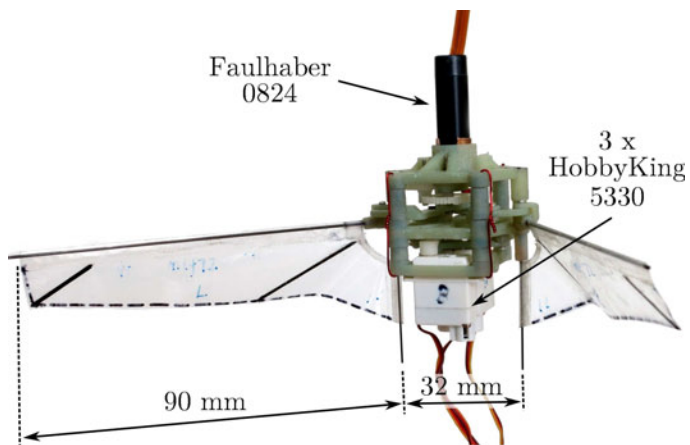


**Figure 7.16:** The assembled prototype with pitch, roll and yaw control via joint displacement.

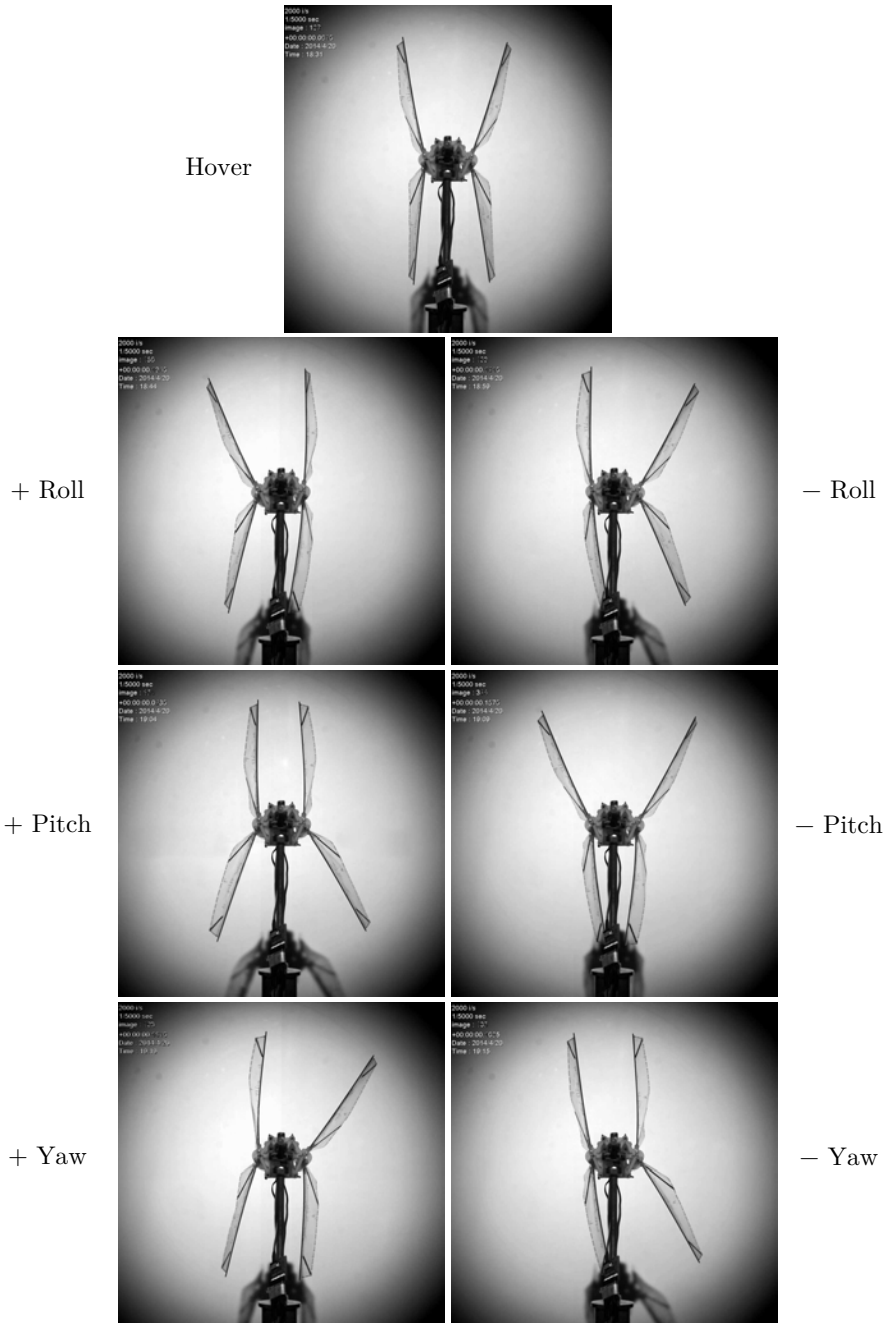


**Figure 7.17:** Extremal positions of the wings recorded with the high-speed camera in the neutral position as well as for the maximum and minimum commands in the 3 DOF. Each image was obtained by blending up to 4 frames with the extremal positions of each wing.

$120^\circ$  due to the wing bars compliance and partly also due to the mechanism backlash. Unless mentioned otherwise, the tests were carried out at a moderate flapping frequency of 15Hz in order to have consistent results along all the tests. For higher frequencies the prototype performance can slightly deteriorate over time due to wear.

The wing extremal positions under maximal and minimal commands of pitch, roll and yaw are displayed in Figure 7.17. The mechanism succeeds to modify the flapping amplitude and offset in the desired manner. The roll and pitch command will be studied in more detail in the following text. The performance in yaw is the same as in pitch, only the left and right wing offset commands have opposite signs.

Figure 7.18 shows the results of amplitude difference control. The servos controlling the wing offset were kept in their nominal position and the roll control servo was commanded from the minimal to the maximal position with a step of 10% of the full range. The left and right wing amplitudes,  $\Phi_L$  and  $\Phi_R$ , are approximately equal for zero servo position. As intended, their difference  $\Delta\Phi = \Phi_R - \Phi_L$  increases/decreases approximately linearly as the servo moves towards the positive/negative limit, where the difference is  $+52^\circ$  and  $-44^\circ$ , respectively. Thus, a good control authority of the roll moment is achieved. The wing offset remains relatively close to zero and the average amplitude  $\bar{\Phi} = (\Phi_R + \Phi_L)/2$  stays approximately constant (around  $155^\circ$ ) in the central part of the servo range. There exist some imperfections, in particular close to the limits, but these should be compensated by the flight controller feedback in future.

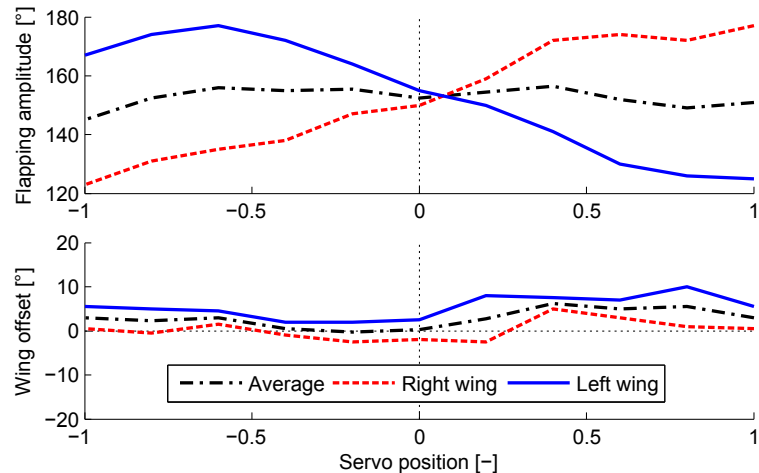


**Figure 7.18:** Amplitude control with the roll servo.

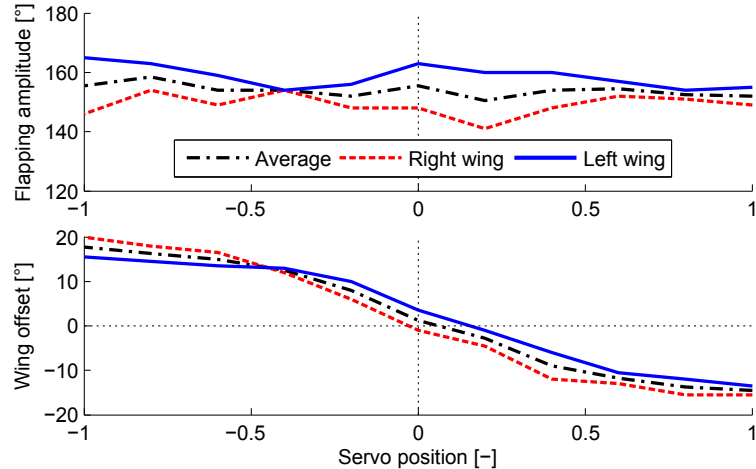


**Figure 7.19:** Offset control with the pair of pitch servos.

The offset control is presented in Figure 7.19. The left and right offset servos were commanded together over the full range, again with a step of 10%. The roll servo was kept at zero. The relationship between the offset servos position and the wing offset is linear and shows a good control authority, even though the slope slightly decreases closer to the servo limits. The maximal and minimal average offset  $\bar{\phi}_0 = (\phi_{0R} + \phi_{0L})/2$  is  $+17.7^\circ$  and  $-14.5^\circ$ , respectively. The amplitude of the left and right wing varies quite a lot, but the average  $\bar{\Phi}$  stays close to  $155^\circ$ . A simultaneous control of the amplitude difference would be necessary to achieve zero roll moment.

The combined commands and resulting coupling effects will be discussed at the end of this section.

#### 7.2.4 Control mechanism dynamics

Figures 7.20 and 7.21 show the dynamics of the transition from minimal to maximal command of pitch and roll, respectively. For this experiment the flapping frequency was around 17Hz. The figures display the wing tip angles, their extremal positions are connected with a full/dashed line and the average position (over the last wing-beat) is displayed as dash-dotted/dotted line for the left/right wing, respectively. An LED was placed on the prototype to indicate the moment of the step command (black line).

As can be seen in Figure 7.20 the transition from maximal to minimal offset occurs within 2 wingbeats. The transition from negative to positive amplitude difference

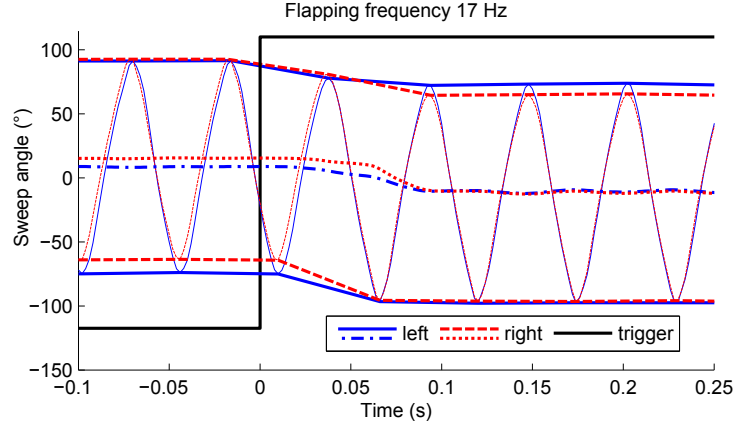


**Figure 7.20:** Pitch up → down command dynamics. Full/dashed line connects the extremal positions, dash-dotted/dotted line represents the mean position (over the last wingbeat).

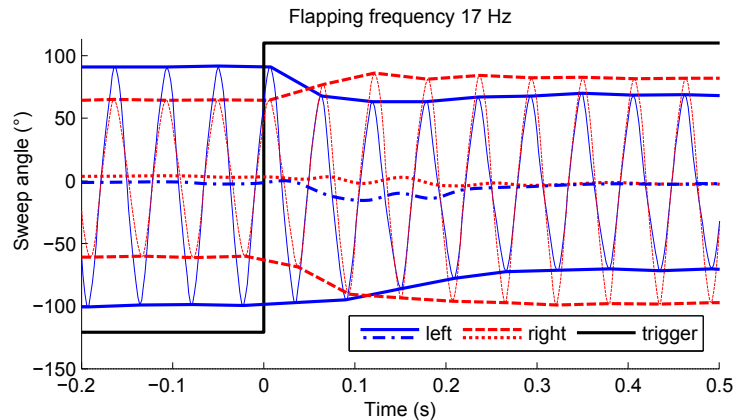


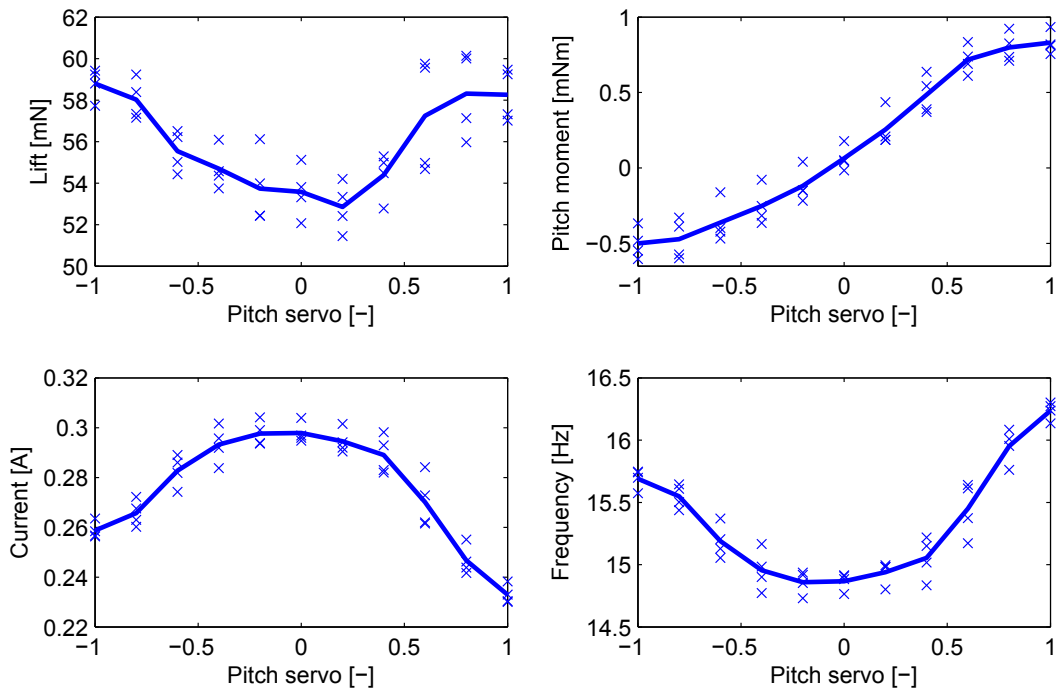
**Figure 7.21:** Roll left → right command dynamics. Full/dashed line connects the extremal positions, dash-dotted/dotted line represents the mean position (over the last wingbeat).

takes around 4 wingbeats (Figure 7.21), however an opposite sign of the difference is achieved already after 2 wingbeats. The same could be observed for the step commands in opposite directions.

The faster pitch response can be explained by a combination of two effects. First, in offset control two servos are employed, one acting on each joint, while in the roll control only a single servo is displacing the two joints. The second reason is that the reaction due to the flapping motion on the displaced joints has a major component in the direction, where the joints are displaced for offset control. This speeds up the offset transition when a change is desired, but has an adverse effect on the mechanism efficiency as the joints keep shaking in this direction during operation.

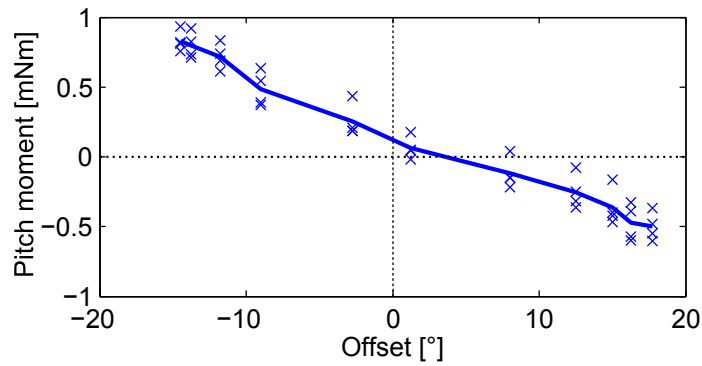
### 7.2.5 Pitch moment and lift generation

Apart from the wing kinematics measurements, the generated lift and pitch moment was measured directly on the force balance presented in Section 6.2.2. Figure 7.22 shows the measured pitch moment, lift, frequency and motor current for the full range of the pitch servos. The motor voltage was kept at 4.2V, which gives a flapping frequency of approximately 15Hz for the nominal servo position. The measured pitch moment ranged from -0.5 mNm to 0.8 mNm. The lift force and the flapping frequency increase and the current decreases when the servos approach the servo limits. This is caused by the shaking of the displaced joints due to flapping (already mentioned earlier) that happens particularly for the central servo positions. The joints get a better fix in the limit positions, where the servo pushes the displaced joints against a wall of the frame, and thus the efficiency increases. The lift varies between 53 and 59 mN and the frequency between 14.9 and 16.2 Hz.



**Figure 7.22:** Lift, pitch moment, motor current and flapping frequency against pitch servos position. Measurement done at 4.2 V leading to 15 Hz at the nominal position. Individual measurements are displayed as crosses, the solid line represents an average of four measurements.

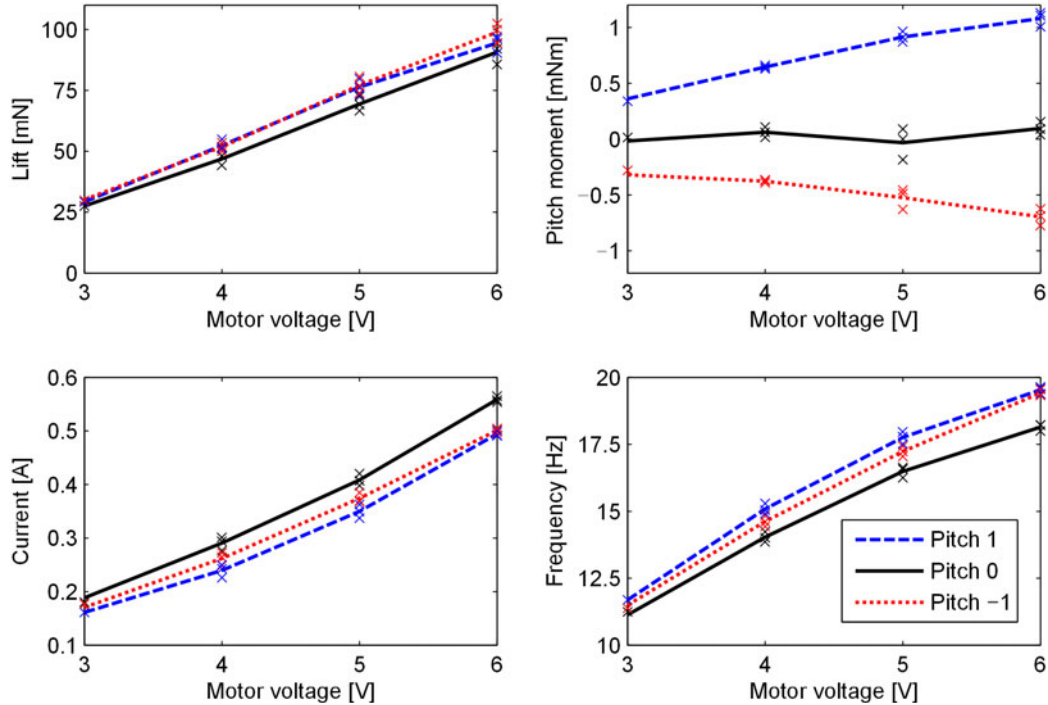
Figure 7.23 combines the moment measurement with the wing kinematics measurement from the previous section. The relationship is approximately linear with a slope of 0.04 mNm per degree of the offset  $\phi_0$ . The non-zero moment produced at zero offset can be explained by a combination of asymmetric wing design (stiffeners glued only on one side of the membrane), different velocity profiles in upstroke and downstroke and by an imperfect alignment of the prototype on the balance. Nevertheless, a compensating moment can be easily introduced by an offset of the COG from the shoulders in the longitudinal direction.



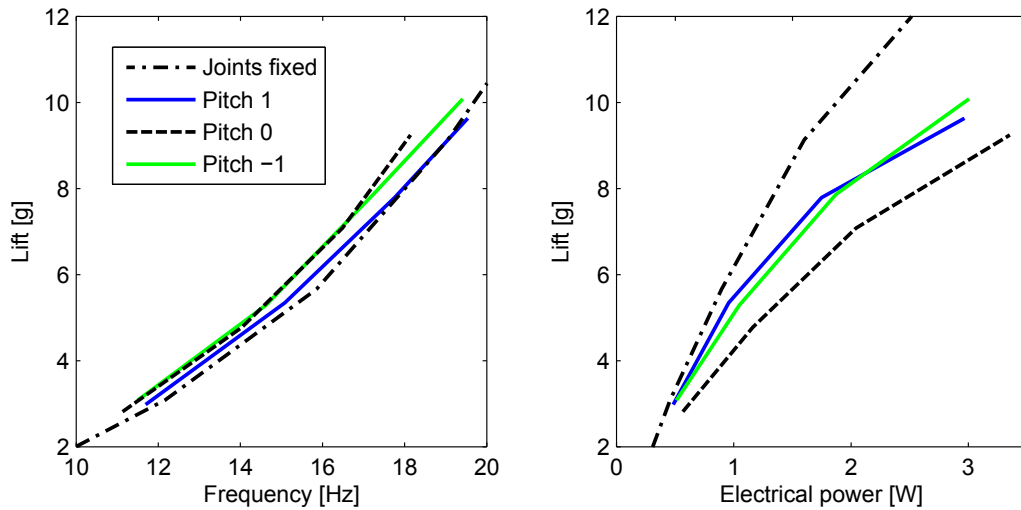
**Figure 7.23:** Pitch moment against wing offset  $\phi_0$ .

Figure 7.24 shows the pitch moment, lift, frequency and motor current for motor voltages up to 6V. The three curves represent the measurements for servo positions -1, 0 and 1, respectively, related to the full range. The behaviour corresponds to the one observed at 15Hz. At the highest tested voltage the mechanism produces pitch moments from -0.7 mNm to 1.1 mNm while the lift ranges between 90 and 100 mN.

The lift vs frequency characteristic is close to the one of the uncontrolled prototype (with fixed joints), see Figure 7.25, with only small differences caused by a variation of the flapping amplitude. However, the electrical power of the controlled version is almost twice as high due to losses in the shaking joints. Thus, the mechanical design of the joint displacement mechanism needs to be improved in order to get a better fix of the joints and, subsequently, a better efficiency.



**Figure 7.24:** Lift, pitch moment, motor current and flapping frequency measured for increasing motor voltage. Black lines represent the zero pitch servos position, red and blue lines represent the minimal and maximal pitch command. The crosses represent individual measurements.



**Figure 7.25:** Pitch moment against wing offset.

### 7.2.6 Combined commands

Finally, combined pitch and roll commands were tested to identify the amount of cross-coupling. Again all the measurements were carried out at a constant motor voltage (4.2V) giving a flapping frequency of around 15Hz at the nominal position of the servos. The measurements were taken at servo positions -0.8, -0.4, 0, 0.4 and 0.8 of the full range for both pitch and roll servos. Thus, 25 measurements were taken in total.

Figure 7.26 shows the amplitude and offset maps of the left and the right wing from the high speed recordings. The camera images combining the extremal wing positions for maximal commands (corners of the maps) are shown in Figure 7.27. We can see that while a small cross-coupling always exists, the roll servo has a dominant effect on the amplitude and the pitch servo has a dominant effect on the offset. Moreover, the relation between the amplitude/offset and roll/pitch servo positions

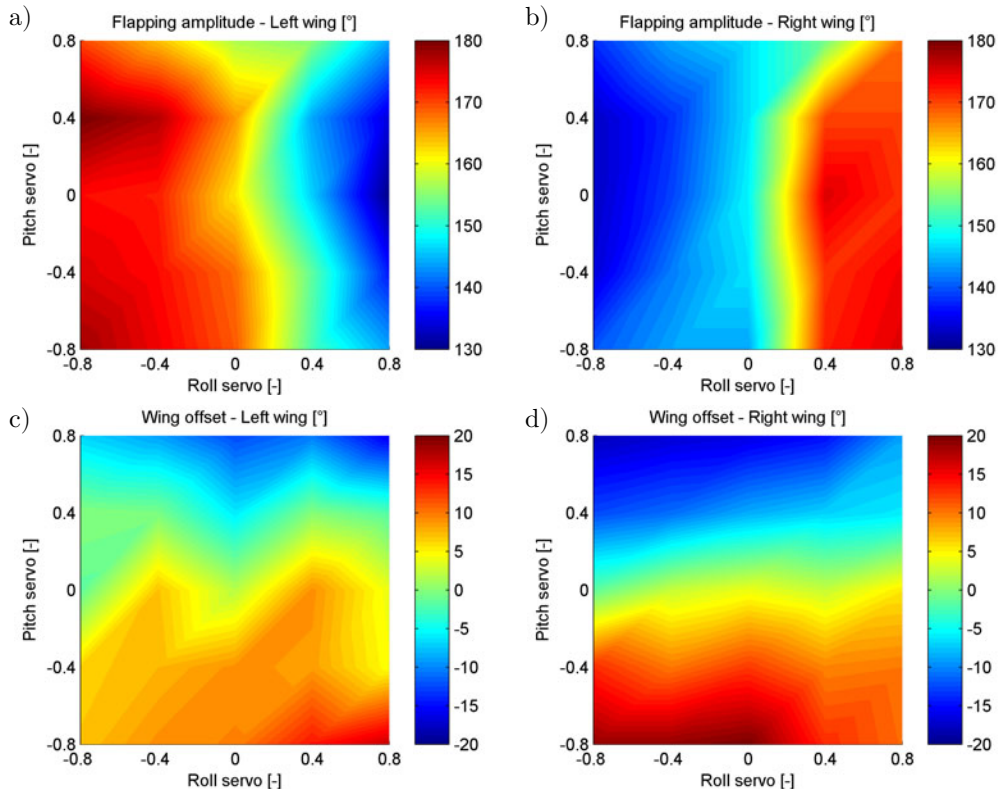


**Figure 7.26:** Experimental results: Kinematics for combined pitch and roll servo commands. a) Left amplitude, b) right amplitude, c) left offset, d) right offset.

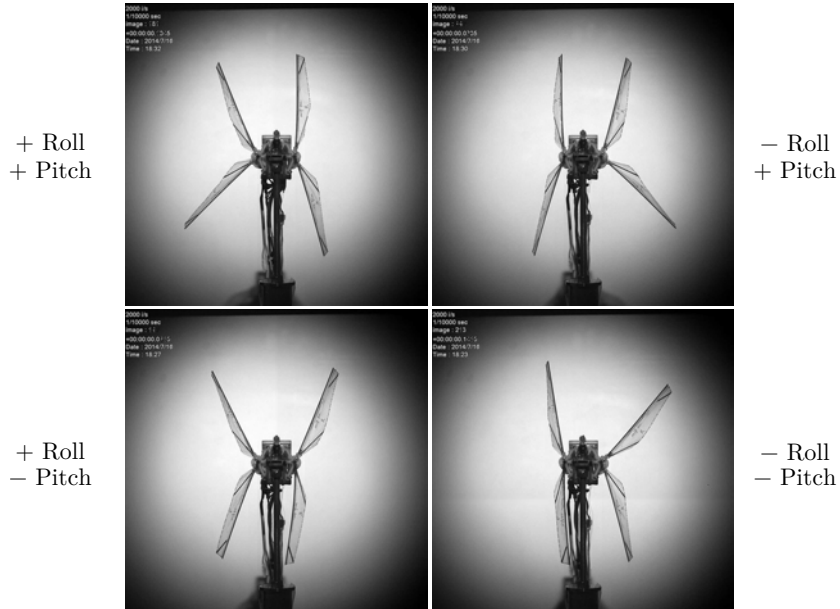


**Figure 7.27:** Extremal positions of the wings recorded with the high-speed camera for the combined commands in pitch and roll. Each image was obtained by blending up to 4 frames with the extremal positions of each wing.

stays always monotonic. Thus, a feedback controller should be able to compensate the coupling effects and the small differences between the left and right wing behaviour, caused by the mechanism imperfections.

The same experiment was repeated with the force balance, the results are shown in Figure 7.28. The maps show the pitch moment and lift force for the selected servo input combinations. The lift map keeps a valley-like shape in the pitch servo direction, similar to what was observed for the pure pitch command and what can be explained by an improper joint fixation in the central pitch servo positions. There is also a smaller increase of lift in the positive roll direction, which most likely comes from the imperfections of the prototype. The minimum and maximum lift is 48 and 59 mN, respectively. The lift force variation is related to the square of frequency times amplitude displayed in Figure 7.29 c), in accordance with equation (6.8).

The pitch moment depends mostly on pitch servo positions, while there are only minor differences when the roll servo position changes. Thus, the minimal and maximal pitch moment values stay at the same levels as for the pure pitch command, -0.4 mNm and 0.8 mNm respectively. The pitch moment corresponds closely to the mean offset shown in Figure 7.29 a).

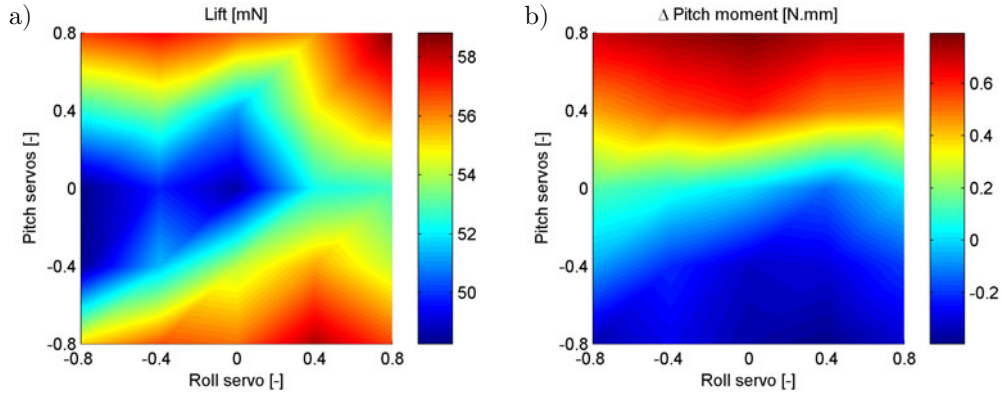


**Figure 7.28:** Experimental results: Force balance measurements for combined pitch and roll servo commands. a) Lift, b) pitch moment. Lift is tied to the square of mean amplitude times frequency in Figure 7.29 a), pitch moment to the mean offset in Figure 7.29 b).

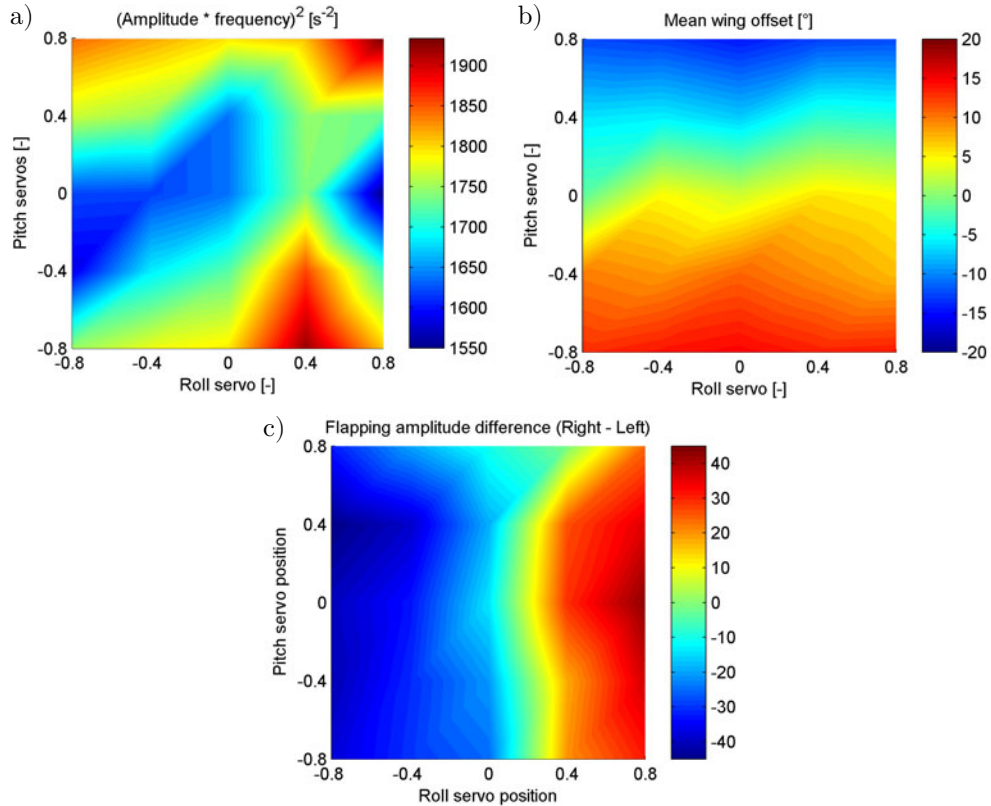


**Figure 7.29:** Experimental results: Kinematics for combined pitch and roll servo commands. a) Square of mean amplitude times frequency, b) mean wing offset, c) flapping amplitude difference.

The roll moment could not be measured directly, but it should correspond to the amplitude difference shown in Figure 7.29 c).

### 7.2.7 Conclusion on amplitude and offset modulation

The second presented control mechanism generates the necessary control moments by modulating the flapping wing amplitude and offset. The wing kinematics modifications are achieved by displacing the joints of the flapping linkage mechanism. It was demonstrated experimentally that sufficient offset ( $\pm 15^\circ$ ) and amplitude differences (above  $\pm 40^\circ$ ) for pitch and roll control can be introduced by very small displacements of the linkage joints (below  $\pm 1mm$ ) in two directions. The transitions between maximum and minimum command takes less than two wingbeats in pitch and about four wingbeats in roll. A very low level of cross-coupling exists for combined commands. The prototype can produce pitch moments between -0.7 mNm and 1.1 mNm (at least 6 times the moment predicted by the flight simulation in Section 5.3) while flapping at frequencies around 18Hz and producing a lift of at least 90mN. The roll moment could not be measured, but should be more than sufficient as the measured amplitude differences are 40 times higher than those predicted by flight simulation.

While the control mechanism succeeds in modifying the wing kinematics and, subsequently, in the moment generation with sufficient dynamics, the prototype efficiency drops significantly compared to the uncontrolled prototype. The drawback of the proposed solution is that the displaced joints need to hold rather large and oscillating reaction forces due to flapping. This causes the joints to shake, which reduces significantly the mechanism performance and at higher frequencies also its lifespan. The motor draws up to twice the electrical power compared to an uncontrolled prototype with fixed joints. Thus, an alternative mechanical solution, which would reduce the effect of the oscillating reaction forces on the servos displacing the joints, should be found.

## 7.3 Discussion and conclusions

Two control mechanisms generating moments around the three body axis (roll, pitch, yaw) were developed and tested. The first solution, based on wing twist modulation, is inspired by the control mechanism of the Nano Hummingbird (Keenon et al., 2012). The second, original solution generates the moments by flapping amplitude and offset modulation through displacements of the flapping mechanism linkage joints. Both control mechanisms succeeded in generating moments that were several

times higher than the moments needed in the flight simulation in Chapter 5. Nevertheless, the experiments revealed that each of the mechanisms has several strong points, but also some weaknesses that require further development.

The advantage of the wing twist modulation mechanism is that it is fully independent on the flapping mechanism. It acts at the wing root bar ends, where the reaction forces, that it needs to hold, are relatively small (compared to the second solution). This is advantageous as it permits the use of smaller and lighter actuators. Moreover, the use of flexible root bars instead of universal joints greatly reduces the mechanism complexity. On the other hand, the wing twist modulation concept requires a specific wing design, whose lift force varies approximately linearly with the root bar deformation. This requires that the wing at the nominal bar position is operated below its maximal lift.

The second mechanism modulating the flapping amplitude and offset works with any wing design. It is an integral part of the flapping mechanism as it displaces one of the linkage joints. This can be considered as beneficial as the whole design is compact and the actuators can be placed close to the flapping mechanism part. On the other hand, any design change of the flapping mechanism requires also a redesign of the joint displacement system. Another drawback of this solution is that the system needs to hold the reaction forces from the displaced joints, which are in particular high in the pitch control direction. This made the joints shake during the operation and resulted into efficiency degradation.

A remaining challenge for both solutions are the actuators. The most fitting actuators for this application on the market, the smallest available micro servos, have an acceptable power, but remain still relatively large and heavy. While they showed sufficient dynamics in the joint displacement system, they were unable to fix the joints completely. Nevertheless, a modified mechanical solution might succeed in reducing the joint shaking.

As an alternative, a shape memory alloy actuator was used in the wing twist modulation system. This actuator is very light and provides satisfactory stroke in static experiments, however its performance decreases significantly under dynamic tests and thus it is not a good candidate for the control actuator.

To conclude, both presented control systems succeed in moment generation, but require further development and testing, focused mostly on efficiency improvements and weight reduction. In future, a combination of both systems might also be considered in order to solve potential cross-coupling of the three generated control moments.

## 7.4 References

- M. Karasek, Y. Nan, I. Romanescu, and A. Preumont. Pitch moment generation and measurement in a robotic hummingbird. *International Journal of Micro Air Vehicles*, 5(4):299–310, 2013. doi:10.1260/1756-8293.5.4.299.
- M. Karasek, A. Hua, Y. Nan, M. Lalami, and A. Preumont. Pitch and roll control mechanism for a hovering flapping wing MAV. In *International Micro Air Vehicle Conference and Flight Competition (IMAV2014), Delft, The Netherlands, August 12-15*, pages 118–125, 2014.
- M. T. Keenon, K. R. Klingebiel, H. Won, and A. Andriukov. Development of the nano hummingbird: A tailless flapping wing micro air vehicle. *AIAA paper 2012-0588*, pages 1–24, 2012.
- D. C. Lagoudas. *Shape Memory Alloys: Modeling and Engineering Applications*. Springer, 2008. doi:10.1007/978-0-387-47685-8.
- K. Y. Ma, P. Chirarattananon, S. B. Fuller, and R. J. Wood. Controlled flight of a biologically inspired, insect-scale robot. *Science*, 340:603–607, 2013. doi:10.1126/science.1231806.
- J. Mohd Jani, M. Leary, A. Subic, and M. A. Gibson. A review of shape memory alloy research, applications and opportunities. *Materials & Design*, 56:1078–1113, 2014. doi:10.1016/j.matdes.2013.11.084.
- SAES Getters. Smartflex wire & springs. [http://www.saesgetters.com/sites/default/files/SmartFlex%20Wire%20%26%20Spring%20datasheets\\_1.pdf](http://www.saesgetters.com/sites/default/files/SmartFlex%20Wire%20%26%20Spring%20datasheets_1.pdf), 2009. Accessed: 18/08/2014.
- T. Q. Truong, V. H. Phan, S. P. Sane, and H. C. Park. Pitching moment generation in an insect-mimicking flapping-wing system. *Journal of Bionic Engineering*, 11(1):36–51, 2014.

## Chapter 8

# Summary and conclusions

This work dealt with development of a hummingbird-sized tail-less flapping wing micro air vehicle capable of hovering. More specifically, the aim of this thesis was to develop a control mechanism that generates the moments controlling the flight by varying the wing motion of each wing independently.

First, the problem was studied theoretically. In Chapter 3, a mathematical model was developed combining quasi-steady aerodynamics with rigid body dynamics. The model was linearised and further reduced. It has been shown that the model gives comparable results to CFD data from the literature. In Chapter 4, stability of the designed MAV was studied showing, in accordance with other studies, that hovering flapping flight is inherently unstable. It has been demonstrated that stability can be achieved with an angular rate feedback, which is most likely used by insects, as long as the wings are placed sufficiently high above the centre of gravity. A flight controller with cascade structure has been designed in Chapter 5. Several ways of generation of the necessary control moments by wing motion changes have been identified. A good control performance has been shown in simulation (using the full, non-linear model) for an example of flapping amplitude and offset (mean wing position) modulation.

A prototype of the robotic hummingbird was designed and tested in Chapter 6. The flapping mechanism has undergone a lot of development. Its dimensions were optimized for symmetric wing motion, which was confirmed by high speed camera measurements. A force balance capable of measuring cycle averaged lift force and pitch moment was built to evaluate the prototype performance. The wing shape was optimized experimentally for maximal lift. The latest prototype, with off-board power and no control, has a lift to mass ratio of nearly 1.3. A take off was demonstrated while the prototype was stabilized by a guide cable.

Last but no least, two types of control mechanisms generating the necessary control moments were designed in Chapter 7. The first solution generates the control moments by modulating the twist of the wings by flexing the wing root bars. The second solution modulates the flapping amplitude and offset via displacements of the flapping mechanism joints in specific directions. Shape memory alloy actuators were employed to drive the first solution, however, the performance was not sufficient due to low bandwidth. Micro-servomotors were used for the second solution and satisfactory response times were achieved. Prototypes of both solutions were tested on the force balance, both generating control moments several times larger than the maximum control moments estimated in the flight control simulation.

## 8.1 Original aspects

The following parts of this work represent an original contribution:

- It has been shown, by comparing several aerodynamic models, that the complex non-linear dynamics of flapping flight, once cycle averaged, can be represented by a reduced linear model, where the decoupled pitch and roll dynamics are characterized by three poles each. The pole configuration depends on the wing position. If the wings are well above the centre of gravity, a simple angular rate feedback stabilizes the system.
- A new flapping mechanism with high amplitude consisting of two stages, a slider-crank and four-bar mechanisms, has been developed. The mechanism output has nearly symmetric velocity profile, which is ideal for hovering flight and a big advantage over single stage linkage mechanisms.
- A new control mechanism concept generating the necessary control moments by amplitude and offset modulation via displacements of the flapping mechanism joints has been developed. The mechanism is tied to a specific flapping mechanism, but is fully independent of the wing design.

## 8.2 Future work

The developed robotic hummingbird demonstrated that it can generate sufficient lift to take-off or sufficient moments to stabilize itself in the air. However, the weight of the current design of the controlled prototype is too high (i) due to the used servo

actuators, (ii) because it was designed for bench tests, where robustness and long life were a priority and (iii) due to a relatively low strength to weight ratio of the photo-polymer material used in the 3D printing process. Thus, further development of the robot prototype is necessary, concentrating mainly on improving the lift production and reducing the weight:

- The control mechanism should be redesigned to better fix the displaced joints. Currently, a significant amount of energy is lost because the joints shake when flapping. A possible solution that uses cams to reduce the forces transferred to the servo actuators is already under development.
- Lightweight actuators with sufficient stroke and power need to be found or developed. The shape memory alloy wires used in this study are light enough, but their response times are too slow and the stroke too short. The micro servomotors have the necessary performance, but they are too heavy, representing almost 30% of the total mass.
- The generated lift should be increased by optimizing further the wing design and by optimizing the gear-ratio for maximal efficiency of a specific motor-mechanism-wing combination.
- The robot structure mass needs to be reduced. It should be redesigned for possible weight savings and a different manufacturing technology, using materials with higher strength to mass ratio, should be considered.

Apart from the mechanical design, robot avionics, including a radio, an attitude sensor, a motor speed controller and a micro-controller needs to be integrated into a sufficiently small and lightweight package, before a stable hovering flight can be achieved.

### 8.3 Publications

The work presented in this thesis has led to the following publications:

#### Journal papers

M. Karasek and A. Preumont. Flapping flight stability in hover: A comparison of various aerodynamic models. *International Journal of Micro Air Vehicles*, 4(3): 203–226, 2012. doi:10.1260/1756-8293.4.3.203.

M. Karasek and A. Preumont. Simulation of flight control of a hummingbird like robot near hover. *Acta Technica*, 58(2):119–139, 2013.

M. Karasek, Y. Nan, I. Romanescu, and A. Preumont. Pitch moment generation and measurement in a robotic hummingbird. *International Journal of Micro Air Vehicles*, 5(4):299–310, 2013. doi:10.1260/1756-8293.5.4.299. The paper received the "Best Paper Award" at IMAV2013 conference.

### Conference proceedings

M. Karasek and A. Preumont. Control of longitudinal flight of a robotic hummingbird model. In *5th ECCOMAS Thematic Conference on Smart Structures and Materials SMART11, conference proceedings CD-ROM*, Saarbrucken, Germany, July 6-8, 2011.

M. Karasek, A. Hua, Y. Nan, M. Lalami, and A. Preumont. Pitch and roll control mechanism for a hovering flapping wing mav. In *International Micro Air Vehicle Conference and Flight Competition (IMAV2014)*, Delft, The Netherlands, August 12-15, pages 118–125, 2014.

### Oral presentations and posters

M. Karasek and A. Preumont. Robotic hummingbird: Simulation model and longitudinal flight control (poster and oral presentation). *International Workshop on Bio-Inspired Robots*, Nantes, France, April 6-8, 2011.

M. Karasek and A. Preumont. Flight simulation and control of a tailless flapping wing MAV near hover (poster). *International Micro Air Vehicle Conference and Flight Competition (IMAV2012)*, Braunschweig, Germany, July 3-6, 2012.

M. Karasek and A. Preumont. Simulation of flight control of a hummingbird like robot near hover (oral presentation). *Engineering Mechanics 2012*, Svatka, Czech Republic, May 14-17, 2012.

M. Karasek, Y. Nan, I. Romanescu, and A. Preumont. Pitch moment generation and measurement in a robotic hummingbird (oral presentation). *International Micro Air Vehicle Conference and Flight Competition (IMAV2013)*, Toulouse, France, September 17-20, 2013.

M. Karasek, I. Romanescu, and A. Preumont. Development of a robotic hummingbird (oral presentation). *International Conference on Manufacturing Systems (ICMS2013)*, Iasi, Romania, October 24-25, 2013.

# General Bibliography

- D. L. Altshuler and R. Dudley. Kinematics of hovering hummingbird flight along simulated and natural elevational gradients. *Journal of Experimental Biology*, 206: 3139–3147, 2003. doi:10.1242/jeb.00540.
- ATI Industrial Automation. Nano17 titanium. [https://www.ati-ia.com/products/ft/ft\\_models.aspx?id=Nano17+Titanium](https://www.ati-ia.com/products/ft/ft_models.aspx?id=Nano17+Titanium), 2014. Accessed: 18/08/2014.
- A. Azuma. *The Biokinetics of Flying and Swimming*. AIAA Education Series. AIAA, 2nd edition edition, 2006.
- A. J. Bergou, L. Ristroph, J. Guckenheimer, I. Cohen, and Z. J. Wang. Fruit flies modulate passive wing pitching to generate in-flight turns. *Physical review letters*, 104(14):1–4, 2010. doi:10.1103/PhysRevLett.104.148101.
- G. J. Berman and Z. J. Wang. Energy-minimizing kinematics in hovering insect flight. *Journal of Fluid Mechanics*, 582:153–168, Jun. 2007. doi:10.1017/S0022112007006209.
- J. M. Birch and M. H. Dickinson. The influence of wingwake interactions on the production of aerodynamic forces in flapping flight. *Journal of Experimental Biology*, 206:2257–2272, 2003. doi:10.1242/jeb.00381.
- J. M. Birch, W. B. Dickson, and M. H. Dickinson. Force production and flow structure of the leading edge vortex on flapping wings at high and low reynolds numbers. *Journal of Experimental Biology*, 207:1063–1072, 2004. doi:10.1242/jeb.00848.
- B. Bruggeman. Improving flight performance of delfly ii in hover by improving wing design and driving mechanism. Master’s thesis, Delft University of Technology, 2010.
- P. Chai, R. Harrykissoon, and R. Dudley. Hummingbird hovering performance in hyperoxic heliox: effects of body mass and sex. *Journal of Experimental Biology*, 199:2745–2755, 1996.

- B. Cheng and X. Deng. Translational and rotational damping of flapping flight and its dynamics and stability at hovering. *IEEE Transactions on Robotics*, 27(5):849–864, Oct. 2011. doi:10.1109/TRO.2011.2156170.
- S. Chung and M. Dorothy. Neurobiologically inspired control of engineered flapping flight. *Journal of Guidance, Control, and Dynamics*, 33(2):440–453, 2010.
- A. T. Conn, C. S. Ling, and S. C. Burgess. Biomimetic analysis of insect wing kinematics for flapping MAVs. *International Journal of Micro Air Vehicles*, 3(1):1–11, 2011. doi:10.1260/1756-8293.3.1.1.
- G. de Croon, K. de Clerq, R. Ruijsink, B. Remes, and C. de Wagter. Design, aerodynamics, and vision-based control of the DelFly. *International Journal of Micro Air Vehicles*, 1(2):71–97, Jun. 2009. doi:10.1260/175682909789498288.
- X. Deng, L. Schenato, and S. Sastry. Flapping flight for biomimetic robotic insects: part II-flight control design. *IEEE Transactions on Robotics*, 22(4):789–803, Aug. 2006a. doi:10.1109/TRO.2006.875483.
- X. Deng, L. Schenato, W. C. Wu, and S. S. Sastry. Flapping flight for biomimetic robotic insects: part I-system modeling. *IEEE Transactions on Robotics*, 22(4):776–788, Aug. 2006b. doi:10.1109/TRO.2006.875480.
- K. Dial, A. Biewener, B. Tobalske, and D. Warrick. Mechanical power output of bird flight. *Nature*, 390(6655):67–70, 1997.
- K. P. Dial. Avian forelimb muscles and nonsteady flight: Can birds fly without using the muscles in their wings? *The Auk*, 109(4):874–885, 1992.
- M. H. Dickinson, F.-O. Lehmann, and K. G. Gtz. The active control of wing rotation by drosophila. *Journal of Experimental Biology*, 182:173–189, 1993.
- M. H. Dickinson, F.-O. Lehmann, and S. P. Sane. Wing rotation and the aerodynamic basis of insect flight. *Science*, 284(5422):1954–1960, Jun. 1999. doi:10.1126/science.284.5422.1954.
- W. B. Dickson, A. D. Straw, C. Poelma, and M. H. Dickinson. An integrative model of insect flight control. *44th AIAA Aerospace Sciences Meeting and Exhibit; Reno, NV; USA; 9-12 Jan*, pages 1–19, 2006.
- D. B. Doman, M. W. Oppenheimer, and D. O. Sigthorsson. Wingbeat shape modulation for flapping-wing micro-air-vehicle control during hover. *Journal of Guidance, Control, and Dynamics*, 33(3):724–739, 2010. doi:10.2514/1.47146.

- R. Dudley. *The Biomechanics Of Insect Flight: Form, Function, Evolution*. Princeton University Press, 2002.
- R. Dudley and C. P. Ellington. Mechanics of forward flight in bumblebees: I. kinematics and morphology. *Journal of Experimental Biology*, 148(1):19–52, 1990.
- C. P. Ellington. The aerodynamics of hovering insect flight. I. the quasi-steady analysis. *Philosophical Transactions of the Royal Society of London. Series B, Biological Sciences*, 305(1122):1–15, Feb. 1984a.
- C. P. Ellington. The aerodynamics of hovering insect flight. II. Morphological parameters. *Philosophical Transactions of the Royal Society of London. Series B, Biological Sciences*, 305(1122):17–40, Feb. 1984b. doi:10.1098/rstb.1984.0050.
- C. P. Ellington. The aerodynamics of hovering insect flight. III. kinematics. *Philosophical Transactions of the Royal Society of London. Series B, Biological Sciences*, 305(1122):41–78, Feb. 1984c.
- C. P. Ellington. The aerodynamics of hovering insect flight. IV. aerodynamic mechanisms. *Philosophical Transactions of the Royal Society of London. Series B, Biological Sciences*, 305(1122):79–113, Feb. 1984d.
- C. P. Ellington. The novel aerodynamics of insect flight: application to micro-air vehicles. *Journal of Experimental Biology*, 202:3439–3448, 1999.
- C. P. Ellington, C. van den Berg, A. P. Willmott, and A. L. R. Thomas. Leading-edge vortices in insect flight. *Nature*, 384:626–630, 1996. doi:10.1038/384626a0.
- I. Faruque and J. S. Humbert. Dipteran insect flight dynamics. Part 1: Longitudinal motion about hover. *Journal of Theoretical Biology*, 264(2):538–552, May. 2010a. doi:10.1016/j.jtbi.2010.02.018.
- I. Faruque and J. S. Humbert. Dipteran insect flight dynamics. Part 2: Lateral-directional motion about hover. *Journal of Theoretical Biology*, 265(3):306–313, Aug. 2010b. doi:10.1016/j.jtbi.2010.05.003.
- Festo. BionicOpter. [http://www.festo.com/cms/en\\_corp/13165.htm](http://www.festo.com/cms/en_corp/13165.htm), 2013. Accessed: 18/08/2014.
- B. M. Finio and R. J. Wood. Distributed power and control actuation in the thoracic mechanics of a robotic insect. *Bioinspiration & biomimetics*, 5(4):045006, 2010. doi:10.1088/1748-3182/5/4/045006.
- Flugtechnik & Leichtbau. Eta glider. <http://www.leichtwerk.de/eta/de/flugerprobung/leistung.html>, 2001. Accessed: 18/08/2014.

- G. F. Franklin, J. Powel, and A. Emami-Naeini. *Feedback Control of Dynamic Systems*. Prentice Hall, 4th edition, 2002.
- S. N. Fry, R. Sayaman, and M. H. Dickinson. The aerodynamics of free-flight maneuvers in drosophila. *Science*, 300(5618):495–498, Apr. 2003.
- S. B. Fuller, M. Karpelson, A. Censi, K. Y. Ma, and R. J. Wood. Controlling free flight of a robotic fly using an onboard vision sensor inspired by insect ocelli. *Journal of The Royal Society Interface*, 11(97), 2014. doi:10.1098/rsif.2014.0281.
- Y. C. Fung. *An introduction to the theory of aeroelasticity*. Dover, New York, 1969.
- S. J. Furst, G. Bunget, and S. Seelecke. Design and fabrication of a bat-inspired flapping-flight platform using shape memory alloy muscles and joints. *Smart Materials and Structures*, 22(1):014011, 2013. doi:10.1088/0964-1726/22/1/014011.
- J. F. Goosen, H. J. Peters, Q. Wang, P. Tiso, and F. van Keulen. Resonance based flapping wing micro air vehicle. In *International Micro Air Vehicle Conference and Flight Competition (IMAV2013), Toulouse, France, September 17-20*, page 8, 2013.
- C. H. Greenewalt. *Hummingbirds*. Dover Publications, 1990.
- S. Hauert, J.-C. Zufferey, and D. Floreano. Evolved swarming without positioning information: an application in aerial communication relay. *Autonomous Robots*, 26(1):21–32, 2009. ISSN 0929-5593. doi:10.1007/s10514-008-9104-9.
- T. L. Hedrick, B. Cheng, and X. Deng. Wingbeat time and the scaling of passive rotational damping in flapping flight. *Science*, 324(5924):252–255, Apr. 2009. doi:10.1126/science.1168431.
- R. Hengstenberg, D. Sandeman, and B. Hengstenberg. Compensatory head roll in the blowfly calliphora during flight. *Proceedings of the Royal society of London. Series B. Biological sciences*, 227(1249):455–482, 1986.
- R. W. Hill, G. A. Wyse, and M. Anderson. *Animal Physiology, companion website: sites.sinauer.com/animalphys3e*. Sinauer Associates, Inc., 2012.
- L. Hines, D. Campolo, and M. Sitti. Liftoff of a motor-driven, flapping-wing microaerial vehicle capable of resonance. *IEEE Transactions on Robotics*, 30(1): 220–231, 2014. doi:10.1109/TRO.2013.2280057.
- M. Karasek and A. Preumont. Flapping flight stability in hover: A comparison of various aerodynamic models. *International Journal of Micro Air Vehicles*, 4(3): 203–226, 2012. doi:10.1260/1756-8293.4.3.203.

- M. Karasek, Y. Nan, I. Romanescu, and A. Preumont. Pitch moment generation and measurement in a robotic hummingbird. *International Journal of Micro Air Vehicles*, 5(4):299–310, 2013. doi:10.1260/1756-8293.5.4.299.
- M. Karasek, A. Hua, Y. Nan, M. Lalami, and A. Preumont. Pitch and roll control mechanism for a hovering flapping wing MAV. In *International Micro Air Vehicle Conference and Flight Competition (IMAV2014), Delft, The Netherlands, August 12-15*, pages 118–125, 2014.
- M. T. Keenon, K. R. Klingebiel, H. Won, and A. Andriukov. Development of the nano hummingbird: A tailless flapping wing micro air vehicle. *AIAA paper 2012-0588*, pages 1–24, 2012.
- M. Kramer. Die zunahme des maximalauftriebes von tragflügeln bei plötzlicher anstellwinkel vergrösserung. *Zeitschrift für Flugtechnik und Motorluftschiffahrt*, 23:185–189, 1932.
- D. C. Lagoudas. *Shape Memory Alloys: Modeling and Engineering Applications*. Springer, 2008. doi:10.1007/978-0-387-47685-8.
- F.-O. Lehmann. The mechanisms of lift enhancement in insect flight. *Naturwissenschaften*, 91(3):101–122, 2004. doi:10.1007/s00114-004-0502-3.
- D. Lentink and M. H. Dickinson. Biofluidynamic scaling of flapping, spinning and translating fins and wings. *Journal of Experimental Biology*, 212(16):2691–2704, 2009. doi:10.1242/jeb.022251.
- K. Y. Ma, P. Chirarattananon, S. B. Fuller, and R. J. Wood. Controlled flight of a biologically inspired, insect-scale robot. *Science*, 340:603–607, 2013. doi:10.1126/science.1231806.
- J. H. Marden. Maximum lift production during takeoff in flying animals. *Journal of Experimental Biology*, 130(1):235–258, 1987.
- MathWorks. Matlab documentation: atan2 function. <http://www.mathworks.com/help/matlab/ref/atan2.html>, 2014. Accessed: 18/08/2014.
- W. J. Maybury and F.-O. Lehmann. The fluid dynamics of flight control by kinematic phase lag variation between two robotic insect wings. *Journal of Experimental Biology*, 207:4707–4726, 2004. doi:10.1242/jeb.01319.
- A. Meskers. High energy density micro-actuation based on gas generation by means of catalysis of liquid chemical energy. Master’s thesis, Delft University of Technology, 2010.

- N. Michael, D. Mellinger, Q. Lindsey, and V. Kumar. The GRASP Multiple Micro UAV Testbed. *IEEE Robotics and Automation*, 17(3):56–65, 2010. doi:10.1109/MRA.2010.937855.
- J. Mohd Jani, M. Leary, A. Subic, and M. A. Gibson. A review of shape memory alloy research, applications and opportunities. *Materials & Design*, 56:1078–1113, 2014. doi:10.1016/j.matdes.2013.11.084.
- F. T. Muijres, L. Johansson, R. Barfield, M. Wolf, G. Spedding, and A. Hedenstrom. Leading-edge vortex improves lift in slow-flying bats. *Science*, 319(5867):1250–1253, 2008.
- G. Neuweiler. *The Biology of Bats*. Oxford University Press, 2000.
- U. M. Norberg. Evolution of vertebrate flight: an aerodynamic model for the transition from gliding to active flight. *American Naturalist*, 126(3):303–327, 1985.
- U. M. L. Norberg. Structure, form, and function of flight in engineering and the living world. *Journal of morphology*, 252(1):52–81, 2002. doi:10.1002/jmor.10013.
- C. T. Orlowski and A. R. Girard. Stability derivatives for a flapping wing MAV in a hover condition using local averaging. In *2011 American Control Conf.*, pages 1604–1609, San Francisco, California, Jun. - Jul. 2011.
- G. D. Padfield. *Helicopter Flight Dynamics: The Theory and Application of Flying Qualities and Simulation Modeling*. Blackwell Science Ltd., 2nd edition, 2007.
- J. H. Park and K.-J. Yoon. Designing a biomimetic ornithopter capable of sustained and controlled flight. *Journal of Bionic Engineering*, 5(1):39–47, 2008.
- C. Pennycuick. Gliding flight of the white-backed vulture *gyps africanus*. *Journal of Experimental Biology*, 55(1):13–38, 1971.
- T. Rakotomamonjy, M. Ouladsine, and T. L. Moing. Longitudinal modelling and control of a flapping-wing micro aerial vehicle. *Control engineering practice*, 18 (7):679–690, Jul. 2010. doi:10.1016/j.conengprac.2010.02.002.
- C. Richter and H. Lipson. Untethered hovering flapping flight of a 3d-printed mechanical insect. *Artificial life*, 17(2):73–86, 2011. doi:10.1162/artl\_a\_00020.
- H. Rifai, J.-F. Guerrero-Castellanos, N. Marchand, and G. Poulin. Bounded attitude control of a flapping wing micro aerial vehicle using direct sensors measurements. In *2009 IEEE International Conference on Robotics and Automation, Kobe, Japan*, pages 3644–3650. 2009 IEEE International Conference on Robotics and Automation, Kobe, Japan, 2009.

- L. Ristroph and S. Childress. Stable hovering of a jellyfish-like flying machine. *Journal of The Royal Society Interface*, 11(92):1–13, 2014. doi:10.1098/rsif.2013.0992.
- L. Ristroph, G. J. Berman, A. J. Bergou, Z. J. Wang, and I. Cohen. Automated hull reconstruction motion tracking (HRMT) applied to sideways maneuvers of free-flying insects. *Journal of Experimental Biology*, 212(9):1324–1335, 2009. doi:10.1242/jeb.025502.
- L. Ristroph, A. J. Bergou, G. Ristroph, K. Coumes, G. J. Berman, J. Guckenheimer, Z. J. Wang, and I. Cohen. Discovering the flight autostabilizer of fruit flies by inducing aerial stumbles. *Proceedings of the National Academy of Sciences*, 107(11):4820–4824, 2010. doi:10.1073/pnas.1000615107.
- L. Ristroph, A. J. Bergou, J. Guckenheimer, Z. J. Wang, and I. Cohen. Paddling mode of forward flight in insects. *Physical review letters*, 106(17):178103, 2011. doi:PhysRevLett.106.178103.
- L. Ristroph, G. Ristroph, S. Morozova, A. J. Bergou, S. Chang, J. Guckenheimer, Z. J. Wang, and I. Cohen. Active and passive stabilization of body pitch in insect flight. *Journal of The Royal Society Interface*, 10(85):1–13, 2013. doi:10.1098/rsif.2013.0237.
- F. Ruffier and N. Franceschini. Optic flow regulation: the key to aircraft automatic guidance. *Robotics and Autonomous Systems*, 50(4):177–194, 2005. doi:10.1016/j.robot.2004.09.016.
- SAES Getters. Smartflex wire & springs. [http://www.saesgetters.com/sites/default/files/SmartFlex%20Wire%20%26%20Spring%20datasheets\\_1.pdf](http://www.saesgetters.com/sites/default/files/SmartFlex%20Wire%20%26%20Spring%20datasheets_1.pdf), 2009. Accessed: 18/08/2014.
- S. P. Sane. The aerodynamics of insect flight. *Journal of Experimental Biology*, 206:4191–4208, 2003. doi:doi:10.1242/jeb.00663.
- S. P. Sane and M. H. Dickinson. The control of flight force by a flapping wing: lift and drag production. *Journal of Experimental Biology*, 204:2607–2626, 2001.
- S. P. Sane and M. H. Dickinson. The aerodynamic effects of wing rotation and a revised quasi-steady model of flapping flight. *Journal of Experimental Biology*, 205:1087–1096, 2002.
- L. I. Sedov. *Two-dimensional problems in hydromechanics and aerodynamics*. Interscience publishers, New York, 1965.
- A. Sherman and M. H. Dickinson. Summation of visual and mechanosensory feedback in drosophila flight control. *Journal of Experimental Biology*, 207(1):133–142, 2004. doi:10.1242/jeb.00731.

- W. Shyy and H. Liu. Flapping wings and aerodynamic lift: the role of leading-edge vortices. *AIAA Journal*, 45(12):2817–2819, 2007.
- W. Shyy, H. Aono, S. Chimakurthi, P. Trizila, C.-K. Kang, C. Cesnik, and H. Liu. Recent progress in flapping wing aerodynamics and aeroelasticity. *Progress in Aerospace Sciences*, 46(7):284–327, Oct. 2010. doi:<http://dx.doi.org/10.1016/j.paerosci.2010.01.001>.
- W. Shyy, H. Aono, C.-K. Kang, and H. Liu. *An Introduction to Flapping Wing Aerodynamics*. Cambridge University Press, 2013.
- M. Sun and J. H. Wu. Aerodynamic force generation and power requirements in forward flight in a fruit fly with modeled wing motion. *Journal of Experimental Biology*, 206:3065–3083, 2003. doi:[doi:10.1242/jeb.00517](https://doi.org/10.1242/jeb.00517).
- M. Sun and Y. Xiong. Dynamic flight stability of a hovering bumblebee. *Journal of Experimental Biology*, 208:447–459, 2005.
- M. Sun, J. Wang, and Y. Xiong. Dynamic flight stability of hovering insects. *Acta Mech. Sinica*, 23(3):231–246, Jun. 2007. doi:[10.1007/s10409-007-0068-3](https://doi.org/10.1007/s10409-007-0068-3).
- H. Tanaka, H. Suzuki, I. Kitamura, M. Maeda, and H. Liu. Lift generation of hummingbird wing models with flexible loosened membranes. In *2013 IEEE/RSJ International Conference on Intelligent Robots and Systems (IROS)*, pages 3777–3783, 2013.
- G. K. Taylor and H. G. Krapp. Sensory systems and flight stability: what do insects measure and why? *Advances in insect physiology*, 34(231-316), 2008. doi:[10.1016/S0065-2806\(07\)34005-8](https://doi.org/10.1016/S0065-2806(07)34005-8).
- G. K. Taylor and A. L. R. Thomas. Dynamic flight stability in the desert locust *schistocerca gregaria*. *Journal of Experimental Biology*, 206(16):2803–2829, Aug. 2003. doi:[10.1242/jeb.00501](https://doi.org/10.1242/jeb.00501).
- G. K. Taylor, R. L. Nudds, and A. L. R. Thomas. Flying and swimming animals cruise at a Strouhal number tuned for high power efficiency. *Nature*, 425:707–711, Oct. 2003. doi:[10.1038/nature02000](https://doi.org/10.1038/nature02000).
- S. Tijmons, G. Croon, B. Remes, C. Wagter, R. Ruijsink, E.-J. Kampen, and Q. Chu. Stereo vision based obstacle avoidance on flapping wing mavs. In Q. Chu, B. Mulder, D. Choukroun, E.-J. Kampen, C. Visser, and G. Looye, editors, *Advances in Aerospace Guidance, Navigation and Control*, pages 463–482. Springer Berlin Heidelberg, 2013. doi:[10.1007/978-3-642-38253-6\\_28](https://doi.org/10.1007/978-3-642-38253-6_28).

- B. W. Tobalske and K. P. Dial. Flight kinematics of black-billed magpies and pigeons over a wide range of speeds. *Journal of Experimental Biology*, 1999(2):263–280, 1996.
- B. W. Tobalske, W. L. Peacock, and K. P. Dial. Kinematics of flap-bounding flight in the zebra finch over a wide range of speeds. *Journal of Experimental Biology*, 202(13):1725–1739, 1999.
- B. W. Tobalske, D. R. Warrick, C. J. Clark, D. R. Powers, T. L. Hedrick, G. A. Hyder, and A. A. Biewener. Three-dimensional kinematics of hummingbird flight. *Journal of Experimental Biology*, 210(13):2368–2382, Jul. 2007. doi:10.1242/jeb.005686.
- T. Q. Truong, V. H. Phan, S. P. Sane, and H. C. Park. Pitching moment generation in an insect-mimicking flapping-wing system. *Journal of Bionic Engineering*, 11 (1):36–51, 2014.
- J. R. Usherwood and C. P. Ellington. The aerodynamics of revolving wings: I. model hawkmoth wings. *Journal of Experimental Biology*, 205:1547–1564, 2002.
- F. van Breugel, W. Regan, and H. Lipson. From insects to machines. *Robotics Automation Magazine, IEEE*, 15(4):68–74, 2008. doi:10.1109/MRA.2008.929923.
- C. van den Berg and C. P. Ellington. The vortex wake of a hoveringmodel hawkmoth. *Philosophical Transactions of the Royal Society of London. Series B: Biological Sciences*, 352:317–328, 1997.
- T. Vanneste, A. Bontemps, X. Q. Bao, S. Grondel, J.-B. Paquet, and E. Cattan. Polymer-based flapping-wing robotic insects: Progresses in wing fabrication, conception and simulation. In *ASME 2011 International Mechanical Engineering Congress and Exposition*, pages 771–778. American Society of Mechanical Engineers, 2011.
- S. Vogel. Flight in drosophila II. variations in stroke parameters and wing contour. *Journal of Experimental Biology*, 46(2):383–392, 1967.
- C. D. Wagter, S. Tijmons, B. Remes, and G. de Croon. Autonomous flight of a 20-gram flapping wing mav with a 4-gram onboard stereo vision system. Accepted at ICRA 2014, 2014.
- P. Walker. Experiments on the growth of circulation about a wing and an apparatus for measuring fluid motion. Technical Report 1402, Air ministry, Aeronautical Research Committee, Reports and memoranda, 1932.

- D. Warrick, T. Hedrick, M. J. Fernndez, B. Tobalske, and A. Biewener. Hummingbird flight. *Current Biology*, 22(12):472–477, 2012.
- D. R. Warrick, B. W. Tobalske, and D. R. Powers. Aerodynamics of the hovering hummingbird. *Nature*, 435:1094–1097, 2005. doi:10.1038/nature03647.
- D. R. Warrick, B. W. Tobalske, and D. R. Powers. Lift production in the hovering hummingbird. *Proceedings of the Royal Society B*, 276:3747–3752, 2009. doi:10.1098/rspb.2009.1003.
- T. Weis-Fogh. Quick estimates of flight fitness in hovering animals, including novel mechanisms for lift production. *Journal of Experimental Biology*, 59(1):169–230, 1973.
- R. Whitford. *Design for air combat*. Jane’s Publishing Company Limited, 1987.
- A. P. Willmott and C. P. Ellington. The mechanics of flight in the hawkmoth *manduca sexta* I. Kinematics of hovering and forward flight. *Journal of Experimental Biology*, 200:2705–2722, 1997.
- R. J. Wood. The first takeoff of a biologically inspired at-scale robotic insect. *IEEE Transactions on Robotics*, 24(2):341–347, Apr. 2008. doi:10.1109/TRO.2008.916997.
- J. Wu and M. Sun. Control for going from hovering to small speed flight of a model insect. *Acta Mech. Sinica*, 25(3):295–302, Jun. 2009. doi:10.1007/s10409-009-0241-y.
- Y. Xiong and M. Sun. Dynamic flight stability of a bumblebee in forward flight. *Acta Mech. Sinica*, 24(1):25–36, Feb. 2008. doi:DOI 10.1007/s10409-007-0121-2.
- L.-J. Yang, C.-K. Hsu, F.-Y. Hsiao, C.-K. Feng, and Y.-K. Shen. A micro-aerial-vehicle (mav) with figure-of-eight flapping induced by flexible wing frames. In *Conference proceedings of 47th AIAA Aerospace Science Meeting, Orlando, USA, 5-8, Jan., 2009 (AIAA-2009-0875)*, page 14. 47th AIAA Aerospace Science Meeting, Orlando, USA, 2009.
- J. Zanker. The wing beat of *drosophila melanogaster*. I. Kinematics. *Philosophical Transactions of the Royal Society of London. Series B, Biological Sciences*, 327 (1238):1–18, 1990.
- J. M. Zanker. How does lateral abdomen deflection contribute to flight control of *drosophila melanogaster*? *Journal of Comparative Physiology A*, 162(5):581–588, 1988.

- J. M. Zanker, M. Egelhaaf, and A.-K. Warzecha. On the coordination of motor output during visual flight control of flies. *Journal of Comparative Physiology A*, 169(2):127–134, 1991.
- P. Zdunich, D. Bilyk, M. MacMaster, D. Loewen, J. DeLaurier, R. Kornbluh, T. Low, S. Stanford, and D. Holeman. Development and testing of the Mentor flapping-wing micro air vehicle. *Journal of Aircraft*, 44(5):1701–1711, 2007.
- Y. Zhang and M. Sun. Dynamic flight stability of a hovering model insect: lateral motion. *Acta Mech. Sinica*, 26(2):175–190, May. 2010a. doi:10.1007/s10409-009-0303-1.
- Y. Zhang and M. Sun. Dynamic flight stability of a hovering model insect: theory versus simulation using equations of motion coupled with navier-stokes equation. *Acta Mech. Sinica*, 26(4):509–520, 2010b. doi:10.1007/s10409-010-0360-5.